מכון ויצמן למדע
WEIZMANN INSTITUTE OF SCIENCE

Thesis for the degree
Doctor of Philosophy

עבודת גמר (תזה) לתואר
דוקטור לפילוסופיה

Submitted to the Scientific Council of the
Weizmann Institute of Science
Rehovot, Israel

מוגשת למועצה המדעית של
מכון ויצמן למדע
רחובות, ישראל

By
Dan Yudilevich

מאת
דן יודילביץ

טכניקות תהודה מגנטית זעירות המבוססות על פגם החנקן-היעדרות ביהלום

Nanoscale magnetic resonance techniques based on the nitrogen-vacancy center in diamond

Advisor:
Dr. Amit Finkler

מנחה:
ד״ר עמית פינקלר

March, 2024

אדר ב׳, ה׳תשפ״ד

מוקדש לשירן, אשתי האהובה, ולגפן וארז, ילדיי המופלאים.
די לי באהבתכם.

Contents

List of Figures

Abstract

Magnetic resonance techniques constitute a powerful toolbox with a vast impact on the natural sciences. Contemporary techniques, however, are only suitable for large ensembles of materials, and details on the structure and dynamics of single molecules are concealed in the averaged picture. Single-molecule magnetic resonance thus holds great promise in revealing phenomena of the structure, dynamics, and quantum processes pertinent to biomolecules, which have hitherto been elusive.

The nitrogen-vacancy (NV) center, a point defect of the diamond crystal, can function as a quantum sensor capable of detecting minute fields in nanoscale volumes. Quantum sensing with NV centers is thus a promising approach toward single-molecule magnetic resonance. Here, I present progress on nanoscale magnetic resonance techniques using NV centers.

The magnetic tomography technique, based on dipolar coupling measurements in a rotating magnetic field, was developed to map the position of single electron spins near NV centers. I demonstrated the technique by locating an individual electron spin $\sim$5 nm from the NV sensor with Ångstrom precision. I then detail a theoretical protocol based on magnetic tomography to map two coupled spins as a route to perform single-molecule distance measurements.

Furthermore, I describe a novel RF spiral antenna developed for fast nuclear spin manipulation based on strong driving fields. Tailored for quantum sensing experiments using the diamond's nitrogen-vacancy (NV) center, the antenna may be applicable to other solid-state defects. I demonstrate it by driving proton spins in an organic sample on the diamond's surface at a Rabi frequency of over 500 kHz and an ^{15}N spin at over 700 kHz. The proton spin flips (π-pulse), briefer than 1 µs, are faster than previously reported for NV-based nuclear magnetic resonance. Fast nuclear spin manipulation benefits nanoscale magnetic resonance and NV experiments utilizing nuclear spins as ancilla qubits.

Finally, I discuss the implications of driving spins with an intense field tilted from the transverse plane in a regime where the driving amplitude is comparable to the spin-state splitting, as our novel RF antenna enables. The rotating wave approximation does not describe the dynamics well in this regime, and a simple recipe to optimize pulse fidelity based on a phase and offset-shifted sine drive is introduced. This approach is of particular value to NV-based experiments but relevant to other solid-state spin systems.

The results and progress I show here represent significant contributions to nanoscale magnetic resonance based on NV centers, particularly toward the goal of single-molecule distance measurements.

Acknowledgments

THIS THESIS AND THE RESEARCH IT SUMMARIZES WOULD NOT HAVE BEEN POSSIBLE WITHOUT THE SUPPORT OF NUMEROUS INDIVIDUALS WHOM I WOULD LIKE TO THANK HERE.

Foremost, I extend my deepest appreciation to my advisor, Dr. Amit Finkler. Your mentorship was a harmonious blend of direction and freedom. You cultivated a pleasant and balanced work environment, the value of which should not be underestimated. Your trust during critical junctures, coupled with the liberty to learn through trial and error, has defined my time here. Our dialogues, ranging from the intricacies of technicalities to the broader vistas of physical concepts, have been wellsprings of enlightenment.

To my esteemed colleagues in the QuEST group — past and present — your camaraderie has been the catalyst for both scientific breakthroughs and personal growth. Every word in this thesis may be traced back to enlightening scientific and technical discussions. Leora Schein-Lubomirsky, Dr. Jitender Kumar, Inbar Zohar, Ariel Smooha, Woody Rosenberg, and Asad Awadallah: your contributions transcend mere research; they are shared experiences that have infused these years with joy amidst the rigors of academia. Special thanks to Leah Fuhrman Javitt and Yonatan Vernik, whose rotation projects contributed to developing the RF spiral antenna.

The pillars of support provided by the Chemical Research Support staff at WIS deserve heartfelt recognition. Alexander Kuprienko's machining prowess, often summoned at the eleventh hour, has been indispensable. Gratitude extends to Assaf Hazan, Leonid Tunik, Sharon Garusi, Dr. Alex Yoffe, and Dr. Ora Bitton for their assistance in nanofabrication; Dr. Hagai Cohen for XPS analysis; and Dr. Raanan Carmieli for EPR analysis and consultation. I thank Dr. Khriesto Shurrush of the G-INCPM for material synthesis.

To the administrative luminaries of the Chemical and Biological Physics department — Terry Debesh, Victoria Ornsthein, and Sigalit Levy — your patience and dexterity have been invaluable. I thank the Perlman building staff - Reshef Azaria, Tamir Chalaf, and Amir Kronenberg- for facilitating a conducive research environment.

The staff of the Physics Core Facilities assisted us in various projects. I thank Lilia Goffer on instrument design, Dr. Michael Rapaport for sharing his cryogenic wisdom; and Haim Sade, Alex Jahanfard, and Uri Boblitski from the mechanical workshop. Their expertise and craftsmanship have been the scaffolding upon which experiments were built.

I acknowledge our collaborators for fruitful work: Prof. Alex Retzker and Dr. Ido Schaefer

(HUJI); Prof. Christian Degen and Konstantin Herb (ETH Zürich); Prof. Olav Schiemann and Lars Westhofen of (Universität Bonn); and Dr. Rainer Stöhr of (Universität Stuttgart). Special thanks to Alon Salhov (HUJI) for our collaboration and invigorating discussions.

Friends and colleagues have contributed valuable wisdom and material at crucial points; I thank Dr. Ron Tenne, Dr. Ori Mor, Dr. Lee Drori, and Dr. Angeliki Giannouli.

Finally, I want to express my gratitude to my family, whose steadfast support has been the cornerstone of my achievements. I am grateful to my parents, whose faith in my abilities gave me the impetus to move forward. To Gali and Ori, whose support during critical times is immeasurable. Last but certainly not least, I would like to convey my boundless appreciation to my beloved wife and best friend, Shiran. Your love and encouragement are my constant anchor, and our beloved children, Gefen and Erez, are a daily reminder of the true beauty of nature.

In this symphony of gratitude, every note represents a soul whose presence has enriched my journey. I sincerely hope that I have not left anyone out, and if I have, I apologize for it. It is not because I lack gratitude but because this period has been overwhelming. To each and every one of you, I want to say a heartfelt thank you.

Declaration

I hereby declare that this thesis summarizes my own independent research. I certify that, to the best of my knowledge and belief, this work contains no material previously published or written by another person except where due reference has been made in the text. The following is the list of contributions by other authors:

- Dr. Jitender Kumar, Department of Chemical and Biological Physics, WIS, constructed significant parts of the low-temperature system discussed in Chapter 2.
- Leora Schein-Lubomirsky, Department of Chemical and Biological Physics, WIS, contributed to the experimental software discussed in Chapter 2.
- Dr. Andrej Denisenko and Dr. Rainer Stöhr, 3. Physikalisches Institut, Universität Stuttgart, fabricated the diamond membrane used in the experiment of Chapter 3.
- Prof. Alex Retzker, Alon Salhov, and Dr. Ido Schaefer, the Racah Institute of Physics, the Hebrew University of Jerusalem, Israel, contributed to the theory presented in Chapter 6. Alon played a key role in developing the theory, and Ido performed the optimal control calculations.
- Konstantin Herb and Prof. Christian Degen, Laboratory for Solid State Physics, ETH Zürich, supplied, and performed surface treatments to the diamond used in the experiment of Chapter 5.
- Dr. Khriesto Shurrush, G-INCPM, WIS, synthesized the nitroxide biradical molecules mentioned in Appendix D. Dr. Raanan Carmieli, Department of Chemical Research Support, WIS, conducted the EPR measurements of these molecules.

List of Abbreviations

Table 1: List of abbreviations used in the text.

AC	Alternating current	NMR	Nuclear magnetic resonance
APD	Avalanche photodiode	NV	Nitrogen-vacancy
AFM	Atomic force microscopy	ODMR	Optically detected magnetic resonance
AWG	Arbitrary waveform generator	OCT	Optimal control theory
CPMG	Carr Purcell Meiboom Gill (pulse sequence)	PL	Photoluminescence
DC	Direct current	RF	Radio-frequency
DD	Dynamical decoupling	RT	Room-temperature
DEER	Double electron-electron resonance	RWA	Rotating-wave approximation
ENDOR	Electron-nuclear double resonance	SL	Spin label
EPR	Electron paramagnetic resonance	SNR	Signal-to-noise ratio
ESLAC	Excited state level anti-crossing	SPM	Scanning probe microscope
ESR	Electron spin resonance	SRIM	Stopping and range of ions in matter
FFT	Fast Fourier transform	T_1	Longitudinal relaxation time
GSLAC	Ground state level anti-crossing	T_2	Transverse relaxation time (decoherence)
IR	Infra-red	T_2^*	Dephasing time
LT	Low-temperature	UHV	Ultra-high vacuum
MRS	Magnetic resonance spectroscopy	WIS	Weizmann Institute of Science
MW	Microwave		

1

Introduction

NANOSCALE MAGNETIC RESONANCE BASED ON NITROGEN-VACANCY CENTERS IS A DIVERSE FIELD AT THE INTERSECTION OF SEVERAL DISCIPLINES, INCLUDING MAGNETIC RESONANCE, ATOMIC AND MOLECULAR PHYSICS, AND CONDENSED MATTER PHYSICS. The following chapter provides relevant background for this thesis. Section 1.1 presents the topic of nanoscale magnetic resonance. Section 1.2 introduces the nitrogen-vacancy center in diamond, and Section 1.3 describes its function as a quantum sensor. Section 1.5 discusses recent advances in applying the nitrogen-vacancy center to the challenges of nanoscale magnetic resonance. Finally, Section 1.6 presents some open questions in the field and the goals of this work in light of these questions.

1.1 NANOSCALE MAGNETIC RESONANCE SPECTROSCOPY

Magnetic resonance techniques probe the spin degrees of freedom in materials and are prominent in physical and life sciences. Notably, magnetic resonance imaging (MRI) is a fascinating example of how the once exotic physical phenomenon of nuclear magnetic resonance (NMR) evolved into a ubiquitous and indispensable diagnostic tool within a few decades. Conventional magnetic resonance techniques, that is, induction-based detection, are generally limited to large ensembles, as detection is based on macroscopic coils to pick up the signal induced by precessing spins. For nuclear magnetic resonance, the limit is $> 10^9$ spins (nanoliter volumes)[1]. The sensitivity of commercial electron paramagnetic resonance (EPR) systems is likewise $\sim 10^9$ spins[2]. Further miniaturization is a subject of ongoing research[3,4], with cutting-edge induction-based EPR reaching sensitivities of a few tens of spins[5,6], and specialized microresonator detection achieving similar sensitivities[7]. Thus, nanoscale magnetic resonance spectroscopy, down to the single-molecule level, remains an open frontier.

Technical abilities have set the resolution of measurement techniques throughout history, setting paradigms for scientific research, and advances in recent years have opened a frontier of single-molecule experiments. Notably, single-molecule spectroscopy techniques that have emerged in recent decades unveil information previously concealed by ensemble-averaged measurements[8]. Similarly, the nascent field of nanoscale magnetic resonance has the potential to uncover information on the structure of molecules and materials, deepening our understanding of their roles in various chemical and biological processes.

Leading approaches toward single-molecule magnetic resonance spectroscopy rely on quantum sensors, where the quantum state of a system is utilized to measure a physical quantity[9]. Quantum sensors can sense minute classical fields over a broad spectrum and detect quantum state evolution via quantum entanglement. The diamond lattice's nitrogen-vacancy (NV) defect is a prevalent, point-like quantum sensor, combining nanometer spatial resolution, high sensitivity, and robustness in a wide range of environments[10].

1.2 THE NITROGEN-VACANCY CENTER IN DIAMOND

The diamond crystal's nitrogen-vacancy (NV) defect, known as the NV center, is one of many different point defects found in diamonds[11]. Over four decades of experimental and theoretical studies have deduced its structure; EPR experiments of diamond crystals[12,13] accumulated much knowledge on the defect, and in recent years by single-defect spectroscopic studies[14]. The NV center today is an emerging quantum sensor, owing to a unique set of characteristics, which include optical spin readout and appreciable quantum coherence under ambient conditions[10].

The NV center is a paramagnetic defect exhibiting spin-dependent photoluminescence (PL), enabling optical measurement of its quantum spin state. This property is the basis for its role as a quantum sensor, as fields affect its electronic structure and spin state evolution so that physical quantities may be measured through the quantum spin state.

In the following section, I discuss the main details of the NV center system at room temperature (RT). As the body of work on the NV center's electronic structure and dynamics is extensive, I focus on the most pertinent information. I primarily relied on a comprehensive review by Doherty et al.[14]; other works are cited where needed. I note that research on the topic is ongoing, so the models and values presented here may be updated in future work.

ELECTRONIC STRUCTURE AND DYNAMICS

The nitrogen-vacancy defect spans two adjacent lattice sites of the diamond's carbon lattice - a nitrogen substitution defect and an adjacent vacancy. The defect's axis (nitrogen to vacancy axis) thus aligns with the $\langle 111\rangle$ family of lattice directions and exhibits a C_{3v} symmetry (see Fig. 1.1(a)).

The NV center has two stable charge states - neutral (NV°) and negatively charged (NV^{-}). Both states fluoresce in the visible-infrared (IR) range. However, the PL rate depends on the electronic ground state's spin state only in the NV^{-} state. The spin-dependent PL rate enables optical readout of its spin state. This characteristic makes the NV^{-} an accessible qubit, attractive for a myriad of

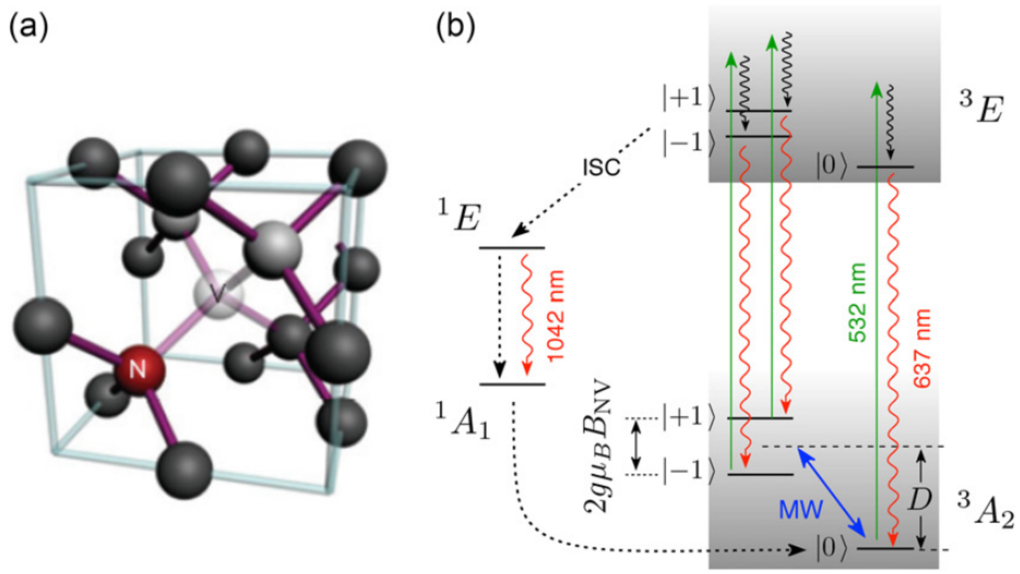

Figure 1.1: NV center structure and energy diagram at room temperature. (a) Schematic description of the nitrogen-vacancy defect within the diamond lattice. (b) Energy diagram of NV$^-$ defect electronic and spin states. The diagram assumes a magnetic field B_{NV} along the NV axis. Reprinted from ref. [15].

quantum sensing and quantum information applications. In this work, we focus only on the NV$^-$ charge state, and from here on, *NV center* will refer to the nitrogen-vacancy defect exclusively in its negatively charged state.

The defect breaks the crystal's translation symmetry, forming highly localized molecular orbitals around the nearest neighbors of the vacancy (three carbon atoms and the substitutional nitrogen). The presently accepted model for NV$^-$ consists of six electrons from dangling bonds - three from the adjacent carbon atoms, two from the nitrogen, and the ionization electron. These electrons occupy molecular orbitals formed from the dangling bonds surrounding the vacancy. The highest occupied electronic state is termed the *ground state*. In Fig. 1.1(b) the ground state is marked by ^{3}A$_2$ (describing its symmetry group). The NV$^-$ ground state is spin-1, so it has a triplet spin manifold. The defect may be excited under proper optical illumination ($>$1.945 eV) to another triplet state, the *excited state*, marked in Fig. 1.1(b) by ^{3}E. The relevant RT energy structure is depicted in Fig. 1.1(b). At low temperatures ($\sim$5 K), the higher-energy molecular orbitals are non-degenerate, resulting in a more complex excited state fine structure. At RT, phonons average the orbitals; this work focuses on the NV center at RT, so I will not discuss the LT fine structure.

The two valence electrons of the defect are strongly coupled, forming a spin-1 system with a singlet state ($S = 0$) and a triplet characterized by a zero-field splitting (ZFS). Due to the symmetry of the defect, the zero-field interaction tensor's principal axis coincides with the axis connecting the nitrogen and the vacancy, known as the NV axis. The coordinate system is set with $\hat{z}$ parallel to the NV axis by convention. The zero-field tensor is axially symmetric. The ground state axial component is $D = 2\pi \times 2.871\,\text{GHz}$, and its transverse component (traditionally marked by E) is zero. The full zero-field tensor is thus:

$$\mathbf{D} = \begin{pmatrix} -\frac{1}{3}D & 0 & 0 \\ 0 & -\frac{1}{3}D & 0 \\ 0 & 0 & \frac{2}{3}D \end{pmatrix} = \begin{pmatrix} 0 & 0 & 0 \\ 0 & 0 & 0 \\ 0 & 0 & D \end{pmatrix} - \frac{1}{3}D \begin{pmatrix} 1 & 0 & 0 \\ 0 & 1 & 0 \\ 0 & 0 & 1 \end{pmatrix} \tag{1.1}$$

Omitting the isotropic term, which only amounts to a constant energy shift, the NV center's ground state spin-Hamiltonian under a magnetic field (**B**) reads[a]:

$$\mathcal{H} = DS_z^2 + \gamma_{nv}\mathbf{B}\cdot\mathbf{S} + \mathbf{S}\cdot\mathcal{A}\cdot\mathbf{I} + \gamma_n\mathbf{B}\cdot\mathbf{I} \tag{1.2}$$

S is the electron spin operator. $\gamma_{nv} = 2\pi \times -28.03\,\frac{\mathrm{GHz}}{\mathrm{T}} \approx 2.8\,\frac{\mathrm{MHz}}{\mathrm{G}}$ is the NV center's electron gyromagnetic ratio, almost identical to that of an isolated electron (less than 0.1% difference). γ_{nv} is also nearly isotropic, with less than 0.01% anisotropicity[13]. **I** is the nuclear spin operator of the nitrogen, which is either spin-1/2 (^{15}N) or spin-1 (^{14}N). In this work, we used exclusively NV centers with ^{15}N, so this is assumed to be a spin-1/2 operator. $\mathcal{A}$ is the hyperfine tensor; in the NV coordinate system described above its values for ^{15}N are $A_{\parallel} = 2\pi\times 3.03$ MHz, $A_{\perp} = 2\pi\times 3.65$ MHz. This term splits the structure by two for ^{15}N. $\gamma_n = -4.317\,\frac{\mathrm{MHz}}{\mathrm{T}}$ is the ^{15}N nuclear gyromagnetic ratio. The excited state Hamiltonian has a similar form as the ground state Hamiltonian shown in Eq. 1.2 but with a different zero-field splitting ($D_{es} = 2\pi \times 1.42$ GHz), and larger hyperfine constants.

For $\mathbf{B} \parallel \hat{z}$, the electronic spin eigenstates of the NV spin Hamiltonian (Eq. 1.2) are the eigenstates of $S_z\ |m_s\rangle\,, m_s \in \{0, \pm 1\}$. This condition, where the field is parallel to the NV axis, is termed an *aligned* field. For $\mathbf{B} = 0$, $|\pm 1\rangle$ are degenerate and split from $|0\rangle$ by 2.871 GHz, and a field $\mathbf{B} = B_0\hat{z}$ splits $|\pm 1\rangle$ symmetrically (i.e., the Zeeman effect), such that the eigenenergies are $E_0 = 0, E_{\pm} = D \pm \gamma_{nv}B_0$.

The singlet state ($S = 0$) is an anti-symmetric state of the system, thus occupying different orbitals and with higher energy than the ground state. The first excited state is a triplet separated by 1.945 eV (637 nm) from the ground state. Off-resonant illumination (<575 nm)[16] may induce a spin-conserving excitation. After a non-radiative decay to the excited state, the defect may relax to the ground state, emitting a photon in the range of 650–800 nm[17] due to a wide phonon side-band.

The excited NV center may relax directly to the ground state. Conversely, there is a probability for a transition to the excited singlet state, known as an inter-system crossing (ISC). The rate of the ISC depends on the excited spin state, with a transition from $m_s = \pm 1$ four times more probable than from the $m_s = 0$ (45% vs. 11%)[16]. From the excited singlet state, the system relaxes a lower metastable singlet state while emitting an IR ($\sim$1042 nm) photon and finally relaxing back to the ground state. The transition from the lower singlet state to the ground state is 60-100 times slower than direct relaxation from the excited state, such that the ISC leads to a temporary “dark” period of the defect. Due to the spin-dependent ISC rates, the average PL rate (α) depends on the spin

---

[a] Here and onward I set $\hbar = 1$, such that the Hamiltonians in this thesis are written in units of angular velocity (e.g., rad/sec). For convenience, experimental data is usually presented and fitted with parameters in units of frequency (e.g., Hz)

state, allowing optical detection of the ground spin state. The PL contrast is the ratio between $m_s = 0$ and the $m_s = \pm 1$ states, defined as[18]:

$$\mathcal{C} = \frac{\alpha_0 - \alpha_{\pm 1}}{\alpha_0} \tag{1.3}$$

where α_s is the PL rate of state m_s. The contrast depends on many factors, notably the rate of $\mathrm{NV}^- \leftrightarrow \mathrm{NV}^0$ transitions (the ionization rate), but it is generally in the range of $\mathcal{C} = 0.15 \sim 0.4$.

During the passage through the singlet state, there is a 45% probability for a $m_s = \pm 1 \rightarrow m_s = 0$ spin transition and a negligible probability for the reverse transition[16]. Due to this transition and the spin-conserving relaxation from the excited state, repeated excitation of the NV center will polarize the spin state to $m_s = 0$, at a rate of $\sim 80\%$[b]. The spin polarization and spin-dependent PL rate are the basis for optically detected magnetic resonance (ODMR). ODMR spectroscopy may be done by varying the frequency of a microwave signal that drives the $|0\rangle \leftrightarrow |\pm 1\rangle$ transitions; when the frequency is at the resonant condition, there appears a decrease in the averaged PL rate, as shown in Fig. 1.2(c). The NV center's spin state may be coherently manipulated and read by combining laser illumination, microwave pulses, and time-dependent PL measurements.

The NV center is a single-photon emitter[21], evident by antibunching photon statistics[22]. This is seen in the measurement of the two-point time correlation function $g^{(2)}(\tau)$ shown in Fig. 1.2(b). Using this measurement, an individual center may be distinguished from a cluster of defects.

The NV center's spin-dependent photodynamics depends on the magnetic field's orientation. When the magnetic field is in an arbitrary direction (i.e., not aligned with the NV axis), the eigenstates of the spin Hamiltonian (Eq. 1.2) will be superpositions of the S_z eigenstates, and the eigenenergies will have a nonlinear dependence on B_0[23]. However, the spin-dependent ISC rates are still linked to the eigenstates of S_z such that the PL contrast $\mathcal{C}$ will change. The contrast is optimal for a field aligned with the NV axis and decreases as a function of the tilt away from the NV axis. The contrast also varies with the field magnitude, and it is susceptible to field misalignment when $B_0 \approx D/\gamma_{nv} \approx 1020$ G. This condition is known as the NV center's ground state level anticrossing (GSLAC), as the $m_s = 0, -1$ states are nearly degenerate ($E_0 \approx E_{-1}$). At RT, a similar effect occurs for $B_0 \sim D_{es}/\gamma_{nv}^{es} = 2\pi \times 1.42\,\mathrm{GHz}/\gamma_{nv}^{es} \approx 510$ G, near the excited state level anticrossing (ESLAC). These features are fundamental to microwave-free magnetometry with NV centers[23,24,25].

1.3 QUANTUM SENSING USING THE NV SPIN SENSOR

The NV center can be a quantum sensor of physical fields coupled to its spin Hamiltonian by various phenomena. Notably, it can sense magnetic fields via the Zeeman interaction[26,27,28,15]; temperature via the zero-field splitting[29,30]; pressure via coupling to the diamond crystal's strain field[31]; and electric field, via the Stark effect[32]. Here, we focus on the NV center as a sensor of magnetic fields and for sensing spins.

Sensing is usually done by placing the NV center in a coherent superposition and allowing it

---

[b] The reported values for the spin polarization rate vary widely, at $42\% - 96\%$[14], and the details of this mechanism remains an open question. Nonetheless, a rate $\sim 80\%$ appears to be in general agreement[19,20]

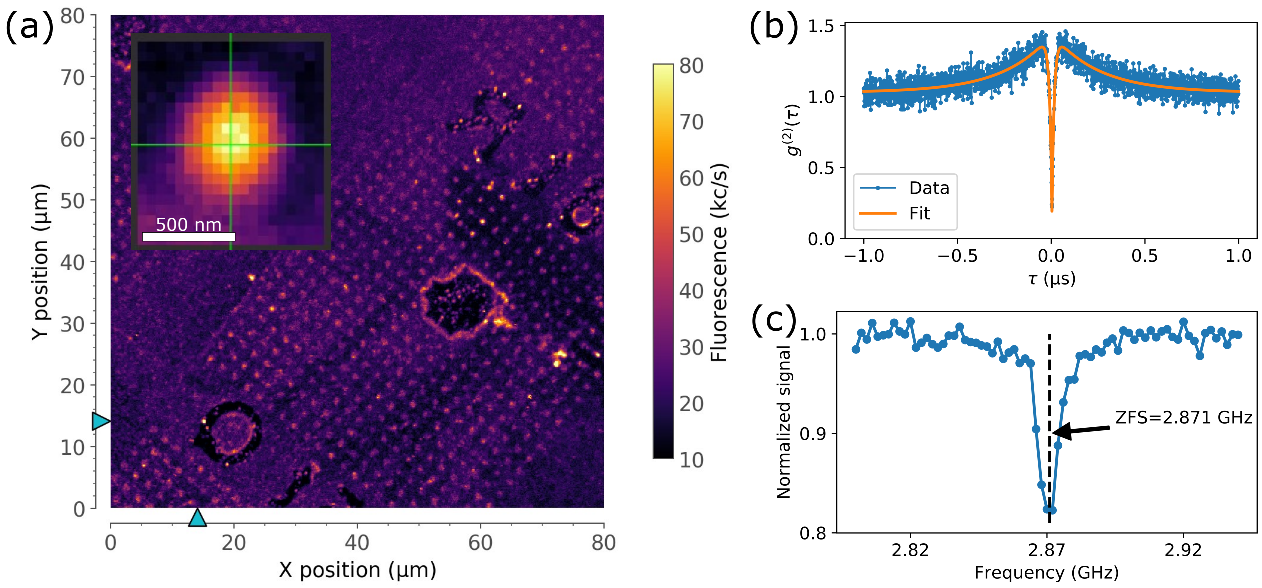

Figure 1.2: Identifying single NV centers. (a) A typical confocal scan of a thin diamond membrane with bright spots representing potential NV centers. The inset is a close-up of a single, diffraction-limited confocal spot. (b) PL signal temporal autocorrelation ($g^2(\tau)$) of a confocal spot, displaying an antibunching dip with $g^2(0) < 0.5$, indicating this is a single quantum emitter. (c) A CW-ODMR measurement of an NV center, exhibiting a transition at the ZFS, 2.871 GHz.

to evolve under the influence of the external field or spins. To do so, a sensor qubit based on a two-level subsystem of the spin-triplet is chosen, for example, the $|0\rangle, |-1\rangle$ qubit. The third state, $|+1\rangle$, is assumed to be far detuned to be neglected. Let's consider the interaction frame (rotating frame) Hamiltonian of this qubit $\mathcal{H}_I$ (see further derivation and details in Appendix A). The time-dependent phase picked up by the qubits superposition state will be[9]:

$$\begin{gathered} |\psi\rangle = \frac{1}{\sqrt{2}}\left(|0\rangle + e^{i\phi(\tau)}\,|-1\rangle\right) \\ \phi(\tau) = \phi(t=0) + \int_0^{\tau} \mathcal{H}_I(t)\,\mathrm{d}t \end{gathered} \tag{1.4}$$

If we neglect any spins coupled to our sensor qubit, and there is just a variable magnetic field to be sensed, then $\mathcal{H}_I = \gamma_{nv}\partial B_z(t)\,S_z$ and the phase picked up during the evolution would be $\phi(\tau) = \phi_0 + \gamma_{nv}\langle\partial B_z\rangle_\tau \tau$, where $\langle\partial B_z\rangle_\tau$ is the average of the sensed field over the period τ.

NV centers are not the most sensitive quantum sensors, and other quantum sensors boast better sensitivity, such as SQUIDs and trapped ions[9]. However, a prominent characteristic of the NV center is its flexibility. Studies demonstrated The NV center's function as a quantum sensor at temperatures from millikelvins[33] to 1000 K[34], and most importantly, at RT. Owing to the protective diamond crystal, NV sensors are tolerant to various environments, notably ambient conditions and various chemical environments[10]. Then, they may be used as sensors of the magnetic resonance of spins near the sensor, e.g., in the diamond lattice or on its surface. NV centers may be utilized in huge ensembles that can sense fields weaker than 1 pT[35]. When addressed individually, NV centers are point-like sensors offering high spatial resolution.

NV centers for quantum sensing are mainly used within artificially grown diamond crystals.

The diamond may be nanoscale crystals, known as nanodiamonds, or larger, single-crystal diamonds. NV centers may then be formed within nanometers of a diamond crystal's surface, known as shallow NVs, and used to probe external electron[36] and nuclear spins[37] on the diamond's surface. The diamond crystals can be fabricated into tips and incorporated into a scanning probe microscope (SPM)[38,39], which can image spins with nanometer resolution[40].

This work focuses on sensing with large single-crystal diamonds, which are thinned to 20–50 μm and are termed diamond membranes. Single-crystal diamonds are grown by chemical vapor deposition (CVD) on specific crystal planes, the most common of which is (100) for kinetic reasons. NV centers lie along the $\langle 111 \rangle$ crystal directions, so in (100) diamonds their axis is tilted by $\arccos\left(1/\sqrt{3}\right) \approx 54.7^\circ$ (the "magic angle") from the normal to the diamond's surface, as shown in Fig. 1.1(a). Processes were developed for growing diamonds along other planes, namely, (111), in which the NV axis may be perpendicular to the surface, and (110), in which the NV axis may be parallel to the surface[41].

1.4 Pulse sequences for quantum sensing

NV center experiments are based on control laser and radio-frequency (RF) pulse sequences to initialize and manipulate the quantum state of the NV electron spin and sometimes other spins in the system. The sequences in this work compose three main components: (i) spin-state initialization, mostly optically, by laser; (ii) spin-state manipulation, mainly by RF pulses interspersed by "dead" or "free evolution" periods; (iii) spin-state readout, mostly done optically. This scheme is depicted in Fig. 1.4(a). There are, naturally, many schemes and exceptions, so in the following section, I focus on a relatively standard scheme used in this work.

The first element is an initialization laser pulse, lasting at least 1.5 μs. At RT, this laser is usually an off-resonant green laser, 520–532 nm, and its power is 0.1–10 mW, depending on the diamond. The last element of the sequence is also a laser pulse, during which the PL rate is recorded, by which the spin state is determined. Several readout schemes exist in the literature, such as photoelectric[42]; spin-to-charge conversion[43]; and low-temperature resonant excitation[44]). Here, I focus on the common averaged spin-dependent PL technique used in this work. The time-dependent PL rate is measured, usually with a resolution of ~1 ns, and the spin state is determined by the PL rate within the first few hundred nanoseconds of the pulse, known as the measurement window. The PL rate of single NV centers is ~ 0.01, so experiments are repeated $> 10^5$ to obtain an appreciable SNR. The measurement yields state probabilities; hence, this method is termed the "averaged" PL technique, in contrast with single-shot techniques. The readout pulse may be followed by another wait period used, for example, to lower the duty cycle of the RF signal.

Mathematically, the measurement may be described by the following operator:

$$P = \sum_{s \in \{0, \pm 1\}} \alpha_s \left| s \right\rangle \left\langle s \right| = \alpha_0 \left(I - C S_z^2 \right) \tag{1.5}$$

where α_0 is the $|0\rangle$ state PL rate, I is the three-dimensional identity matrix, and C is the PL contrast defined in Eq. 1.3. The measurement axis $\hat{z}$ is always parallel to the NV axis, independent of the

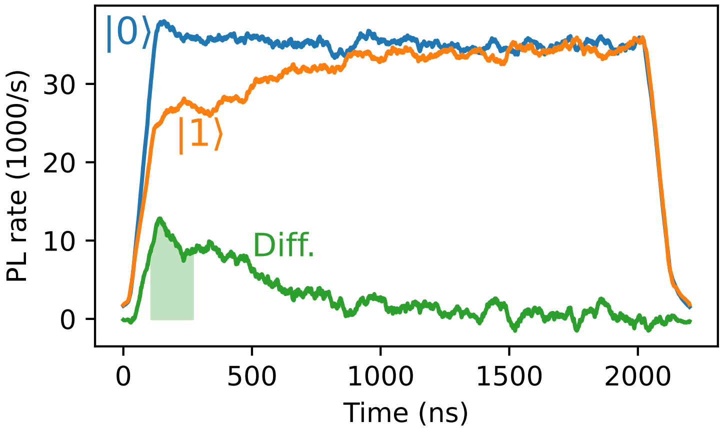

Figure 1.3: Spin-dependent photoluminescence of an NV center. The time-dependent PL trace of an NV center during a laser pulse is shown for a single NV initiated to $m_s = 0$ (blue) and $m_s = 1$ (orange). The difference between the traces is shown in green, and the green shading highlights the optimal counting window. The data was averaged for 5×10^5 repetitions and smoothed for presentation purposes.

magnetic field, and the $m_s = \pm 1$ states may not be distinguished. Fig. 1.3 shows the result of a time-dependent PL measurement for two different initial spin states - $m_s = 0, m_s = 1$. In this experiment, the contrast was greatest for 110–270 ns since the start of the laser pulse. By measuring the average PL rate α_m within this window, the measured state may be determined according to:

$$p\left(m_s = 0\right) = \frac{\alpha_m - \alpha_{\pm 1}}{\alpha_0 - \alpha_{\pm 1}} \tag{1.6}$$

$$p\left(m_s = -1\right) + p\left(m_s = +1\right) = 1 - p\left(m_s = 0\right) \tag{1.7}$$

More information is needed to distinguish between the $m_s = \pm 1$ states; for example, if there is a sufficient magnetic field, we may assume that one of these states is sufficiently detuned and that manipulation pulses may only excite the resonant transition.

The signal-to-noise ratio in the averaged PL (photon summation) technique is given by[18]:

$$SNR = \sqrt{\alpha_0} \frac{\mathcal{C}}{\sqrt{2 - \mathcal{C}}} \tag{1.8}$$

After initializing the NV center with a laser pulse, a series of RF pulses to manipulate the NV electronic state usually follows, depending on the experiment. Over the decades, magnetic resonance research has introduced numerous pulse sequences to reveal information on the sample under study and tackle imperfections in the experimental setup and noisy environments. These sequences were applied in quantum sensing with NV centers, with proper adaptations and further extensions (quantum computing research has drawn similar inspiration from NMR[45]). The pulse sequences manipulate and prepare the spin state to measure the desired signal from the phase acquired during state evolution. Fig. 1.4(b) depicts some standard sequences, and Fig. 1.4(c) shows typical (but not exclusive) outcomes of the sequences. In what follows, I elaborate on the example sequences given in Fig. 1.4:

- **Rabi**: In a Rabi experiment (or *time* Rabi), a varying RF pulse drives the spin state periodically between $|0\rangle \leftrightarrow |1\rangle$, resulting in *Rabi oscillations*. This is mostly used to tune the pulse durations: the duration of a half cycle is a π-pulse, a quarter cycle is a $\pi/2$-pulse, etc. Rabi can also measure the RF signal's amplitude and certain aspects of the qubit's decoherence.

- **Pulsed ODMR**: In ODMR, the frequency of the RF pulses is swept for a constant pulse duration; when the resonance condition is met ($|0\rangle \leftrightarrow |\pm 1\rangle$), the PL signal dips. ODMR may also be generated by applying a simultaneous constant-wave (CW) RF signal and laser, termed CW-ODMR. ODMR is mainly used to determine the transition frequency of the NV center, and it may also be used for DC magnetometry.

- **Ramsey**: is analogous to the "free induction decay" of conventional NMR. The spin qubit is placed in a coherent superposition state by a $\frac{\pi}{2}$ pulse, e.g., $\left(|0\rangle - i\,|1\rangle\right)/\sqrt{2}$, and then left to evolve. It accumulates phase according to the detuning of the pulses from the transitions. Finally, the superposition state is projected back onto the S_z basis with another $\frac{\pi}{2}$ pulse to be read out optically. The hyperfine structure may be apparent by the frequencies of the signal. The signal's decay is known as the dephasing time, T_2^*, which is bounded by the spin's decoherence T_2 and is usually lowered due to magnetic field drift and other low-frequency (>100 Hz) noise sources.

- **Spin-echo**: also known as Hahn echo sequence, it is similar to the Ramsey sequence but with a refocusing π-pulse during the evolution period[c]. If the first evolution is held constant while the second evolution period is swept, an "echo" - a refocusing of the spin's coherence - appears when the two periods are equal[48]. This measurement is, however, not employed frequently. If the two periods are equated and the total evolution time τ is swept, the signal decays according to the spin's decoherence time T_2. This is the simplest form of dynamical decoupling (DD), as the refocusing π-pulse "decouples" the spin from its environment. The signal may feature "collapses" due to coherent interactions with the surrounding spin-bath[48].

- **T_1**: the laser pulse initialized the spin to $|0\rangle$. A subsequent π-pulse will transition it to $|\pm 1\rangle$, from which it will gradually relax to a thermal state ($\rho = \sum_{0,-1,+1} |m_s\rangle \langle m_s|$. The π-pulse may also be omitted to measure the relaxation from $|0\rangle$.

- **CPMG**: The Carr-Purcell-Meiboom-Gill (CPMG) family of sequences are higher-order versions of the spin-echo, with a series of π-pulses. The phase of the *pi*-pulses is also shifted by 90° from the first $\frac{\pi}{2}$, a feature that compensates for pulse errors. These sequences may extend the spin coherence time by an order of magnitude[49,50,51], and reportedly up to 1 sec[52,53]. The sequence will decay according to the extended decoherence time (T_2^{CPMG}) and may feature resonances from the surrounding spin-bath or AC fields[54].

---

[c] This sequence is not actually what Hahn presented in his 1950 "spin echoes" manuscript[46]. A $\frac{\pi}{2} - \tau - \pi - \tau$ sequence was first presented by Carr and Purcell[47] to refocus diffusion in NMR. Here, it is supplemented by a final $\frac{\pi}{2}$ to project the state on the S_z basis.

- **Correlation spectroscopy** is a class of sequences based on two identical DD "blocks", spaced by a correlation delay time. The evolution time of the DD sequences (τ) is equal and constant, and the correlation delay is varied. If τ is set to match a resonance of the DD, the signal may oscillate. The correlation spectroscopy's signal decays on the order of the spin's longitudinal relaxation $T_1 \gg T_2$ and is thus helpful in extending the sensing time to increase spectral resolution.

In sequences ending with a $\frac{\pi}{2}$-pulse that projects the superposition state onto the S_z basis (e.g., Ramsey, Spin-echo, etc.), it is useful to repeat the experiment with $\frac{\pi}{2}$-pulses with alternating phases, e.g., 0° and 180°, usually denoted as pulses along $\pm\hat{x}$. This gives opposing projections on the S_z basis, and the signals are then subtracted such that zero corresponds to a mixed state (e.g., $\rho = \frac{1}{2}\left(\left|0\right\rangle\left\langle 0\right| + \left|1\right\rangle\left\langle 1\right|\right)$, and the maximal (minimal) value corresponds to $\left|0\right\rangle$ ($\left|1\right\rangle$).

Studies on NV centers have demonstrated dozens of other pulse sequences, such as elaborate DD sequences[55], two-dimensional spectroscopy[56], and double resonance sequences. The latter is a wide range of techniques where RF pulses are also applied to other spin species to probe coherent interactions with the NV center[57,36,58] and transfer polarization[59,60,61]. Chapter 3 includes further discussion and experimental results on double electron-electron resonance (DEER), and Chapter 5 discusses electron-nuclear double resonance (ENDOR).

1.5 NANOSCALE AND SINGLE-SPIN MAGNETIC RESONANCE USING THE NITROGEN-VACANCY CENTER IN DIAMOND

First, a clarification regarding the terminology: detection of magnetic resonance in single spins, such as an ODMR of a single NV center, is, in fact, single-spin magnetic resonance. Magnetic resonance of single spins by optical means was reported in 1993 for pentacene[62,63], and in 1997 for an NV- defect in diamond[17]. Magnetic resonance of single solid-state spins with electrical means has also been demonstrated in silicon devices[64,65]. However, these examples are limited to systems with specific coupling between the spin degrees of freedom and electronic levels. Here, we focus on studies for nanoscale detection of magnetic resonance in an arbitrary target species.

Traditional magnetic resonance study is divided into NMR and EPR (also known as electron spin resonance, ESR). The magnetic moments of electron spins are about a thousand times larger than that of nuclear spins, warranting distinct techniques and instrumentation. EPR and NMR using NV centers were achieved on the nanoscale in similar experimental scenarios.

Recent years saw tremendous advancement toward single-molecule magnetic resonance, and the scores of published studies on the subject, including in broad-scope journals, indicate the interest of a broad scientific community in this goal. Studies based on magnetic resonance force microscopy[66,67] and scanning tunneling microscopy[68,69,70] accomplished important landmarks in single-spin magnetic resonance. Yet, much work on nanoscale magnetic resonance has focused on the NV center as the sensor, indicating the promise of this strategy. Fig. 1.5 presents illustrations from a few of the many notable studies reviewed in the following section.

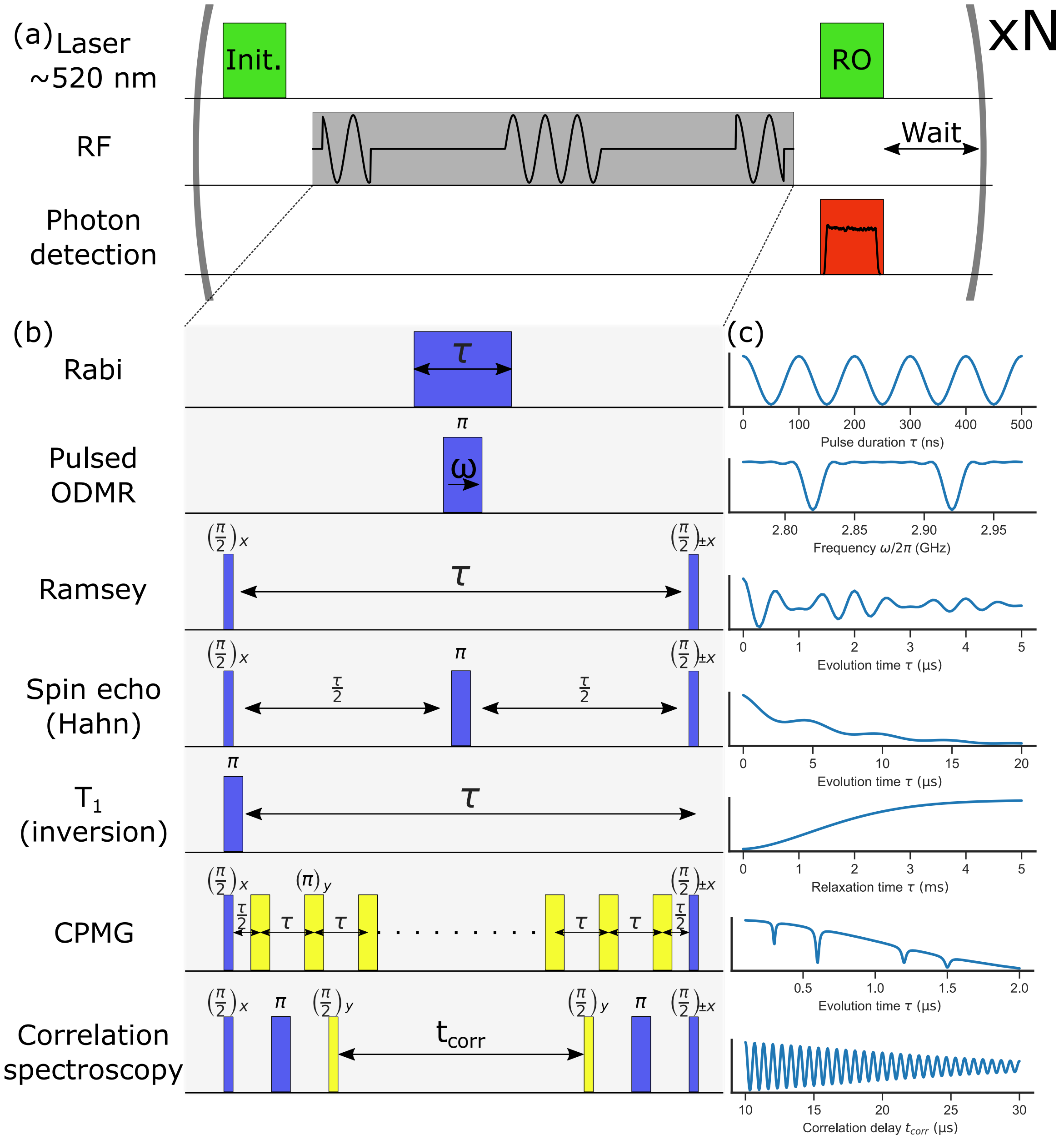

Figure 1.4: Typical NV pulse sequences. (a) The structure of a pulse sequence, with an initialization laser pulse and a readout laser pulse during which the PL is readout. In between, the spin state is manipulated by RF pulses interspersed with free evolution periods. (b) Basic RF pulse sequences are titled with their standard names. (c) Typical results of the corresponding sequences in (b) are drawn schematically.

NANOSCALE NMR WITH NV CENTERS

The first benchmarking experiments, nanoscale NMR with NV centers, were done on ^{13}C nuclear spins, naturally present in the diamond lattice. Experiments studied the coherent coupling between the NV electron spin and ^{13}C nuclear spins[48,71]; optical dynamic nuclear polarization and coherent manipulation of proximate nuclear spins[72,73]; and sensing and controlling the weakly-coupled ^{13}C nuclear spin bath[74,75,76]. Theoretical studies also highlighted the role ^{13}C spins play in the decoherence of single NV centers[77,78]. Later studies utilized the high sensitivity of the NV center to map clusters of ^{13}C spins[79,80], culminating in the precise mapping of dozens of ^{13}C spins[81,82,83] with sub-Ångstrom resolution[84]. Mapping ^{13}C clusters demonstrated the potential of nanoscale spin imaging, these clusters later serving as a pioneering quantum processor[85,86]. NV-NMR was also demonstrated on adsorbate protons on the diamond's surface[87,88], and of a single proton in the diamond crystal[89].

The study of nuclear spins within the diamond crystal laid the foundations for detecting spins outside the diamond, usually on its surface, denoted as external spins in this thesis. Shallow NV centers were used to detect the NMR of protons (^{1}H) in organic materials on the diamond's surface[58,37], and even molecular diffusion[90]. NV center sensors in diamond crystals were coupled with SPMs, placing an organic sample on a tip to obtain a nano-MRI of the sample[91]. The SPM geometry can also be inverted, such that the NV center is the scanning probe[38,39,40], and this approach was applied widely to study condensed matter phenomena with unprecedented resolution[92].

In recent years, novel methods have been developed to improving the spectral resolution of a single NV center sensor. These include correlation sequences, where the sensing time is limited by the NV center's longitudinal relaxation time (T_1)[93,90]; use of nuclear spins as memory qubits, which extends the sensing time to the nuclear spins' longitudinal relaxation time[94,95,96,97]; and stroboscopic probing of the NMR signal, where the frequency resolution, set by an external clock, is less than 1 mHz [98,99,100]. These advances enabled microscale NMR of protons in an organic sample ($\sim$10 pL volume) on the diamond's surface with a resolution of several hertz, using an NV ensemble to enhance sensitivity[101]. NV-based NMR of micro- and nanoscale samples was demonstrated on several chemical species, including ^{1}H and ^{13}C [37]; ^{2}H [95]; ^{19}F [102, 96]; ^{29}Si [103] and ^{31}P [102].

NANOSCALE AND SINGLE-SPIN EPR WITH NV CENTERS

Alongside the advances in nanoscale NMR with NV centers, there was some work on nanoscale EPR with NV centers. These include the detection of the EPR signal of an ensemble of spins in radical molecules (DPPH) on the diamond's surface[36], a single paramagnetic molecule with Gd^{3+} covalently bonded to the diamond's surface[104], and copper ions in salt crystals[105]. Diamond crystals host various paramagnetic defects, serving as subjects of study, such as individual electron spins, known as "dark spins" on and inside the diamond crystal[61,88]. Using a gradient induced by a magnetic tip, single dark spins in the diamond were mapped with nanometer resolution[106], demonstrating a promising approach for nanoscale spin imaging. Substitutional nitrogen defects with $S = 1/2$, known as P1 centers, are common in diamonds with NV centers (due to the ion implantation process). EPR of P1 centers was also studied in this context[107], including at zero

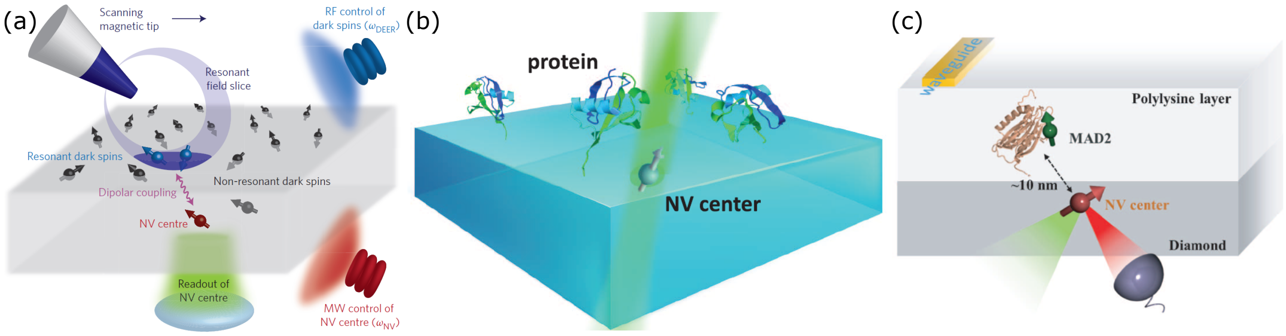

Figure 1.5: Examples of nanoscale magnetic resonance with NV centers from previous studies. (a) Subnanometer resolution magnetic resonance imaging of individual spins in a diamond, by Grinolds et al., ref. [106]. (b) EPR of a single spin-labeled protein on the diamond's surface with a shallow NV center, by Shi et al., ref. [118]. (c) NMR detection of single proteins with shallow NV center, by Lovchinsky et al., ref. [95].

magnetic field[108,109], and at 4.2 T[110]. Further work included detecting unknown electron-nuclear spin defects in diamond[111], but it has yet to be fully characterized and categorized. Careful control and detection of paramagnetic defects also allowed measuring a minute-long coherence time of an electron spin pair[112].

Spin labels are organic complexes with unpaired electrons widely used in conventional EPR spectroscopy to label organic molecules[113,114]. Spin labels are attached to specific sites in organic molecules using advanced chemistry techniques. Often, two or three spin labels are attached to different sites on the molecule, and by measuring the coupling between the two spin labels, their distance may be deduced. Thus, the molecule's structure and dynamics may be studied in various conditions and environments[115,116], including within biological cells[117]. There is much interest in transferring these techniques to the nanoscale. Studies in this context have measured the EPR spectrum of covalently bonded nitroxide radicals[57] and of a single spin label attached to a protein with an NV center at RT[118]. Another experiment measured the distance between spin labels in a small ensemble of a few molecules[119].

SENSING USING SHALLOW NV CENTERS

Nanoscale magnetic resonance experiments with single NV centers are typically based on a diamond with a dilute NV layer (1-10 ppb) close to the surface, and the sample of interest is on the diamond's surface. Nanoscale experiments, especially single-spin experiments, require shallow NV centers that reside within a few nanometers of the surface because the sensing volume is proportional to the NV depth[37]. NV depth may be estimated numerically using a computational method "Stopping and Range of Ions in Matter" (SRIM)[120], and can also be measured directly using NV-NMR of immersion oil on the surface[121].

Shallow NVs offer the coveted nanometer spatial resolution and often below. However, the proximity to the surface means that shallow NVs are also highly susceptible to noise of surface defects. The noise spectrum is thought to be predominantly composed of magnetic noise from paramagnetic defects and electric noise from charge hopping[122,123,124,125,126]. The noise drastically dampens the NV relaxation times[127] - including longitudinal relaxation (T_1), transverse relaxation, or decoherence (T_2) and dephasing (T_2^*). For example, Myers et al. showed that for NV depths above 30 nm, the decoherence time (T_2) is $\sim$300 µs and independent of depth. However, the T_2 drops drastically with decreasing depth, and well below 20 µs for NVs less than 10 nm deep[122]. This result is crucial, as the sensitivity for many sensing protocols scales as $T_2^{-\frac{1}{2}}$. In addition to shortening relaxation times, the surface probably destabilizes the NV charge state[128,129], decreasing the spin state optical contrast, which subsequently hampers the sensor's performance.

The degradation of shallow NV sensor properties prompted studies to improve sensor coherence and charge stability. Promising active strategies for improving coherence were introduced, such as driving the surface spin bath[130] or applying a strong electric field[131]. However, the most prominent are surface engineering strategies, with studies suggesting surface terminations such as nitrogen[132] and oxygen[133,134] may improve sensor performance. Placing graphene on the diamond surface has also enhanced the coherence time and reduced the density of surface paramagnetic defects[135]. All shallow sensor enhancement studies must also consider chemical attachment or adsorption of samples to be sensed[136].

1.6 OPEN QUESTIONS AND RESEARCH GOALS

Magnetic resonance is indispensable to scientific progress in physics, chemistry, and biology. However, conventional techniques are limited to huge ensembles. Applying generic magnetic resonance methods, such as NMR and distance measurements by EPR, at the nanoscale and single-molecule level has yet to be realized.

The past decade saw significant advances in nanoscale and atomic-scale magnetic resonance, mainly with the NV center in diamond as a quantum sensor. However, there is still much more work developing methods to apply NMR and EPR to samples of interest, such as organic molecules. Notably, the goal of single-molecule distance measurements with spin labels attached to a molecule has yet to be achieved.

Single-molecule distance measurements may be realized by mapping the positions of individual electronic spins near our sensor. Thus, a technique for mapping single electron spins' positions is constructive. These techniques may also find value in quantum information processing, such as characterizing a spin-qubit network based on organic molecules.

Techniques of nanoscale NMR with single NV centers are limited by sensor relaxation times - such as longitudinal relaxation (T_1) or decoherence (T_2). The driving frequencies of nuclear spins in NV-based NMR were limited to tens of kilohertz, implying lengthy pulses that prevent applying complex sequences within the limited sensing time. Thus, it is of value to develop tools and methods for fast manipulation of nuclear spins in the sample of interest to apply generic NMR sequences within the limited sensing times.

From these, we derive the following research goals:

- **Single-spin mapping:** Demonstrate NV-based single-spin mapping techniques with sub-nanometer resolution.

- **Fast nuclear spin manipulation:** Develop an instrument for strong RF driving compatible with NV magnetometry. Demonstrate fast nuclear spin driving to facilitate fast nuclear spin within the limited coherence time of NV center sensors.

- **Single-molecule distance measurements:** Develop a scheme for single-molecule distance measurements based on mapping individual spins.

2

Experimental setup and methods

THE PRIMARY EXPERIMENTAL SETUP USED IN THIS WORK IS A ROOM-TEMPERATURE (RT) CONFOCAL MICROSCOPE TAILORED FOR QUANTUM EXPERIMENTS WITH NV CENTERS. The home-built setup comprises four main components: an optical system, an RF and microwave system, a magnetic field system, and software control. The optical system, used to excite the NV center and read out its spin state, is detailed in Section 2.1. The RF and microwave setup, used to manipulate quantum spin states, is outlined in Section 2.2. The systems for magnetic field control, used to configure a desired magnetic field, are discussed in Section 2.3. The entire setup is orchestrated by computer via dedicated software, outlined in Section 2.4. Section 2.5 discusses this study's central sample preparation methods.

Lastly, Section 2.6 is dedicated to discussing our low-temperature (LT) system, which allows performing similar experiments detailed here at cryogenic temperatures ($\sim$5 K) and at ultra-high vacuum. Some of the experiments planned initially required cryogenic conditions, but these did not materialize in this study due to various technical difficulties. Nonetheless, Section 2.6 shows some proof-of-concept experiments from the LT system.

2.1 OPTICAL SYSTEM

For this work, I built a confocal microscope setup shared by the ambient and LT-UHV sample stages. Using the setup, we can scan the sample, excite NV centers, and measure their time-dependent PL. The optical setup consists of excitation, sample, and detection units, described in Fig. 2.1. The following section details the elements of the optical setup.

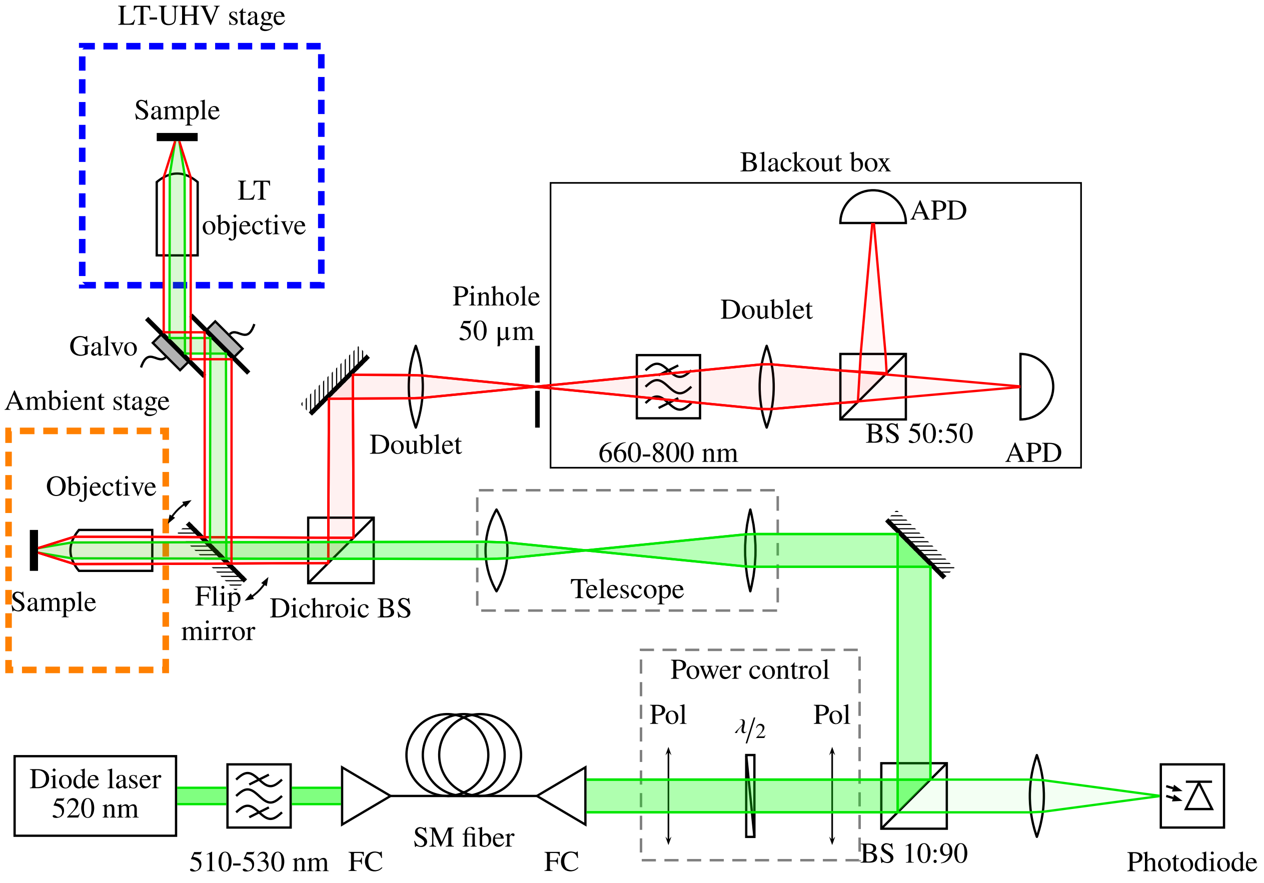

Figure 2.1: Schematic of confocal optical setup.

Excitation unit

The main element of the excitation unit is a 520 nm (green) diode laser module (LABS GmbH, DLnsec 520 nm, 80 µW). Spectroscopic measurements showed its actual wavelength is ∼524 nm. The module includes an external modulation port, by which we modulate the laser via an AWG to generate pulses at rates of up to 100 MHz. The module's output power may be modulated via software by a built-in driver. However, decreasing the output power below its maximum extended the pulse rise time and decreased power stability; thus, I used the laser exclusively at its maximal power and modulated the power optically, as is described later on. The module includes an aspheric lens, which collimates the laser beam, generating an elliptical profile. The laser beam is then passed through a bandpass filter to block possible subharmonics (e.g., in the IR range) and coupled into a single-mode fiber. The purpose of the fiber is to convert the input laser into a single mode with a spatial Gaussian profile. Due to limited coupling efficiency, only about 20% of the original power remains after the fiber.

The beam is then passed through the power control unit, which consists of a linear polarizer, a half-wave plate ($\lambda/2$ in Fig. 2.1) on a computer-controlled electronic rotation stage, and another linear polarizer. The two polarizers are aligned with the laser's output polarization. The half-wave plate reflects the light's polarization about its fast axis, so rotating the half-wave plate rotates the polarization away from the initial polarization axis. The polarization's projection on the second

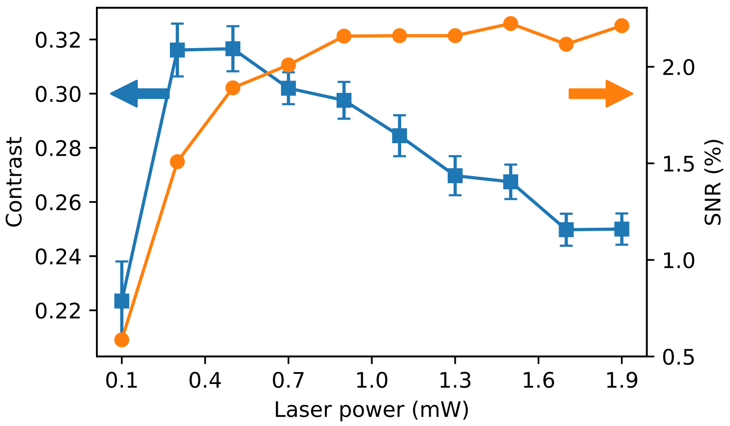

Figure 2.2: Optimizing excitation laser power. The optimal excitation laser power is found by measuring the contrast and SNR per iteration of the NV center as a function of laser power.

polarizer determines the power exiting the unit. This polarizer-$\lambda/2$-polarizer configuration allows power control without varying its polarization, which may affect the optical coupling to the NV center.

A beam splitter diverts 10% of the power to a photodiode used to monitor the laser power, serving as feedback to set the desired laser power. The diode's signal was calibrated according to the laser power output from the RT objective. The unit allows controlling the laser power at the sample in a broad dynamic range (0.01–5 mW) with a precision of <5 µW without compromising the laser rise time and stability. The excitation beam at this point is about 9 mm wide, while the RT (LT) objective's back aperture is 3.24 mm (4.7 mm), implying that between 50%-90% of the excitation power would be lost. Thus, we use two singlet lenses in a telescope configuration to narrow the beam diameter to ~5 mm. The excitation beam then reaches a 650 nm dichroic beam splitter, the junction between the excitation, sample, and detection units.

The excitation laser power is optimized *in situ* by measuring the spin-dependent PL rate of the NV center. Two possible metrics for calibration are the PL contrast and the SNR (the values are defined in Section 1.4). Typical calibration curves are shown in Fig. 2.2; the contrast peaks at ~0.3 mW, while the SNR increases gradually and plateaus at ~1 mW of incident power. However, often we may prefer not to optimize the SNR (i.e., the total duration of an experiment) but rather the total light energy incident on the sample (e.g., for sensitive biomolecules): $E_{tot} = P_{laser}Nt_{laser}$, where N is the number of repetitions and t_{laser} is the laser duration per repetition. The number of iterations required to achieve unit SNR is $N = 1/SNR$, and so the value to minimize is the *power-per-SNR*. This increases monotonically with laser power for >0.1 mW, so to minimize the total energy it is preferable to lower the laser power to $\lesssim$ 0.1 mW, at the expense of contrast or SNR.

Ambient sample unit

Each sample unit (ambient and LT-UHV) includes a sample holder, an objective lens, and a sample scanning mechanism. The access to the two sample units is switched using an electronic flip mirror.

The ambient stage has a three-axis closed-loop scanning piezo stage (Piezosystem Jena GmbH, TRITOR 102 SG, actuated by an NV 40/3 CLE) for fine lateral positioning and focusing. The piezo stage has an aperture, and the sample is accessed optically from below such that the excitation beam is static and the sample moves. Coarse focusing of the sample is done by moving the objective lens (Olympus MPLFLN100x) with a manual linear positioner. Coarse lateral positioning of the sample is done with a two-axis linear stage actuated by computer-controlled closed-loop stepper motors.

The sample is usually positioned at the focal plane of the objective, such that the collimated beam reaching the back aperture of the objective is focused onto the sample. Light emitted from the sample, PL and reflected excitation light, is collected by the objective and propagates along the same path as the incident light.

LT-UHV sample unit

The LT-UHV sample stage sits inside a UHV chamber and is thermally coupled to a cryostat. The stage includes a three-axis, home-built, open-loop piezo-stage with a resolution of $\sim$1 μm. The piezo stage is used for coarse lateral positioning and coarse and fine focusing.

In this stage, imaging is done while the sample is static by a two-axis scanning galvo mirror system (Thorlabs, GVS212/M), which scans the laser beam across the back aperture of the objective (attocube systems AG, LT-APO/VISIR/0.82). Ideally, this should be done using a pair of scan lenses between the scanning mirrors and the objective. However, the geometry of the UHV chamber did not allow this, and we managed without this addition. The compromise is in the quality and range of the image, with negligible impact on PL contrast.

Detection unit

The detection unit begins after the dichroic beam splitter (567 nm long-pass), which transmits all of the NV center's emission along with a little reflected green light from the sample. An achromatic doublet lens focuses the beam onto a 50 μm pinhole, which spatially filters out-of-focus rays from the beam. Another doublet is positioned at twice the focal length from the pinhole. A 50:50 beamsplitter splits the beam, and at two focal lengths from the second doublet, the beam is focused on two avalanche photodiodes (APD) arranged in a Hanbury-Brown and Twiss configuration. The detectors (Excelitas Technologies Corp., SPCM-AQRH-12) are enclosed in a blackout box to minimize unwanted light sources, and experiments are conducted in a dark room. The signal from the detectors is measured by a time tagger card (Swabian Instruments GmbH, TimeTagger 20), gated by an arbitrary waveform generator (AWG) (see Section 2.2).

After the dichroic mirror, the reflected green light power is $\lesssim$ 10 nW, or approximately $\times 10^5$ the NV PL signal. So, an additional 660–800 nm bandpass filter after the pinhole filters out most of the reflected green light (the optical density of the filter is $10^6 - 10^7$ at 520 nm) such that the background signal from the reflected light is a few thousand photons per second for an excitation power of $\sim$500 μW.

2.2 RF AND MICROWAVE SYSTEM

We controlled the quantum state of the electron and nuclear spins with RF fields in the range of $\sim$1 MHz to $\sim$5 GHz. Fields of a few to hundreds of MHz are usually termed "RF" and are mainly associated with nuclear spins and spin-1/2 electron spins (at magnetic fields used in this work). Fields in the GHz range are usually termed "microwave (MW)" and are mainly associated with the NV electron spin.

The RF and microwave system consists of the generation and delivery units. The generation comprises all the hardware to generate the intense RF and MW pulses required for spin control. Delivery comprises the specialized waveguides and antennas required to efficiently irradiate spins in the sample. The following section details these elements.

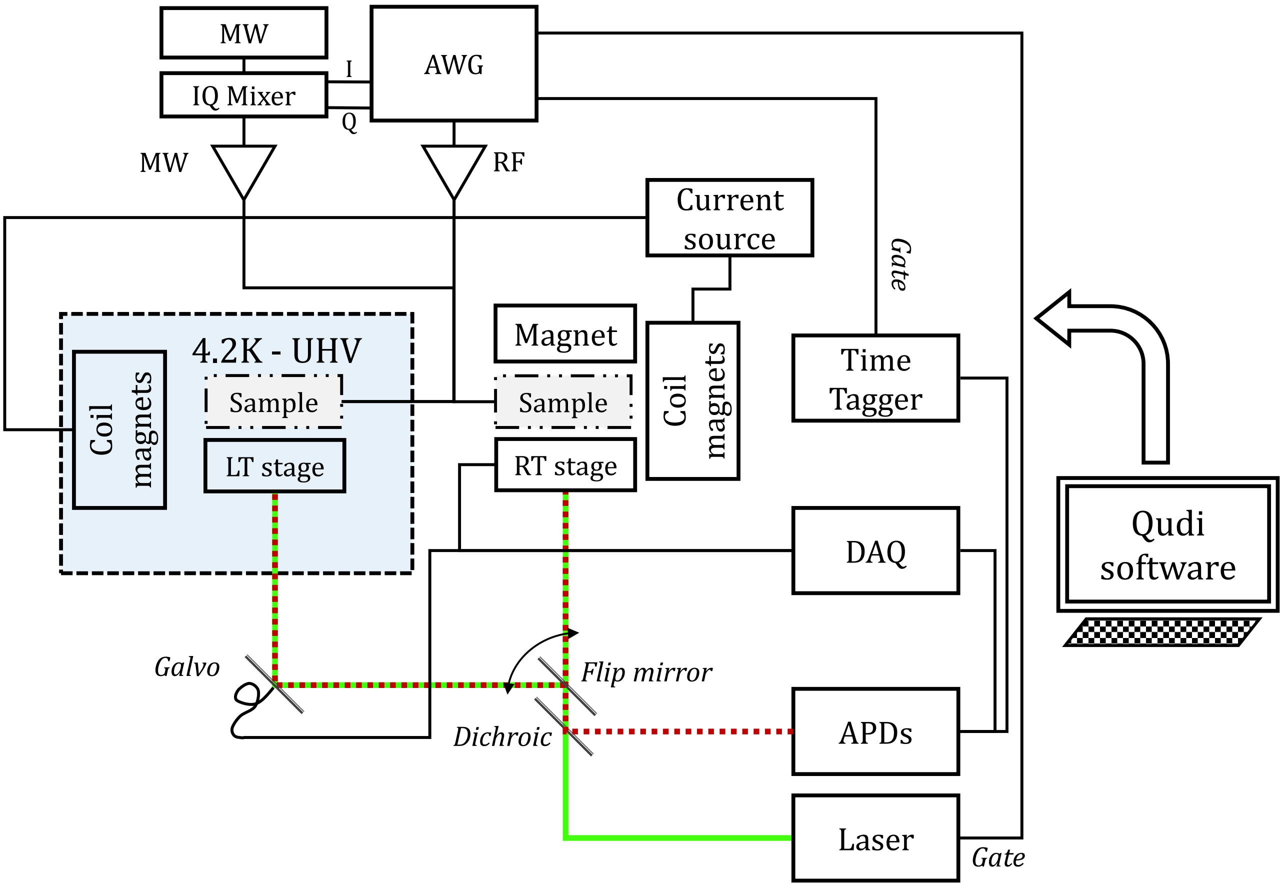

Figure 2.3: Schematic of electronic components of the system. The figure shows the various electronic components, including RF and microwave generation, stage and magnet control, and their mutual connections.

2.2.1 SIGNAL GENERATION

In this setup, pulse sequences were orchestrated by an arbitrary waveform generator (AWG; Spectrum Instrumentation GmbH, DN2.663-04; four analog channels, six digital channels, 1.25 GSa/s). To generate signals beyond the bandwidth of the AWG (>400 MHz), particularly MW signals, we used a vector signal generator (Rohde & Schwarz SGS100A, 1 MHz to 6 GHz). MW pulses were generated by IQ modulation (single-sideband), with two analog signals from the AWG connected to an internal IQ modulator in the signal generator. Signals in the AWG's bandwidth were usually synthesized directly from the AWG.

Microwave signals were amplified by a custom-made solid-state linear amplifier (Elite RF LLC, M.02006G424550, 20–6000 MHz, 15 W, 45 dB gain). To protect the amplifier from reflected signals, the amplifier's output was connected to an RF circulator (Aerotek Co., LTD., D60-1FFF 1-2 GHz; or F61-1FFF 2-4 GHz). RF signals were amplified by a high-power amplifier (Mini-circuits, LZY-22+, 0.1-200 MHz, 50 W).

2.2.2 Signal delivery

I employed several devices to deliver the signals to the sample: a coplanar waveguide, copper wire antenna, and an RF spiral antenna for up to 20 MHz. The design and testing of the RF spiral antenna is at the focus of Chapter 5 and is detailed there.

Coplanar waveguide for quantum sensing with NV centers

I fabricated a coplanar waveguide for efficient signal delivery in the MW range. For this, I developed a fabrication process of copper waveguides on glass substrates (standard 170 μW thick, square 22 mm microscope slides). The fabrication process started with e-beam evaporation of 5 nm-Cr and 300 nm-Cu layers on cleaned glass substrates. Then, a negative of the waveguide pattern was patterned by lithography on the copper layer. Afterward, the copper waveguide was electroplated into the patterned trenches to a height of ~15 μm. Finally, the photoresist was removed, and then the broad copper and chrome layers were etched away such that the waveguide pattern was the only metal left on the substrate.

The waveguide's dimensions may vary, but here I used one with a central conductor 20 μm wide separated from the ground conductors by 200 μm. Fig. 2.4(a) is a photo of the coplanar waveguide. Fig. 2.4(b) is its transmission characteristics (S_{21} parameter) for the range of 0–4 GHz, after subtracting the transmission loss through the connecting cables, such that what is presented is solely the transmission loss through the waveguide. At 0.35 GHz, the system exhibits a resonance, a dip in the transmission. However, for 0.5–4 GHz, the waveguide has a relatively flat transmission, tapering off by 2 dB as the frequency increases. The consistent transmission makes the waveguide suitable for driving spins with MW.

The sample was placed on the waveguide at its center, usually glued to the glass by wax (clear Crystalbond), and the thin diamond membranes were glued with the NV layer facing up. A disadvantage of this configuration is that the NV spins are relatively far from the antenna - (~50 μm - depending on the membrane. The distance decreases the Rabi frequency to driving amplitude ratio. Also, glass substrates are fragile and tend to break with handling.

Copper wire antenna

In some experiments, such as the magnetic tomography experiments of Chapter 3, we used a copper wire to irradiate the sample with RF for spin manipulation. The copper wire (50 μm thick,

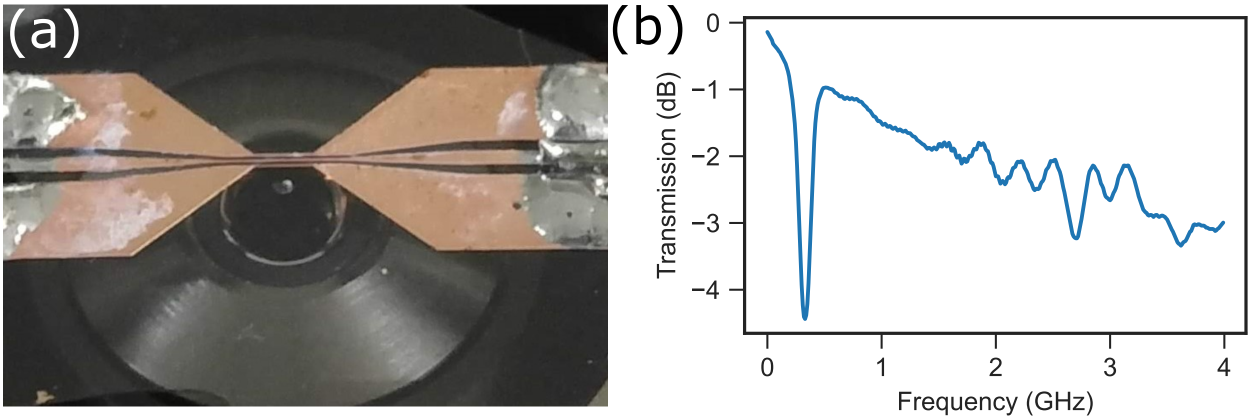

Figure 2.4: A coplanar waveguide for quantum sensing with NV centers. (a) Photo of the copper coplanar waveguide fabricated on a glass slide. (b) Transmission (S_{21} parameter) spectrum of the coplanar waveguide, as measured with a vector network analyzer after subtracting the cable loss.

99.99% copper) was placed over the diamond and pressed onto the sample, such that the antenna was much more proximate to the spins than in the coplanar waveguide setup. This resulted in higher Rabi frequencies, up to 60 MHz for an input driving power of ≈10 W.

The substrate was a flexible printed circuit we designed, made of gold-plated copper traces on a polyimide substrate (prepared for production and manufactured by Bitronics Ltd., Kiryat Ono, Israel). The circuit was glued by epoxy to a sapphire substrate, which is much more robust compared to a glass slide. The sapphire substrate had a 1 mm hole for optical access (the sapphire crystal's refractive index and fluorescent defects prevent access through it). The polyimide substrate had a corresponding manually punctured hole, and the diamond was placed above the hole and glued by wax.

2.3 Room-temperature magnet systems

Quantum spin experiments often require magnetic field control, to control the energy levels via the Zeeman term of the Hamiltonian. In this setup, we incorporated two types of magnet systems: a permanent magnet system, based on positioning a permanent magnet in the vicinity of the sample, and a vector electromagnet. The permanent magnet's primary advantages are affordability and wide dynamic range (10–1000 G). Its disadvantages are limited stability due to temperature and mechanical fluctuations[137] and limited control over the field's magnitude and orientation. The vector magnet, on the other hand, offers higher stability, precise control in arbitrary orientations, but a much more limited magnetic field magnitude (<20 G). In this section, I discuss the details of the setups and their operation.

2.3.1 Permanent magnet system

In this work, I controlled the RT magnetic field primarily using a permanent magnet positioned by a computerized tri-axis motor stage (Thorlabs MTS25/M-Z8). I used cylindrical N52 (NdFeB) magnets, polarized through their axis, and most often a 1/8" diameter, 3/8" length magnet that can induce fields of a few hundred gauss. The magnet was super-glued to an arm connected to the stage, and positioning was done via computer code.

The magnet may be modeled as a magnetic dipole when the distance from the sample is larger than the magnet's diameter. At a shorter distance, additional multipoles of the magnet should be considered. I worked at distances of (>3 mm), where this model provides a sufficiently accurate description of the magnetic landscape. For a more accurate simulation, the magnetic field may be modeled by finite element simulations, such as that found in the supplementary information of ref. [138].

Aligning the permanent magnet's field

Most NV experiments are carried out with a magnetic field aligned with the NV center's zero-field axis (usually denoted as $\hat{z}$), as this preserves the NV center's zero-field spin eigenspace and maximizes the optical contrast between the spin states. As discussed in Section 1.2, a misaligned magnetic field, with a component transverse to the NV center's axis, leads to spin-state mixing and subsequently alters the steady-state PL rate of an NV center. We utilize this feature to align the field with the NV center's axis.

I denote the magnet's coordinates system by a subscript "m", such that the $x_m y_m$-plane is parallel to the diamond's surface. I also assume the diamonds are single-crystal (100)-cut diamonds, as was used exclusively in this work. Thus, the NV center's axis ($\hat{z}$) is tilted by $\arccos\sqrt{\frac{1}{3}} \approx 54.7^\circ$ from $\hat{z}_m$. The alignment procedure of a permanent magnet is based on scanning the magnet's position in the $x_m y_m$-plane and measuring the NV center's PL rate as a function of position. As a misaligned field will decrease the NV center's steady-state PL, the aligned position should be apparent by a local maximum of the PL scan (a bright spot). Fig. 2.5 compares a simulation of a dipole's magnetic field with a measurement of the PL as a function of the magnet's lateral position (x_m, y_m) at a constant height z_m. The results are shown for an NV oriented along $\sqrt{\frac{2}{3}}\hat{y}_m + \sqrt{\frac{1}{3}}\hat{z}_m$, with an upright magnet (its moment is parallel to $\hat{z}_m$), similar to the experiment. The simulation demonstrates how the measured PL landscape (Fig. 2.5(c), (f)) is determined by the transverse field's magnitude (Fig. 2.5(a), (d)). Using a transition rate model[23], the PL contrast in the magnet scan can be simulated quantitatively after proper calibration (Fig. 2.5(b), (e)). The axial magnetic field at the aligned point was 254 G, measured by ODMR, and the simulation parameters were calibrated accordingly.

The duration of magnet scans is roughly proportional to the number of pixels, with a 100 pixels-scan taking approximately two minutes. To align the magnetic field efficiently, the alignment procedure is done by an automated script that performs successive low-resolution scans, each focusing on the PL maximum of the previous scan. The final scan is usually 10x10 pixels with a pixel size of 10–20 μm, which is the stability limit of the stage. Simulations show that for a precision of ± 20 μm, at 500 G, the misalignment should be up to 0.4°.

The PL extinction is related to the magnitude of the transverse field and reaches its maximum around the ESLAC ($\sim$510 G) and GSLAC ($\sim$1020 G), where even small deviations from the aligned condition will lead to significant PL rate reduction. So, this procedure is only effective when the

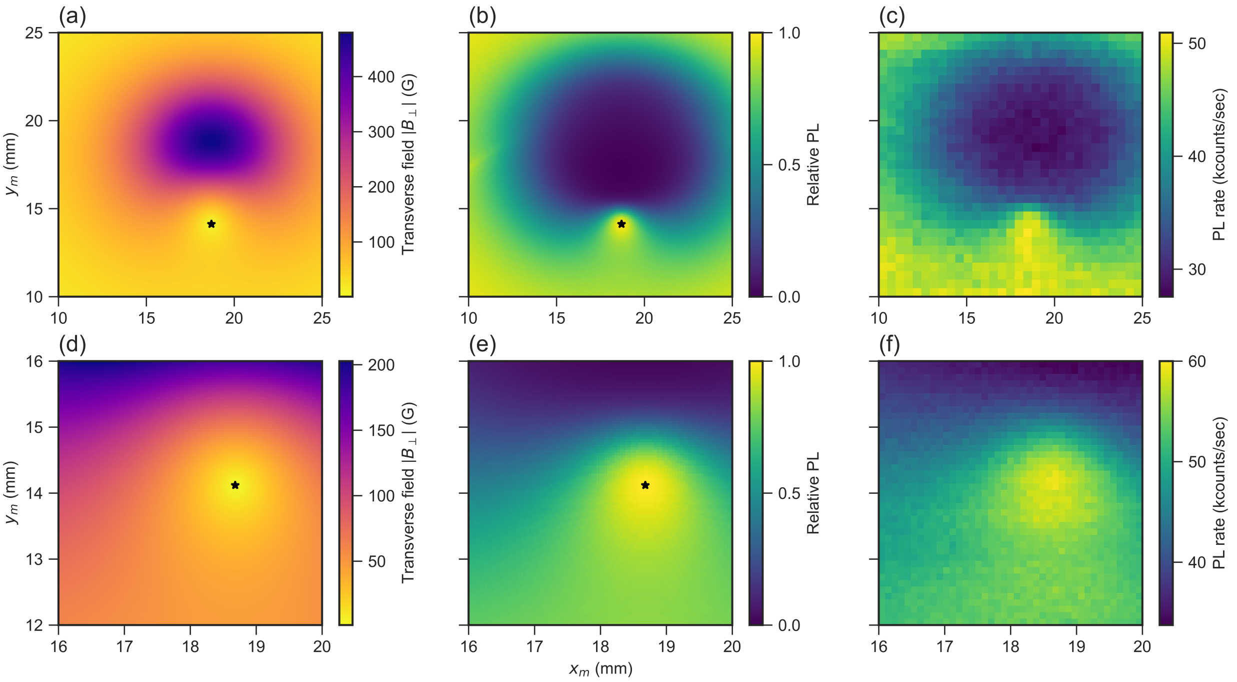

Figure 2.5: Magnetic field alignment with a permanent magnet. (a), (d) The transverse component to the NV axis of a simulated dipole's magnetic field ($B_\perp$) as a function of the magnet's lateral position (x_m, y_m) at a constant height (z_m). The star marks the aligned position (where $B_\perp = 0$). (b), (e) Simulation of the NV's PL as a function of the magnet's lateral position. (c), (f) Experimental measurement of the NV's PL as a function of the magnet position. The top row is a wide-range scan, and the bottom row is a focus around the alignment point.

transverse field is <250 G, below which the contrast due to PL extinction is low, and the local maximum of the aligned position would not be clear. To align the field for low fields (>200 G), I used a different approach.

The dipolar symmetry of the magnet implies that the aligned positions (x_m^*, y_m^*) at each plane z_m lie on a straight axis. I denote the sample's position as x_m^0, y_m^0, z_m^0, assume that the sample (100) plane is normal to $\hat{z}_m$, and assume that the sample's [110] orientation is along $\cos(\alpha)\,\hat{x}_m + \sin(\alpha)\,\hat{y}_m$. The alignment axes equation for the four NV orientations ($n \in 0, 1, 2, 3$) were derived together with the corresponding parallel field along this axis:

$$\begin{aligned} x_m^*(z_m) &= x_m^0 + \frac{1}{\sqrt{2}}\left(z_m - z_m^0\right)\cos\left(\alpha + \frac{n\pi}{2}\right) \\ y_m^*(z_m) &= y_m^0 + \frac{1}{\sqrt{2}}\left(z_m - z_m^0\right)\sin\left(\alpha + \frac{n\pi}{2}\right) \end{aligned} \tag{2.1}$$

$$B_\parallel\left(x_m^*, y_m^*, z_m\right) = \mathcal{M}\frac{\mu_0}{4\pi}\frac{2\sqrt{2}}{3\left(z_m - z_m^0\right)^3} \tag{2.2}$$

Here, $\mathcal{M}$ is the magnetic moment of a specific magnet. If we know z_m^0, a single calibration point may determine it, otherwise two points are required. Fig. 2.6 depicts the alignment axis as a function of z_m along with the expected aligned field at each height of the magnet, for the aforementioned cylindrical 1/8" × 3/8" NdFeB magnet. It should be noted that the magnet coordinates

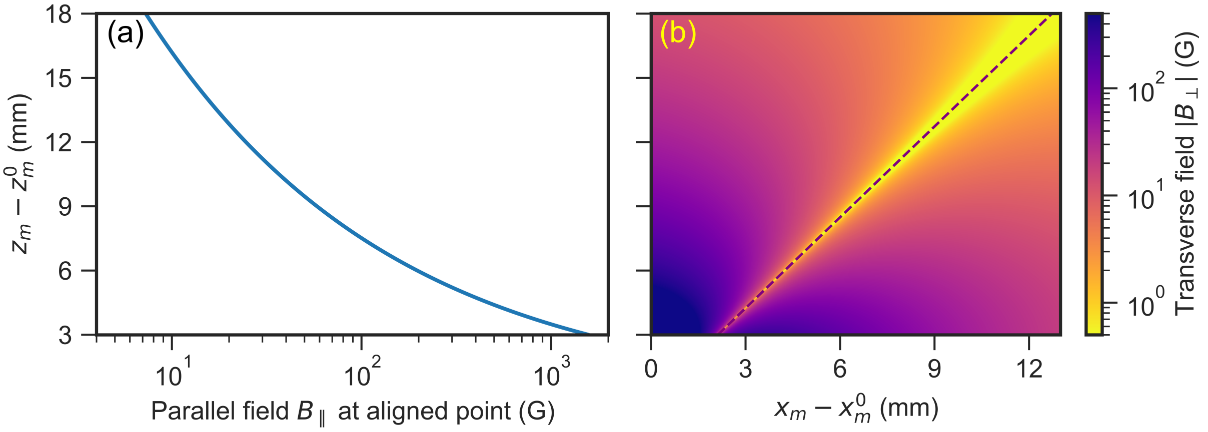

Figure 2.6: Alignment axis of a permanent magnet. (a) The calculated field $B_\parallel$ at the alignment coordinates for each height. (b) Simulated transverse magnetic field in a cross-section containing the NV axis. The alignment axis, where $B_\perp = 0$, is marked by a dashed line. The NV was assumed to be parallel to the $y_m z_m$-plane.

x_m, y_m, z_m are the coordinates of the approximated dipole at the magnet's center.

These results assisted in aligning the magnet for low fields. To do so, I found 4-5 alignment points in a region where it is possible to align the magnet according to the PL scan (at z_m values where the aligned field is 400–800 G). From these points, I found the axis $\{x_m^*(z_m), y_m^*(z_m)\}$, and using Eq. 2.2, reached the desired aligned field with a precision of about 10%.

The diamonds we used in this work were all single-crystal (100) cut diamonds, which means that all the NVs within the diamond belong to one of four orientations. The alignment axes of each of these orientations depend on the placement of the sample. Still, after finding one of these axes, the three other alignment axes could be predicted according to Eq. 2.1 and verified by localized scans.

Previous works utilized more thorough techniques to align the magnetic field beyond the >0.5° mentioned above. Notably, this can be done by acquiring ODMR spectra as a function of magnet position[139], thermal echo sequences[82], or by the 15N ESEEM of NV centers[140,139]. However, during this work, the optical method described above sufficed.

VECTOR ELECTROMAGNET

During this study, I designed and constructed an RT vector magnet. The design was based on a vector magnet designed at Max Planck Institute of Solid State Research, Stuttgart, for a low-temperature setup[141]. The magnet consists of three conical copper coils tilted at 54.7° (the magic angle) from the normal to the sample plane, sitting above the sample. Fig. 2.7(a-b) shows photographs of the coils from the side and top views, showing the respective position of the sample. The tilt angle was chosen according to the NV center's axis in a (100)-diamond. The coils' position was set so the sample sat at the intersection of three coil axes. The coils are connected to a massive aluminum block cooled by water to dissipate heat generated by the current. The magnet system also features a hole, which enables us to supplement the electromagnet with a permanent magnet.

Currents in the coils were driven by three stable current sources (ITEST, BE2811), and we can run up to 0.8 A through each coil before reaching the saturation voltage of the current source.

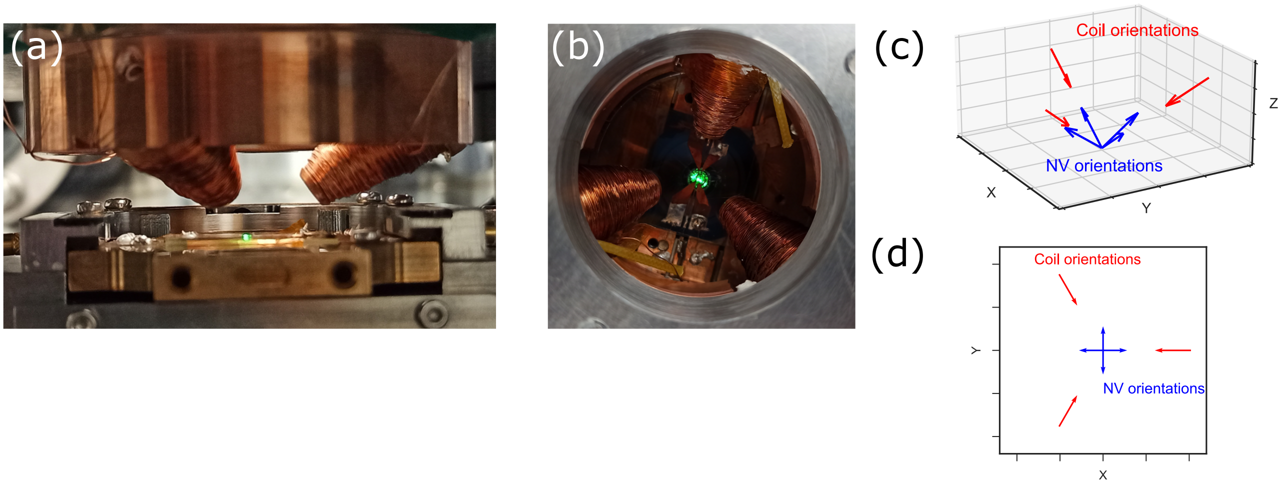

Figure 2.7: RT vector magnet. (a) The side-view of the magnet coils above the sample shows the magic angle tilt of the coils. (b) The top view of the coils; the sample is in the center (illuminated in green). (c) Schematic description of the orientation of the three coils and four possible orientations of an NV center in the diamond crystal. (d) Projection of the vector shown in (c) onto the sample plane (xy-plane).

The current source's stability ultimately limits the vector electromagnet's precision, calculated to be ~1 mG, but this has yet to be confirmed.

Compared to a Helmholtz configuration, this configuration compromises homogeneity in favor of compactness while still inducing substantial fields. We opted for this compromise as nanoscale magnetic resonance experiments do not require homogeneity beyond a volume of $\sim\ (20\,\mathrm{nm})^3$. The vector magnet can apply a field of 15 G in all orientations and up to 20 G for some directions.

Aligning the vector electromagnet

The vector electromagnet provides fields of up to 20 G, so it cannot be aligned optically with the alignment axis technique previously discussed. I aligned the vector magnet by sweeping the field and acquiring ODMR spectra at each point. I performed a one-dimensional sweep of a field tilted at 54.7° from the normal to the sample plane and at various azimuth angles $\phi = 0\text{–}360°$. The single parameter sweep is efficient and can determine the aligned field orientation by the point of maximal splitting between the $|0\rangle \leftrightarrow |1\rangle$ and $|0\rangle \leftrightarrow |-1\rangle$ transitions of the ODMR.

Arbitrary magnetic fields were generated by assuming that each of the three coils generates a field at a tilt of 54.7° from the normal to the sample plane and positioned at spacings of 120° in the sample plane. This geometry is described in Fig. 2.7(c) and in the projection onto the sample plane of Fig. 2.7(d). I assume the field is proportional to the current, a valid assumption for a copper core coil. Under these assumptions, we can calculate the required currents to generate a field in any arbitrary direction, particularly to generate a sweep of the field at a tilt of 54.7°.

The vector electromagnet allows us to apply fields in arbitrary directions with high precision and relative flexibility (compared to a mechanical stage). This is particularly relevant for potential magnetic tomography experiments (the subject of Chapter 3). While it was not employed for those experiments, it will be of great value in future ones. Precise control of magnetic fields is also of value for zero-field experiments. We demonstrated the vector electromagnet's potential for these

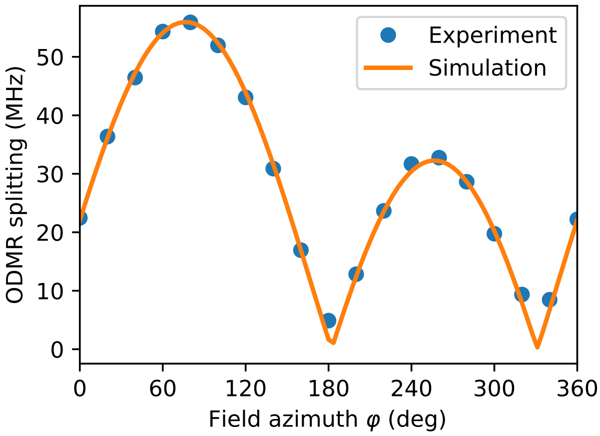

Figure 2.8: Aligning the vector electromagnet. A sweep of the magnetic field azimuth, at a constant magnitude and tilted from the sample plane at $\sim 54.7°$. The peak point marks the aligned orientation for this NV. Blue circles are the experimental data, and the orange curve is a simulation, correcting for deviations in the magnetic field angle.

experiments by canceling out the ambient magnetic field without any permanent magnet in the vicinity. The ambient field was measured to be $\sim$0.4 G, which is consistent with the value of the geomagnetic (Earth) field; this small field is apparent in the narrowing linewidth at true zero-field.

2.4 EXPERIMENT SOFTWARE

The experiments were controlled with the Qudi software suite (2019 version)[142], an open-source Python-based software. We made adaptations to our specific setup and experimental needs, such as adding new hardware modules to communicate with our specific hardware. Within the Qudi framework, I developed automation software that enables running measurement tasks with feedback. The automation scheme starts with a list of predefined points of interest - potential NV centers - within a single confocal scan. It has a flexible interface to choose a variety of tasks to perform on each point of interest, such as magnet scans or $g^2(\tau)$ autocorrelation measurements. The same scheme may be used to perform a series of experiments on a single point of interest for a list of sequences with some varying parameters, e.g., the position of the permanent magnet.

2.5 DIAMOND SAMPLES AND THEIR PREPARATION

The experiments detailed in this thesis used quantum-grade, single-crystal diamond membranes, where the sample plane is parallel to the (100) crystal plane. The diamonds were synthesized by Element Six (UK) Ltd. and then sliced and polished to a thickness of 20–50 µm. Shallow NV centers were created by implanting $15N^+$ ions at 5–10 keV, electron irradiation and annealing in a vacuum of $<10^{-7}$ Torr at 850 °C.

The diamonds we used were patterned with conical nanopillars by lithography to enhance the PL signal[143]. The nanopillars enhance the photon collection efficiency of NV centers' fluorescence by approximately an order of magnitude. This enhancement implies approximately a three-fold improvement in sensitivity[9], but it also has importance on the amount of laser energy impacted

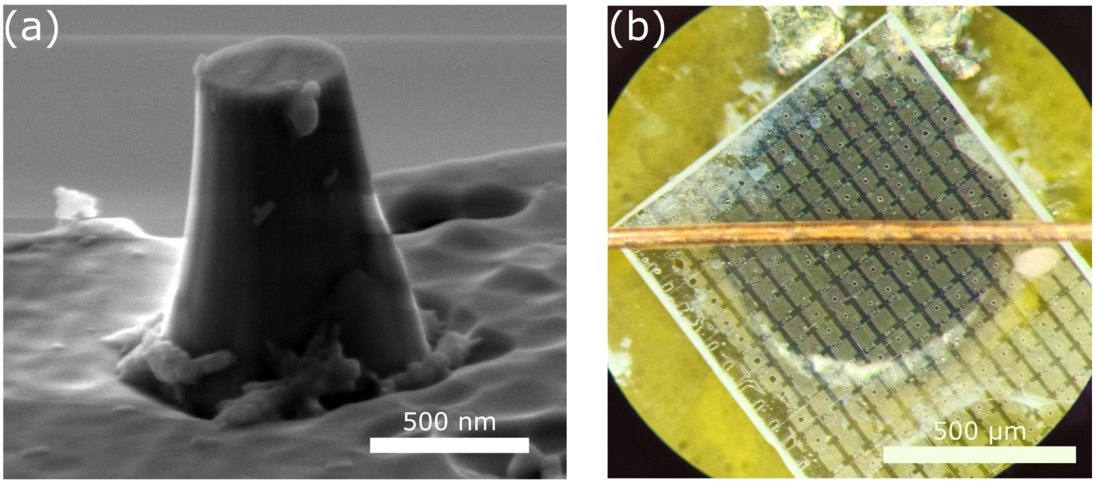

Figure 2.9: A diamond membrane with nanopillars. The diamond samples in this work were thin membranes patterned with arrays of nanopillars to enhance PL collection efficiency. (a) A scanning electron micrograph of a diamond nanopillar (micrograph by Dr. Amit Finkler). (b) A light microscope image of a diamond membrane, where the nanopillar arrays (square patterns) are apparent. The diamond is placed on a sapphire-polyimide substrate, with a copper wire on top for RF delivery.

on the sample. The nanopillars concentrate the laser, and thus, the NV centers are saturated at much lower incident laser powers, ~0.5 mW; in a bulk diamond, this may be ten times higher. The nanopillar structure also decreases the amount of laser transmitted through the diamond surface. Thus, employing nanopillars reduces the total amount of laser energy by 1-2 orders of magnitude. This is a crucial improvement for sensitive samples, such as organic materials.

Before experiments, we prepared the surface of the diamond by a standard procedure of boiling in an acid solution[134]. The solution is a 1:1:1 mixture of 65% nitric acid, 95% sulfuric acid, and 70% perchloric acid[144]. We placed the diamond in the acids in a reflux apparatus and kept it at a soft boil for approximately four to six hours. Following the process, the diamond was washed several times with triple distilled water to wash away residual acid. Then, the water was gradually replaced by isopropyl alcohol, and lastly, the membrane was dried under a gentle flow of dry nitrogen gas.

2.6 Low-temperature system

We constructed and tested a low-temperature ultra-high vacuum system for nanoscale magnetic resonance experiments with NV centers[a]. The setup is paired with the RT system described before, sharing the same optics (see Fig. 2.1) and electronics. The low-temperature stage resides within an ultra-high vacuum (UHV) chamber attached to a 4.2 K liquid helium cryostat (CRYOVAC GmbH & Co. KG). The sample stage includes an objective lens for optical access, RF connections, and a superconducting vector magnet (in a similar configuration to the RT vector magnet described in Section 2.3). The stage is based on a home-built three-axis, open-loop piezo motor to position and focus the sample (driven by attocube systems AG, ANC300). The stage also includes preparation for an AFM, but this has not been implemented at the time of writing.

Following the improvements we initiated, the cryostat's thermal isolation was improved to achieve a liquid helium hold-time of 6.5 days, enough to carry out complex experiments without the need

---

[a] Dr. Jitender Kumar constructed the sample stage and other significant elements of the LT system

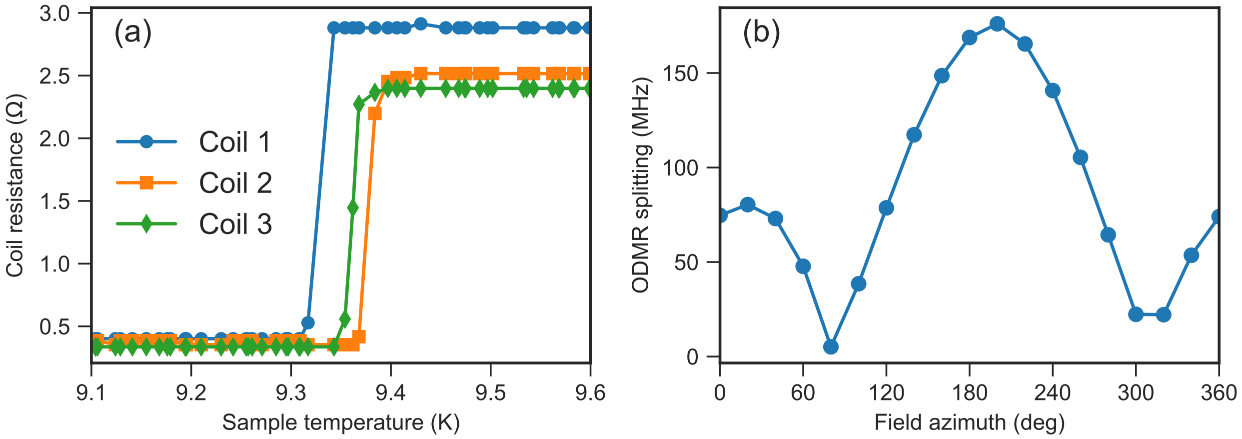

Figure 2.10: LT superconducting magnet characterization. (a) Resistance of each of the three coils forming the LT vector magnet as a function of temperature at the sample. The superconducting transition is apparent at ∼9.35 K. (b) ODMR splitting of an NV center as a function of the magnetic field's azimuth, revealing the alignment azimuth for this NV center. The root-mean-square current was 1 A.

to interrupt to fill cryogenic liquids. The sample has a base temperature of ∼5 K, measured by a sensor near the sample, slightly higher than the bath's temperature. Inputting RF into the system heats the stage, and the operation limit is 9 K due to the magnet's superconducting transition. Thus, operation should was done carefully, and the duty cycle of pulse sequences was decreased by dead times to avoid overheating.

Fig. 2.10 presents some data from characterizing the LT superconducting vector magnet. Fig. 2.10(a) shows the resistance of each of the three magnet coils, measured by monitoring the voltage under constant current of 10 mA. The superconducting transition is apparent at ≈9.35 K. The variance is due to a temperature gradient in the system. Fig. 2.10(b) shows an NV center's ODMR splitting as a function of the magnet's field azimuth at a root-mean-square current of 1 A (as previously discussed in Section 2.3). The peak of the plot shows the approximate alignment position of the magnet; as is evident by comparing it to the RT vector magnet (Fig. 2.8), the splitting here is larger, while the magnet was operated at approximately half its saturation current - 1.9–2.65 A. This variance stems from coil differences (due to manufacturing or integration variations). Thus, we conclude that the maximal obtainable field in the LT system ranges from 60–85 G, depending on field orientation.

Fig. 2.11 is demonstrative data from the LT system. This set of experiments, along with the ability to obtain clear confocal images of the sample in the system, constitute a proof-of-concept data set. As the optical and RF units of the RT system are shared by the LT system, any experiment based on more complex pulse sequences may be carried out.

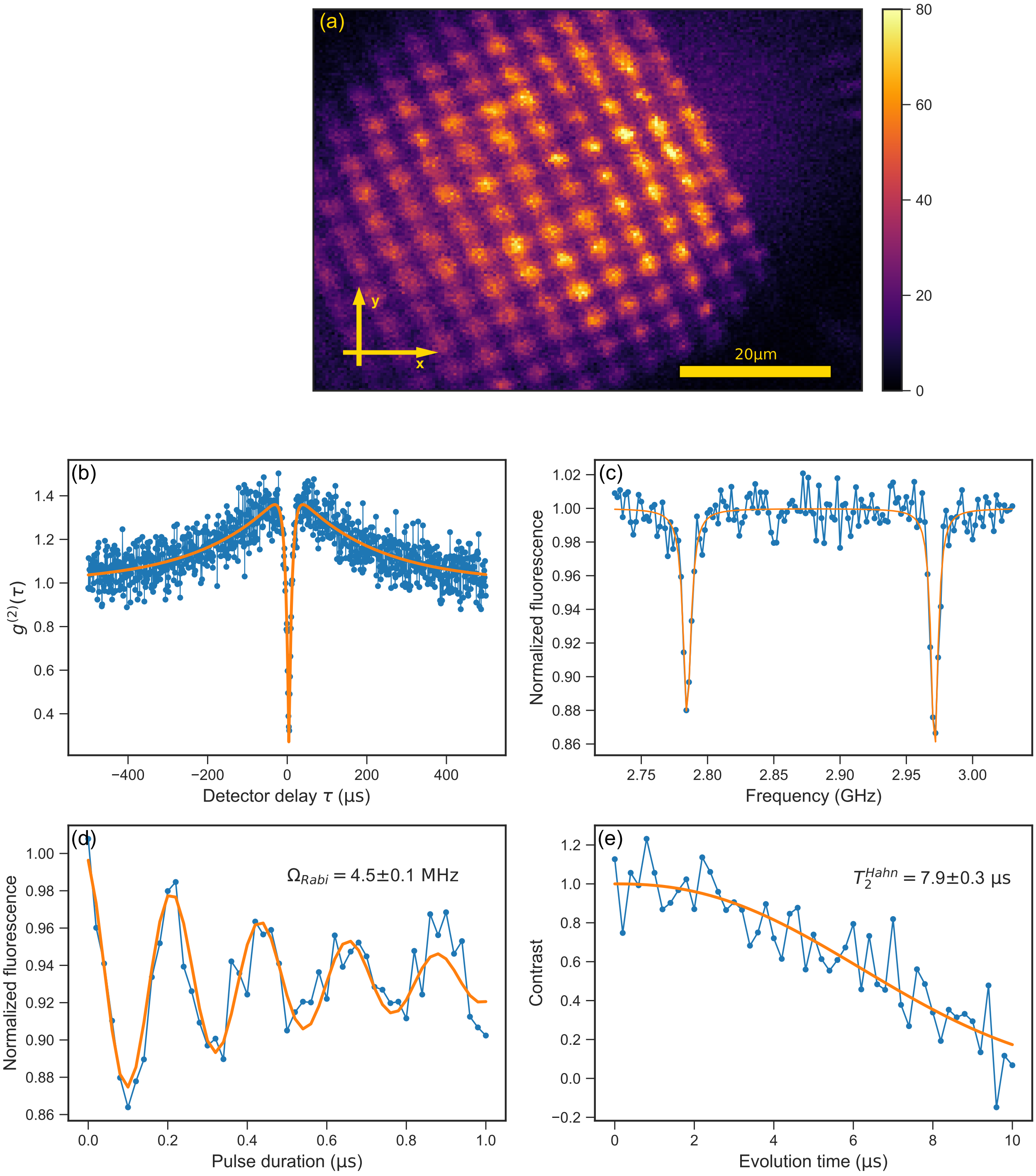

Figure 2.11: Demonstrative measurements of NV centers at 5.5K. (a) Confocal scan of a diamond membrane with nanopillars in the LT system. (b) NV center fluorescence autocorrelation. The anti-bunching dip below 0.5 indicates it is a single quantum emitter. (c) ODMR spectrum of a single NV center exhibiting Zeeman spitting due to a magnetic field induced by a superconducting vector magnet. The magnet can induce fields up to $87\,\mathrm{G}$. (d) Rabi oscillations of a single NV center, with a driving frequency of $(4.49 \pm 0.05)\,\mathrm{MHz}$ and an optical contrast of 14%. (e) Spin-echo decay of an NV center, exhibiting a coherence time of $T_2 = (7.9 \pm 0.3)\,\mu\mathrm{s}$.

3

Mapping electron spins at the nanoscale with magnetic tomography

In this chapter, I present a protocol for locating electron spins near a quantum spin sensor using a varying magnetic field vector. The varying magnetic field modulates the dipolar coupling frequency between a target spin and the sensor spin, as depicted in Fig. 3.1(a). I demonstrate the protocol using a spin system of an NV center spin as a sensor and surrounding "dark spins" in the diamond's lattice. Using the protocol, I find a spin's full position coordinates with Ångstrom-scale precision, a ten-fold improvement in accuracy compared to results with similar techniques. I further discuss the working parameter range of the technique and determine the position of another, more distant, electron with lesser precision to illustrate a potential route to single-molecule distance measurements. Finally, I show the protocol's applicability to nitroxide spin labels, which are ubiquitous in biomolecule distance measurement studies.

Parts of this chapter appeared in a manuscript titled "Mapping Single Electron Spins with Magnetic Tomography", published in Physical Review Applied[145].

3.1 Background

Magnetic resonance spectroscopy (MRS) has been indispensable for determining the structure and function of biomolecules, such as proteins[146,147]. Electron paramagnetic resonance (EPR), for example, is used to study the structure of organic molecules by measuring the distance between two radicals with unpaired electrons attached to predetermined parts of the molecule (i.e., spin labels)[116,148]. Conventional magnetic resonance techniques rely on the signal from large ensembles

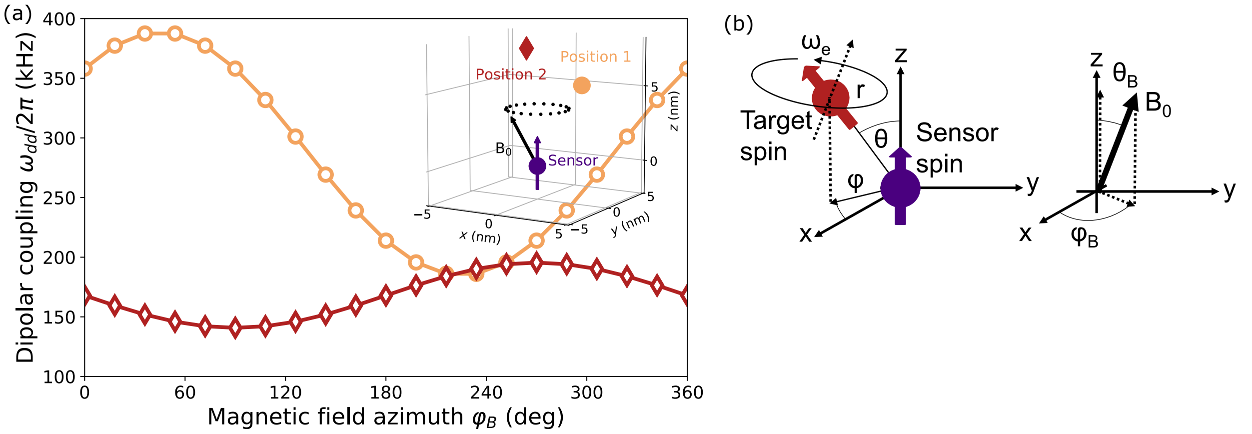

Figure 3.1: Magnetic tomography concept and notations. (a) A simulation of the dipolar coupling frequency modulation by a tilted magnetic field. The curves show distinct dipolar coupling oscillations for two target spin positions shown in the inset. The simulation was done for a magnetic field tilted at a polar angle $\theta_B = 29^\circ$ and a varying azimuth ϕ_B. The oscillation's amplitude, offset, and phase contain the target spin position information. (b) A description of the system and notations. The system includes a sensor spin at the origin whose quantization axis is $\hat{\mathbf{z}}$, and I describe the target spin's position in spherical coordinates (r, θ, φ). The external magnetic field vector is described by the magnitude B_0, a tilt angle from the sensor's axis θ_B, and an azimuth of ϕ_B.

of molecules and thus measure a mean value. Nanoscale techniques sensitive to specific ensemble constituents may augment ensemble techniques and reveal new information.

The diamond's nitrogen-vacancy (NV) center is an atomic defect in the diamond crystal that can function as a quantum sensor of magnetic fields in nanoscale volumes[149]. Quantum sensing with the NV center is a promising platform for nanoscale MRS[150], potentially extending the methods to the single-molecule limit. In recent years, nanoscale nuclear magnetic resonance using NV centers has been demonstrated[37,58], down to the single protein level[95], as well as NV-based EPR spectroscopy of single molecules[118,119].

By mapping the precise positions of spin labels attached to individual organic molecules, it would be possible to elucidate the structure of a single molecule. Mapping the positions of individual electron spins is likewise relevant for characterizing organic quantum networks, a proposed platform for quantum processors[151]. Such mapping has been demonstrated with magnetic resonance force microscopy[66], NV-based magnetometer coupled with a scanning magnetic tip[106], scanning tunneling microscopy[152,69], and inductive-based EPR imaging[153]. Nuclear spin mapping is a related endeavor: recent studies mapped ^{13}C spin clusters in a diamond lattice around an NV center sensor based on detecting the spins' Larmor precession[82,81,83]. However, it is impractical for electron spins due to the similarity between the sensor and target spin's gyromagnetic factor.

Previous studies have utilized variable magnetic field orientations to locate electron spins surrounding an NV sensor by modulating the dipolar coupling. Sushkov et al.[88] introduced the concept to locate so-called "quantum reporters", surface spins on the diamond, to sense proton magnetic resonance. In this work, they located a spin with nanometer precision. Cooper et al.[111] employed the technique to range the distance of electron-nuclear spin defects from the NV sensor. In what follows, I describe and analyze an extension of their protocols to fully determine the position of spins surrounding the NV sensor and demonstrate it with precedent Ångstrom precision.

3.2 MAPPING PROTOCOL

The mapping protocol is based on measuring the dipolar coupling ω_{dd} between the sensor spin and a target spin as a function of the external magnetic field's (B_0) orientation. To do so, I tilt the magnetic field from the sensor's axis and sweep along a full 360° trajectory around the axis, analogous to computerized tomography[154]. The orientation of B_0 modulates the dipolar coupling, such that the position of the spin is encoded in the modulation.

Let us consider a system of a sensor spin ($\mathbf{S}_{nv}$) with an axial symmetric zero-field splitting (D), coupled to a proximate target spin ($\mathbf{S}_e$), under an external magnetic field ($\mathbf{B} = B_0\hat{\mathbf{b}}$). The NV center in diamond is the archetypal sensor; however, other candidate solid-state spin defects may meet these criteria, e.g., SiV in SiC[155]. I choose the coordinate system such that $\hat{\mathbf{z}}$ is the zero-field splitting axis; γ_{nv} (γ_e) is the sensor (target) spin gyromagnetic ratio. The following Hamiltonian thus describes the sensor-target spin system:

$$\mathcal{H} = D{S^z_{nv}}^2 + \gamma_{nv}\mathbf{B}\cdot\mathbf{S}_{nv} + \gamma_e\mathbf{B}\cdot\mathbf{S}_e + \mathcal{H}_{int} \tag{3.1}$$

Here I neglected the hyperfine coupling to the nitrogen spin of the NV center (∼3 MHz), as it will be negligible relative to the Zeeman splitting (>100 MHz) and the RF driving of NV center spin (∼10 MHz) considered here. The interaction Hamiltonian between two electron spins is given by[2]:

$$\mathcal{H}_{int} = \underbrace{J(\mathbf{r}_{nv},\mathbf{r}_e)\,\mathbf{S}_{nv}\cdot\mathbf{S}_e}_{\text{exchange int.}} + \underbrace{\mathbf{S}_{nv}\cdot\mathbb{D}_{dd}\cdot\mathbf{S}_e}_{\text{dipole−dipole int.}} \tag{3.2}$$

J is an exchange coupling factor that depends on the distance between the two electrons; $\mathbf{D}_{dd}$ is the dipole-dipole tensor. For sufficiently distant spins ($\gtrsim 1.5$ nm)[115], the exchange interaction may be neglected, and the interaction may be approximated by a dipole-dipole interaction:

$$\mathcal{H}_{dd} = -\frac{\mu_0\gamma_{nv}\gamma_e\hbar}{2r^3}\left(3\left(\mathbf{S}_{nv}\cdot\hat{\mathbf{r}}\right)\left(\mathbf{S}_e\cdot\hat{\mathbf{r}}\right) - \mathbf{S}_{nv}\cdot\mathbf{S}_e\right) \tag{3.3}$$

I consider a regime where $\mathcal{H}_{dd} \ll \gamma_{nv/e}B_0 \ll D$, so that the zero-field term dominates the eigenstates of the sensor spin, and its Zeeman term dominates the eigenstates of the target spin. Invoking the secular approximation, I neglect the sensor and target spin operator components that do not commute with $S^z_{nv} = \mathbf{S}_{nv}\cdot\hat{\mathbf{z}}$, $S^b_e = \mathbf{S}_e\cdot\hat{\mathbf{b}}$, accordingly. I obtain the following approximated term for the dipole-dipole interaction:

$$\begin{aligned}\mathcal{H}_{dd} &\approx -\frac{\mu_0\gamma_{nv}\gamma_e\hbar}{2r^3}\left(3\left(\hat{\mathbf{z}}\cdot\hat{r}\right)\left(\hat{\mathbf{b}}\cdot\hat{r}\right) - \hat{\mathbf{z}}\cdot\hat{r}\right)S^z_{nv}S^b_e\\ &\equiv \omega_{dd}(\mathbf{r},\hat{\mathbf{b}})S^z_{nv}S^b_e\end{aligned} \tag{3.4}$$

Here, $\mathbf{r} = r\hat{\mathbf{r}}$ is the vector connecting the two spins, and I defined the field-dependent dipolar coupling strength $\omega_{dd}(\mathbf{r},\hat{\mathbf{b}})$.

It is convenient to analyze the system in spherical coordinates, where the sensor's position is set as the origin, and the target position is given by the distance r, a polar angle θ, and azimuth ϕ. The magnetic field orientation is described by the polar angle θ_B (the tilt from $\hat{\mathbf{z}}$) and the azimuth ϕ_B. Fig. 3.1(b) depicts the coordinate systems and their notations. I then write the dipolar coupling strength as a function of the target spin coordinates and the magnetic field orientation:

$$\begin{aligned}\omega_{dd}(\mathbf{r},\hat{\mathbf{b}}) = -\frac{\mu_0\gamma_{nv}\gamma_e\hbar}{2r^3}\Big[&\left(3\cos^2\theta-1\right)\cos\theta_B + \\ &+\frac{3}{2}\sin\theta_B\sin 2\theta\cos\left(\phi_B-\phi\right)\Big]\end{aligned} \tag{3.5}$$

For the case of $\mathbf{B} \parallel \hat{\mathbf{z}}$, a field aligned with the sensor's axis, the second term of Eq. 3.5 vanishes, and the dipolar coupling becomes a function of r and θ alone. However, sampling ω_{dd} at several magnetic field orientations (i.e., several sets of $(\theta_B,\ \phi_B)$) provides information to identify the target spin position.

To extract the available information on the position of the target spin from the dipolar coupling, let us consider an experiment where the magnetic field orientation is varied to extract $(r,\ \theta,\ \phi)$. Eq. 3.5 has the form of a shifted sine, so it is convenient to perform a tomography-like sweep of the magnetic field's azimuth ϕ_B at a constant tilt angle θ_B, estimating ω_{dd} at each orientation. ω_{dd} oscillates over ϕ_B with parameters encoding the spin's position. The azimuth of the spin ϕ is encoded in the sine's phase; the distance r and polar angle θ may be extracted numerically by solving a set of nonlinear equations for the sine's offset and amplitude.

Fig. 3.1(a) illustrates a sweep of the magnetic field azimuth for two different target spin positions, exhibiting distinct sine curves. Three sampling points are sufficient to extract three variables. However, utilizing the added information on the sinusoidal shape will provide a more robust estimation and validate the theory.

3.3 EXPERIMENTAL METHODS

In this experiment, I used a quantum grade (100)-cut diamond fabricated by Element6, sliced and polished to 15 μm thickness. Shallow NV centers were created by implanting ^{15}N ions at 5 keV and annealing in a vacuum of $<10^{-7}$ Torr at 975 °C. The diamond was subsequently patterned with nanopillars by lithography and reactive ion etching. Andrej Denisenko and Rainer Stöhr, 3. Physikalisches Institut, Universität Stuttgart, created the NV centers and fabricated the nanopillars (respectively). The generated NV centers are approximately (8.0 ± 3.1) nm deep, according to SRIM simulations. The experiment was conducted on our RT setup (see Chapter 2 for details).

I demonstrate single spin mapping using magnetic tomography on a system composed of a single shallow NV center in diamond as the sensor and two proximate unpaired electrons (spin-$\frac{1}{2}$) as the target spins. One of the target spins or both are possibly a stable surface spin[57,106,88], but later on, I argue that this is unlikely. So, the spins' precise nature is unknown.

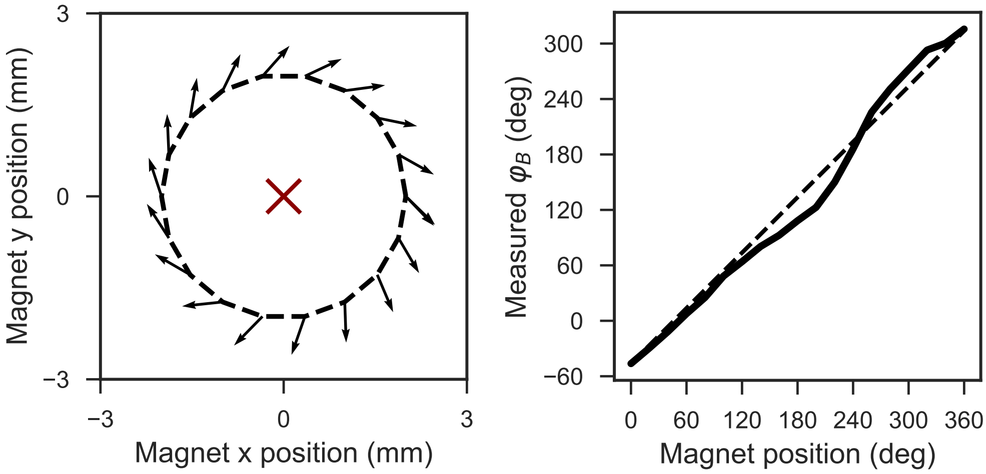

Figure 3.2: Transverse field orientation over the magnet path. (a) The orientation of the magnetic field along an azimuthal sweep, plotted as a function of the magnet's position. The arrows denote the field's orientation in the plane transverse to the NV axis. (b) The field's azimuth ϕ_B as a function of the position along the circular path.

Controlling and characterizing the magnetic field

A crucial aspect of the magnetic tomography technique is careful and precise magnetic field control (B_0). I used a permanent magnet positioned by a tri-axis motor stage (the vector electromagnet, as mentioned in Chapter 2, was not available yet). Thus, I controlled the magnitude and direction by moving the physical position of the permanent magnet. I aligned the magnetic field at approximately 35 G by the procedure for aligning a low magnetic field described in Section 2.3.

Magnetic tomography is based on a rotating magnetic field vector. To realize this, I first find the alignment point at the desired field magnitude. To rotate the magnet field vector at a specific tilt angle, I swept the magnet's position around the alignment point in a circle parallel to the diamond's surface (at a constant z_m). A trajectory with a larger radius leads to a larger tilt angle.

I verify that the circular path rotates the magnetic field vector by measuring the magnetic field vector over such a path. The complete magnetic field vector was determined using a vector magnetometry technique previously described by Maertz et al.[156]. The measurement relies on measuring the ODMR spectra of NV centers from all four orientations, from which I extracted the complete magnet field vector.

I rotated the magnet over a circular path, with a radius of 2 mm, around the alignment point of an NV center chosen as the reference orientation. I then sampled the ODMR spectra every 20° and repeated the process with the same path for all four NV center orientations. Fig. 3.2 depicts the characterization of the field vector over the circular path. Fig. 3.2(a) shows the orientation (arrows) of the field's transverse component at each of the sampling points over the circular path (dashed line); the arrows' direction is the fields' azimuth (ϕ_B). Fig. 3.2(b) plots the field's azimuth ϕ_B versus the position along the path given by the position along the circular path (solid line), and it is compared with the ideal case (dashed line). This measurement indicates that sweeping the magnet's position as described leads to the desired field modulation.

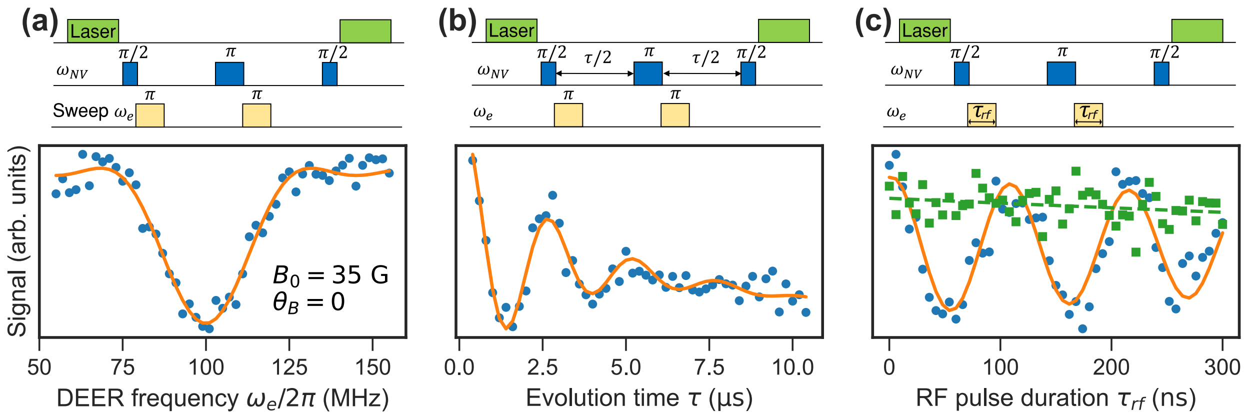

Figure 3.3: Measuring the dipolar coupling of proximate spins with DEER. (a) The top panel depicts the DEER pulse sequence to measure the electron spin resonance of spins proximate to the sensor. The blue dots in the plot are the sensor signal as a function of the DEER frequency ω_e, and the orange curve is a fit to the squared sinc function. Here, $B_0 = 35$ G is aligned with the sensor's axis. (b) The top panel shows the DEER pulse sequence to measure the dipolar coupling strength. I set ω_e to the resonance frequency (obtained in (a)), and the duration of the spin-echo τ was varied. The orange line is a fit to a decaying sine. (c) The top panel depicts the DEER pulse sequence to observe Rabi oscillations of the target spin. It consists of a DEER sequence while fixing ω_e and the evolution time (acquired in (a) and (b)) and sweeping the duration of the RF pulses. The data (blue circles) was fitted to a decaying sine (solid orange line). The measurement was repeated with off-resonant RF pulses (green squares and dashed curve) exhibiting only slight decay of the sensor state.

Measuring the dipolar coupling by DEER

I detected electron spins coupled to the sensor by a double electron-electron resonance (DEER) protocol, which has been discussed in the past in this context[157,36,106,119]. The pulse sequence (see Fig. 3.3) is based on a spin-echo (Hahn echo) on the sensor spin, decoupling it from the surrounding spin-bath to extend its coherence[36]. The spin echo is supplemented by a pulse resonant with the target spin that flips its state midway through the spin echo, recoupling the sensor spin's evolution with the field of the target spin. For technical reasons, the target spin pulse (ω_e) is applied right after the π-pulse to the sensor spin. Also, another target spin pulse is applied at the beginning of the first evolution period. From the spin physics perspective, this pulse is redundant, as it only flips the initial state of the target spin; however, it serves to "balance" the second pulse's effect on the sensor spin's evolution during the second free evolution period[36].

I acquired a resonance spectrum of surrounding spins by sweeping the target spin pulses' frequency ω_e. Sweeping the duration (τ) of the spin-echo evolution modulates the interaction time, and the resulting signal will be modulated according to the dipolar coupling strength of the spins[106,119]. A large ensemble of spins (the bath) usually affects the sensor's spin evolution. Still, due to the r^{-3} scaling of the dipolar interaction, most of the signal originates from a volume of several nanometers radius around the sensor. If a few spins exist in this volume, their dipolar coupling frequencies will dominate, while the distant spin-bath will manifest as decoherence[57]. For a single target spin, the signal will oscillate at twice the dipolar coupling frequency (see derivation in Appendix A.3).

To find the proper pulse time for the target spin manipulation, I performed a Rabi measurement on the target spin. The sequence is similar to the DEER-frequency sequence, but I fixed the target spin frequency (ω_e) and the evolution (τ) while varying the RF pulse duration (Fig. 3.3(c) top panel). The bottom panel of Fig. 3.3(c) shows the resultant signal, exhibiting oscillations of the NV state, representing nutations of the target electron spin state.

While the DEER data is quite robust, I wanted to rule out any trivial artifacts that may arise from incorporating RF pulses into the spin-echo sequence. To do so, I repeated the target spin Rabi sequence but sufficiently detuned the RF pulses ($\omega_e = 200$ MHz) such that the pulses are not resonant with the target spin. As a result, the sequence should effectively behave like a spin-echo. Fig. 3.3(c) compares data from a sequence with resonant pulses (blue circles), which exhibit Rabi oscillations, with a sequence with off-resonance pulses (green squares), which exhibit only slight decay of the sensor state, probably due to the effect of the RF pulse.

3.4 MAPPING THE POSITION OF A PROXIMATE SPIN

To map the position of the proximate spin, I estimated the dipolar coupling strength at various orientations of the magnetic field. The measurements were done at a low magnetic field to minimize contrast loss due to a transverse magnetic field[23] ($B_0 \approx 38$ G; slightly higher than shown in Fig. 3.3(a), which was taken at an aligned field). I swept the magnetic field's azimuth (ϕ_B) at an approximately constant tilt (θ_B) and magnitude (B_0).

CALCULATING THE MAGNETIC FIELD TILT ANGLE θ_B

The field vector must be accurately assessed to estimate the spin's position correctly. To do so, I measured the ODMR spectrum of the NV center and the DEER spectrum of the target spins at each magnet position. From the target spin resonance frequency ω_{deer} and the NV transitions, I calculated the magnetic field tilt angle θ_B. I assumed there are no other significant terms in the Hamiltonian so that the target spin is quantized along the magnet field's axis, such that I could extract the field magnitude according to:

$$B_0 = \frac{\omega_{deer}}{\gamma_e} \tag{3.6}$$

Next, I utilized the NV center's $|0\rangle \leftrightarrow |-1\rangle$ transition frequency from an ODMR measurement, inputting this frequency and B_0, and by least-square minimization, I extracted the value of θ_B by diagonalizing the NV Hamiltonian in the presence of a non-aligned field, using $\theta_B^{init} = \arccos\left(\left(D - \gamma_{nv} B_0\right)/\gamma_e B_0\right)$ as an initial guess:

$$\mathcal{H} = DS_z^2 + \gamma_{nv} B_0 \left(\sin\left(\theta_B\right) S_x + \cos\left(\theta_B\right) S_z\right) \tag{3.7}$$

From this, I obtained a precise estimation of the magnetic tilt angle θ_B for each sampling point, to be later used to fit the data and extract the spin position.

MAGNETIC FIELD AZIMUTH SWEEPS

Per the protocol outlined in Section 3.2, I swept the azimuth of the magnetic field ϕ_B at a roughly constant tilt angle θ_B. Fig. 3.4 presents the results for a sweep of the magnetic field azimuth $\phi_B =$

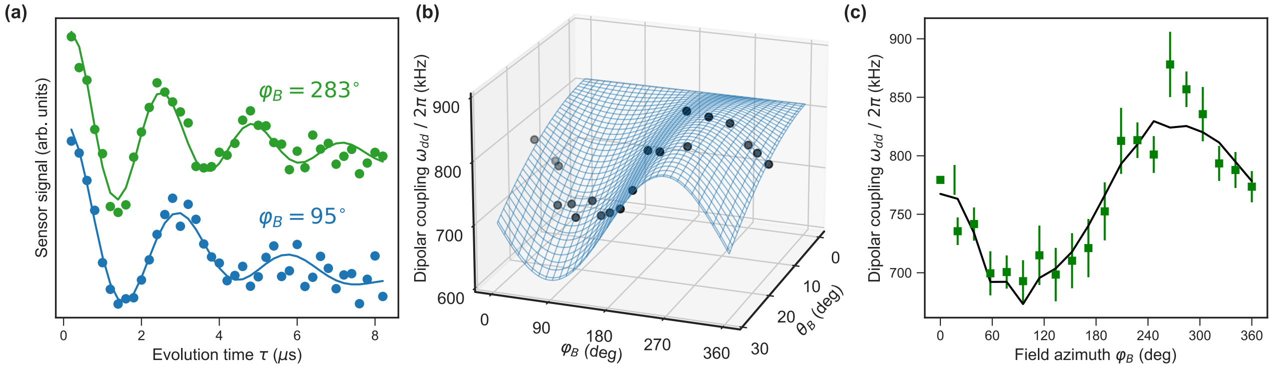

Figure 3.4: Magnetic azimuth scan to locate a spin by magnetic tomography. (a) Examples of dipolar coupling measurements for two different magnetic field azimuths ϕ_B, exhibiting two distinct dipolar coupling frequencies. Lines are fits to $f(\tau) = A\sin\left(\frac{1}{2}\omega_{dd}\tau+\varphi\right)e^{-\frac{\tau}{T_2}}$. (b) The estimated dipolar coupling frequencies at different magnetic field orientations are shown in black, and each has a different ϕ_B and θ_B. The points are fit to an $\omega_{dd}\left(\theta_B, \phi_B\right)$ manifold according to Eq. 3.5, where the target spin coordinates r, θ, ϕ are free parameters. The blue manifold is the fitted function. (c) The projection of the data points from (b) on the $\theta_B = 0$ plane, just as a function of magnetic field azimuth ϕ_B. The black line is the fit to Eq. 3.5, incorporating variations in θ_B.

0–360°. Fig. 3.4(a) depicts two sample DEER dipolar coupling measurements at different ϕ_B, highlighting the distinct frequencies. The magnetic field tilt θ_B varied over the sweep at an average angle of $\langle\theta_B\rangle = 19.4^\circ$. Fig. 3.4(b) depicts the dipolar coupling values extracted from the DEER measurements as a function of the magnetic field orientation (black dots), where θ_B was extracted as described in the previous section. I then fitted the set of measured $\omega_{dd}\left(\phi_B, \theta_B\right)$ to the model for $\omega\left(\mathbf{r}, \hat{\mathbf{b}}\right)$ (Eq. 3.5), such that the spin position coordinates (r, θ, ϕ) were the variable parameters in the fit. The resultant fit manifold is plotted in Fig. 3.4(b) (light blue surface). For clarity, Fig. 3.4(c) displays the *projection* of the data points (green squares), just as a function of ϕ_B; i.e., it is the curve $\omega_{dd}\left(\phi_B\right) = \omega_{dd}\left(\phi_B, \theta_B\left(\phi_B\right)\right)$, and is thus not a smooth sine. The fit function (solid black line) resembles a broken sine due to the incorporation of variation in θ_B. Nonetheless, in Fig. 3.4(c) it is apparent that $\omega_{dd}\left(\phi_B\right)$ oscillates over a single period, consistent with Eq. 3.5. The value of ϕ is given in reference to ϕ_B, which is set arbitrarily. However, from the magnet's trajectory, the position of the spin can then be translated to a real-world position in the lab coordinate system.

Fig. 3.4(b-c) plots show the most robust result, measured for a circular path of the magnet with a 2 mm radius around the alignment position. The magnet path corresponds to an azimuth scan with a tilt angle of approximately 19.4°. I repeated the experiment for several trajectories of the magnet with radii of 0.5–2 mm, corresponding to increasing values of magnetic field tilt θ_B. The results are presented in Fig. 3.5 for different magnet path radii. The black lines in the figures are sinusoidal fits to demonstrate the relation to the theory; the amplitude of the sine fit is noted for each dataset. While this analysis is not as rigorous as the fit shown in Fig. 3.4(b), which incorporated the variation in the magnetic field tilt, it illustrates how the ω_{dd} modulation amplitude increases for larger scan radii, which corresponds to a greater tilt angle, as expected from Eq. 3.5.

From the analysis of the 2 mm scan in Fig. 3.4, I obtain the target spin coordinates (the coordinates are noted with the subscript 1 because, as shown later in Section 3.6, another target spin is

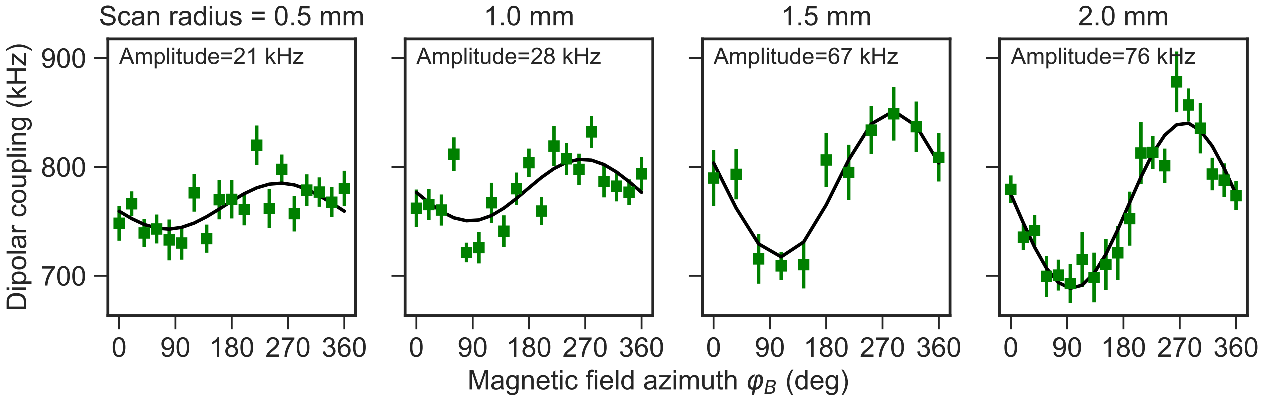

Figure 3.5: Azimuth sweeps at different field tilts. Azimuth sweeps of the dipolar coupling were taken at several magnetic field tilts θ_B, determined by magnet path radius. For larger θ_B, the modulation amplitude increased. Black solid lines are sine fits to outline the modulation amplitude, denoted in each plot. The data of the main text appears in the rightmost plot (largest tilt angle).

observed when the measurement is conducted at a higher magnetic field):

$$r_1 = (4.89 \pm 0.02)\,\mathrm{nm};\ \theta_1 = (9.0 \pm 0.9)^\circ;\ \phi_1 = (-98 \pm 6)^\circ \tag{3.8}$$

The estimated spin position is plotted graphically in Fig. 3.6. The position is given by a flat ellipsoid; Fig. 3.6(bottom) shows its projection on the xy-plane ($z = 0$), and Fig. 3.6(top) shows its projection on a ρz-plane at $\phi = -98^\circ$. The measured position makes it unlikely that this is a surface spin: if so, the upper bound of the NVs depth would be $r_1 \cos(54.7^\circ - \theta_1) \approx 3.4\,\mathrm{nm}$. This is not probable, considering the implantation energy of the diamond.

3.5 PRECISION OF SPIN LOCATION

It is of value to characterize the precision of the measurement by defining an uncertainty volume. The uncertainty volume ΔV can be thought of heuristically as a box with sides of Δr, $r\Delta\theta$, $r\sin(\theta)\,\Delta\phi$, where Δr, $\Delta\theta$, $\Delta\phi$ are the confidence intervals extracted from fit the data to Eq. 3.5. The volume of this box is:

$$\begin{aligned}\Delta V &= \int_{\phi-\Delta\phi}^{\phi+\Delta\phi} \mathrm{d}\phi' \int_{\theta-\Delta\theta}^{\theta+\Delta\theta} \sin(\theta')\,\mathrm{d}\theta' \int_{r-\Delta r}^{r+\Delta r} r'^2 \mathrm{d}r' = \\ &= 2\Delta\phi\left(\cos(\theta-\Delta\theta) - \cos(\theta+\Delta\theta)\right)\frac{(r+\Delta r)^3 - (r-\Delta r)^3}{3} = \\ &= 4\Delta\phi\sin(\theta)\underbrace{\sin(\Delta\theta)}_{\approx\Delta\theta}\frac{6r^2\Delta r + \overbrace{\cancel{\Delta r^3}}^{\ll\Delta r}}{3} = 8r^2\sin(\theta)\,\Delta r\Delta\theta\Delta\phi\end{aligned} \tag{3.9}$$

Then, for clarity, I define the location precision as a metric with units of length (e.g., nanometer), $\Delta R = \Delta V^{\frac{1}{3}}$:

$$\Delta R \equiv \left(8r^2\sin(\theta)\,\Delta r\Delta\theta\Delta\phi\right)^{\frac{1}{3}} \tag{3.10}$$

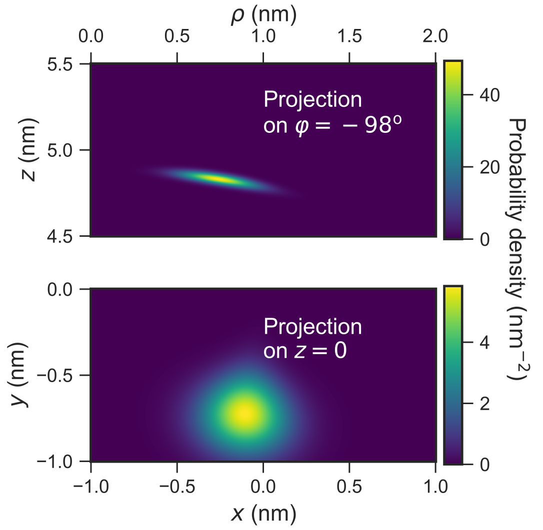

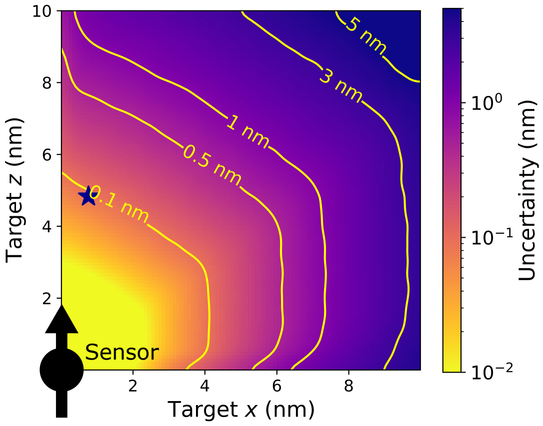

Figure 3.6: Measured spin position heat map. Probability maps for the position of the target spin, as extracted from the data in Fig. 3.4, presented as a projection on a ρz-plane ($\rho \equiv \sqrt{x^2+y^2}$) at $\phi = -98°$, and a projection on the xy-plane ($z = 0$).

Figure 3.7: Location precision of electron spins. The location uncertainty ΔR vs. target spin coordinates ($x = r\sin\theta$, $z = r\cos\theta$), assuming $\Delta\omega_{dd} = 20\,\mathrm{kHz}$. Contours denote equal levels of uncertainty. The blue star marks the experiment's spin position.

This is can be thought of as the "radius" of an uncertainty sphere, although as shown in Fig 3.6, the distribution has an ellipsoid or disk-like shape.

From the confidence intervals of the experiment data fit (Fig. 3.4(b)), I estimated the uncertainty of the target spin position to be $\Delta R = 0.09\,\mathrm{nm}$. The largest uncertainty is along the $\hat{\phi}$ axis, with $r\sin(\theta)\,\Delta\phi = 0.09\,\mathrm{nm}$.

Precision as a function of target spin coordinates

To assess the method's applicability, I analyze the dependence of the location precision ΔR on the spin's position and sensor's characteristics. Underlying ΔR is the dipolar frequency sensitivity, which depends on the system parameters – such as the sensor decoherence time T_2 – and the specific protocol. As these aspects have been discussed in previous works[9], it is more interesting to focus the discussion on unique aspects of this protocol. Thus, I assumed a given frequency uncertainty $\Delta\omega_{dd}$ and calculated the uncertainty's dependence on the position of a target spin. The location uncertainty is proportional to the frequency uncertainty ($\Delta R \propto \Delta\omega_{dd}$), so the functional dependence of $\Delta R(\mathbf{r})$ would be independent of the choice of $\Delta\omega_{dd}$, and the presented results can be scaled according to any other value. For the discussion, I use a value similar to the experiment, $\Delta\omega_{dd} = 2\pi \times 20\,\mathrm{kHz}$ (in the aforementioned experiment, the uncertainty was in the range of 12–28 kHz).

I simulated the measurement by calculating the dipolar coupling modulation over an azimuth sweep according to Eq. 3.5 and then added noise to the array by adding random, normally distributed values with a standard deviation of $\Delta\omega_{dd}$. I fit the noisy array to a sine and extracted the coordinates. Finally, I repeated the process for each set of coordinates $N = 100$ times. The standard deviation of the extracted coordinates over the N repetitions is taken to be the uncertainty of the measurement. The calculated $\Delta R\,(r,\ \theta)$, plotted in Fig. 3.7. Due to the symmetry of $\omega_{dd}(\mathbf{r},\hat{\mathbf{b}})$, ΔR does not depend on the target spin's azimuth ϕ. The uncertainty values calculated for the target spin position were consistent with the measured values.

I found that the uncertainty is minimal for $\theta \to 0$ and maximal for $\theta \to 90^\circ$. At $\theta = 90^\circ$, the second term of Eq. 3.5 vanishes, eliminating the information on the spin's azimuth ϕ, such that for spins near $\theta = 90^\circ$, only the distance r and polar angle θ are observable. Also, Eq. 3.5 is centrosymmetric, so there will always be (at least) two solutions for every data set. In many scenarios, however, these ambiguities may be resolved with prior information on the system. For example, when imaging a sample on the crystal's surface, target spins will be in a thin slice on the surface, within a single hemisphere around the sensor[37]. Nonetheless, target spins over 10 nm away from the sensor in the range of $\theta = [0^\circ, 45^\circ]$ may be located with a precision better than 2 nm. This makes it appealing to use sensors whose axis is normal to the surface, e.g., an NV center in a diamond grown on the (111) crystal plane[158].

PRECISION AS A FUNCTION OF MAGNETIC FIELD PARAMETERS

The protocol is based on a tilted magnetic field, and I also explore the impact of the field parameters – magnitude B_0 and tilt θ_B – for the case of an NV center sensor. The NV center's function as a magnetometer usually relies on an optical measurement of the spin state within a two-state subspace of the spin-1 states, e.g., $|m_s = 0\rangle$, $|m_s = +1\rangle$. As discussed in Section 1.3, the optical contrast between the states is maximal for a field aligned with the center's zero-field splitting axis and decreases in the presence of a transverse field[23]. As the measurement requires a transverse magnetic field to modulate the dipolar coupling, there is a competition between the modulation amplitude and the contrast drop. Thus, it is interesting to analyze the uncertainty as a function of the magnetic field B_0 and field tilt angle θ_B to find the optimal conditions.

I assumed that the location uncertainty is proportional to the frequency estimation uncertainty $\Delta R \propto \Delta\omega_{dd}$, which can be shown numerically. The sensitivity of the sensor $\mathcal{S}$ determines the frequency estimation uncertainty. Thus, the following relations are derived:

$$\Delta\omega_{dd} \propto \mathcal{S} \propto \frac{1}{\mathcal{R}\sqrt{T_2 t_m}} \tag{3.11}$$

The last transition is based on the derivation of a quantum sensor's sensitivity, described by Degen et al. [9]. $\mathcal{R}$ is a unitless readout efficiency parameter, T_2 is the sensor's coherence time, and t_m is the total measurement time (integration time). An NV center read out by its spin-dependent PL will have a low optical contrast ($\mathcal{C} \ll 1$). In this case, the readout efficiency is approximately proportional to the optical contrast $\mathcal{R} \propto \mathcal{C}$, and I obtain that the frequency estimation uncertainty is proportional to the readout efficiency:

$$\Delta\omega_{dd} \propto \frac{1}{\mathcal{R}} \underbrace{\to}_{\mathcal{C}\ll 1} (\mathcal{R} \propto \mathcal{C}) \to \Delta\omega_{dd} \propto \frac{1}{\mathcal{C}} \tag{3.12}$$

The optical contrast's dependence on the magnetic field vector, $\mathcal{C}\,(B_0,\ \theta_B)$, does not have an

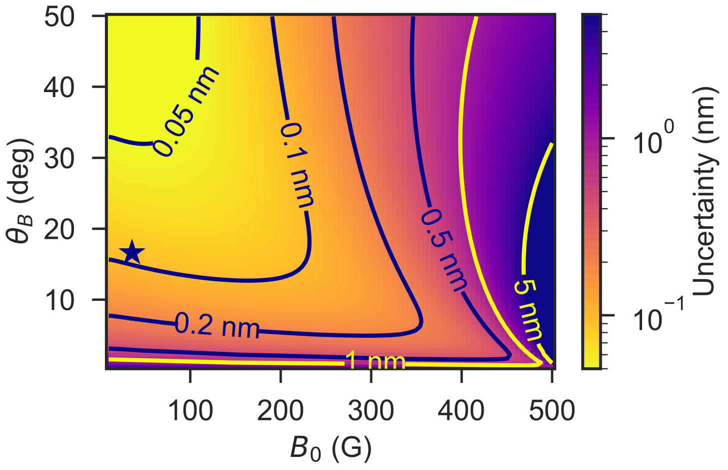

Figure 3.8: Parameter space for the tilted field scan. The location uncertainty is plotted as a function of magnetic field vector (B_0, θ_B). The target spin coordinates were taken from the experiment described in Section 3.4. The modulation of ω_{dd} increases for higher magnetic field tilts θ_B. Still, the dipolar frequency estimation is hampered by a decrease in contrast to the NV sensor due to a transverse field. Spin location assessment is optimized for larger field tilts and low field magnitudes. The star marks the magnetic field vector used in the experiment.

explicit formula. However, it can be solved numerically from a set of rate equations formulated by Tetienne et al.[23]. I calculate $\mathcal{C}(B_0,\ \theta_B)$ according to Tetienne et al. and incorporate it into our model via Eq. 3.12.

The dipolar coupling modulation amplitude is the factor that generates the *position contrast* in the tomography measurement, so I assume that the position uncertainty is proportional to the modulation amplitude (Eq. 3.5), which can be validated numerically:

$$\text{Amplitude} = -\frac{3\mu_0\gamma_{nv}\gamma_e\hbar}{8\pi r^3}\sin\theta_B\sin 2\theta\cos\left(\phi_B - \phi\right) \tag{3.13}$$

Thus, the following relation is obtained:

$$\Delta R\left(B_0,\ \theta_B\right) = \mathcal{A}\left(\mathcal{S},\mathbf{r}\right)\frac{\sin\left(\theta_B\right)}{\mathcal{C}\left(B_0,\ \theta_B\right)} \tag{3.14}$$

$\mathcal{A}(\mathcal{S},\mathbf{r})$ is a factor that depends on the sensor's sensitivity $(\mathcal{S})$ and the target spin's coordinates $(\mathbf{r})$. Thus, one can optimize the measurement for a particular sensor and target spin by choosing the optimal magnetic field vector.

To illustrate the relation of Eq. 3.14, I calculated $\Delta R\left(B_0,\ \theta_B\right)$ for an example set of parameters, plotted in Fig. 3.8. I used the parameters from the experiment described in this work: the measured spin's coordinates, the dipolar coupling uncertainty, and the specific magnetic field parameters. Using the experimental data, I extracted the sensor-specific proportionality factor $\mathcal{A}(\mathcal{S},\mathbf{r})$ for this case. I then calculated the expected uncertainty by solving the Hamiltonian of the system. A star marks the parameters of the experiment. The optimal precision is achieved for a low B_0 that still satisfies $\omega_0 \gg \omega_{dd}$ and for $\theta_B \sim 45°$. As seen in Eq. 3.14, the functional form of $\Delta R\left(B_0,\ \theta_B\right)$ will remain the same for other parameters $(\mathcal{S},\mathbf{r})$, and the values will scale accordingly.

At fields near the NV center ESLAC at 510 G, there is a sharp decrease in contrast for any finite transverse field, and the uncertainty is considerable. For any field satisfying the condition $\mathcal{H}_{dd} \ll \omega_0 \ll D$, the dipolar coupling modulation amplitude does not depend on B_0, and only on θ_B. The criterion is satisfied for $B_0 \gtrsim 10\,\mathrm{G}$. The uncertainty is minimized for a maximal tilt of $\theta_B \approx 45^\circ$ and minimal field $B_0 \approx 10\,\mathrm{G}$.

3.6 MAGNETIC TOMOGRAPHY OF TWO SPINS AT A MODERATE MAGNETIC FIELD

I attempted to perform spin mapping by magnetic tomography at a moderate magnetic field of $B_0 = 417\,\mathrm{G}$ (chronologically, these experiments preceded the lower field experiments). There was motivation to work in this field despite its lower compatibility with the magnetic tomography protocol. Most importantly, the NV coherence time T_2 is generally longer at fields of a few hundred gauss than at a few tens of gauss[77,139] (cf. Fig. C.1(c) in Appendix C). As the dipolar coupling frequency estimation is inversely dependent on T_2, working in a regime where the T_2 is longer is favorable. Also, there were two technical advantages: first, aligning the magnetic field for $B_0 \sim 500\,\mathrm{G}$ is simpler. Second, working in this field is possible with one amplifier (see further details in Section 2.2).

The T_2 enhancement at a higher field enabled us to observe two frequencies in the dipolar coupling measurement (Fig. 3.10(a)), which presumably originates from a second electron spin interacting with the sensor. Thus, I obtained the dipolar coupling of two different electrons at each point of the magnetic field trajectory. Unfortunately, the trajectories used were probably suboptimal, partially due to limited magnetic field control based on a permanent magnet's mechanical motion, without any feedback on the field. Nonetheless, I extracted the data from the experiments by estimating the magnetic field tilt angle θ_B for this experiment.

The data for the tomography experiment at 417 G is featured in Fig. 3.9. I swept the magnet along a circular trajectory of radius 0.1 mm around the alignment point of the NV. A DEER measurement was acquired at each point, which exhibited beating oscillations due to two frequency components, ω_a, ω_b. I attribute the carrier frequency, $\omega_{dd,1} = (\omega_a + \omega_b)/2$, with the coupling to a closer electron (labeled by the subscript 1), the one observed in the low-field experiments (Section 3.4). I attribute the envelope (modulation) frequency $\omega_{dd,2} = (\omega_a - \omega_b)/2$ to a second electron (labeled by the subscript 2). The modulation of the dipolar coupling to the first target spin ($\omega_{dd,1}$) over the azimuthal sweep is shown at the top of Fig. 3.10(a), with a fit to a single period sine (orange curve and the confidence interval is denoted by the shading). From the DEER spectrum and ODMR spectrum at each point, I estimated the field tilt angle to be $\theta_B = (2.0 \pm 0.9)^\circ$. Using θ_B and the sine fit to the modulation of $\omega_{dd,1}$, I estimated the first electron spin coordinates according to Eq. 3.5:

$$r_1^{hf} = (4.99 \pm 0.13)\,\mathrm{nm};\; \theta_1^{hf} = (9.8 \pm 7.1)^\circ;\; \phi_1^{hf} = (-92 \pm 17)^\circ \tag{3.15}$$

with an uncertainty volume of $dV_1^{hf} = 0.03\,\mathrm{nm}^3$, $\left(dR_1 = \left(dV_1^{hf}\right)^{1/3} = 0.31\,\mathrm{nm}\right)$. These values are consistent with the more precise low-field measurements. The uncertainty is also consistent

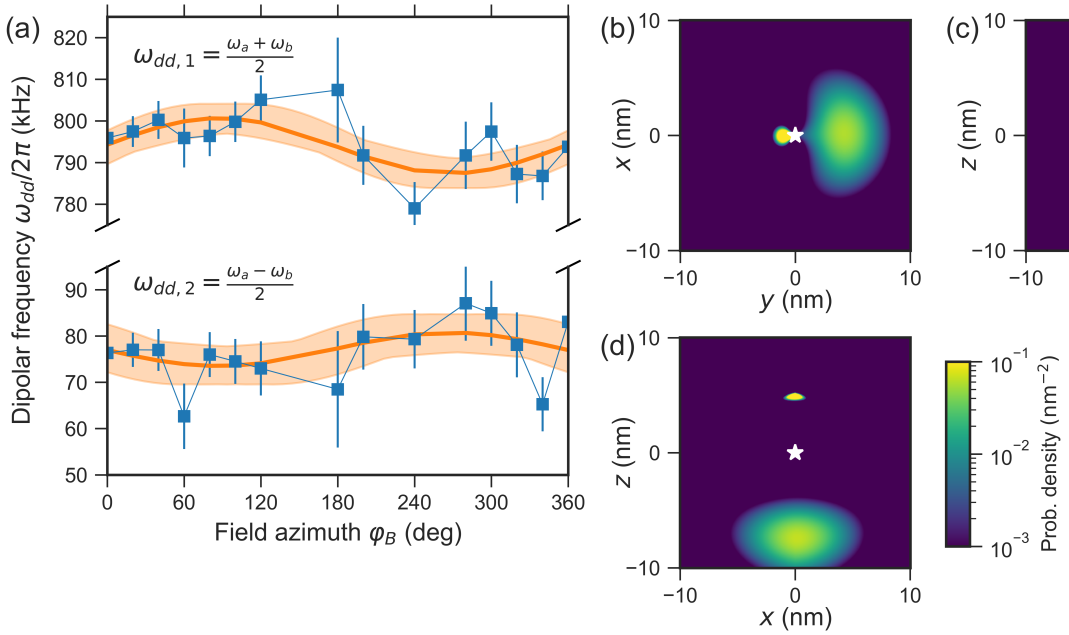

Figure 3.9: Magnetic tomography of two spins at a moderate magnetic field. DEER measurements were performed along an azimuthal trajectory of the magnetic field. At each point, two frequencies were extracted from the measurement, ω_a, ω_b. (a) The modulation of $\omega_{dd,1} = (\omega_a + \omega_b)/2$, a coupling that is associated with a spin closer to the sensor, and the modulation of $\omega_{dd,2} = (\omega_a - \omega_b)/2$, a coupling that is associated with a spin farther from the sensor. The blue squares are data points, the orange curves are sine fits, and the light orange shadings represent the confidence intervals of the fits. (b-d) Probability distribution maps for the two spins relative to the sensor (white star), as projected on different planes. The bright yellow spot is the closer spin, with higher location precision, and the bigger spot represents the probable position of the farther spin.

with the calculations of Eq. 3.14 and Fig. 3.8: for the parameters used here, I expected a location uncertainty of ~0.5 nm.

The extended coherence time allowed locating the second target spin, whose coupling is $\omega_{dd,2} \approx \sim 75\,\mathrm{kHz}$, which means it is approximately twice as distant from the sensor as the first electron. As such, the location precision is much lower, and the location signal – the amplitude of the oscillation over an azimuthal sweep of the magnetic field – is on the order of the noise, the dipolar coupling frequency error ($\delta\omega_{dd,2} \approx 4\,\mathrm{kHz}$). However, this does not prevent locating the spin; it only decreases its precision. Thus, for the second target spin, I estimate the coordinates:

$$r_2^{hf} = (8.2 \pm 2.2)\,\mathrm{nm};\ \theta_2^{hf} = (147 \pm 17)^\circ;\ \phi_2^{hf} = (-87 \pm 36)^\circ \tag{3.16}$$

with an uncertainty volume of $dV_2^{hf} = 29\,\mathrm{nm}^3$, ($dR_2 = \left(dV_2^{hf}\right)^{1/3} = 3.1\,\mathrm{nm}$). These values are consistent with the analysis for the uncertainty as a function of the target spin's position (Fig. 3.7): inputting the values for this experiment (field, spin position, frequency estimation uncertainty) into the analysis of Section 3.5, it yields a position uncertainty of 1.5 nm.

For the solution in Eq. 3.16, the two target spins are separated by $d_{12} \approx 12\,\mathrm{nm}$, and their mutual dipolar interaction is $\omega_{12} \approx 50\,\mathrm{kHz}$ when the field is aligned along $\hat{z}$ (the NV axis). Recalling that the magnetic tomography protocol is centrosymmetric, another valid solution is the reflection of these coordinates about the center: $\theta_2^{hf} = (36 \pm 13)^\circ$; $\phi_2^{hf} = (84 \pm 27)^\circ$. This solution means that the two target spins are much closer ($d_{12} \approx 6\,\mathrm{nm}$), with a much stronger dipolar interaction

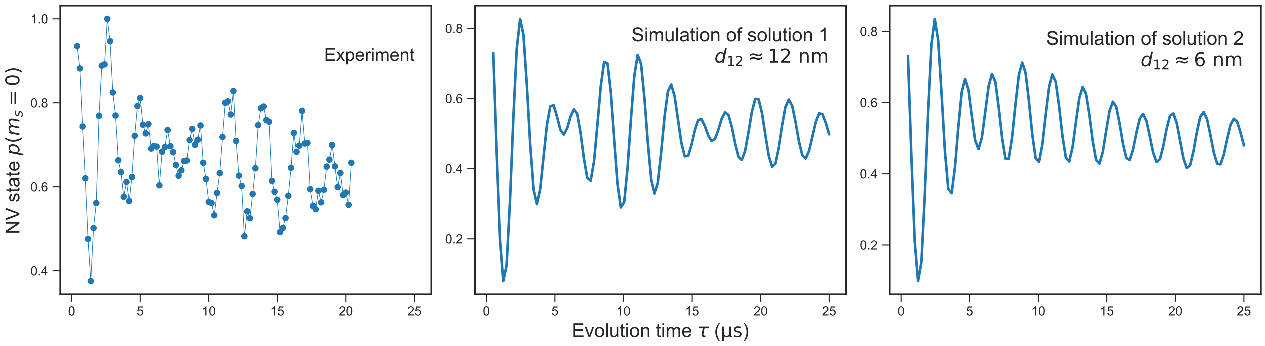

Figure 3.10: DEER experiment and simulation with two target spins. (a) DEER measurement at 417 G, exhibiting two frequencies, probably due to coupling to two electron spins. (b) Simulation of a DEER experiment where the two spins are separated by $d_{12} \approx 12\,\mathrm{nm}$, according to the coordinates obtained in the mapping experiment. (c) Simulation of a DEER experiment where the two spins are separated by $d_{12} \approx 6\,\mathrm{nm}$ (the alternative solution).

between the two target spins, $\omega_{12} \approx 180\,\mathrm{kHz}$. Notably, in this case, $\omega_{12} > \omega_{dd,2}$. However, the apparent beatings in the DEER dipolar coupling measurement hint that the target spins' mutual interaction is weaker than their respective interaction with the sensor. Thus, if the first spin is considered to be at the coordinates denoted in Eq. 3.8, then Eq. 3.16 is a more consistent solution for the second spin's position. This is supported by DEER simulations for the two solutions, as shown in Fig. 3.10, and compared with an experiment. The simulation of the first solution where the spins are separated by $d_{12} \approx 12\,\mathrm{nm}$ exhibits two distinct frequencies (apparent by a beating oscillation), qualitatively agreeing with the experiment. Conversely, for the solution where the spins are separated by $d_{12} \approx 6\,\mathrm{nm}$, the dynamics are markedly distinct and inconsistent with the experimental observation.

3.7 MAGNETIC TOMOGRAPHY OF AN ELECTRON-NUCLEAR SYSTEM - A THEORETICAL STUDY

So far, I have discussed locating an electron spin that does not interact with nuclear spins. However, in many scenarios, the target electron spin may interact significantly with nearby nuclear spins, as with nitroxide radicals, the most common spin label type. Adding a hyperfine interaction term with a nucleus, $\mathbf{S}_e \cdot \mathbb{A}_{hf} \cdot \mathbf{I}$, modifies the spin Hamiltonian (Eq. 3.1). I expect a subsequent modification to $\omega_{dd}\left(\mathbf{r}, \hat{\mathbf{b}}\right)$ (Eq. 3.5), as the assumption that the Zeeman term dominates the eigenstates of the target spin is no longer valid. In this section, I analyze by theory and simulations the impact of the hyperfine coupling on the magnetic tomography protocol to understand its applicability to electron-nuclear spin systems.

For this discussion, I focus on the case of nitroxide radicals, where the electron spin is coupled by hyperfine constants of $\sim 2\pi \times 100\,\mathrm{MHz}$ to the adjacent nitrogen nuclear spin (^{14}N or ^{15}N)[159]. At fields of tens of gauss, the hyperfine term is comparable to $\gamma_e B_0$. I study the applicability of the magnetic tomography method to nitroxide spin labels by numerically simulating a magnetic azimuth sweep of the dipolar coupling between an NV sensor and a nitroxide spin label.

Spin Hamiltonian with a hyperfine interaction to the target spin

The following Hamiltonian describes the sensor-target system (e.g., NV-nitroxide):

$$\mathcal{H} = D{S_{nv}^{z}}^{2} + \gamma_{nv}\mathbf{B}\cdot\mathbf{S}_{nv} + \gamma_{e}\mathbf{B}\cdot\mathbf{S}_{e} + \gamma_{n}\mathbf{B}\cdot\mathbf{I}_{n} + \mathbf{S}_{nv}\cdot\mathbb{D}_{ee}\cdot\mathbf{S}_{e} + \mathbf{S}_{e}\cdot\mathbb{A}_{hf}\cdot\mathbf{I}_{n} \tag{3.17}$$

Here $\mathbb{D}_{ee}$ is the dipolar coupling tensor between the sensor and target electron spins; $\mathbf{I}_n$ is the nuclear spin operator; γ_n is the nuclear gyromagnetic ratio; $\mathbb{A}_{hf}$ is the hyperfine coupling tensor between the target electron spin and the associated nuclear spin. The nuclear Zeeman term, $\gamma_n\mathbf{B}\cdot\mathbf{I}_n$ is usually negligible because $\frac{\gamma_n}{\gamma_e} \lesssim 10^{-3}$. While the discussion is focused on the case of nitroxide radicals, the conclusions are general for any system with similar hyperfine constants.

The hyperfine coupling tensor is diagonalizable for a set of axes known as the principal axes. In its principal axes, the nitroxide spin label's hyperfine tensor is of the form:

$$\mathbb{A}_{sl}^{p} = \begin{pmatrix} A_{\perp} & & \\ & A_{\perp} & \\ & & A_{\|} \end{pmatrix} \tag{3.18}$$

For a nitroxide with an ^{14}N isotope ($I = 1$ nuclear spin; 99.636% abundance), $A_{\|} \sim 2\pi \times 100\,\text{MHz}$, $A_{\perp} \sim 2\pi \times 15\,\text{MHz}$; for an ^{15}N ($I = \frac{1}{2}$; 0.364% abundance), $A_{\|} = 2\pi \times 140\,\text{MHz}$, $A_{\perp} = 2\pi\times \sim 25\,\text{MHz}$, and the exact values depends on the particular molecule, and solvent[159]. In the following simulations, I used the values for PyMeOH (1-oxyl-2,2,5,5-tetramethylpyrrolin-3-yl methanol) in glycerol, with an ^{14}N: $A_{\|} = 2\pi \times 101.4\,\text{MHz}$, $A_{\perp} = 2\pi \times 14.7\,\text{MHz}$.

Alignment of nitroxide electron spin axis

The measurement proposed in this chapter relies on the electron spin quantization axis aligning with the magnetic field. However, in the magnetic field regime discussed in Section 3.2 (a few tens of gauss), the hyperfine term is similar in magnitude to the target electron Zeeman term. So, adding the hyperfine term may invalidate the assumption that the electron spin quantization axis aligns with the magnetic field. I study this theoretically by solving the eigenstates of a target electron-nuclear spin Hamiltonian. For this purpose, the sensor spin may be excluded from the Hamiltonian because the sensor-target coupling is much smaller than the electron-nuclear Hamiltonian $\mathcal{H}_{dd} \ll \mathcal{H}_{tar}$, so its impact on the eigenstates is negligible.

I choose the coordinate system such that the magnetic field is aligned with the $\hat{\mathbf{z}}$ axis, and the hyperfine's principal axes are tilted from $\hat{\mathbf{z}}$ by an angle of $\theta_{sl} \in \left[0, \frac{\pi}{2}\right]$. Due to cylindrical symmetry, I can set arbitrarily $\phi_{sl} = 0$. The Hamiltonian of the system is thus:

$$\begin{aligned} \mathcal{H}_{tar} &= \gamma_e B_z S_e^z + \mathbf{S}_e\cdot\mathbb{A}_{hf}\cdot\mathbf{I}_n \\ \mathbb{A}_{hf} &= R^y\left(\theta_{sl}\right)\mathbb{A}_{sl}^{p}R^y\left(\theta_{sl}\right)^T \end{aligned} \tag{3.19}$$

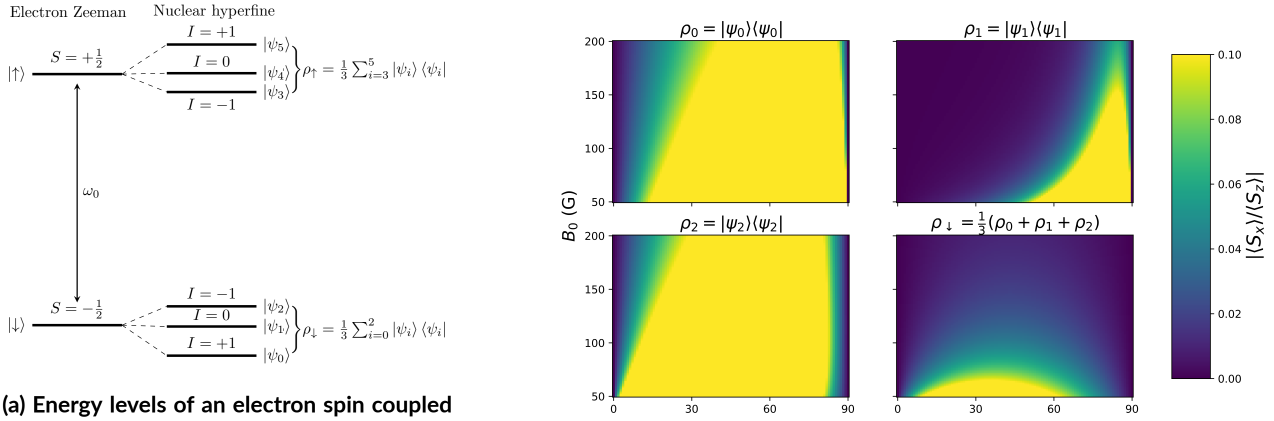

(a) Energy levels of an electron spin coupled to an $S=1$ nuclear spin. The primary split is the electron Zeeman interaction, ω_0, and then further splitting due to the hyperfine interaction. $\rho_\uparrow, \rho_\downarrow$ represent states of a polarized electron spin and a nuclear spin in thermal distribution.

(b) $|\langle S_x\rangle / \langle S_z\rangle|$ calculated for different states. The ratio is calculated as a function of the magnetic field and the angle between the hyperfine axis and the magnetic field. For the mixed state $\rho_\downarrow$, $|\langle S_x\rangle / \langle S_z\rangle| \ll 1$ for any angle at fields of 100 G and above. This indicates that the electron spin is approximately quantized along the magnetic field axis for all orientations.

Figure 3.11: Comparison of $|\langle S_x\rangle / \langle S_z\rangle|$ for different states of a nitroxide spin Hamiltonian.

Here $R^y(\theta)$ is the rotation matrix around the y axis:

$$R^y(\theta) = \begin{pmatrix} \cos\theta & 0 & \sin\theta \\ 0 & 1 & 0 \\ -\sin\theta & 0 & \cos\theta \end{pmatrix} \tag{3.20}$$

The Hamiltonian is a tensor product of two- and three-dimensional Hilbert spaces with six eigenstates. For the case that $\gamma_e B_z > \mathbb{A}_{sl}$, then the three lower eigenenergies are associated with lower energy states of the electron spin operator. The three higher eigenenergies are associated with higher energy states of the electron spin operator, as depicted in the diagram in Fig. 3.11a. Each state is associated with a different eigenstate of the nuclear spin operator in each manifold. The states are denoted as $|\psi_i\rangle$ according to their energies. The eigenstates are not necessarily eigenstates of $S_z I_z$, e.g., $|\psi_0\rangle \neq |\downarrow\rangle|+1\rangle$ (unless $\theta_{sl} = 0, \pi$).

The fact that the states are not eigenstates of $S_z I_z$ is evident in the calculation presented in Fig. 3.11b. Here, I calculated numerically (with the QuTiP package) the value of $|\langle Sx\rangle / \langle S_z\rangle| = |\mathrm{Tr}(\rho S_x) / \mathrm{Tr}(\rho S_z)|$ for different eigenstates of the nitroxide Hamiltonian (Eq. 3.19). $|\langle S_x\rangle / \langle S_z\rangle|$ for the three eigenstates of the lower manifold $(|\psi_0\rangle, |\psi_1\rangle, |\psi_2\rangle)$ are compared with the mixed state $\rho_\downarrow = \sum_{i=0}^{2} |\psi_i\rangle\langle\psi_i|$, a thermal ensemble of these three states (see diagram in Fig. 3.11a).

In the pure eigenstates of $S_z I_z$, the value of $|\langle S_x\rangle / \langle S_z\rangle|$ is not negligible for some values of θ_{sl} for moderate fields of up to 200 G. That is, for these states, the transverse components of the electron spin operator (S_x, S_y) cannot be neglected when calculating $\langle\mathcal{H}_{dd}\rangle$. However, in the mixed state $\rho_\downarrow$, for fields of ∼100 G and above, $|\langle S_x\rangle / \langle S_z\rangle| \ll 1$. Then, it may be assumed that the electron spin is quantized along the external magnetic in the mixed state for such moderate fields for such moderate fields.

The mixed state $\rho_{\downarrow}$ is relevant when sensing such nitroxide radicals; even at cryogenic temperatures, the nuclear spin polarization is negligible. For example, at $T = 4\,\mathrm{K}$ and $B = 200\,\mathrm{G}$, $\gamma_I B/kT < 10^{-3}$, so per the Boltzmann distribution the nuclear spin polarization is $< 0.05\%$[a]. From this, I deduce that when considering the mixed state, the secular approximation may be applied to the spin Hamiltonian of Eq. 3.17. If the hyperfine transitions are driven simultaneously, i.e., $\rho_{\downarrow} \leftrightarrow \rho_{\uparrow}$, terms that do not commute with S_z may be omitted. From here, it follows that the model for $\omega_{dd}\left(\mathbf{r}, \hat{\mathbf{b}}\right)$ of Eq. 3.5 is applicable also for nitroxide radicals under these conditions (i.e., $B_0 > 100\,\mathrm{G}$).

Calculating azimuth sweeps of nitroxide radicals

I theoretically analyzed the behavior of magnetic tomography mapping of a nitroxide spin label. To do so, I calculated the modulation of the dipolar coupling under an azimuth sweep of the magnetic field. As an example, arbitrary spin label position ($r = 5\,\mathrm{nm}$, $\theta = 0.3\,\mathrm{rad}$, $\phi = 1.5\,\mathrm{rad}$) and an arbitrary orientation of the hyperfine principal axes ($\theta_{sl} = 1\,\mathrm{rad}$, $\phi_{sl} = 1\,\mathrm{rad}$) was used. I calculated the variation of the dipolar coupling ($\langle \mathcal{H}_{dd} \rangle$) under fields in the range of $B_0 = 20$–$100\,\mathrm{G}$ and a magnetic field tilt of $\theta_B = 0.5\,\mathrm{rad} \approx 28^\circ$. As previously described, the nuclear spin was assumed to be in a thermal state, i.e., equal probabilities of the nucleus $S = 1$ states. The simulations are presented in Fig. 3.12, and compared with the theoretical model for $\omega_{dd}\left(\mathbf{r}, \hat{\mathbf{b}}\right)$ (Eq. 3.5).

At 20 G, the simulated azimuth sweep deviates significantly from the model and approaches the theoretical model as the field increases. The theoretical model approximates the simulated curve well at a field of $B_0 = 100\,\mathrm{G}$. This is consistent with the electron spin state analysis (Fig. 3.11b). While a field of 100 G entails a decrease in precision due to the transverse field, the previous calculations show that it still allows mapping spins with Ångstrom precision if the dipolar frequency estimation is similar to the experiment (Fig. 3.8). For the case of a hyperfine coupled spin, however, a more precise location estimation may be obtained by fitting to a calculated $\omega_{dd}(\mathbf{r}, \mathbf{B})$, instead of the analytical term.

The magnetic tomography model $\omega_{dd}\left(\mathbf{r}, \hat{\mathbf{b}}\right)$ of Eq. 3.5 applies for a hyperfine coupled spin already at a moderate field of 100 G despite the Zeeman term being on the same order of the hyperfine parameter ($A_{\parallel} \approx 2\pi \times 101.4\,\mathrm{MHz} \sim \gamma_e B_0 \approx 2\pi \times 280\,\mathrm{MHz}$) and not negligible. This stems from the fact that, for a thermal ensemble of the nuclear spin states at 100 G, the *expectation value* of the target electron spin operator perpendicular to the field axis $\hat{\mathbf{b}}$ satisfies $\left|\langle S_e^{\perp} \rangle \,/\, \langle S_e^{b} \rangle\right| \ll 1$. This means that the secular approximation is also applicable in this scenario, so Eq. 3.5 constitutes a valid approximation. Thus, the magnetic tomography method may also apply to mapping nitroxide spin labels and similar hyperfine-coupled electron spins.

---

[a] $\mathcal{P} \equiv \rho_{\uparrow}\left(1 - \frac{\rho_{\uparrow}}{\rho_{\downarrow}}\right) = \rho_{\uparrow}\left(1 - \exp\left(-\frac{\gamma_I B}{kT}\right)\right) < 10^{-3}\rho_{\uparrow} \rightarrow \mathcal{P} < 0.5 \times 10^{-3}$

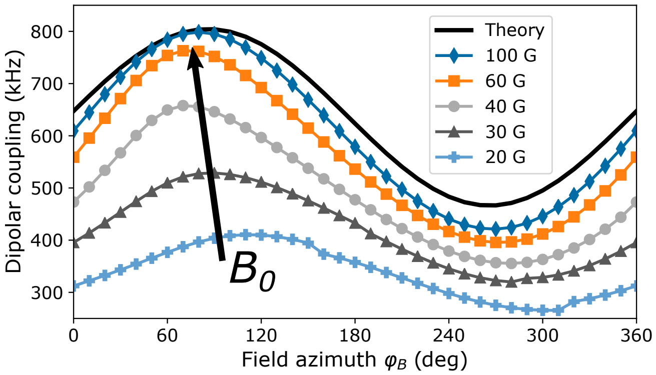

Figure 3.12: Magnetic azimuth sweep of nitroxide spin labels. A comparison of numerically calculated azimuth sweeps of a nitroxide radical (^{14}N) at different field magnitudes. The electron spin is arbitrarily positioned, with an arbitrary orientation of the hyperfine axes. The curves are compared to the theoretical model for $\omega_{dd}\left(\mathbf{r}, \hat{\mathbf{b}}\right)$. At $B_0 \gtrsim 100\,\mathrm{G}$, the calculated curve is well approximated by the theoretical model.

3.8 DISCUSSION AND CONCLUSIONS

NV centers in diamond are a leading platform for nanoscale magnetometry, particularly for single-molecule magnetic resonance tasks. Here, I demonstrated a method to map the locations of spins in the vicinity of an NV center sensor with Ångstrom-scale precision. The location precision of the spin demonstrated here is one order of magnitude higher than previously reported for a similar magnetic field scanning experiment ($\sim$1 nm)[88] and a spin imaging technique based on a scanning magnetic tip (1.5 nm)[106]. Magnetic resonance imaging demonstrated recently with a scanning tunneling microscope exhibited superior precision but requires strict conditions[69,70]. Notably, the magnetic tomography method does not require a scanning probe setup, which is operationally complex, and the procedure is operable at both ambient and cryogenic conditions.

Spin mapping with Ångstrom resolution may provide added value for applications such as single-molecule distance measurements. For this, the positions of a pair of spin labels attached to a biomolecule would be measured, from which the distance is directly inferred. To do so, the dipolar coupling to each spin needs to be measured as a function of the magnetic field direction and fitted to $\omega_{dd}\left(\mathbf{r}, \hat{\mathbf{b}}\right)$ (Eq. 3.5). A minimal frequency resolution is needed to distinguish between the dipolar coupling of two or more spins, and it is given by the coherence time of the sensor $\delta\omega \sim \frac{1}{T_2}$. Another approach is selective addressing by separating the targets' electron spin resonances, which allows measuring each spin's dipolar coupling separately[111]. Selective addressing may also be achieved by attaching spin labels with distinct resonance spectra, such as nitroxide radicals with different nitrogen isotopes (^{14}N, ^{15}N)[160,161].

The uncertainty of the measurement is proportional to the uncertainty of frequency estimation, so techniques that lengthen the coherence time and improve the sensor readout efficiency would enhance the spin location precision. Nonetheless, with nanometer precision up to 10 nm away from the sensor, the method can be used for sensing spin labels on molecules external to the diamond crystal. Thus, the magnetic tomography method is relevant for studying the structure of individual molecules by spin-label distance measurements or high-resolution characterization of quantum spin networks.

In the experiment at a moderate field, I mapped the position of two target spins and deduced the distance between them. This outlines a route for single-molecule distance measurements, where the position of two different spins is measured relative to the sensor, and then their distance may be precisely evaluated. However, this experiment features a critical caveat: the sensor lies between the two spins, which is unrealistic. In Chapter 4, I theoretically address the issue of single molecule distance measurements using magnetic tomography and suggest how to handle the mutual interaction between the two mapped spins.

4

Single-molecule distance measurements by magnetic tomography - a theoretical treatment

AN APPEALING GOAL IN NANOSCALE MAGNETIC RESONANCE IS THE REALIZATION OF SINGLE-MOLECULE DISTANCE MEASUREMENTS, AN ESTABLISHED METHOD OF CHARACTERIZING ORGANIC MOLECULE STRUCTURE. Distance measurements using EPR is an established method for characterizing organic molecule structure and function by measuring the distance between two spin label (SL) molecules, radicals attached to known sites along a large organic molecule. The past decade has witnessed steady progress in the field of nanoscale magnetic resonance. Studies included milestones in the field of single-molecule NMR[82,83,95], and single-molecule EPR[118,119], but single-molecule distance measurements have yet to be demonstrated.

In this chapter, I present a theoretical proposal for realizing single-molecule distance measurements based on the concepts of magnetic tomography presented in Chapter 3. The idea is demonstrated on a system of an NV sensor and two electron spins, representing an organic molecule with two SLs attached at a distance of 4 nm from each other. The approach is to map the position of the two radicals in the NV coordinate system, from which the distance between the radicals is directly deduced.

I assume spin labels do not have significant hyperfine terms in the derivation and numerical calculations. This is the case for the trityl radical, a nascent SL molecule that is also suitable for RT experiments[162,163]. Trityl radicals are suitable for this protocol due to the lack of significant hyperfine terms and prolonged relaxation times. This is based on an actual molecule synthesized at WIS, discussed in Appendix D.

Let us consider a system of three spins: the NV spin $\mathbf{S}_{nv}$, our sensor, and two spins, $\mathbf{S}_a, \mathbf{S}_b$, representing the SLs attached to a molecule. I neglect hyperfine terms, assuming the Zeeman and driving terms are much larger than any hyperfine constants. This assumption holds for the hyperfine coupling to the NV center's nitrogen spin (~3 MHz) and the trityl radicals with negligible hyperfine constants[164]. I assume that all the spins are far enough (>1.5 nm), so they only exhibit dipole-dipole interactions, and the exchange interaction may be neglected.

The lab-frame Hamiltonian of the system, under an aligned magnetic field $\mathbf{B}_0 = \frac{\omega_0}{\gamma_e}\hat{z}$, is:

$$\begin{aligned} \mathcal{H}_{lab} &= (D+\omega_0)\, S^z_{nv} + \omega_0 S^z_a + \omega_0 S^z_b + \sum_{i,j\in\{a,b,nv\}} \mathbf{S}_i \mathbb{D}_{ij} \mathbf{S}_j \\ \mathbf{S}_i \mathbb{D}_{ij} \mathbf{S}_j &= \frac{\mu_0 \gamma_i \gamma_j \hbar}{2 r^3_{ij}} \left[\mathbf{S}_i \cdot \mathbf{S}_j - 3\left(\mathbf{S}_i \cdot \hat{r}_{ij}\right)\left(\mathbf{S}_j \cdot \hat{r}_{ij}\right)\right] \end{aligned} \tag{4.1}$$

Here, I assumed, for simplicity, that the NV is a two-level system by taking the $\{|0\rangle, |1\rangle\}$ subspace of the NV spin. D is the zero-field splitting and $\omega_0 = \gamma_{nv} B_0$. The last term is a pairwise sum over the three different dipole-dipole interactions.

We move to a triple-rotating frame by a $T(t) = \prod_s e^{-i\omega_s t S^z_s}$ transformation at the spins' Larmor frequencies ω_s, which are ω_0 for the SLs, and $D + \omega_0$ for the NV. Under this transformation, the Zeeman terms of the lab-frame Hamiltonian (Eq. 4.1) will cancel out, except for detunings. The detunings, which will be refocused by the DEER sequence, are omitted. Invoking the secular approximation, the remaining terms of the rotating frame Hamiltonian, in the absence of driving, are thus:

$$\mathcal{H}_{rot} = J_a S^z_{nv} S^z_a + J_b S^z_{nv} S^z_b + 4F S^z_a S^z_b - F\left(S^+_a S^-_b + S^-_a S^+_b\right) \tag{4.2}$$

The NV-SL couplings are labeled by $J_{a/b}$ and the SL-SL couplings by $4F$ (the factor of 4 is used for convenience later on):

$$J_i\left(r_{i,nv}, \theta_{i,nv}\right) = \frac{\mu_0 \gamma_i \gamma_{nv} \hbar}{2 r^3_{i,nv}} \left(1 - 3\cos^2\left(\theta_{i,nv}\right)\right) \tag{4.3}$$

$$4F\left(r_{a,b}, \theta_{a,b}\right) = \frac{\mu_0 \gamma_a \gamma_b \hbar}{2 r^3_{a,b}} \left(1 - 3\cos^2\left(\theta_{a,b}\right)\right) \tag{4.4}$$

Assuming the NV and SLs have distinct Larmor frequencies, only the secular terms are kept for the NV-SL dipole-dipole couplings (first and second terms in Eq. 4.2). The SLs have equal Larmor frequencies, so we must incorporate the pseudo-secular term in the SL-SL coupling, the last term of Eq. 4.2). The remaining terms in the spin-spin couplings - the pseudo-secular term of the NV-SL couplings and all the non-secular terms - will gain a fast oscillating phase in the rotating frame. Thus, under the RWA, these terms may be neglected in the rotating frame Hamiltonian. A detailed derivation is in Appendix A.

I calculated the expected result of a DEER sequence on the NV center by calculating the evolution under this Hamiltonian. I assume that the NV is initialized to $\frac{|0\rangle+|1\rangle}{\sqrt{2}}$, while the spin labels start in a thermal state $\rho^{sl}_{th} = \frac{1}{4} I_4$. The expected measurement of a DEER sequence, without relaxation, namely $C(\tau) \equiv \langle S_x \rangle (\tau) = \mathrm{tr}\left(\rho(\tau) S_x\right)$:

$$C(\tau) = \frac{1}{2}\sin^2\left(\frac{\bar{J}\tau}{2}\right) + \frac{\Delta J^2}{2\left(\Delta J^2 + F^2\right)}\sin^2\left(\frac{\sqrt{\Delta J^2 + F^2}\,\tau}{2}\right)\cos^2\left(\frac{F\tau}{2}\right) = \tag{4.5}$$

$$\begin{aligned} &= \frac{3\Delta J^2 + 2F^2}{8\left(\Delta J^2 + F^2\right)} - \frac{1}{4}\cos\left(\bar{J}\tau\right) + \frac{\Delta J^2}{8\left(\Delta J^2 + F^2\right)}\left(\cos\left(F\tau\right) - \cos\left(\sqrt{\Delta J^2 + F^2}\,\tau\right)\right) + \\ &- \frac{\Delta J^2}{16\left(\Delta J^2 + F^2\right)}\left(\cos\left(\left(F + \sqrt{\Delta J^2 + F^2}\right)\tau\right) + \cos\left(\left(F - \sqrt{\Delta J^2 + F^2}\right)\tau\right)\right) \end{aligned} \tag{4.6}$$

$$\begin{aligned} \bar{J} &\equiv \frac{J_a + J_b}{2} \\ \Delta J &\equiv \frac{|J_a - J_b|}{2} \end{aligned} \tag{4.7}$$

In the case of $F = 0$, the signal takes on the form of $C(\tau) = \frac{1}{2} - \frac{1}{4}\cos\left(\bar{J}\tau\right) - \frac{1}{4}\cos\left(\Delta J\tau\right)$, which is consistent with previous derivations.[119]. Relaxation will manifest as an exponential decay coefficient for each term in Eq.4.5. The second term of Eq. 4.5 originates from the spin labels' coherences and should exhibit faster decay on the scale of the spin label's T^{sl}_2.

From Eq. 4.5, three regimes with distinct dynamics are recognizable. In the limit of $F \ll \Delta J$, a two-frequency signal at $\bar{J}$, ΔJ is expected. This is similar to the dynamics observed in Fig. 3.10. In the other extreme, for $F \gg \Delta J$, a single oscillation at $\bar{J}$ is expected. In the regime of $F \sim \Delta J$, the dynamics become more complex, characterized by five frequencies. These frequencies are apparent in the expansion of the term in Eq. 4.6. Analyzing a five-frequency signal with relaxation-induced broadening may result in ambiguities and erroneous results due to over-fitting.

A potential strategy arising from these observations is to align the magnetic field in a direction that would eliminate the radical-radical dipolar coupling. The dynamics without the radical-radical coupling are reduced to the dual-frequency dynamics. From this more straightforward measurement, we can infer the coupling of the NV to each of the spin labels.

Recalling the term for the dipolar coupling coefficient (Eq. 4.4), if the field is at the magic angle to the biradical axis (54.7°), we expect $F \to 0$. The points that satisfy this condition lie on a cone around the spin-spin axis. Thus, a sweep of the magnetic field on a proper trajectory on this cone should provide sufficient information to identify the positions of the two spins.

4.2 Mapping strategy

The strategy proposed here is to identify the biradical axis orientation and align the field's orientation $\hat{b}$ such that it forms a magic angle (54.7°) with the biradical axis $\hat{f}$ (see Fig. 4.1(a)):

$$\hat{b} \cdot \hat{f} = 1/\sqrt{3} \approx \cos\left(54.7^{\circ}\right) \tag{4.8}$$

According to Eq. 4.4, SL-SL coupling at this angle is zero. A manifold of points satisfies the condition of Eq. 4.8. Adding the constraint of a constant field magnitude defines a circle, the intersection of the cone, and a sphere of constant field magnitude. Thus, a trajectory that satisfies

$\hat{b} \cdot \hat{f} = 1/\sqrt{3}$ and constant field is obtained – a series of points where the field's orientation varies, while the SL-SL coupling is maintained at zero (Fig. 4.1(a), dotted circle). By measuring DEER along this trajectory, enough information may be gathered to locate both spins separately, using the concept of magnetic tomography presented previously in Chapter 3.

The mapping protocol can thus be based on the following steps:

1. Identify an NV center potentially coupled to a single biradical by standard DEER at a magnetic field aligned with the NV axis. An example of such a spectrum is depicted in Fig. 4.2.
2. Apply the magnetic tomography protocol described in Chapter 3. Assuming that the biradical axis is roughly flat on the diamond's surface, then the angle between the biradical axis and the NV axis (i.e., $\arccos\left(\hat{f} \cdot \hat{z}\right)$) is between 35.3° to 90°. This implies an azimuth sweep may be done at a tilt angle of $\theta_B \leq 35°$. Fig. 4.1(b) depicts the trajectory of the magnetic field sweep (dashed circle) with regards to the NV axis and the biradical axis. Over the azimuth sweep, there should be at least two points where the field is at the magic angle to the biradical axis. At these points, $F \to 0$ should be apparent in the DEER frequency components.
3. From the magnetic field coordinates $\left(\theta_B, \phi_B\right)$ of the points satisfying $\hat{b} \cdot \hat{f} = 1/\sqrt{3}$, the orientation of the biradical axis may be deduced. Then, we perform a series of DEER measurements along a trajectory that forms a magic angle with the biradical axis, such that the biradical dipolar coupling is approximately zero. Fig. 4.1(b) depicts this trajectory (dotted circle). The orange curve highlights the part of the trajectory along this circle with a small magnetic field tilt angle away from the aligned field ($\theta_B \leq 35°$). From the variation of these two frequencies, we can reconstruct the positions of the two radicals, according to the magnetic tomography term $\omega_{dd}(\mathbf{r}, \hat{\mathbf{b}})$ Eq. 3.5.

4.3 NUMERICAL SIMULATIONS OF BIRADICAL MAPPING WITH DEER

I simulated the NV-biradical system using QuTip, a Python package for simulating quantum systems. The system consisted of three spins with the gyromagnetic ratio of free electrons (γ_e), and hyperfine couplings to nearby nuclear spins were neglected. As the system is complex, to avoid erroneous assumptions, the simulation was done in a lab-frame Hamiltonian without any rotating-wave assumptions. Also, all RF driving pulses were realistic, i.e., not "hard" pulses that are infinitely short, to account for power broadening effects, etc. The relevant scenario is when the NV sensor has a single biradical molecule nearby on the diamond's surface. Thus, the two biradical spins were positioned on a plane assumed to be the diamond's surface at a distance d above the NV spin. The two biradical spins were positioned arbitrarily, and there was no particular assumption on the orientation of the biradical.

First, let us analyze a simulation neglecting relaxation processes ($T_{1/2}^{sl/nv} \to \infty$) to see the spectrum without overlapping close frequency components. Fig. 4.2 shows a fast Fourier transform spectrum of such a simulation. All five frequency components of the derived biradical DEER signal $C(\tau)$ (Eq. 4.6) are identified and constitute the leading frequencies in the signal, validating

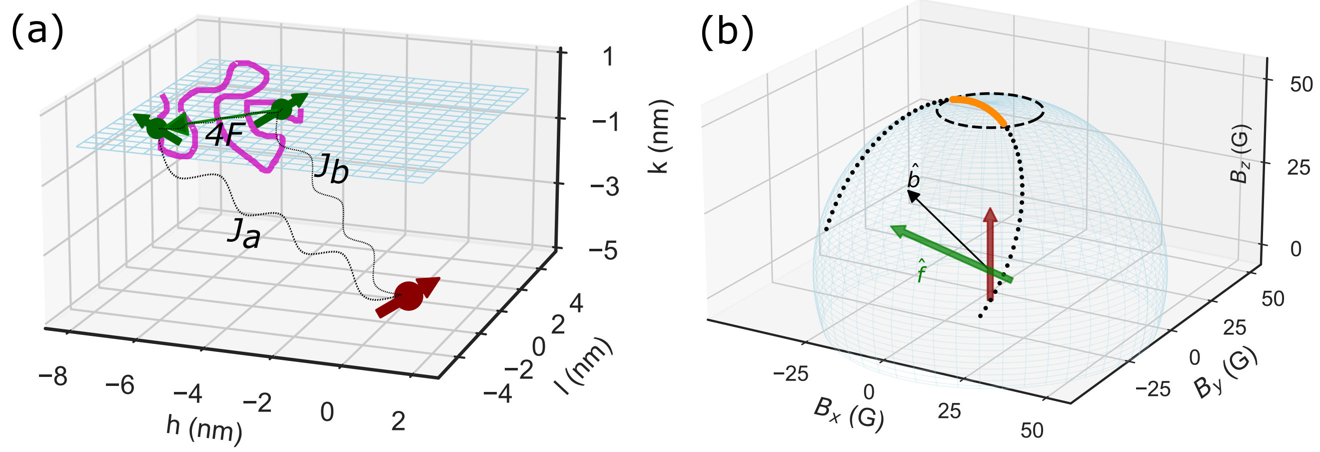

Figure 4.1: NV-biradical system and magnetic field trajectories for measuring distance. (a) Schematic description of the system: the NV sensor spin (dark red) is 5 nm beneath the diamond's surface (blue mesh). On the surface are two spins (green) depicting spin labels attached to a molecule (schematically described by the pink squiggle). The spin labels are separated by 4 nm and a coupling $4F$, with couplings J_a,J_b to the sensor. (b) Visualization of the different magnetic field trajectories. The NV axis (dark red arrow) points along $\hat{z}$. The light blue sphere is the manifold of all field orientations at a magnitude of 50 G. The dashed circle represents the initial tomography sweep at a constant tilt angle of ($\theta_B = 17.2°$) for $\phi_B = 0$–$360°$. The green arrow ($\hat{f}$represents the biradical axis orientation. The dotted curve marks the 50 G fields at a magic angle to the biradical axis. The orange dots are the points sampled to estimate the NV-radical couplings.

the derivation. The additional peak near zero is related to the constant "DC" term (first term in Eq. 4.6).

I then simulated an NV-biradical system, incorporating realistic relaxation to demonstrate the protocol for measuring the distance between the two radicals of a single biradical molecule. I used literature values for the trityl RT relaxation rates: $T_2^{sl} = 4\ \mu s$, $T_1^{sl} = 16\ \mu s$[165]. The NV was assumed to be reasonably shallow - 5 nm beneath the diamond's surface, and appropriate relaxation rates for this type of NV were chosen - $T_2^{nv} = 10\ \mu s$, $T_1^{nv} = 1\ ms$[122]. At least one of the radicals was assumed to be within a 4 nm radius of the NV center's zenith on the diamond surface. The biradical (SL-SL) distance was set to be 4 nm. However, no other particular assumptions were made on the molecule's position, orientation, or spin-spin couplings; they were generated randomly.

Fig. 4.3 demonstrates the mapping protocol described above numerically. The simulations were done on the example NV-biradical system shown in Fig. 4.1. Fig. 4.3(a) shows an example of a DEER trace for such a system, where the is tilted at an arbitrary position (*not* at a magic angle to the radical-radical axis), and (c) is its FFT. The expected values of $\bar{J}$, ΔJ are marked on the FFT spectrum. In contrast, Fig. 4.3(b) shows a DEER trace where the field is at the magic angle to the radical-radical axis: in its FFT in Fig. 4.3(d), it is apparent that the two prominent frequency components are $\bar{J}$, ΔJ. It is evident, by comparing Fig. 4.3(a) and Fig. 4.2 how the frequency components converged into two components at $\bar{J}$, ΔJ.

When analyzing the frequency components of $C(\tau)$ (Eq. 4.6), it is apparent that the most prominent signal will always be at a frequency of $\bar{J}$, and for $F \gg \Delta J$ it will be the only significant frequency. This is the case when $r_{a/b,nv} \ll r_{a,b}$; i.e., the SLs are much farther from the NV than they are from each other. This limiting case can be treated as a single $S = 1$ system interacting with the

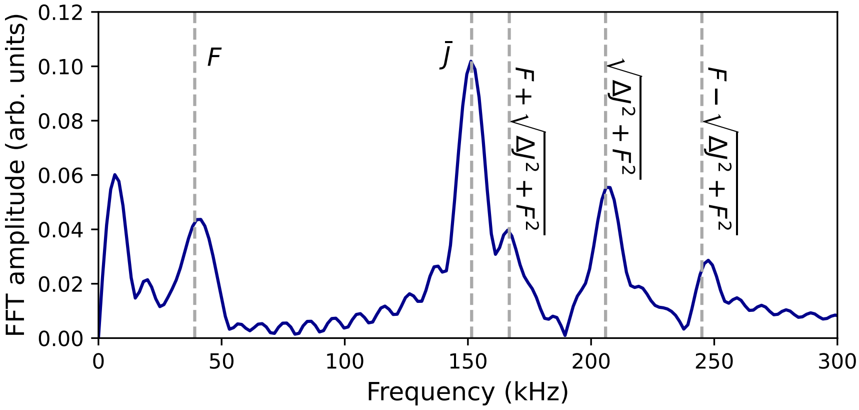

Figure 4.2: Simulating DEER measurement of an NV center with a proximate biradical. The FFT of the DEER time trace is presented. The frequency components predicted by Eq. 4.5 are marked by dashed-gray vertical lines, and all correspond to observed frequency components in the simulated FFT spectrum.

NV center. For the case of $F \lesssim \Delta J$, there will be two more significant frequency components, at $\sqrt{\Delta J^2 + F^2}$ and F, with roughly half the amplitude of $\bar{J}$. However, the F component stems from the SL-SL coherence, so its amplitude is damped according to the ratio of T_2^{sl}/T_1^{sl}. Thus, the two leading frequency components of the DEER signal are $\bar{J}$ and $\sqrt{\Delta J^2 + F^2}$. The second most prominent frequency component satisfies $\sqrt{\Delta J^2 + F^2} \geq |\Delta J|$ and achieves its minimum for $F = 0$.

The frequency analysis suggests that monitoring the two leading frequency components of the DEER time trace can identify the magnetic field orientation for which $F = 0$ (when $\hat{b} \cdot \hat{f} = 1/\sqrt{3}$). This is demonstrated in Fig. 4.3(e), where the frequencies of the two leading components of DEER traces are presented as a function of magnetic field azimuth over an azimuth sweep (the trajectory of the azimuth sweep at a constant tilt angle θ_B is marked by a dashed line in Fig. 4.1(b)). The fitted frequency components (orange squares and blue circles for the first and second frequencies) are compared with the calculated values of $\bar{J},\ \Delta J$ for each magnetic field orientation. At the points where the magnetic field trajectory satisfied $\hat{b} \cdot \hat{f} = 1/\sqrt{3}$, a dip in the curve fitted frequency curve is observed. The dips indicate where the second frequency $\sqrt{\Delta J^2 + F^2}$ reaches its minimum, i.e., $\sqrt{\Delta J^2 + F^2} \rightarrow |\Delta J|$. Using these dips, the biradical axis $\hat{f}$ may be deduced, and the trajectory for which $\hat{b} \cdot \hat{f} = 1/\sqrt{3}$ determined. Then, a magnetic field sweep along this trajectory may be carried out.

Fig. 4.3(f) demonstrates a sweep of the magnetic field along a trajectory for which $\hat{b} \cdot \hat{f} = 1/\sqrt{3}$, marked by an orange curve in Fig. 4.1(b). The two dominant frequency components in the DEER time traces along this trajectory correspond to $\bar{J},\ \Delta J$, as is exemplified in Fig. 4.3(d). Fig. 4.3(f) compared the leading extracted frequency components with the calculated values of $\bar{J},\ \Delta J$, showing excellent agreement. From the variation of these two frequencies, the positions of the two radicals may be reconstructed.

An alternative strategy is identifying the biradical axis orientation as prescribed above and extracting the NV-SL couplings J_a, J_b at the magnetic field orientation satisfying $\hat{b} \cdot \hat{f} = 1/\sqrt{3}$. Then, the value of F may be assessed from the frequency components for the case of another field orientation, for example, when aligned with the NV axis. These two strategies may also be combined to

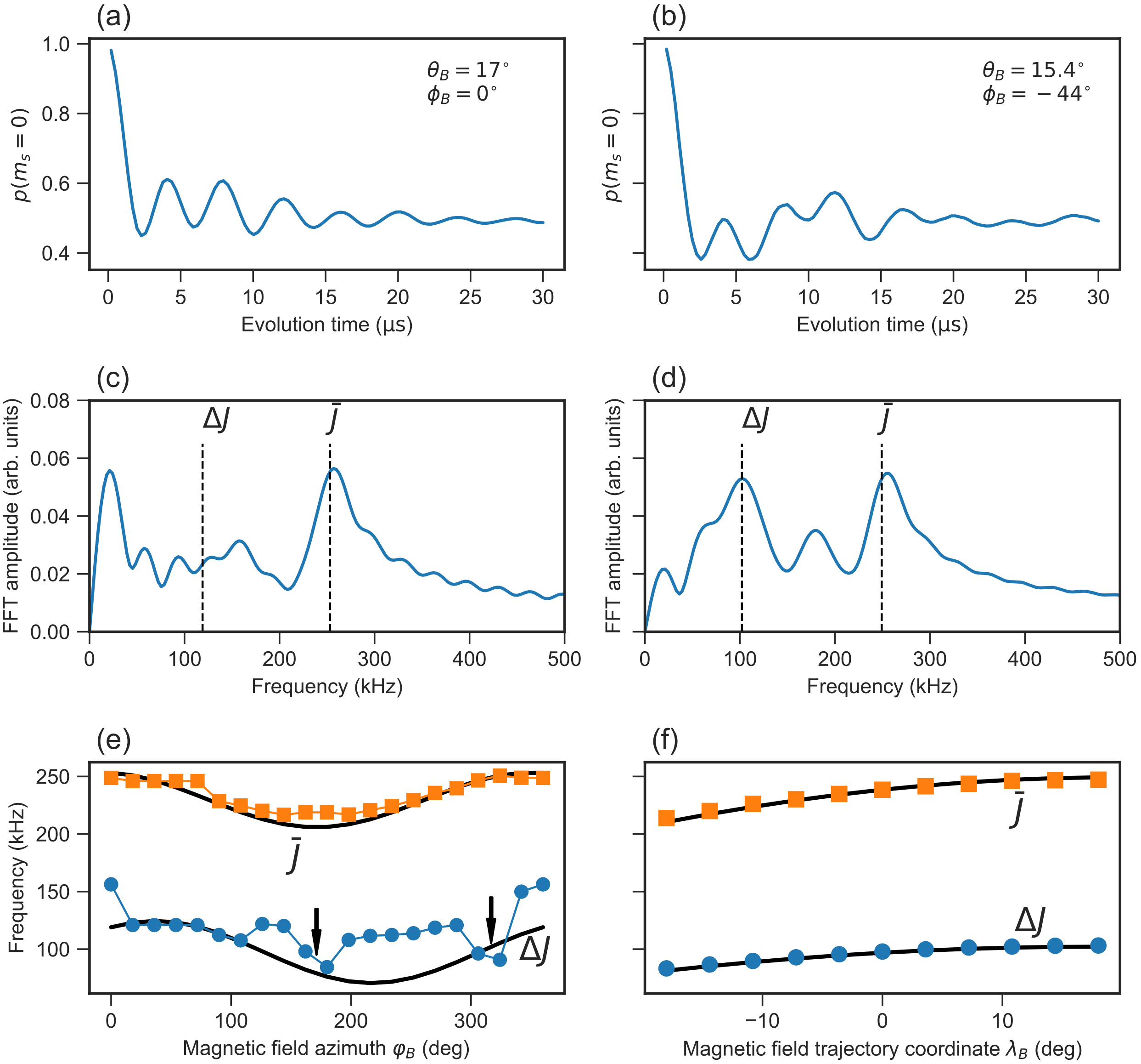

Figure 4.3: Biradical magnetic tomography simulations. (a) An example of a simulated DEER time trace, with the field tilted from the aligned axis as part of an azimuth sweep. (b) Like (a), but with the field titled at a magic angle to the SL-SL axis to cancel out the SL-SL coupling. (c-d) FFT of (a-b) (respectively), with the theoretical values of $\bar{J}$, ΔJ according to Eq. 3.5. In (c), there is no dominant frequency component at ΔJ, but in (d), the two dominant frequencies correspond to these values. (e) The two dominant frequencies extracted from DEER time traces in a simulation of a magnetic field azimuth sweep at $\theta_B = 17^\circ$ (the dashed curve in Fig. 4.1(b)). The extracted values from the simulation (orange squares and blue circles) are plotted alongside the calculated values for $\bar{J}$, ΔJ at each point (solid black lines). The frequencies do not match due to the radical-radical coupling F. Two points along the trajectory where the field creates a magic angle to the biradical axis are marked by arrows (where the dashed circle crosses the dotted circle in Fig. 4.1(b)); they appear as dips in the lower frequency because $F \to 0$. (f) Like (e) but a field sweep that maintains a magic angle to the biradical axis (orange curve in Fig. 4.1(b)). Here, the two dominant frequencies of the simulated time trace (orange squares and blue circles) fit well with the calculated curves for $\bar{J}$, ΔJ according to Eq. 3.5, demonstrating how to extract the positions of the two radicals from such a measurement.

validate the results.

4.4 Discussion and conclusions

I have presented here a protocol to map the position of individual spins in a biradical molecule, even in the presence of significant coupling between the two SLs, on par with their coupling to the sensor. A previous work to do so did not address the spin-spin coupling[88], which, as we've shown, is crucial in predicting the dynamics.

Based on the concepts of magnetic tomography presented previously in Chapter 3, the protocol described here introduces a route for single-molecule distance measurements based on a variable magnetic field. It may be realized with an experimental setup as we've presented here, namely, using a vector magnet (Section 2.3). The protocol does not require more complicated instrumentation, such as an AFM as a source of a magnetic field gradient[106].

The available information in the DEER traces was extracted using a derived analytical term for the expected DEER time trace of two spins and an NV sensor. The SL-SL axis orientation may be identified by sampling several magnetic field orientations and then effectively canceling the SL-SL coupling using a correctly orientated magnetic field. Then, the interpretation of the time traces becomes more straightforward. This is crucial in the presence of noise and decoherence.

I demonstrated the protocol numerically, with an example system of an NV sensor and two other spins, emulating spin labels attached to a molecule. The system was constructed randomly, placing only constraints on the distance from the sensor to render it relevant for sensing. This protocol may be demonstrated similarly on various configurations of this system. However, an implied assumption is that the spins are immobilized, which may be possible by lowering the temperature or encapsulating the molecule in a solid matrix. This strategy does not apply to mobile samples; other strategies should be considered.

A significant challenge in the described experiment is the data analysis, as a DEER trace exhibits at least five frequency components. While this is somewhat alleviated by sampling various magnetic fields, without careful analysis, overfitting may lead to erroneous results. It is thus beneficial to consider elaborate data-fitting algorithms, such as Monte Carlo simulations or machine learning algorithms. Nonetheless, as evident, even the simple least square fitting of a proper function may predict the dynamics well.

5

Strong driving of nuclear spins at the nanoscale

IN THIS CHAPTER, I APPROACH THE ISSUE OF STRONG DRIVING OF NUCLEAR SPINS WITH A NOVEL ANTENNA DESIGN TAILORED FOR NV MAGNETOMETRY AND POTENTIALLY COMPATIBLE WITH ADDITIONAL SOLID-STATE SPIN SYSTEMS. The antenna is a micrometer-scale planar spiral capable of delivering intense RF pulses to a diamond sample. I characterize the antenna's characteristics and performance. Demonstrating the antenna's function by driving proton (^{1}H) spins, I observe spin state Rabi oscillations at frequencies surpassing 500 kHz. I further demonstrate the antenna by driving the NV centers ^{15}N spin at Rabi frequencies of over 700 kHz and study the characteristics of the strongly driven nitrogen spin.

Parts of this chapter appeared in a manuscript titled "Coherent manipulation of nuclear spins in the strong driving regime", published in the New Journal of Physics[166].

5.1 BACKGROUND

Quantum sensing with solid-state spin sensors, such as the nitrogen-vacancy (NV) center in diamond, frequently involves manipulating nuclear spin states. Nuclear spins may be part of the sample of interest, as in the case of nanoscale nuclear magnetic resonance (NMR) spectroscopy, which relies on sequences of radio-frequency (RF) pulses applied to the sample to recover information on its chemical structure[58,87,96,82,167]. Solid-state nuclear spins around the sensor in the crystal lattice are also utilized as ancilla qubits for various sensing tasks. These include storing the quantum state of a sensor to retrieve it repeatedly[95,96]; memory qubits to prolong the sensing time[97];

qubits for frequency conversion[168]; and as ancilla qubits for vector magnetometry[169].

Most experiments until now relied on weak RF driving fields, as the antennas were usually the same line used to manipulate the electronic spin. However, the difference in the gyromagnetic ratio of electronic spins and nuclear spins ($\gamma_{^1H}/\gamma_e \sim 10^{-3}$, $\gamma_{^{13}C}/\gamma_e \sim 10^{-4}$) means that the driving strength ($\Omega_d \approx \gamma B_1$) will be vastly weaker for nuclear spins. As the pulse duration is generally inversely proportional to the driving strength ($t_p \propto \frac{1}{\gamma B_1}$), weaker driving fields imply much lengthier manipulation pulses, with a standard π-pulse lasting a few tens of microseconds[73,58,95]. These prolonged pulses lead to longer measurement times and, thus, reduced sensitivity[9]. They may also impede the application of elaborate pulse sequences, as the sensing time in NV-based NMR is limited by the spin relaxation time of the NV center (T_1)[93], or a nuclear memory[96].

Fast manipulation of nuclear spins by strong RF driving fields can better utilize the limited sensing time of NV center sensors, generate broadband excitation of the nuclear spin resonance, and enable novel sensing protocols[170]. A work by Fuchs et al.[171], who demonstrated strong driving for the NV center electron spin at a rate of ~1 GHz, should be acknowledged. This was done using a microstrip patterned by lithography directly on the diamond's surface. Extrapolating this value to nuclear spins, such as ^{1}H, implies a potential driving rate of over 1 MHz. However, this is not a flexible experimental approach as it does not allow frequent sample replacement. A similar setup to that discussed in this chapter has been reported by Herb et al.[172], where they demonstrated a broadband RF coil antenna by driving ^{13}C spins in diamond at ~70 kHz. The highest reported driving rates for protons in NV-based NMR are 50–80 kHz[58,96].

5.2 Experimental methods

The experiments were performed on the room-temperature setup described in Chapter 2. Low-frequency RF pulses (~1 MHz) were directly synthesized by the AWG, amplified by a 50 W RF amplifier, and irradiated to the sample via our novel spiral antenna, discussed in depth in Section 5.3. The NV center electronic spins were controlled by MW pulses, delivered by a wire drawn above the sample. The experimental scheme is illustrated in Fig. 5.1(a)). Direct current for DC characterization was supplied by Rohde & Schwarz HMP4040 power supply.

The diamond for this experiment was grown by Element Six (UK) Ltd. and fabricated by QZabre AG. The diamond sample was a 50 μm-thick electronic grade, single-crystal (100)-cut diamond membrane, with shallow NV centers created by implanting ^{15}N$^+$ ions at 5 keV and annealing at 850 °C. The surface was patterned with nanopillar waveguides to enhance the photon collection. The diamond was glued to a glass coverslip using Norland NOA63 optical adhesive, so the optical access was through the glass.

For proton sensing, a small drop of microscope immersion oil (Cargille Type LDF, very low autofluorescence immersion oil, with a refractive index of $n = 1.518$ was applied to the diamond's surface (pillar-side) with a sterile syringe. I applied a small amount of oil so that the oil flooded the entire surface of the diamond, including the pillars.

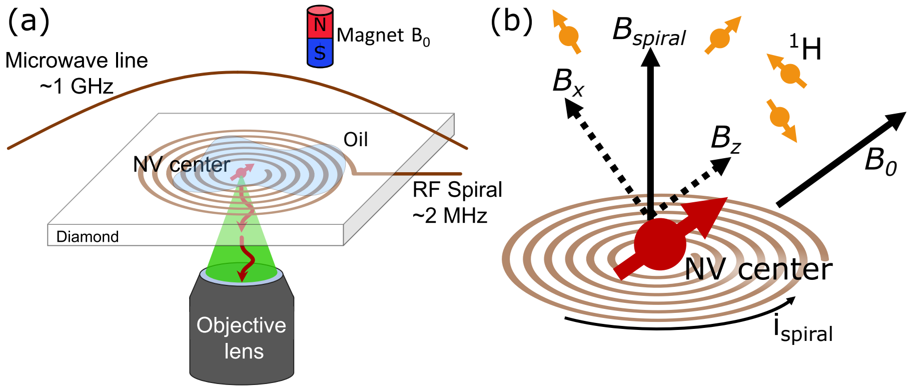

Figure 5.1: Schematic of the experimental system with the spiral antenna for strong driving of nuclear spins (not to scale). (a) The RF spiral antenna sits underneath a thin diamond sample with NV centers in nanopillar waveguides. The NV centers are addressed optically through an aperture in the antenna. Microwave signals to the NV center are applied with a thin copper wire drawn above the diamond sample. Immersion oil with ^{1}H is placed atop the diamond. (b) The static magnetic field B_0 is aligned with the NV center's axis. The spiral antenna's field is approximately perpendicular to the diamond's surface, inducing an RF field component along the NV's axis (B_z) and a component perpendicular to B_0 (B_x).

5.3 PLANAR SPIRAL RADIO-FREQUENCY ANTENNA

ANTENNA DESIGN AND FABRICATION

We designed the RF antenna as a planar spiral, with compatibility in a typical NV magnetometry apparatus was the fundamental design principle. Fig. 5.1(a) depicts the setup schematically; the diamond is placed directly on the antenna to enhance the magnetic field induced at the sample's position, and a small aperture at the center of the spiral allows optical access to NV centers.

The antenna was fabricated using flexible printed circuit technology based on copper traces on a polyimide substrate, suitable for ultra-high vacuum and cryogenic environments. The planar geometry can accommodate a scanning probe, such as an atomic force microscope, which may be used, for example, to carry a sample[67] or create a magnetic field gradient[106]. The leading design principle was to minimize the inner loop of the antenna and trace distance. The ultimate dimensions were determined by the minimal production capabilities: the inner loop diameter is 600 µm, at the center of which is a 200 µm-diameter optical aperture. The sample's area of interest is placed on the aperture (Fig. 5.2(b)). The antenna included two spiral layers, separated by a 20 µm thick polyimide layer and connected at the center by a via surrounding the aperture. The traces were made of gold-finished copper, 20 µm thick, 100 µm wide, and spaced by 100 µm. The circuit was prepared for production and manufactured by Bitronics Ltd., Kiryat Ono, Israel.

I initially estimated the antenna's field by modeling the spiral as a series of N concentric current loops to assess it. The antenna's field-to-current ratio scales logarithmically with the number of turns N, so the number of turns should be increased for a larger field-per-current ratio. On the other hand, the antenna's resistance - and dissipated power - scales quadratically. So, the field-to-power ratio peaks at $N = 3$ for the trace dimensions used here (see Fig. 5.2(c)). The optimal design would depend on the setup, operational preferences (e.g., minimizing heating or maximizing the field), and hardware constraints (e.g., maximum input power). For this work, I chose an antenna with $N = 15$ loops. The calculated field was 136 $\frac{\mathrm{G}}{\mathrm{A}}$ for this number of loops. The calculated resis-

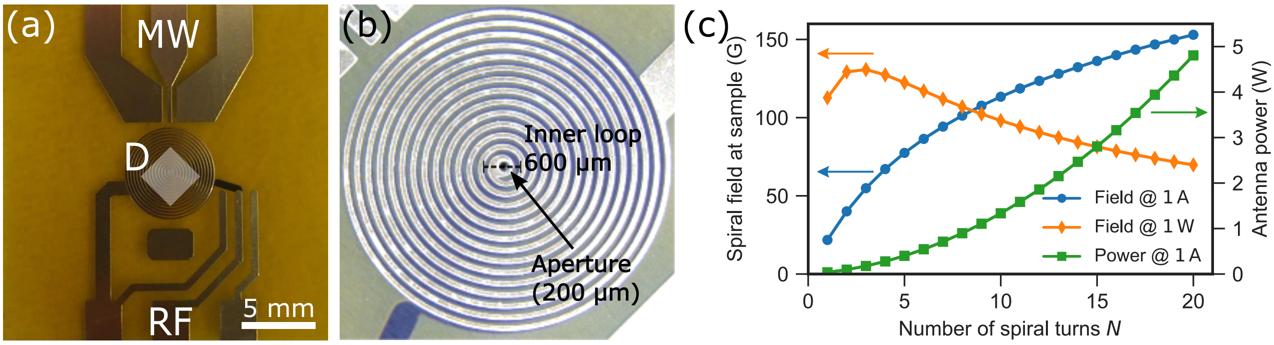

Figure 5.2: Spiral RF antenna design. (a) Photo of the antenna circuit. RF (MW) denotes the signal input connections. The transparent white square schematically depicts the diamond's position. (b) Microscope image of the spiral antenna. The sample sits on the antenna, and the working region is directly above the aperture. (c) Calculation of the dependence of the spiral's field on the number of turns.

tance of the antenna was $R_{\text{model}} = 2.8\ \Omega$, in good agreement with the measured DC resistance of the antenna of $R_{\text{ant}} = 3.0\ \Omega$.

The fabricated flexible circuit was bonded to a sapphire plate (22 mm × 22 mm × 0.3 mm, 1 mm hole in the center, Swiss Jewel Company) with thermally conductive epoxy (Epo-Tek H74F). The sapphire provides a rigid substrate for the sample and assists in removing heat dissipated in the antenna.

The RF signals to the antenna were synthesized by an arbitrary waveform generator and amplified before being delivered to the system. The antenna was terminated by a load ($R_L = 47.4\ \Omega$) to improve impedance matching and increase the system's bandwidth[172]. The load resistor dissipates most of the input power ($\sim 90\%$), and the maximal current is determined mainly by this load. As the load dissipates most of the power but limits the maximum current, the large number of turns ($N = 15$) was beneficial in maximizing the field.

Fig. 5.3 shows a finite element simulation of the antenna's field distribution. The figure depicts the field along a cross-section of the antenna's center and where the sample sits. The simulation confirms that the expected magnetic field has approximately uniform magnitude and orientation over the projected sample position. The magnetic field for a 1 A current at the experiment's sample position was estimated to be (136 ± 1) G, in excellent agreement with the prediction from the simple model of concentric current loops. The field vector was nearly perpendicular to the spiral plane, with a slight tilt of $(1.0 \pm 0.7)^\circ$.

ANTENNA CHARACTERIZATION

I characterized the antenna's bandwidth by analyzing the system's transmission spectrum with a network analyzer. The 3 dB bandwidth of the antenna is approximately 22 MHz, as observed in the transmission spectrum of the system (S_{21} parameter, Fig. 5.4(b)). The antenna's bandwidth allows working with bias fields of up to 0.5 T (for detecting proton spins). Such bias fields are required to utilize a nuclear spin in the diamond as a quantum memory[157,95]. Additionally, the large bandwidth enables the transmission of pulses shorter than a microsecond without significant

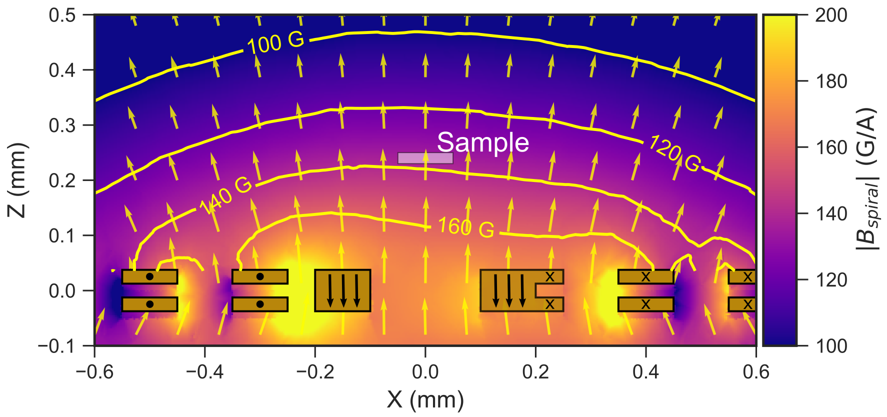

Figure 5.3: Finite element simulation of antenna's magnetic field. Finite-element simulation of the antenna's field, focusing on the region of interest. The image shows a cross-section along the dashed line in Fig. 5.2(b). The color map and contours depict the magnitude of the magnitude of the magnetic field, and the arrows show the projection of the field's orientation on the XZ plane. The golden polygons depict the cross-section of the spiral's trace. The markings inside the polygons denote the direction of the simulated current. The semitransparent rectangle marks the sample's position in the current experiment.

distortion.

I characterized the magnetic field vector emitted by the antenna using *in situ* static magnetic field measurements with the NV center. A direct current through the antenna was swept, and ODMR spectra were acquired at different currents around $B_0 = 0$ (the initial ambient field was $B_0 < 0.5$ G). Each spectrum featured two resonances relating to the $m_s = 0 \leftrightarrow m_s = \pm 1$ transitions of the NV center. The NV center transition frequencies were extracted as a function of the current through the spiral, and the result is plotted in Fig. 5.4(b). The transitions are not linearly dependent on the magnetic field as the spiral's field is not aligned with the NV center's axis (see schematic in Fig. 5.1(b). I calculated the dependence of the field magnitude on the current and the field's tilt from the NV center's axis by diagonalizing the following spin Hamiltonian[173]:

$$\mathcal{H} = DS_z^2 + \gamma_e B_{\text{spiral}} \left(\cos\left(\theta_d\right) S_x + \sin\left(\theta_d\right) S_z\right) + a_z S_z^2 + a_\perp \left(S_y^2 - S_x^2\right) \tag{5.1}$$

Here, the tilt of the spiral drive field away from the plane transverse to the NV axis (xy-plane) is denoted as θ_d; $a_z, a_\perp$ are coefficients accounting for a strain field that split the transitions at $B_{\text{spiral}} = 0$ and shifts their center away from D. From the data I extracted $a_z = 2\pi \times (-3.01 \pm 0.30)$ MHz, $a_\perp = 2\pi \times (17.48 \pm 0.36)$ MHz. The field was assumed to be proportional to the current, i.e., $B_{\text{spiral}}\left(I_{\text{spiral}}\right) = bI_{\text{spiral}}$, as there is no significant mass of magnetic material in the vicinity. Under this assumption, I found the field-to-current ratio b by fitting the transitions as a function of spiral current I_{spiral} and the field's tilt θ_d, which is assumed to be constant as a function of the current.

The DC field-to-current ratio was estimated to be $B / I_{\text{spiral}} = (113 \pm 16)\,\frac{\text{G}}{\text{A}}$, in good agreement with the theoretical predictions and finite-element simulations. The field's angle is measured to be tilted from the plane transverse to the NV axis by $\theta_d = (36.5 \pm 5.8)^\circ$. This corresponds to a tilt of $\sim 1.2^\circ$ from the normal to the spiral plane. As the NV center lies at an angle of $\sim 54.7^\circ$ to the diamond surface, parallel to the spiral plane, the measured orientation is consistent with our expectation that the planar spiral antenna induces a field normal to its plane.

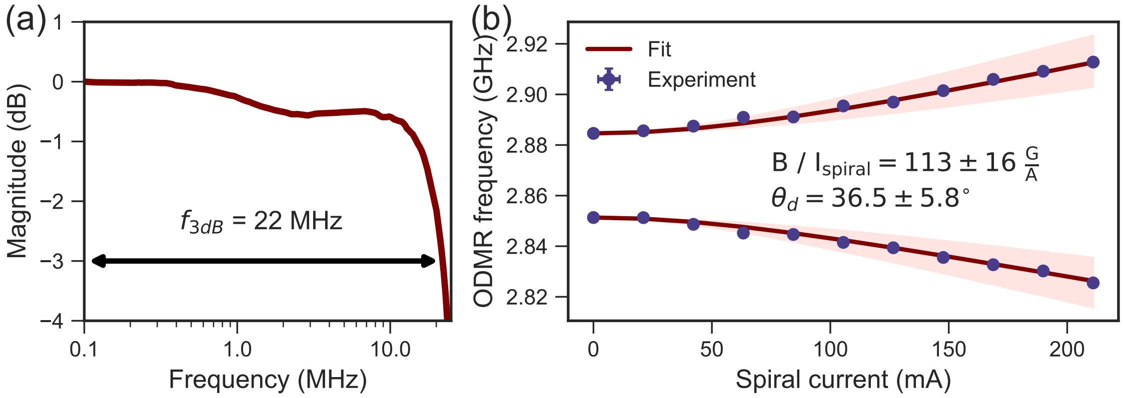

Figure 5.4: Spiral RF antenna characterization. (a) Transmission characteristics of the antenna (S_{21} parameter). (b) Direct current magnetic field characterization. The NV center level shifts were measured in a series of ODMR spectra with varying currents through the spiral. The data was fitted to a model incorporating the magnetic field tilt and a strain field. The pink areas mark the confidence intervals of the fit.

In a sensing experiment, as discussed in the following section, there will usually be an applied quantizing magnetic field ($\vec{B}_0$) along the NV center's axis ($\hat{z}$ in Fig. 5.1(b)). Under the RWA, the transverse component (B_x in Fig. 5.1(b)) drives the spins and is proportional to the Rabi frequency. From the DC characterization, it is estimated to be $B_x\ /\ I_{\mathrm{spiral}} = B\cos\left(\theta_d\right)/I_{spiral} = (92 \pm 14)\ \frac{\mathrm{G}}{\mathrm{A}}$ (the magnitude might be attenuated according to the transmission at the specific frequency, as described in Fig. 5.4(b)).

5.4 FAST ^{1}H RABI OSCILLATIONS

I demonstrated the antenna's function by driving Rabi oscillations in a proton spin ensemble of an organic sample on the diamond's surface. As a preliminary experiment, proton nuclear magnetic resonance was sensed with a variant of the XY8-N dynamical decoupling sequence. XY8 sequences are from the family of CPMG sequences, but with alternating π-pulse phases in blocks of eight pulses, as depicted in Fig. 5.5(a). N denotes the repetitions of the XY8 blocks. Here, I used a randomized XY8 (RXY8-N); this variant of the XY8 sequence[37] is augmented by adding a random global phase to each XY8 pulse block[174]. The random phase shift suppresses spurious harmonics of ^{13}C spins[87].

Fig. 5.6(c) presents a representative RXY8-10 trace with a dip at $\tau = 179.5$ ns, consistent with the expected position of the proton Larmor frequency ($B_0 \approx 652$ G, $f_{\mathrm{H}} \approx 2.78$ MHz). This is an indication that the NV senses the proton's oscillating magnetization. The sensed volume is $(\sim 10\,\mathrm{nm})^3$ and includes $\sim 10^5$ spins[37], so the measured signal should be interpreted as the total magnetization of the ensemble. For additional data on proton NMR experiments and information on the data normalization, see Appendix B.

To further indicate the presence of the protons' NMR signal, I performed a correlation spectroscopy sequence[37,93]. The sequence, depicted in Fig. 5.5(b), is based on XY8-4 sensing blocks with $\tau = 179.5$ ns, spaced by a varying correlation time (in the correlation sequence the XY8 phases were not randomized). The correlation trace and its fast Fourier transform spectrum are presented

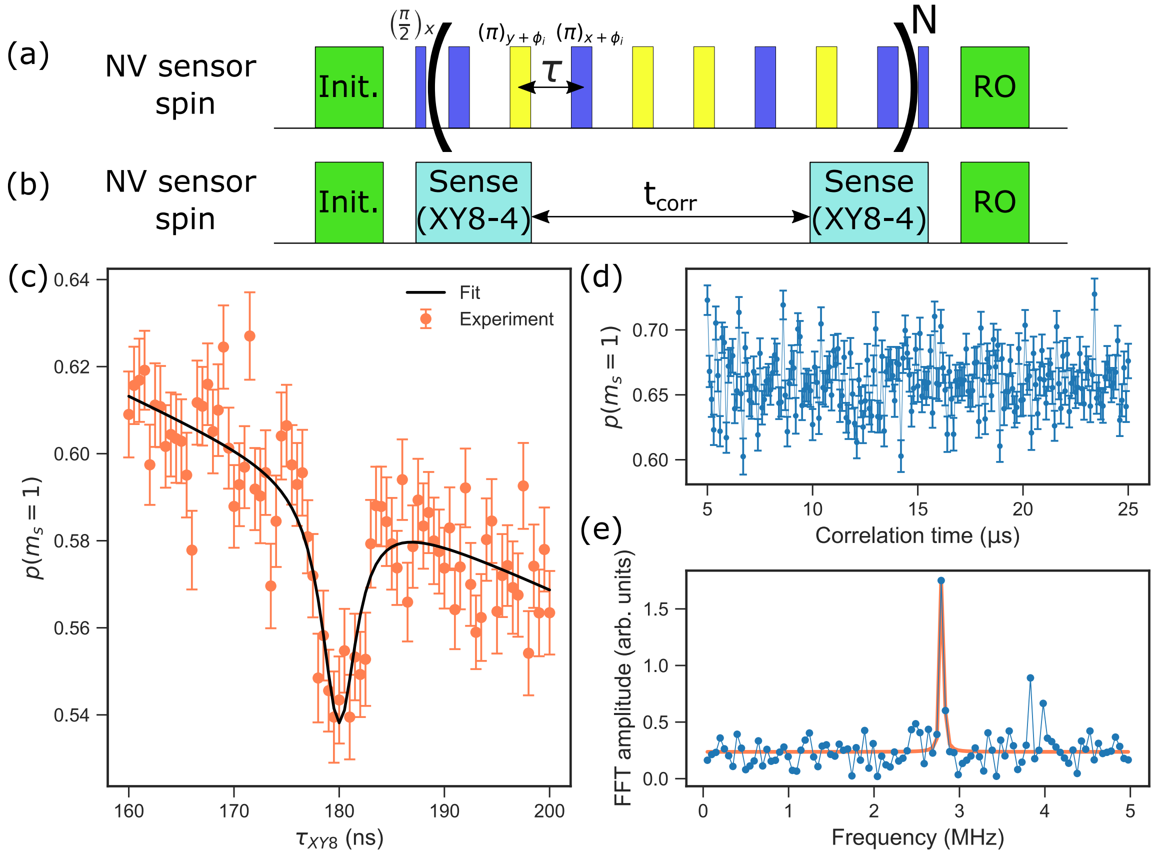

Figure 5.5: NMR of ^{1}H spins on the diamond's surface. (a) A diagram of the randomized XY8-N (RXY8-N) pulse sequence used to sense the ^{1}H nuclear magnetic resonance. (b) The correlation sequence is based on two XY8-4 dynamical decoupling blocks for detecting the proton resonance frequency. (c) RXY8-10 trace, exhibiting a dip at the condition $\tau = \frac{1}{2f_{^1H}}$, where $f_{^1H}$ is the ^{1}H Larmor frequency. The trace was fitted with a Lorentzian line shape on a linear background. (d) Correlation spectroscopy time trace encapsulates the proton signal phase oscillations as a function of the correlation time (t_{corr}). (e) The FFT spectrum of the signal in (d), exhibiting a peak at (2.80 ± 0.01) MHz, is in good agreement with the expected resonance.

in Fig. 5.5(d)-(e). While the time trace is noisy, a dominant peak at the expected frequency is evident in the Fourier spectrum. This experiment is a vital verification, as the Rabi experiment is based on a correlation measurement.

I then employed a correlation spectroscopy sequence with RF pulses[175,96] to observe proton Rabi oscillations, as depicted in Fig. 5.6(a). The correlation delay, i.e., the spacing between the two sensing blocks, was fixed at 20 μm. The RF pulses were tuned to the proton Larmor frequency and positioned so their centers were precisely at the center of the correlation delay. The RF pulses drive the nuclear magnetization, inducing a $|\uparrow\rangle \leftrightarrow |\downarrow\rangle$ transition. The experimental data featured oscillations that I interpret as Rabi oscillations of the proton spins.

The Rabi oscillations are plotted in Fig. 5.6(b) for several driving powers corresponding to different spiral currents. The oscillations were fitted to a decaying sine function, from which the driving frequency (Ω_d) was extracted. Fig. 5.6(c) summarizes the observed driving frequencies as a function of spiral currents. The current values are the peak currents estimated by measuring the voltage on the load resistor terminating the spiral antenna. The peak current was estimated according to the peak voltage of the driving waveform as observed on an oscilloscope. The driving frequency is proportional to the driving current, as expected. A maximal driving frequency of

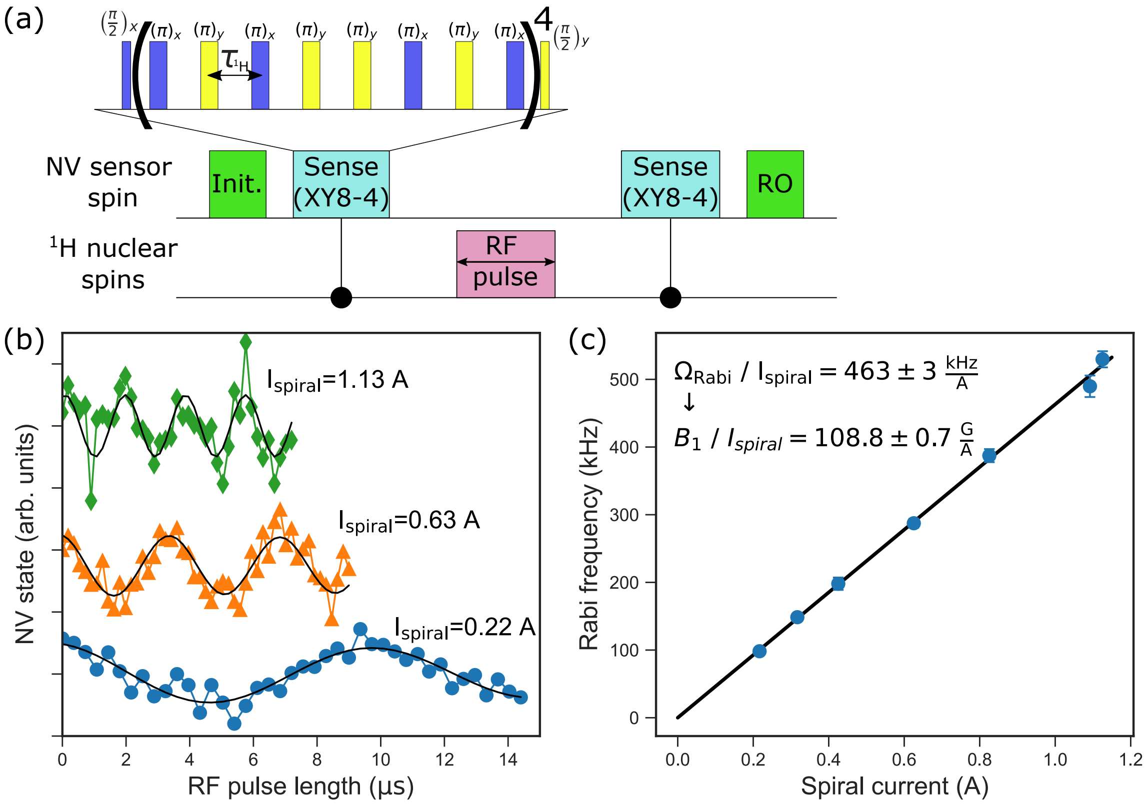

Figure 5.6: Fast Rabi oscillations of ^{1}H nuclear spins. (a) Diagram of the pulse sequence used to observe ^{1}H nuclear spin Rabi oscillations. The nuclear spin precession was detected by correlating two XY8-4 dynamical decoupling blocks tuned to the ^{1}H frequency found in Fig. 5.5. A varying radio frequency pulse tuned to the ^{1}H frequency during the correlation time drives the ^{1}H spin state. (b) Rabi oscillations of the ^{1}H spins for different current amplitudes driven through the spiral antenna. (c) Summary of several Rabi frequencies measured, with a linear dependence on the current through the antenna.

(530 ± 12) kHz was achieved, ultimately limited by our amplifier's saturation power.

I estimate a driving frequency-to-current ratio of $\Omega_d \ / \ I_{\text{spiral}} = (463 \pm 3)$ kHz/A. From this ratio, the field-to-current ratio of the transverse field was estimated at 2.78 MHz to be $B_1 \ / \ I_{\text{spiral}} = (108.8 \pm 0.7) \ \frac{\text{G}}{\text{A}}$; this is in good agreement with the value expected from *in situ* DC measurement $((92 \pm 14) \ \frac{\text{G}}{\text{A}})$ presented previously and the finite-element simulations $((111.0 \pm 0.8) \ \frac{\text{G}}{\text{A}})$.

The oscillation frequencies were approximately 50–500 kHz, so in terms of the Larmor frequency, the driving was in the range of $\Omega_d < \frac{\omega_0}{5}$. At $\omega_0/5$, there are deviations from the RWA sinusoidal dynamics of several percent; however, the average still follows a sine. Thus, I analyzed the resultant dynamics at all driving powers with sine functions, invoking the RWA. The variation from a smooth sine, mostly visible at higher powers, may be partly attributed to deviations from the RWA, along with other factors, such as the impact of the RF signal on the sensor (see Section 5.6).

The RF introduces plenty of power into the system: the highest driving amplitude shown here corresponds roughly to the saturation power of the amplifier (~50 W). At this output power, the current is approximately 1.1 A, which corresponds to about 3.3 W of power dissipated at the antenna. The subsequent heating manifests as a reversible shift of the diamond sample, presumably due to the thermal expansion of the substrate and antenna (for other, more sensitive samples, the heating might have additional adverse effects). Heating was handled by lowering the duty cycle using dead times after each sequence run. At a current of ∼1.1 A, the duty cycle of the RF was set to be $\sim 2\%$.

5.5 Strong driving of the NV center's ^{15}N spin

In the previous section, I demonstrated the strong driving of nuclear spins in a sample external to the diamond. In this section, I discuss the strong driving of nuclear spins strongly coupled to the sensor spin, namely, the NV electron spin.

The NV center's electronic spin is coupled by hyperfine coupling to various nuclear spins in the diamond, such as ^{13}C[48,71] in the diamond lattice, naturally present at an abundance of $\sim$ 1.1%, unless the diamond was synthesized with a modified isotope composition. The NV center's electronic spin is also hyperfine-coupled to the center's nitrogen spin, as nitrogen's stable isotopes, ^{14}N and ^{15}N, are paramagnetic with $S = 1$, and $S = \frac{1}{2}$ (respectively). Thus, all NV center electron spins are coupled to either nitrogen spin with hyperfine coupling parameters of ∼3 MHz[13].

The nuclear spins around the NV center are a useful resource in various aspects: as ancilla qubits for enhancing quantum sensing with NV electronic spin[176,97,137,175], vector magnetometry sensors[169,168], quantum information processing nodes[177,86,178], and a platform for fundamental quantum science[179,85].

NV-^{15}N hyperfine Hamiltonian with RF driving

The Hamiltonian of the NV electron spin-nuclear spin system is:

$$\mathcal{H} = DS_z^2 + \gamma_{nv} B_0 S_z + \gamma_n B_0 I_z + \underbrace{\mathbf{S} \cdot \mathcal{A} \cdot \mathbf{I}}_{\mathcal{H}_{hf}} + \mathcal{H}_d \tag{5.2}$$

Here $\mathbf{I}$ is the nuclear spin operator; γ_n is the nuclear spin gyromagnetic ratio; $\mathcal{H}_{hf}$ is the hyperfine Hamiltonian, $\mathcal{A}$ is the hyperfine tensor, and $\mathcal{H}_d$ is some driving Hamiltonian. Due to symmetry considerations, the hyperfine term may be simplified to:

$$\mathcal{H}_{hf} = A_{\|} S_z I_z + A_{\perp} \left(S_x I_x + S_y I_y \right) \tag{5.3}$$

$A_{\|}, A_{\perp}$ are the hyperfine terms parallel and perpendicular to the NV axis. For ^{15}N they are $A_{\|} = 2\pi \times 3.03$ MHz and $A_{\perp} = 2\pi \times 3.65$ MHz[13], $\gamma_n = 2\pi \times -4.316$ MHz/T.

The driving Hamiltonian is given by:

$$\mathcal{H}_d = B_1 \left(\hat{x} + \tan\left(\theta_d\right) \hat{z} \right) \cdot \left(\gamma_{nv} \mathbf{S} + \gamma_n \mathbf{I} \right) \tag{5.4}$$

B_1 is the magnitude of the driving field along $\hat{x}$; $\theta_d \in \left[0, \frac{\pi}{2}\right)$ is the tilt of the driving field away from the plane normal to B_0 ($\theta_d = 0$ represents an ideal driving field along $\hat{x}$). I note that in this form, the magnitude of the field depends on θ_d and is $B_1 \sqrt{1 + \tan^2\left(\theta_d\right)} \geq B_1$. For the spiral antenna described in Section 5.3, $\theta_d = \arccos\left(\sqrt{\frac{2}{3}}\right) \approx 35°$. This is the value used in the dynamic simulations of the Hamiltonian of Eq. 5.2.

MANIPULATING AND SENSING HYPERFINE-COUPLED NUCLEAR SPINS

The nuclear spins near the NV center may be polarized, and their state may be detected by leveraging the strong hyperfine coupling to the NV electron spin. Polarization transfer from the electron spin to the nuclear spin has been discussed in the literature extensively; notable techniques include Hamiltonian engineering[180] and SWAP gates[181,182]. Here, I utilized an optical pumping technique based on a flip-flop process between the electron and nuclear spin while the defect is in the excited state[72]. The flip-flop process is most probable near the NV's excited state level anticrossing (ESLAC) at $B_0 \approx 510$ G.

The NV spin may sense the nuclear spin state by applying a π-pulse to the electronic spin, conditioned on the state of ^{15}N (a CX gate of the two-qubit system)[73]. In practice, this is done using a low-power, narrow-band π-pulse and thus selective to one of the hyperfine-split transitions of the electron spin. Fig. 5.7(a) depicts the sequence, and figures (b)-(d) show NV ODMR spectra at different fields. At a field of 509 G, approximately at the ESLAC, the ^{15}N is almost completely polarized $\mathcal{P} = 0.98$[a], which is apparent by the absence of a dip at the anticipated position of the $|-1, \downarrow\rangle \leftrightarrow |0, \downarrow\rangle$ transition. At a field of 637 G, farther from the ESLAC, the nuclear spin polarization immediately after the laser pulse ($t_{delay} = 0$) is significantly lower at $\mathcal{P} = 0.67$. These values are consistent with previous reports. Adding a delay after the laser pulse allows the nuclear spin to relax back to the thermalized state, and for $t_{delay} = 100$ µs, the polarization decreased to $\mathcal{P} = 0.29$.

From the data in Fig. 5.7(c)-(d) the T_1 of the ^{15}N spin was estimated to be $\sim$120 µs. This relatively short lifetime is due to the proximity to the ESLAC, and its value is consistent with previous reports[183]. This fact makes it unfavorable as a quantum memory for experiments done at B_0 fields of several hundred gauss. The reduction in overall optical contrast seen in Fig. 5.7(d) is related to the simultaneous relaxation of the electronic spin, a separate but related process to the nuclear spin relaxation.

FAST RABI OSCILLATIONS OF ^{15}N SPIN

With the ability to polarize and read out the nuclear spin state, I demonstrated fast, coherent manipulation of the spins. This was demonstrated by driving the nuclear spin with a resonant RF pulse, tuned to the nuclear spin transition given by $\omega_n = A_{\parallel} - \gamma_n B_0$. Fig 5.8(a) depicts the pulse sequence: after laser initialization of the system to the state $|m_s = 0, m_i = \uparrow\rangle$, the electron is transferred to the $m_s = -1$ state by a MW π-pulse. This pulse does not have to be selective (the nuclear spin is polarized at this point), so applying an intense π-pulse is preferable. The faster, intense pulses are more efficient by up to a factor of 3 as the NV spin state tends to dephase during the long selective pulses. Then, an RF pulse of varying duration induces the $|-1, \uparrow\rangle \leftrightarrow |-1, \downarrow\rangle$ transition. Finally, a narrow π-pulse is applied to the NV spin at the $|-1, \uparrow\rangle \leftrightarrow |0, \uparrow\rangle$ frequency to selectively transfer only the population at the $m_i = \uparrow$ state. The NV state is subsequently read out

---

[a] The polarization $\mathcal{P}$ is defined as the difference in state probabilities (or populations): $\mathcal{P} = p_{\uparrow} - p_{\downarrow}$. Assuming the RF pulses are identical within this band, the dip amplitudes are proportional to the probability. So, $\mathcal{P} = (a_{\uparrow} - a_{\downarrow}) / (a_{\uparrow} + a_{\downarrow})$, where a_i is the amplitude related to state i in Fig. 5.7.

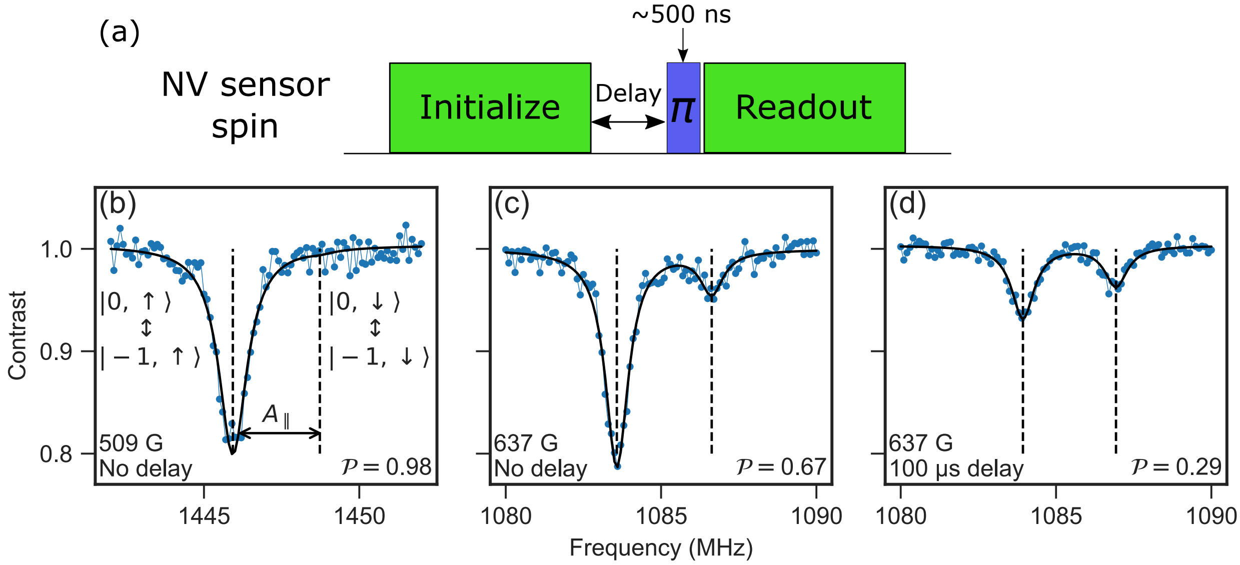

Figure 5.7: Selective addressing of nuclear spin transitions. (a) Pulsed ODMR sequence to polarize and selectively address hyperfine-split transitions of the NV center spin. The Rabi frequency was set to $\sim 1\,\mathrm{MHz}$, corresponding to a π-pulse duration of $\sim 500\,\mathrm{ns}$. (b)-(d) Pulsed ODMR spectra at different B_0 fields and delay times (denoted at the bottom left of each figure). The plots show different polarization rates $\mathcal{P}$ of the ^{15}N spin, denoted at the bottom right. Blue circles denote experimental data; the black solid is a double Lorentzian fit of the data; dashed lines denote the position of specific electronic spin transitions.

optically. The resulting signal oscillated as a function of RF pulse duration, interpreted as nuclear spin Rabi oscillations.

Fig. 5.8(b)-(h) shows Rabi oscillations at various driving amplitudes, corresponding to different driving field strengths (B_1), measured at $B_0 = 509\,\mathrm{G}$. The driving field was calculated using the current-to-field ratio calculated in Section 5.4 for proton Rabi oscillations. Rabi oscillations of over 700 kHz were observed, which, to my knowledge, is by far the fastest measured Rabi frequency (Ω_n) for a nuclear spin in the diamond at this magnetic field. Sangtawesin et al. achieved Rabi frequencies of up to 1 MHz in the vicinity of the GSLAC, ~1000 G, where the effective gyromagnetic ratio is significantly enhanced; in contrast, at 512 G they measured a maximal frequency of ~50 kHz[184].

The trend of the Ω_n vs. B_1 is shown in Fig. 5.8(i), which summarizes the observed Rabi frequencies, as extracted from the measurements (Fig. 5.8(b)-(h)) by fitting the data to a sine model. The experimental values of Ω_n vs. B_1 are compared to a theoretical curve obtained by numerical simulation of the driven system described by the Hamiltonian in Eq. 5.2.

A prominent feature of the hyperfine-coupled nuclear spin is an enhanced ratio between B_1 and Ω_n. This can be formulated as an enhanced effective gyromagnetic ratio γ_n^{eff} (to clarify, this factor only applies to the relation between Ω_n/B_1, and not to the level splitting's dependence on the external field ω_0/B_0). Smeltzer et al.[73] provided an approximate term for the Rabi frequency's dependence on the field[73], and later Chen et al.[185] derived γ_n^{eff} an analytic term under the RWA for ^{14}N. Here, I rewrite it for ^{15}N (notably, I dropped the quadrupole moment, which is zero for spin-1/2):

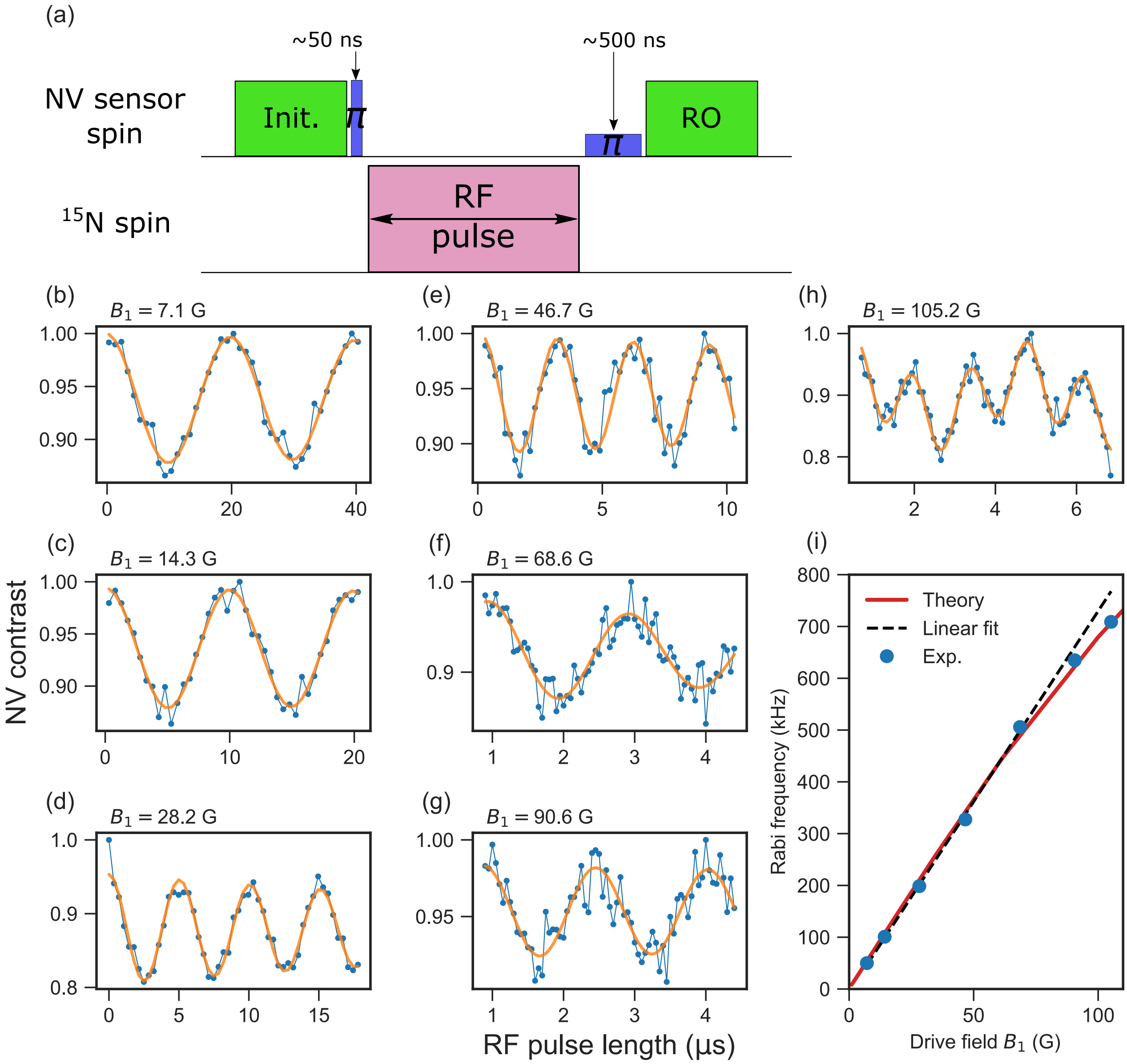

Figure 5.8: Rabi oscillations of the NV center's ^{15}N spin. (a) The nuclear Rabi sequence. (b)-(h) Rabi oscillations of the nuclear spin as observed via the NV sensor state. Blue circles are experimental data, and the orange solid curves are fitted decaying sines with either a single frequency (b-g) or two frequencies (h). (i) Plotting the fitted Rabi frequencies from (b-h) vs. the driving field (blue circles). The red solid line is a theoretical curve based on simulations. The dashed line is a linear fit of the first four data points to extract the effective gyromagnetic ratio.

$$\gamma_n^{eff} = \gamma_n \left(1 + \frac{\gamma_{nv}}{\gamma_n} \frac{A_\perp}{D + \gamma_{nv}B_0 - A_\perp + \gamma_n B_0}\right) \tag{5.5}$$

This is γ_n^{eff} when the electron spin is in the $m_s = -1$ state, which is the relevant state for our experiment. The effective gyromagnetic ratio is thus B_0 dependent, and as we show, it also exhibits a B_1 dependence. Sangtawesin et al. demonstrated the B_0 dependence and the expected singularity at $B_0 \approx= D/\gamma_{nv}$. the GSLAC[184].

Measured here for a single value of B_0, a linear dependence is expected at weak driving fields, i.e., $B_1 \ll B_0$. I extracted the effective gyromagnetic ratio in the weak driving regime by fitting the experimental points at lowest fields ($B_1 < 50\,\mathrm{G}$) to a linear fit and obtain a value of $\gamma_n^{eff} = (7.36 \pm 0.15)\,\mathrm{kHz/G}$, in excellent agreement with the simulations ($7.4\,\mathrm{kHz/G}$). This value is also consistent with the model in Eq. 5.5, which predicts $7.5\,\mathrm{kHz/G}$, and with Sangtawesin et al.[184]. The linear fit is presented in Fig. 5.8(i) and compared with the experiment and theory.

Interestingly, a nonlinear dependence on B_1 is apparent in Fig. 5.8(i) for $B_1 \gtrsim 100\,\mathrm{G}$, where the effective gyromagnetic ratio decreases (the data and deviates below the linear fit). The theoretical simulations well predict this. The simulations also predict the driving frequency to saturate above $200\,\mathrm{G}$ and at approximately $300\,\mathrm{G}$, the ordered oscillations transition to erratic dynamics. However, our experimental setup did not allow us to achieve driving amplitudes of $300\,\mathrm{G}$, needed for observing this breakdown at $B_0 = 509\,\mathrm{G}$.

To my knowledge, the nonlinear regime was not addressed theoretically in the literature. The rigorous derivation by Chen et al. assumed low driving fields, as was in their experiments, and thus invoked the RWA. The nonlinear dependence emerges when the driving amplitude approaches the electron spin splitting, $B_1 \sim D/\gamma_{nv} + B_0$. Sangtawesin et al. observed a deviation from a linear trend at the GSLAC at low driving amplitudes and also a subsequent breakdown of the sinusoidal behavior for slightly higher fields[184]. But, near the GSLAC, the dynamics are dominated by the slight separation of the electron spin levels ($m_s = 0, -1$), which is on the order of the nuclear hyperfine splitting. A further expansion to higher orders may shed light on the dynamics at higher fields.

I note that, for the highest driving field presented here ($105.2\,\mathrm{G}$, corresponding to a peak current of $0.97\,\mathrm{A}$ through the spiral), the oscillatory Rabi dynamics were characterized by an additional modulation at a frequency of $\sim 2.8\,\mathrm{MHz}$ (Fig. 5.8(h); due to aliasing it appears as a $\sim 200\,\mathrm{kHz}$ modulation). I could not eliminate this modulation, but it was presumably the result of a residual signal in the antenna. A lingering signal may be present after the intended end of the RF pulse, which modulates the NV (sensor) state at the signal's frequency; in this case, it is at the ^{15}N resonance.

Fig. 5.9 shows NMR experiments of the NV center's ^{15}N at a few samples driving strengths, compared with a simulation based on the Hamiltonian of Eq. 5.2. The sequence is similar to that shown in Fig. 5.8(a), with a fixed RF pulse duration and varying driving frequency. The simulation was conducted without fitting parameters, only setting the driving amplitude according to the experiment. The simulation shows an excellent fit with the experiment for the lower driving frequencies. The line shape expectedly broadens with driving frequency; however, the shape significantly deviates from the theoretical simulation for very strong driving amplitudes. Notably,

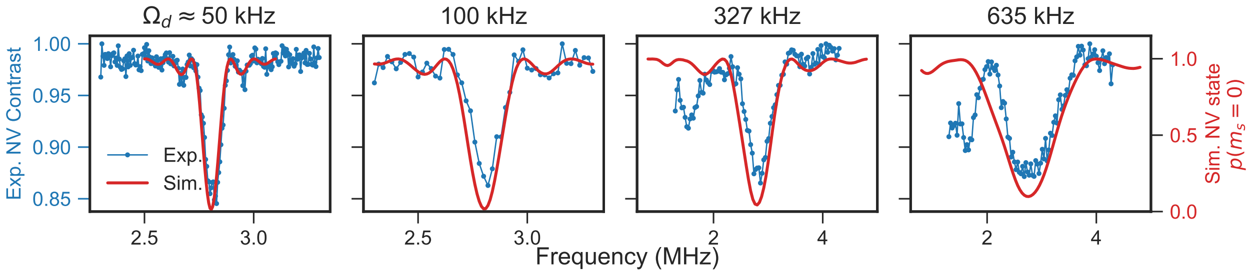

Figure 5.9: NMR of the NV center's ^{15}N spin at different driving strengths. NMR spectrum at different driving strengths (blue dots) compared with a simulation (red curves).

another feature appears at ~1.5 MHz, the source of which has yet to be clarified.

5.6 SENSOR STATE MODULATION BY THE DRIVING FIELD

Under weak driving, the nuclear spin manipulation pulses should have a negligible effect on the sensor's (e.g., NV center electron spin) state. The driving field (B_{rf}) is much smaller than the transitions, namely, ω_{rf}, $\gamma_{nv} B_{rf} \ll D \pm \gamma_{nv} B_0$, so the driving term in the Hamiltonian is negligible. Also, the driving frequency (ω_{rf}) is usually far detuned from the NV center's transitions, i.e., $\omega_{rf} \ll D \pm \gamma_{nv} B_0$, and so a resonant effect may be neglected. However, strong driving implies $B_{rf} \sim B_0$ and often $\gamma_{nv} B_{rf} \sim D \pm \gamma_{nv} B_0$. Thus, while there is still no resonant effect, the driving term in the Hamiltonian becomes non-negligible even if the frequency is far detuned from the transition.

Considering just the NV spin Hamiltonian under the driving field (this is the Hamiltonian of Eq. 5.2, omitting the nuclear spin terms):

$$\mathcal{H}(t) = \Delta S_z + \Omega \sin\left(\omega_{rf} t + \phi_{rf}\right)\left(S_x + \tan\theta_d S_z\right) \tag{5.6}$$

Here, I simplified the static Hamiltonian to a two-level system with a splitting $\Delta = D - \gamma_{nv} B_0$, and the driving strength is $\Omega = \gamma_{nv} B_1$. In the proton driving experiments (Fig. 5.6) with the strongest driving, the ratio of the terms was $\frac{\Omega}{\Delta} \approx \frac{1}{5}$

Eq. 5.6 can be rewritten as:

$$\mathcal{H}(t) = \left(\vec{\Delta} + \vec{\Omega}(t)\right) \cdot \vec{S} \tag{5.7}$$

$$\vec{\Delta} = \Delta \hat{z} \tag{5.8}$$

$$\vec{\Omega}(t) = \Omega \sin\left(\omega_{rf} t + \phi_{rf}\right)\hat{x} + \Omega \tan\left(\theta_d\right)\sin\left(\omega_{rf} t + \phi_{rf}\right)\hat{z} \tag{5.9}$$

An approximate solution for $\langle S_z \rangle (t)$ may be obtained in a heuristic approach. The driving frequency is much lower than the Larmor frequency, i.e., $\omega_{rf} \ll \Delta$, so that the driving term can be treated as quasi-static. Then, the dynamics of the spin state are adiabatic. Setting $\phi_{rf} = 0$, then $\mathcal{H}(t = 0) \propto S_z$. As time progresses, the Hamiltonian evolves slowly away from the $\hat{z}$. If the system is initialized to an eigenstate of S_z, the evolution will follow the vector $\vec{\Delta} + \vec{\Omega}(t)$ in an adiabatic man-

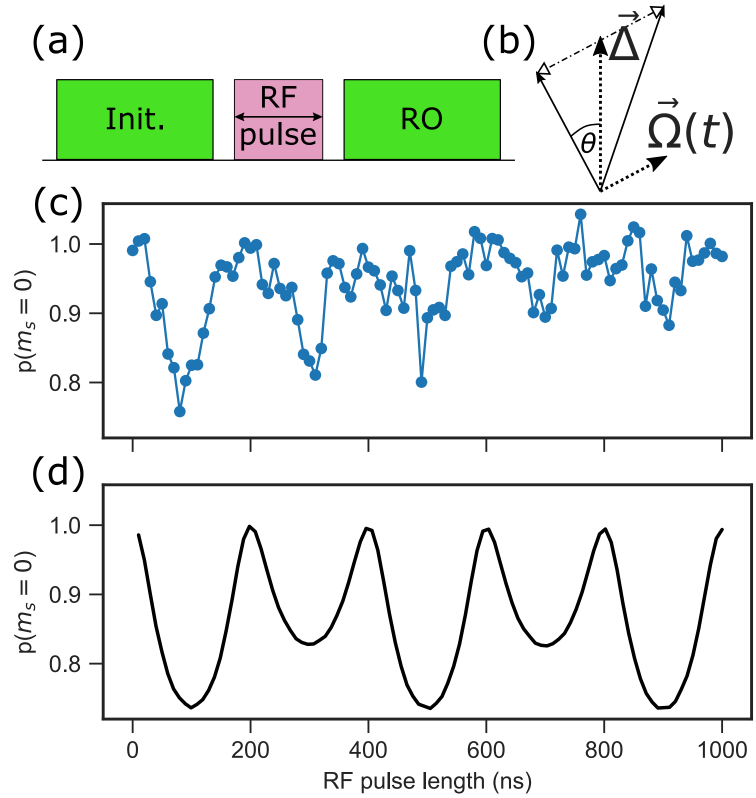

Figure 5.10: Modulation of the NV state by the RF pulses. (a) The applied pulse sequence: A laser pulse first polarizes the state to $|0\rangle$, an RF pulse that is very off-resonant is applied for varying durations, and another laser pulse reads out the spin state and repolarizes the spin. (b) Schematic depiction of the magnetic field vectors. The total field oscillates between the two solid arrows, $\vec{\Delta} \pm \vec{\Omega}$, along the dashed-dotted line. The spin state follows the field's direction. (c) Measurement of the sequence in (a), demonstrating the modulation of the spin state. (d) Simulation of the pulse sequence, which shows qualitative agreement with the measurement.

ner. Fig. 5.10(b) depicts the evolution of the magnetic field vector over time. The vector oscillates between $\vec{\Delta} \pm \vec{\Omega}$ along the axis marked by the dash-dot line.

Fig. 5.10(c) shows data from a measurement of the NV spin state modulation as a result of an intense off-resonant RF pulse ($\omega_{rf} = 2\pi \times 2.5\,\mathrm{MHz}$, $B_{rf} \approx 124\,\mathrm{G}$), with $\phi_{rf} = 0$, compared to a simulation of this sequence. Significant modulation of the NV spin state due to the RF pulse is observed, with the simulation qualitatively fitting the experiment during the initial 400 ns. After that, dephasing induced by the driving field's noise dominates the signal (this effect was not incorporated in the simulation).

Two leading conclusions from this experiment and analysis are that (a) the RF pulse modulates the state coherently, and (b) the initial NV state is recovered when the driving pulse ends with the signal at zero. For a rectangular pulse with $\phi_{rf} = 0$, this occurs periodically at half the period of the RF frequency, i.e., for $t = \pi n/\omega_{rf}$, $n \in \mathbb{N}$. I implemented these observations in the proton driving experiments (Fig. 5.6) by applying signals with $\phi_{rf} = 0$ and sample at half the period of the RF frequency.

In the ^{15}N driving experiments, I used an alternative approach based on smooth pulse envelopes to ensure that the driving signal ends at zero at any given pulse duration and ϕ_{rf}.

SMOOTH PULSE ENVELOPES

Utilizing a smooth pulse envelope is an alternative approach to mitigate sensor noise due to RF pulses. “Smooth” means that the pulse envelope does not have rapid variations compared with the signal’s frequency, unlike the standard rectangular pulse envelope. In what follows, I show that these are crucial when applying strong driving fields.

There are various smooth pulse envelopes, such as Gaussian or sine envelopes. Here, I chose an error-function pulse envelope, which has been employed previously in this context[177]:

$$\varepsilon_{erf}(t) = \frac{1}{2}\left(\mathrm{erf}\left(2\frac{t-(t_0+\delta t)}{\delta t}\right) - \mathrm{erf}\left(2\frac{t-(t_1-\delta t)}{\delta t}\right)\right) \tag{5.10}$$

where t_0 (t_1) are the pulse’s start (end) times, and δt is the rise and fall time of the envelope. Mathematically, error-function envelopes are always continuous. Practically, a minimal rise and fall time is needed. To illustrate, let us consider that if δt is much shorter than the sensor’s Larmor period, it effectively behaves as a rectangular pulse. Thus, the pulse envelope’s variation should be *slow* compared to a relevant timescale. In this case, the rise time must be much longer than the NV center’s Larmor period, i.e., $\Delta \times \delta t \gg 1$. Another constraint is the limited bandwidth of the antenna, which is much lower than the NV center’s Larmor frequency (22 MHz vs. 1.4 GHz). So, I set $\delta t > 300$ ns, which satisfies both conditions.

The advantage of the smooth error-function pulse envelopes is exemplified in Fig. 5.11, which compares an ^{15}N driving experiment with a rectangular pulse envelope and a slowly rising error-function pulse envelope. The rectangular pulses were set with $\phi_{rf} = 0$ and sampled at half-period of the driving frequency. The two traces were taken with the same driving amplitude. It is evident that the measured trace for the rectangular pulse is much more noisy. The reason that the rectangular pulses induce such a noisy result may be attributed to a ringing effect of the antenna, whereby an RF field persists for a short time after the pulse ends. This noise may be attributed to the ringing’s effect on the driven nuclear spin or the sensor spin. A smooth pulse envelope assists in mitigating this issue, and its benefits are evident from this example.

5.7 DISCUSSION AND CONCLUSIONS

In this chapter, I discussed the strong driving of nuclear spins in the nanoscale for quantum sensing with NV centers. Strong driving may be applied on target spins in nanoscale NMR or ancilla qubits in the diamond around the NV sensor. To enable the strong driving of nuclear spins, we developed a broadband spiral antenna tailored for quantum sensing experiments with NV centers. The antenna’s bandwidth suits nuclear spins at fields up to 0.5 T. The antenna was characterized using *in-situ* DC magnetometry with NV centers, showing that the antenna boasts a field-to-current ratio of (116 ± 3) G. This is in good agreement with theoretical calculations and finite element simulations. The field-to-current ratio of the spiral antenna is three-fold better than the state-of-the-art, and the field-to-power ratio is over ten-fold better[172]. Thus, owing to a low field-to-current ratio, it is possible to drive spins at appreciable driving frequencies with low power con-

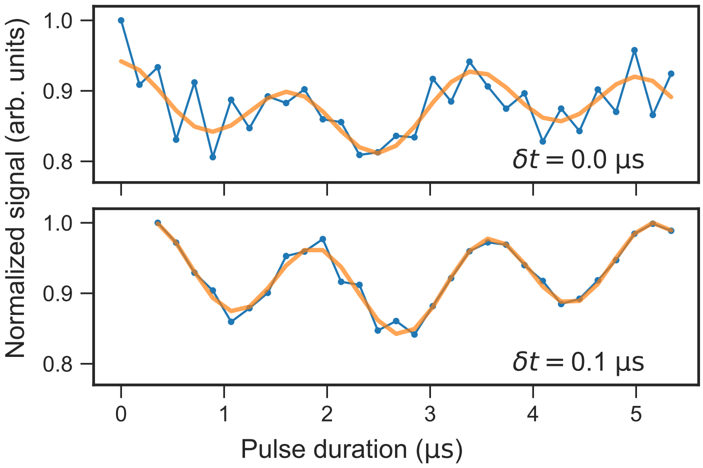

Figure 5.11: Rectangular pulses vs. a smooth pulse envelope. Rabi oscillations of ^{15}N under an RF driving pulse with a rectangular pulse shape (top) and an error function pulse envelope (bottom). The error function is configured with a rise and fall time $\delta t = 0.1\,\mu$s. Blue circles are the experimental data, and the solid orange line is a double-sine fit to guide the eye.

sumption, e.g., a Rabi frequency of over 100 kHz requires <2.5 W input power, making it especially appropriate for sensitive samples or cryogenic environments.

Using the antenna, ^{1}H spins in an immersion oil sample on the diamond were driven at over 500 kHz, faster than previously reported. I further demonstrated the antenna by driving the NV center's nitrogen nuclear spin, commonly used as a quantum memory qubit for repetitive readout or to prolong the sensing time. The NV's ^{15}N spin was driven at rates of over 700 kHz, and I estimated the effective gyromagnetic ratio to be (7.36 ± 0.15) kHz/G, in good agreement with simulations and previous reports. At the strongest driving fields, the NV-^{15}N electron-nuclear spin system entered a nonlinear regime, where the Rabi frequency to driving field ratio deviated from a linear trend, as predicted by our simulations.

I further discussed the impact of the strong nuclear spin driving on the NV sensor state. I demonstrated the benefit of a smooth pulse envelope to mitigate the sensor noise, which was implemented in the ^{15}N driving experiments.

The results shown here constitute an important contribution to studying fast nuclear spin manipulation. Fast manipulation by strong driving will help facilitate nanoscale NMR experiments with NV centers and enable experiments where the sensing time is limited and requires fast manipulation pulses.

6

Optimal spin manipulation by strong and tilted drives

THE PREVIOUS CHAPTER DISCUSSED AN EXPERIMENTAL SYSTEM FOR FAST AND COHERENT SPIN MANIPULATION. THIS RELIES ON CONTROL FIELDS IN A REGIME WHERE THE DRIVING STRENGTH Ω_d APPROACHES THE ENERGY SPLITTING (I.E., $\Omega_d \lesssim \omega_0$). Alongside the experimental challenges of producing strong driving fields, working in this regime poses a theoretical control challenge. In this chapter, I present a novel theoretical approach to optimize the fidelity of control pulses from strong and tilted driving, which is particularly suitable for driving fields that are noisy or not fully characterized.

The work shown in this chapter was done in collaboration with the group of Prof. Alex Retzker of the Racah Institute of Physics, the Hebrew University of Jerusalem. The offset-sine pulses theory was developed with Alon Salhov, and Dr. Ido Schaefer derived the optimal control theory waveforms. This study forms part of a manuscript titled "Coherent manipulation of nuclear spins in the strong driving regime ", published in the New Journal of Physics[166].

6.1 BACKGROUND

The precision of a quantum operation on a qubit is crucial for quantum technologies, and much effort has been devoted to optimizing the fidelity of control pulses. Quantum computing algorithms involve a series of operations on several qubits, so operation errors accumulate. Quantum error correction codes may correct these errors if the physical qubits' error rate does not surpass a code-dependent threshold, known as the fault-tolerance threshold. Currently, the minimal fidelity for fault-tolerant quantum computation is 0.9925[186,187]. There is no similar fundamental threshold for the operation fidelity in quantum sensing. Here, the relevant measure is the sensitivity of a sensor, the minimal detectable signal per unit time. The sensitivity's dependence on the fidelity depends on the protocol but is roughly proportional to the pulse fidelity. It is thus essential to optimize pulses so that they achieve maximal fidelity.

The issue of strong driving has attracted interest, especially for quantum information processing, where intense driving can accelerate operations and increase the speed of quantum processors[188,189]. Optimal control theory (OCT) strategies have been employed to optimize quantum control in a strong driving regime. In particular, the concept of time-optimal control fields[190] has been introduced to identify the shortest possible signals to control a qubit state[191,192]. Studies demonstrated that bang-bang control sequences are the quickest form, and bang-bang driving at rates exceeding the energy splitting (ω_0) has been demonstrated on solid-state qubits[193]. Other OCT-derived waveforms have also been demonstrated for solid-state qubit controls[194].

OCT approaches require a precise description of the driving field and the qubit. Namely, a precise description of the Hamiltonian is required to formulate an optimal control signal, e.g., the B_0 field and relative orientation and magnitude of the driving (the $\vec{B}_1$ vector). Errors in the estimated parameters will lead to lower performance compared to the initial forecast by simulations[194]. It is possible to optimize the OCT signal by *in situ* optimization (either closed- or open-loop). However, as OCT signals are generally based on waveforms with many degrees of freedom, the parameter space is complex, so that the optimization may be resource-intensive in terms of time and computation. Thus, from an experimental point of view, it is valuable to contract the parameter space by identifying a few parameters to optimize.

The antenna presented in Chapter 5 generates a field that is tilted away from the ideal driving plane of the NV center (i.e., $\theta_d > 0$). In Chapter 5, the angle for a case of the typical (100)-cut diamonds was discussed, but the drive would also be tilted for the more exotic (111), (110) diamonds. In general, most solid-state qubit experiments featured a tilted drive, as without dedicated engineering of the antenna, the drive vector would not lie within the plane transverse to the quantization axis (from now on referred to as $\hat{z}$). Tilted drives are found in various solid-state spin qubit systems in addition to the NV center in diamond, such as the SiV defect in diamond[195], defects in SiC[196] and h-BN[197]. Tilted drives are also characteristic of superconducting flux qubits[198]. However, to our knowledge, optimizing strong tilted drives has not been discussed in the literature. Thus, formulating an optimal control protocol that suits strong tilted drives is of particular value.

6.2 The rotating wave approximation of a tilted drive Hamiltonian

Quantum operations on spin qubits are usually applied using resonant RF control fields. The control fields are mostly linearly polarized, and, as previously mentioned, they are often tilted away from the ideal driving plane, the plane transverse to the spin's quantization axis (denoted as the *xy*-plane). Quantum operations are usually analyzed by transforming into a rotating frame of reference.

The following lab-frame Hamiltonian describes a two-level system driven by a tilted driving field:

$$\mathcal{H} = \frac{\omega_0}{2}\sigma_z + \Omega_d f(t)\left(\sigma_x + \tan\left(\theta_d\right)\sigma_z\right) \tag{6.1}$$

where ω_0 is the energy splitting of the two-level system, Ω_d is the maximum driving field amplitude, $|f(t)| \leq 1$ is the waveform, and $\theta_d \in \left[0, \frac{\pi}{2}\right)$ is the driving field's tilt angle from $\hat{x}$. Fig. 6.1(a) depicts the setting. Under this definition, the drive vector is not normalized; the field's magnitude depends on the angle θ_d.

Let us consider a simple sine drive waveform that is resonant with the qubit's transition:

$$\mathcal{H} = \frac{\omega_0}{2}\sigma_z + \Omega_d \sin\left(\omega_0 t + \phi_d\right)\left(\sigma_x + \tan\left(\theta_d\right)\sigma_z\right) \tag{6.2}$$

By applying a rotating frame transformation to the Schrödinger equation at the frequency of the drive, $U = \exp\left(i\frac{\omega_0 t}{2}\sigma_z\right)$, we obtain the rotating frame Hamiltonian (see full derivation in Appendix A.1):

$$\begin{aligned}\mathcal{H}_{rot} = {} & \frac{\Omega_d}{2}\left(\sin\left(\phi_d\right)\sigma_x - \cos\left(\phi_d\right)\sigma_y\right) + \\ & + \frac{\Omega_d}{2}\left(\sin\left(\omega_0 t + \phi_d\right)\sigma_x + \cos\left(\omega_0 t + \phi_d\right)\sigma_y\right) + \\ & + \Omega_d \sin\left(\frac{\omega_0 t}{2} + \phi_d\right)\tan\left(\theta_d\right)\sigma_z\end{aligned} \tag{6.3}$$

The timescale $1/\Omega_d$ will determine the dynamics. Thus, for weak driving strengths ($\Omega_d \ll \omega_0$), the second term, known as the counter-rotating term, may be neglected because it varies rapidly compared to the timescale. The contribution of the counter-rotating term will average out periodically on the timescale of $1/\Omega_d$. For the same reason, we can neglect the last term, the longitudinal term. This is known as the rotating-wave approximation (RWA), and we get the RWA Hamiltonian:

$$\mathcal{H}_{RWA} = \frac{\Omega_d}{2}\left(\sin\left(\phi_d\right)\sigma_x - \cos\left(\phi_d\right)\sigma_y\right) \tag{6.4}$$

Under the RWA, the dynamics are well approximated by sinusoidal state transitions, known as Rabi oscillations[199]. The first-order correction to the RWA is known as the Bloch-Siegert shift[200], which adds to the first term of the rotating frame Hamiltonian (Eq. 6.4) a σ_z term proportional to $\left(\Omega_d/\omega_0\right)^2$. The Bloch-Siegert shift accounts for slight shifts to the expected resonance frequency in an otherwise undistorted resonance curve, which arise when driving fields are not perfectly circular. This correction is sufficient when $\Omega_d \ll \omega_0$ or for nearly circular driving fields. Higher-order corrections are necessary for a linear driving field with $\Omega_d \lesssim \omega_0$. In this regime, the deviations from an ideal drive (that is, a non-ideal drive with linear polarization that has a longitudinal component) will markedly alter the dynamics[171]. Without proper adaptations, this "breakdown" of the RWA results in the deterioration of pulse fidelity. Thus, designing the signals to optimize an operation's fidelity in a strong driving regime is crucial.

6.3 RESONANT OFFSET-SINE DRIVING PULSES

In what follows, I describe a straightforward approach to generate control signals in the $\Omega_d \lesssim \omega_0$ regime for high-fidelity operations. It is shown that optimizing just one or two parameters of a simple sine signal with an offset may provide sufficient fidelity in this regime. Thus, we termed it "offset-sine" pulses. The approach is motivated analytically using a clear physical picture, and I illustrate its validity numerically and compare it to optimal control-derived signals. I argue that the offset-sine signals bear benefits over optimal control-derived signals while providing similar and sufficiently high fidelity rates. The focus is on the optimization of the π-pulse, which is to be reached at $t_\pi \sim \frac{\pi}{\Omega_d}$ (a precise definition follows below).

In the weak-driving regime, the significance of the drive phase ϕ_d is in determining the axis of the static term in the rotating-frame Hamiltonian (Eq. 6.4). The counter-rotating term will add a slight dependence on ϕ_d that may slightly impact the pulse fidelity, but for very weak drives ($\Omega_d \ll \omega_0$), this will be negligible. In contrast, in the strong-driving regime ($\Omega_d \lesssim \omega_0$) the dynamics depends on ϕ_d to a growing extent as Ω_d approaches ω_0. The dependence is introduced via the counter-rotating and longitudinal terms, which we neglected under the RWA: as Ω_d increases, the oscillations at ω_0 are no longer fast compared to Ω_d. Alternatively, we can base this on the observation that finite-duration sine waveforms contain a DC component. This becomes evident when inspecting the zero-frequency Fourier component of the pulse:

$$\frac{2\Omega_d}{\pi}\int_0^{\pi/\Omega_d} \sin\left(\omega_0 t + \phi_d\right) \mathrm{d}t = \frac{4\Omega_d}{\pi\omega_0}\sin\left(\pi\omega_0/2\Omega_d + \phi_d\right)\sin\left(\pi\omega_0/2\Omega_d\right) \tag{6.5}$$

Here, we calculated the term for a π-pulse of duration $t_\pi = \pi/\Omega_d$, which defines a π-pulse in the weak driving regime. The sine functions give a value bounded by ±1, while the coefficient scales as Ω_d/ω_0; thus, this term is negligible for $\Omega_d \ll \omega_0$. However, this is no longer negligible for $\Omega_d/\omega_0 \sim 1$, and the value for a fixed Ω_d will oscillate with ϕ_d. Interestingly, this DC component vanishes for $\Omega_d = \omega_0/2n,\ n \in \mathbb{N}$, a feature discussed later. In any case, this observation suggests that the RF phase will act as an important degree of freedom, which controls the contribution of this DC component. The interplay between the different terms of the Hamiltonian offers flexibility for pulse fidelity optimization.

Utilizing the phase ϕ_d is a potential route to mitigate the effects of the counter-rotating term in the $\Omega_d \lesssim \omega_0$ regime and thus optimize pulse fidelity rates in this regime. It should be noted that the phase of the driving field was shown to be important in the strong driving regime in NMR more than five decades ago[201]. More recently, the phase's effect was shown in single solid-state qubit experiments[202,203] and NMR[204]. However, the phase has not been discussed in the context of tilted drives.

Let us also consider the particular case of driving at an amplitude of $\Omega_d = \frac{\omega_0}{2\tan(\theta_d)}$. In this case, a constant (DC) waveform equal to -1 yields an ideal driving Hamiltonian $\mathcal{H} = \Omega_d\sigma_x$. This motivates us to consider an additional DC offset to the drive, serving as another DC component that may be controlled to optimize the pulse. To my knowledge, DC offsets have not been considered in this context.

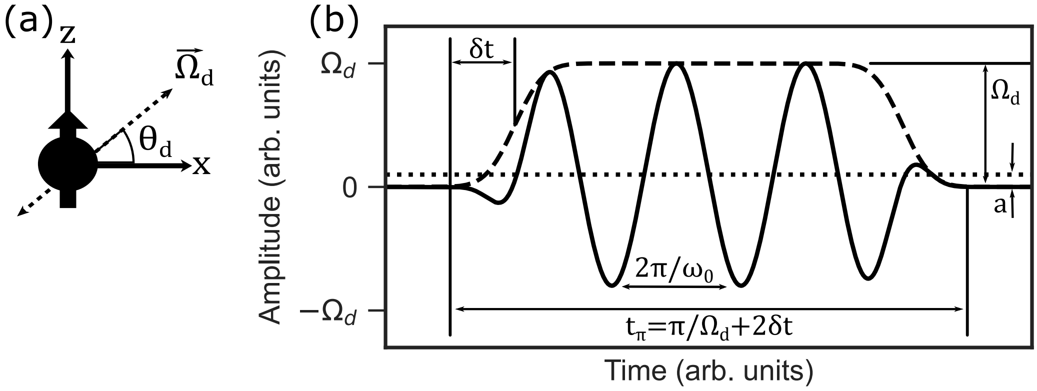

Figure 6.1: Notations of strong driving pulses. (a) The spin is quantized along $\hat{z}$, and the driving vector is tilted away from $\hat{x}$ by an angle θ_d. (b) The pulse is described by a sine multiplied by an envelope function (dashed curve), in this case, an error function envelope. δt is the envelope's rise time (time to reach half the maximal amplitude). Ω_d is the maximal driving amplitude; a is the DC offset from zero of the sine's base (dotted line); The signal frequency is the Larmor frequency ω_0; t_π is the total pulse duration.

These observations motivate us to consider waveforms $f(t)$ based on an "offset-sine" waveform:

$$f(t) \equiv \varepsilon(t)\left(a + (1 - |a|)\sin\left(\omega_0 t + \phi_d\right)\right) \tag{6.6}$$

where the optimization parameters are $|a| \leq 1$ (the DC offset component) and ϕ_d (the phase). $\varepsilon(t)$ is a pulse shaping envelope function. For $a = 0$, we obtain a standard sine (symmetric around 0), while for $|a| = 1$, we get a constant DC drive pulse (shaped into a pulse by the envelope $\varepsilon(t)$).

Error-function pulse envelope

In Eq. 6.6, the pulse's envelope function $0 \leq \varepsilon(t) \leq 1$ was introduced. By definition, it is zero at the pulse edges ($\varepsilon(t_0) = \varepsilon\left(t_{pulse}\right) = 0$). A simple rectangle function (i.e., rectangular pulse shape) is often used as the envelope for weak driving. However, as realistic transmission lines always have limited bandwidth, a discontinuous $\varepsilon(t)$ will result in a distorted signal, and this distortion is significant for strong and short pulses. A smooth envelope function with finite rise and fall times can fit the signal into a prescribed bandwidth[45] and also mitigate sensor noise, as discussed also in Section 5.6. For the sake of this discussion, I focus on an error-function pulse envelope[177]. I rewrite here the term for the error-function envelope for clarity:

$$\varepsilon_{erf}(t) = \frac{1}{2}\left(\operatorname{erf}\left(2\frac{t - (t_0 + \delta t)}{\delta t}\right) - \operatorname{erf}\left(2\frac{t - (t_1 - \delta t)}{\delta t}\right)\right) \tag{6.7}$$

t_0 is the pulse start time, t_1 is the pulse end time, and δt is the pulse rise (fall) time. Since we assume $t_1 - t_0 \gg 2\delta t$, the envelope function satisfies: $\varepsilon_{erf}(t_0 + \delta t) = \varepsilon_{erf}(t_1 - \delta t) = 0.5$. Fig. 6.1(b) depicts an offset-sine pulse and its different parameters.

Defining π-pulse duration

I define the π-pulse duration according to its definition for the weak-driving regime - $\Omega_d \ll \omega_0$. For simplicity, let us consider the rotating-frame Hamiltonian (Eq. 6.4) of a rectangular pulse, such that $\mathcal{H}_{RWA} = -\frac{\Omega_d}{2}\sigma_y$ is constant in time. We choose $\phi_d = 0$ and assume the system is initialized to $|\uparrow\rangle$, without loss of generality. A full state transfer is achieved for a π rotation about $\hat{y}$, and its duration is denoted by t_π:

$$|\downarrow\rangle = \exp\left(-i\int_0^{t_\pi} \mathrm{d}t\mathcal{H}_{RWA}(t)\right)|\uparrow\rangle \exp\left(i\frac{\Omega_d t_\pi}{2}\sigma_y\right)|\uparrow\rangle \tag{6.8}$$

The exponent in the last term is a rotation about $\hat{y}$ $\left(R_y(\alpha) \equiv \exp\left(i\frac{\alpha}{2}\sigma_y\right)\right)$ by an angle of $\Omega_d t_\pi$. A full state transfer is achieved for a rotation by an angle of π, from which we get the definition:

$$t_\pi \equiv \frac{\pi}{\Omega_d} \tag{6.9}$$

For a general pulse envelope, $\mathcal{H}_{RWA} = -\varepsilon(t)\frac{\Omega_d}{2}\sigma_y$. In this case, let us define a π-pulse by a criterion on the pulse's envelope $|\varepsilon(t)| \leq 1$, to yield a similar result upon the integrating:

$$\int_0^{t_\pi} \mathrm{d}t\mathcal{H}_{RWA}(t) = -\frac{\Omega_d\sigma_y}{2}\int_0^{t_\pi}\varepsilon(t)\,\mathrm{d}t = -\frac{\pi}{2}\sigma_y \tag{6.10}$$

$$\rightarrow \int_0^{t_\pi}\varepsilon(t)\,\mathrm{d}t \equiv \frac{\pi}{\Omega_d} \tag{6.11}$$

The integral over the error-function envelope as defined in Eq. 6.7[a]:

$$\int_0^{t_\pi}\varepsilon_{erf}(t)\,\mathrm{d}t \approx \int_{-\infty}^{\infty}\varepsilon_{erf}(t)\,\mathrm{d}t = t_1 - t_0 - 2\delta t \tag{6.12}$$

and it is equated to $\frac{\pi}{\Omega_d}$ By defining the pulse duration as $t_\pi = t_1 - t_0$, the definition for the duration of a π-pulse with an error-function envelope is obtained:

$$t_\pi = \frac{\pi}{\Omega_d} + 2\delta t \tag{6.13}$$

6.4 OPTIMIZING CONTROL PULSES BASED ON THE OFFSET-SINE WAVEFORM

I demonstrate the performance of the offset-sine waveforms by numerically calculating the state evolution of a qubit under such a drive Hamiltonian (Eq. 6.1 and Eq. 6.6). Example driving amplitudes of $\Omega_d = \frac{\omega_0}{10}, \frac{\omega_0}{3}, \omega_0$ are considered. I focus on π-pulses, i.e., flipping the initial state $|\uparrow\rangle$ with the goal of maximizing the probability for $|\downarrow\rangle$. Still, a similar demonstration may be done on $\pi/2$-pulses, and so forth. As an illustration, I chose parameters inspired by the spiral antenna of Chapter 5, namely, a drive tilt of $\theta_d = 35.3°$, and limit the signals to a bandwidth of $\lesssim \frac{\omega_0}{10}$ using an error-function envelope with a rise-time $\delta t = \frac{\pi}{10\omega_0}$. The pulse durations are extrapolated from the weak driving regime and set to be $t_\pi = \frac{\pi}{\Omega_d} + 2\delta t$. Achieving a full state flip is possible in shorter pulse duration for $\Omega_d \sim \omega_0$ [171]; however, the parameter space was limited by fixing the pulse duration to this value.

---

[a] For $\delta t < \frac{t_1 - t_0}{4}$, $\int_0^{t_\pi}\varepsilon_{erf}(t)\,\mathrm{d}t / \int_{-\infty}^{\infty}\varepsilon_{erf}(t) > 0.99985$. Thus, the infinite integral is a valid approximation.

I performed numerical calculations using QuTiP, a Python package for simulating quantum dynamics[205]. All calculations were done by propagating a lab-frame Hamiltonian as defined in Eqs. 6.1 and 6.6, using an arbitrary value $\omega_0 = 2\pi \times 280\,\mathrm{MHz}$. Driving strengths were defined in proportion to ω_0. All relaxation processes were neglected.

The final state fidelity was calculated according to the following:

$$\mathcal{F} = |\langle \psi(t_\pi) \mid \downarrow \rangle|^2 = \frac{1}{2} - \frac{1}{2}\langle \sigma_z \rangle \tag{6.14}$$

Where appropriate, the results were recorded in terms of infidelity, $1 - \mathcal{F}$, to contrast the results between different parameters.

I numerically calculate the pulse fidelity under the driving field for each driving amplitude, sampling various phase (ϕ_d) and offset (a) values. The results are presented in Fig. 6.2 (top row) in terms of infidelity. Fig. 6.2 (center row) shows the state evolution for various driving signals at the driving amplitude of the corresponding column. Evolutions are shown for various phases at zero-offset ($a = 0$, light gray curves), with the zero-offset phase yielding the best (worst) pulse fidelity marked by dashed (dotted) curves. Evolutions under an optimal offset-sine drive are marked by red curves. The optimal offset-sines have offset and phase corresponding to the coordinates of minimum infidelity in the diagrams of the top row, i.e., the brightest points. The bottom row shows the waveforms corresponding to the different state evolutions in the center row.

The center row of Fig. 6.2 illustrates how increasing the driving strength Ω_d from $\frac{\omega_0}{10}$ to ω_0 leads to increasing deviation from the standard sinusoidal evolution characteristic of the RWA. For the stronger drive amplitudes, adjusting the drive phase ϕ_d is crucial: for the extreme case of $\Omega_d = \omega_0$, a correct choice of drive phase ϕ_d will yield $\mathcal{F} \approx 0.94$, while the worst choice returns to the initial state ($\mathcal{F} \approx 0$). This demonstrates how the drive phase is a single optimization parameter to optimize intense drive pulses and obtain pulse fidelities over 0.9, sufficient for quantum sensing tasks. The optimal choice of phase would depend on the driving amplitude and envelope function[206].

Optimization of the DC offset, in addition to the phase, significantly impacts the final state fidelity for the highest drive amplitudes. For example, at $\Omega_d = \omega_0$, adding a proper offset will increase the fidelity to $\mathcal{F} > 0.999$, beyond the fault-tolerance threshold for some quantum computer architectures[186,187].

The DC offset was introduced as a novel optimization parameter, which may be significant, particularly for a driving field tilted by θ_d from $\hat{z}$. The drive tilt is an additional resource: a tilted drive can achieve higher fidelities than driving fields purely along $\hat{x}$ when both the phase and offset are optimized. This is evident in Fig. 6.3(a)-(c), where the pulse fidelity for an optimal offset-sine is shown for a range of driving field tilts, starting from an ideal field along $\hat{x}$ ($\theta_d = 0$) up to a field along $\hat{x} + \hat{z}$ ($\theta_d = 45°$). For drives with a tilt angle $\theta_d \lesssim 15°$, phase optimization is sufficient to achieve fidelities over 0.999 even for a drive $\Omega_d = \omega_0$. However, for the strongest drives, optimizing the pulse's DC offset is needed at drive tilts of $\theta_d > 15°$.

Fig. 6.3(d) compares phase-only optimization with phase and offset optimization for a driving field tilted at $\theta_d = \arccos\left(\sqrt{\frac{2}{3}}\right) \approx 35.3°$, the same value used in Fig. 6.2). The comparison is shown over a range of driving strengths $\omega_0/10 \leq \Omega_d \leq \omega_0$. Optimizing only the phase yields fidelity of

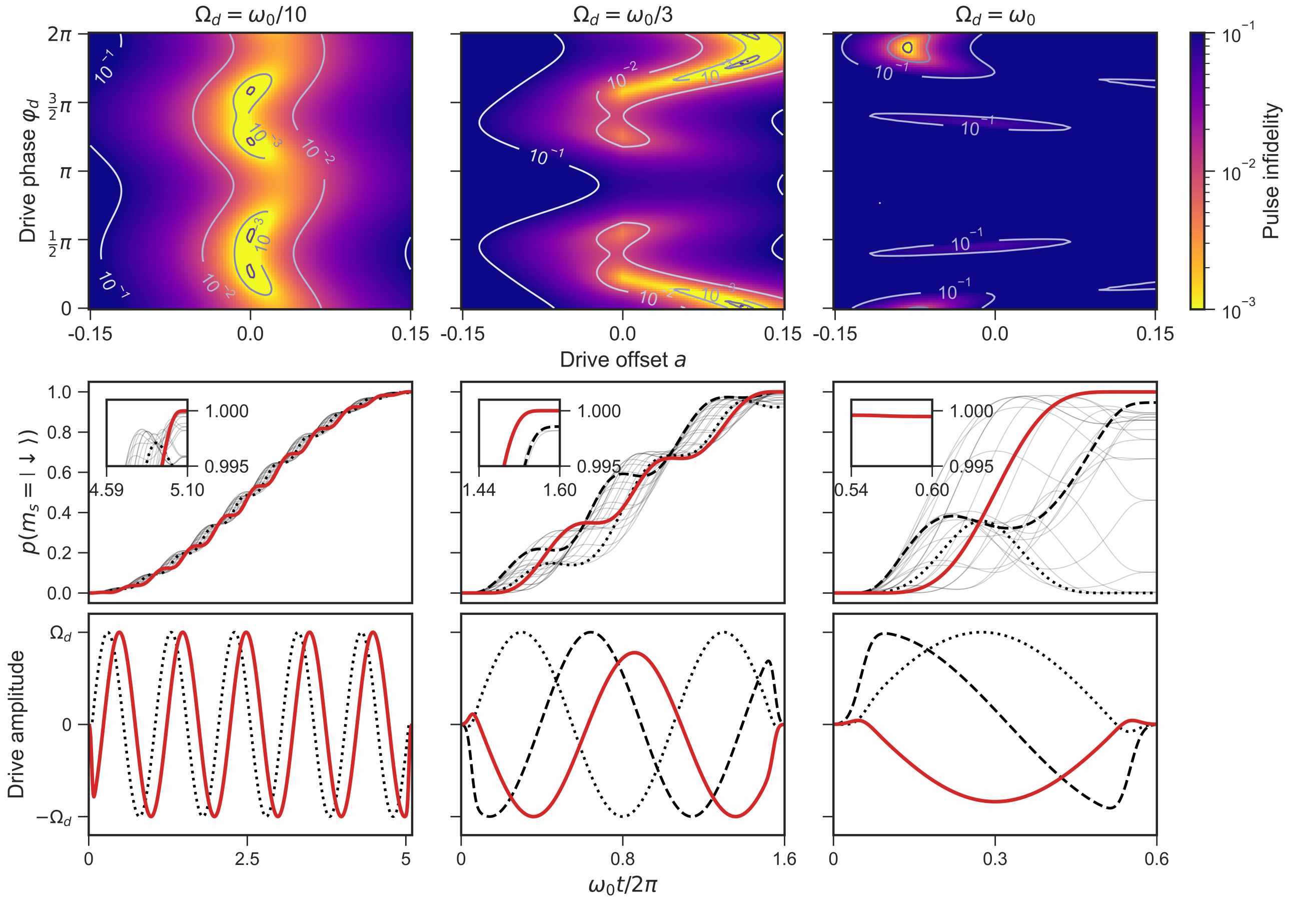

Figure 6.2: Optimizing offset sine π-pulse drives at different driving strengths. Top row: Calculating pulse infidelity for several driving strengths Ω_d as a function of pulse drive phase ϕ_d and offset a. Center row: spin state evolution for pulses at the corresponding drive strengths. Trajectories for many values of ϕ_d at $a = 0$ are shown in light curves. The best (worst) ϕ_d values for $a = 0$ are marked by dashed (dotted) curves. Evolution for pulses with both optimal phase and offset are shown by solid red curves. Insets focus on the pulses' ends to highlight the final fidelity for each case. Bottom row: the waveforms corresponding to the trajectories drawn in the center row, with matching curve format.

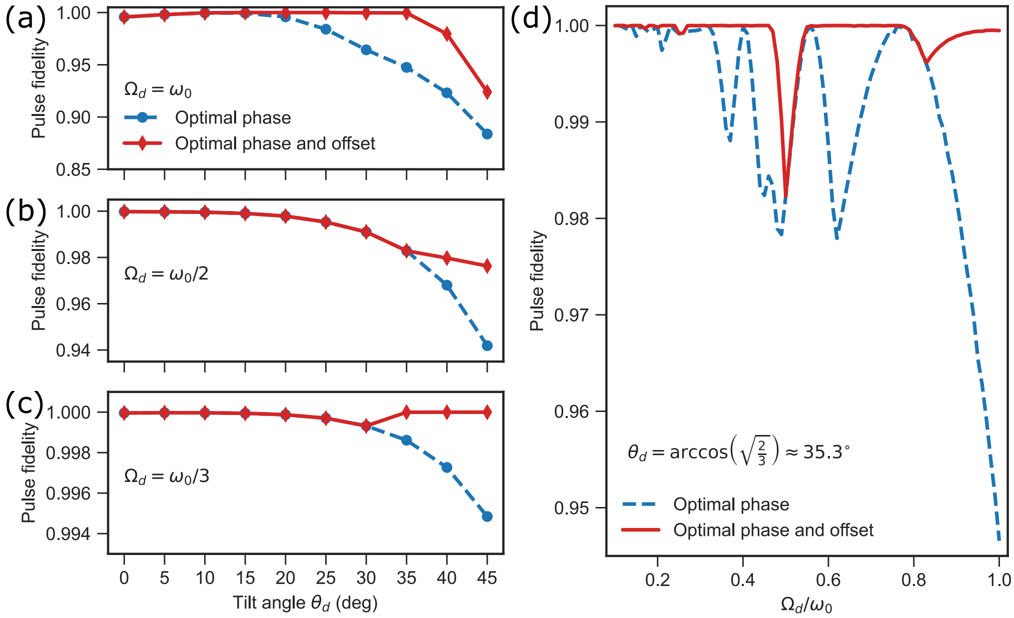

Figure 6.3: Fidelity of optimized offset-sine pulses over different parameters. (a)-(c) Fidelity of optimal offset-sine π-pulses as a function of the drive tilt angle for $\Omega_d = \omega_0,\ \omega_0/2,\ \omega_0/3$, comparing only phase optimization at zero offset, and optimizing the phase and offset. (c) Fidelity of optimal offset-sine pulses at a drive tilt of $\theta_d \approx 35.3^\circ$ as a function of drive amplitude Ω_d.

over 0.94 for all values, while DC offset optimization is crucial for achieving fidelity rates of over 0.999 for most driving amplitudes.

Interestingly, $\Omega_d = \omega_0/2$ exhibits a singularity, and to lesser extent $\Omega_d = \omega_0/4$. This may be attributed to the fact that, for $\Omega_d = \omega_0/2n,\ n \in \mathbb{N}$, the zero-frequency Fourier component (DC component) vanishes (Eq. 6.5). This effect becomes more significant as θ_d increases, as is evident from Fig. 6.3(b), which further supports the interpretation of an interplay between the pulse's DC component and the longitudinal component of the drive. The fidelity may be optimized by incorporating a DC offset (red curve in the figure). Then, the optimized offset-sine fidelity, $\mathcal{F} \approx 0.98$, is sufficient for many applications, such as quantum sensing. Otherwise, it could be overcome by avoiding the singularity by slightly changing the drive amplitude.

6.5 COMPARING WITH OPTIMAL CONTROL THEORY SIGNALS

The offset-sine optimization strategy is compared with control signals generated by quantum optimal control theory (OCT)[207,208,209,210,211]. In OCT, the optimization task is formulated as a functional object maximization using variational calculus. This yields a set of control equations, which are solved numerically by optimization algorithms. The optimization target is the maximization of the occupation of $|\downarrow\rangle$ at a predefined final time, $t_\pi = \frac{\pi}{\Omega_d} + 2\delta t$, as defined previously.

Additional restrictions were added to the control problem to generate realistic waveforms, which are also comparable to the previously discussed offset-sine waveforms. First, the total energy of the drive was restricted to keep the peak amplitude in the region of a defined Ω_d. Second, the spectral composition of the drive was restricted to $< 10\omega_0$, analogous to the restriction imposed by the previously mentioned error-function envelope. Lastly, the waveform's amplitude and time

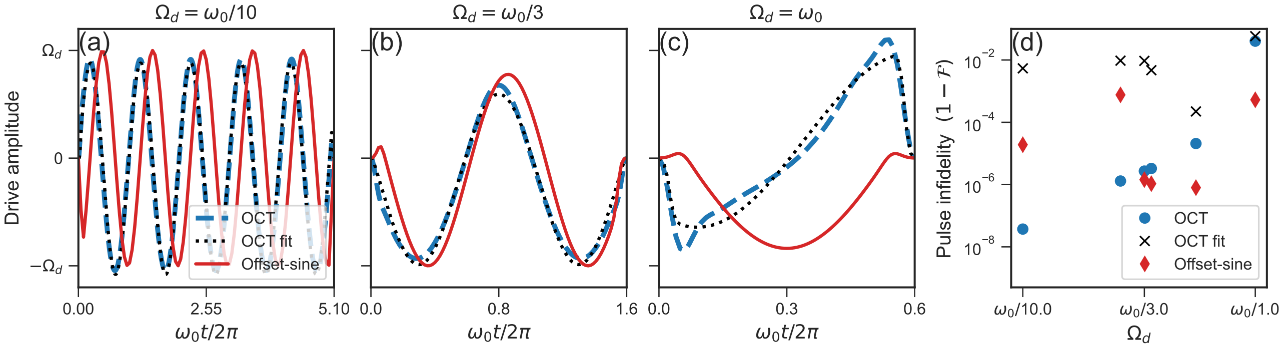

Figure 6.4: Comparing OCT drive signals with offset sine drives. (a)-(c) Drive signals for different drive strengths Ω_d denoted above the plots, corresponding to different pulse durations $t_\pi = \frac{\pi}{\Omega_d} + 2\delta t$. The blue dashed curves are OCT waveforms. The dotted black curves are approximations of the OCT waveform by an offset-sine obtained by least-square fitting (OCT fit). The solid red curves are optimized offset-sine waveforms. (d) Infidelity rates of the driving signals for each of the shown waveforms.

derivative at the pulse edges were set to zero to ensure a smooth shape (further details on the OCT methods appear in the supplement material of our publication[166]).

The optimization problem was solved for similar parameters as before: a drive tilt of $\theta_d = 35.3°$, at driving amplitudes of $\Omega_d = \omega_0, \frac{\omega_0}{1.8}, \frac{\omega_0}{2.8}, \frac{\omega_0}{3}, \frac{\omega_0}{3.8}, \frac{\omega_0}{10}$. However, it should be clarified that as the restriction was imposed on the energy (and not amplitude), the actual waveforms deviated slightly from the maximal amplitude values.

I compared the OCT signals with two forms of offset-sine signals. First, I generated an approximation to the OCT signal, obtained by a least-square fitting of the OCT signal to Eq. 6.6. Second, I compared the OCT signal to the optimal offset-sine obtained by optimizing the offset and phase for the same parameters. These are the optimal waveforms depicted by solid red curves in Fig. 6.2(bottom row). Signals for $\Omega_d = \omega_0, \frac{\omega_0}{3}, \frac{\omega_0}{10}$ are presented in Fig. 6.4(a)-(c). The fitted offset-sine closely approximates the OCT-generated signals well, especially for the case of $\Omega_d = \omega_0/10, \omega_0/3$. Although a qualitative observation, it further supports the offset-sine approach.

A quantitative comparison is found in Fig. 6.4(d). The figure compares the pulse fidelity rates for the different signals: OCT, offset-sines approximation of the OCT, and an optimized offset-sine (for clarity, the data is presented in terms of infidelity $1-\mathcal{F}$). The optimized offset-sine signals differ from the OCT signals but provide comparable fidelity rates, with $\mathcal{F} > 0.999$. Interestingly, for the highest drive amplitude considered here, the fidelity rate of the optimized offset-sine even surpasses that of the OCT signal. While the difference ($< 10^{-6}$ vs. 2×10^{-5}) presumably stems from the optimization procedure, it highlights the performance of the optimized offset-sine waveforms.

6.6 CHALLENGES TOWARD EXPERIMENTAL DEMONSTRATION OF THE THEORY

To test the theory experimentally, a drive-to-splitting ratio (Ω_d/ω_0), where the effect is clear and pronounced above the noise level, must be achieved. Unfortunately, technical challenges regarding limited signal power and sensor coherence time prevented us from achieving this regime. While in simulations, the deviations from the RWA are apparent even at $\Omega_d = \omega_0/10$, in an experiment, the effect was hidden under measurement error. The drive amplitude should be $\Omega_d \geq \omega_0/3$ to observe clearly in an experiment.

In the strong driving of ^{1}H spins experiment (Section 5.4), I achieved a maximum ratio of $\Omega_d \approx \omega_0/5.5$. The deviations from smooth sinusoidal dynamics may not be unambiguously attributed to strong driving at this driving rate and with the observed experimental error. For the ^{15}N, driving (Section 5.5), the dynamics are more complex due to the hyperfine term, which dominates the nuclear Hamiltonian. Thus, I could not observe the effect discussed in this chapter with the mentioned experimental conditions.

The two options to increase the Ω_d/ω_0 ratio are to increase Ω_d or decrease ω_0. The saturation power of our amplifier limited the maximal driving amplitude, so it could not be improved with our current instrumentation. The other route is to decrease ω_0 by lowering the magnetic field B_0. However, reducing ω_0 introduces another complication: longer sensor coherence time (T_2) is required to sense the proton Larmor precession. A dynamical decoupling sequence with m pulses (e.g., for XY8-10, $m = 80$) requires $\pi m/\omega_0 \lesssim T_2$. In the diamond used in Chapter 5, the T_2 of the NV centers was generally too short to allow efficient detection at a lower field.

While the current experimental setting did not permit higher Ω_d/ω_0 ratios, I assert it is not a fundamental boundary. First, more powerful amplifiers are available. Second, the T_2 values characterized the specific diamond we were working with. Lengthier T_2 are achievable and have been reported in the past. For example, longer coherence times may be achieved by different surface treatments[134], ^{12}C enriched diamonds[212,58], or using deeper (higher implantation depth) NV centers[121,213].

It should be noted that, of the two routes to achieve a larger Ω_d/ω_0 ratio, lowering ω_0 is a more realistic avenue. From a sensitivity perspective, both options are similar: to avoid the overheating of the system and sample from the intense RF signal, the pulses must be applied at low duty cycles (in the proton driving experiment, Section 5.4, the duty cycle was $\sim 2\%$). Thus, the duty cycle and, subsequently, the measurement time is proportional to Ω_d. Likewise, the duration of the dynamical decoupling sequence for sensing (e.g., XY8, as in Section 5.4) is inversely proportional to ω_0. Thus, the total measurement time would have to increase in both cases. However, increasing the power applied to the antenna increases the risk of electrical breakdown of components.

6.7 Discussion and conclusions

In this chapter, I discussed the issue of fast qubit manipulation in a strong driving regime where $\Omega_d \lesssim \omega_0$. Short high-fidelity operations based on resonant offset-sine drive pulses for spin control may be optimized by varying the drive field's phase and offset. The offset-sine approach was presented as an alternative to existing approaches for designing strong driving pulses, namely optimal control theory[194] and bang-bang control sequences[191]. In our comparison, it achieved fidelity rates comparable to optimal control-derived signals. Pulse fidelities over 0.95 may be achieved by optimizing the drive phase, while varying the offset may bring fidelity rates over 0.999, above the fault-tolerance threshold.

The optimal offset-sine scheme discussed here is especially suitable for tilted driving fields, which are ubiquitous but have not been addressed in the optimal control literature to date. Moreover, the offset-sine signals are especially suited for *in situ* optimization. The plots of Fig. 6.2(top row) constitute optimization landscapes. A clear and straightforward optimization landscape facilitates efficient *in situ* optimization schemes by quicker sampling of the compact parameter space. This is valuable for experiments, as the driving field is noisy or not fully characterized. The offset-sine signal may be optimized experimentally by varying over one or two parameters, namely the drive phase and DC offset. In contrast, OCT approaches often require a high-dimensional optimization landscape (the OCT waveforms described here had 50-250 degrees of freedom), which may be complex and not readily characterized.

The fidelity rates of the OCT and optimized offset-sine waveforms differ; in some cases, the OCT fidelity was favorable. However, the actual rate would likely be lower due to deviations between the simulated and actual drive parameters; for example, driving noise or a limited bandwidth might hamper the actual fidelity[194]. This emphasizes the benefit of a strategy that accelerates *in situ* optimization to minimize deviations between the actual and simulated conditions.

The theory outlined here was not verified experimentally due to technical challenges; however, these do not constitute a fundamental limit. Future work on optimizing our NV center's T_2 may enable the realization of proton-driving experiments at lower fields, achieving higher Ω_d/ω_0 ratios. The theory may also be validated with other experimental schemes, such as driving a dressed qubit[193] or using lithographically patterned microstrips on the diamond surface, which induce strong fields[171]. Empirical testing of the theory may validate it and shed light on additional phenomena concerning spin control by strong tilted driving fields.

7

Discussion

In this work, I addressed some significant challenges in the field of nanoscale magnetic resonance based on NV center magnetometry. We built an experimental setup for NV magnetometry based on a confocal microscope with magnetic field control and quantum spin state control using RF fields. We also developed and demonstrated a low-temperature setup for NV magnetometry.

Chapter 3 discussed the magnetic tomography protocol developed for mapping spins near NV centers with subnanometer resolution. The protocol relies on simple magnetic field control and does not require complex instrumentation such as a scanning probe microscope. Importantly, I showed that this protocol can be used potentially to map the positions of spins and be utilized for compelling purposes such as single-molecule distance measurements or characterizing quantum spin networks. I further discussed its applicability to well-known nitroxide spin labels. In Chapter 4, I discussed in theory and simulations how to apply the concepts of magnetic tomography on coupled spins for the purpose of mapping the position of two spins on a single molecule. Single-molecule distance measurements may be a beneficial tool for biochemical and quantum information research.

To render single-spin mapping a widely applicable technique, the vicinity of the NV centers should be relatively void of other spins that may mask the target spin's signal or interact with them. However, the diamond's surface often exhibits a high density of paramagnetic defects or surface spins. In a recent study, Dwyer et al. estimate the surface spin density at $0.001–0.05\ \mathrm{nm}^{-2}$, corresponding to a mean spin-spin distance of $15–2.5\ \mathrm{nm}$[126]. Even the lower bound makes it very difficult to perform sensing without the presence of surface spins. The study has shown that this may be significantly improved by proper surface treatments that alter the surface chemistry of the diamond. Notably, annealing in an oxygen environment has significantly reduced the surface spin density[134,126,88]. During this work, I did not focus on the surface chemistry of the diamond; however, it appears to be a crucial step to realize single spin mapping of arbitrary samples on the diamond's surface.

In Chapter 5, I demonstrated a novel antenna tailored for NV experiments that can drive nuclear spins rapidly and with relatively low power input. The demonstrated Rabi frequencies are unprecedented for NV-based NMR and are close to the highest reports for conventional, induction-based NMR[214,215,216]. This is useful for shortening pulse durations and enabling broadband excitation. Shorter pulse durations may improve the sensitivity of detection protocols by shortening the overall sequence duration. Shorter pulses may also improve the sensitivity of protocols utilizing a nuclear spin near the NV sensor spin as a memory qubit that is repetitively measured. In these protocols, the nuclear spin state is sampled dozens of times[217,137], so nuclear spin manipulation constitutes a significant part of the acquisition time.

In the experiment, we showed that, due to the impact on the NV sensor state, nuclear spin manipulation must be done with the NV sensor *not* in a coherent superposition, as in a typical ENDOR experiment. A contrary example is the work by Mamin et al.[58]. In their experiment, they used a relatively deep NV with a highly long coherence time ($T_2^{echo} = 600$ μs), which allowed them to manipulate the nuclear spins with lengthy pulses ($t_p \approx 5$ μs). In this case, the RF pulses did not corrupt the sensor state because they were relatively weak ($B_1 \sim 12$ G). Similar examples include studies by Bradley et al.[177] and Abobeih et al.[82], that also employed very low driving amplitudes, $B_1 \lesssim 5$ G. Thus, a strong driving experiment would probably have to follow a scheme where the sensor state is stored in a longitudinal state, as shown in Chapter 5.

7.1 OUTLOOK

NANOSCALE NMR WITH STRONG DRIVING OF NUCLEAR SPINS

Chapter 5 experiment demonstrated an antenna for strong driving of nuclear spins. In the experiment, I demonstrated a fundamental pulse sequence on the proton spins, namely Rabi oscillations. Now, with a shortened pulse duration, this system may be instrumental in further work on nanoscale NMR using more complex pulse sequences employed in conventional NMR, starting from nuclear spin-echos and sequences that probe the coupling between proton and carbon nuclear spins (e.g., INEPT, HSQC, etc.).

In Chapter 6, I presented a theoretical strategy to cope with infidelity stemming from the intense driving of spins in a tilted field. Unfortunately, due to technical challenges detailed in the chapter, we failed to realize the theory experimentally. Observing this effect and demonstrating the strategy in an experiment is interesting. This would be of value both in validating the theory and uncovering other effects relating to this setting.

SINGLE-MOLECULE DISTANCE MEASUREMENTS

We have made preparations for demonstrating single-molecule distance measurements based on the concept of magnetic tomography described in Chapter 4. For this, we have procured several types of rigid organic molecules with spin labels attached at specific distances, known as "EPR yardsticks"[218] (further details are elaborated in Appendix D). The strategy is to immobilize the molecules in a polymer matrix[118] and apply them at a low concentration to the diamond's surface to minimize interaction between them.

A significant challenge in the biradical mapping strategy is the presence of paramagnetic defects on the diamond's surface. These defects might "mask" the signal of the target spins or couple with them, distorting the signal. Thus, work needs to be done to reduce the concentration of paramagnetic defects on the surface of the diamond. This work is mainly on the surface chemistry of the diamond surface.

The magnetic tomography protocol may be enhanced by employing a robust magnetic gradient, with field gradients of at least a few gauss per nanometer. The gradient will create spectral separation of the spins - separating the resonances of the target spins (e.g., spin-labels connected to a molecule) and separating these from surface spins' resonances. This will allow selective addressing of the target spins to measure their specific coupling to the NV sensor without the ambiguity from simultaneous addressing of target spins and other paramagnetic defects.

The gradient for such a "magnetic gradient tomography" protocol may be provided by a magnetic tip, as shown in the past by Grinolds et al.[106], with a gradient of $>2\,\mathrm{G/nm}$. A significant drawback of such a magnetic tip is that it induces a strong magnetic field perpendicular to the NV axis. To overcome this, the gradient tip should be held static and not in a scanning configuration. The external applied magnetic field (B_0), which is effectively homogeneous within the nanoscale volume, can compensate for the tip's transverse field component. Then, the mapping is done with magnetic tomography, with small tilts of the field. This approach mitigates the adverse effects of the transverse field while maintaining the desired gradient. Thus, the gradient facilitates selective addressing, and the mapping of each spin is done separately by magnetic tomography.

The gradient may also be facilitated by a current-on-tip device currently being developed in our group. Then, the gradient may be varied on a static tip by ramping the tip's current. However, this has yet to be demonstrated.

A

Rotating frame derivations

A.1 ROTATING FRAME TRANSFORMATION OF A LINEARLY-POLARIZED TILTED DRIVE

Let us consider a simple sine drive waveform slightly detuned from the qubit's transition at $\omega_d = \omega_0 - \Delta$:

$$\mathcal{H} = \frac{\omega_0}{2}\sigma_z + \Omega_d \sin\left(\frac{\omega_d t}{2} + \phi_d\right)\left(\sigma_x + \tan\left(\theta_d\right)\sigma_z\right) \tag{A.1}$$

We apply a rotating frame transformation at the frequency of the drive with the unitary operator $T = \exp\left(i\frac{\omega_d t}{2}\sigma_z\right)$ to the Schrödinger equation [219]. We denote the rotating frame Hamiltonian as $\mathcal{H}_{rot}$, and the rotating frame wavefunction as $|\psi_r\rangle$:

$$|\psi_r\rangle = T|\psi\rangle \tag{A.2}$$

$$\tag{A.3}$$

Plugging $|\psi_r\rangle$ into the Schrödinger equation:

$$i\frac{\partial}{\partial t}|\psi\rangle = \mathcal{H}|\psi\rangle \rightarrow i\frac{\partial}{\partial t}T^{\dagger}|\psi_r\rangle = \mathcal{H}T^{\dagger}|\psi_r\rangle \tag{A.4}$$

$$\tag{A.5}$$

We calculate the time derivative and plug it back into the Schrödinger equation, to get the rotating frame Hamiltonian:

$$i\frac{\partial}{\partial t}\left(T^\dagger\left|\psi_r\right\rangle\right) = i\frac{\partial T^\dagger}{\partial t}\left|\psi_r\right\rangle + T^\dagger i\frac{\partial}{\partial t}\left|\psi_r\right\rangle \tag{A.6}$$

$$\rightarrow T^\dagger i\frac{\partial}{\partial t}\left|\psi_r\right\rangle = \left(\mathcal{H}T^\dagger - i\frac{\partial T^\dagger}{\partial t}\right)\left|\psi_r\right\rangle \tag{A.7}$$

$$\times T \tag{A.8}$$

$$i\frac{\partial}{\partial t}\left|\psi_r\right\rangle = \underbrace{\left(T\mathcal{H}T^\dagger - iT\frac{\partial T^\dagger}{\partial t}\right)}_{\mathcal{H}_{rot}}\left|\psi_r\right\rangle \tag{A.9}$$

Now, we calculate the rotating frame Hamiltonian. Let us first see what we get from the σ_x term, using an expansion for nested commutators:

$$T\sigma_x T^\dagger = \exp\left(i\frac{\omega_d t}{2}\sigma_z\right)\sigma_x \exp\left(-i\frac{\omega_d t}{2}\sigma_z\right) = \tag{A.10}$$

$$= \sigma_x + i\frac{\omega_d t}{2}\underbrace{\left[\sigma_z, \sigma_x\right]}_{2i\sigma_y} - \frac{\left(\omega_d t\right)^2}{4\times 2!}\underbrace{\left[\sigma_z, \left[\sigma_z, \sigma_x\right]\right]}_{4\sigma_x} - i\frac{\left(\omega_d t\right)^3}{8\times 3!}\underbrace{\left[\sigma_z\left[\sigma_z, \left[\sigma_z, \sigma_x\right]\right]\right]}_{8i\sigma_y} + \ldots = \tag{A.11}$$

$$= \sigma_x - \omega_d t\sigma_y - \frac{\left(\omega_d t\right)^2}{2}\sigma_x + \frac{\left(\omega_d t\right)^3}{6}\sigma_y + \ldots = \tag{A.12}$$

$$= \sigma_x \cos\left(\frac{\omega_d t}{2}\right) - \sigma_y \sin\left(\frac{\omega_d t}{2}\right) \tag{A.13}$$

$$\rightarrow \sin\left(\frac{\omega_d t}{2} + \phi_d\right)\left(\sigma_x \cos\left(\frac{\omega_d t}{2}\right) - \sigma_y \sin\left(\frac{\omega_d t}{2}\right)\right) = \tag{A.14}$$

$$= \frac{1}{2}\left(\sin\left(\omega_d t + \phi_d\right) + \sin\left(\phi_d\right)\right)\sigma_x - \frac{1}{2}\left(\cos\left(\phi_d\right) - \cos\left(\omega_d t + \phi_d\right)\right)\sigma_y \tag{A.15}$$

and, of course, $T\sigma_z T^\dagger = \sigma_z$. From here, we get the rotating-frame Hamiltonian for a linearly-polarized tilted drive:

$$\mathcal{H}_{rot} = \frac{\Delta}{2}\sigma_z + \frac{\Omega_d}{2}\left(\sin\left(\phi_d\right)\sigma_x - \cos\left(\phi_d\right)\sigma_y\right) + \tag{A.16}$$

$$+ \frac{\Omega_d}{2}\left(\sin\left(\omega_d t + \phi_d\right)\sigma_x + \cos\left(\omega_d t + \phi_d\right)\sigma_y\right) + \tag{A.17}$$

$$+ \Omega_d \sin\left(\frac{\omega_d t}{2} + \phi_d\right)\tan\left(\theta_d\right)\sigma_z \tag{A.18}$$

The first term represents the detuning that vanishes for $\omega_d \rightarrow \omega_0$. The second term induces the state transition around an axis defined by ϕ_d. The third term is commonly dubbed the "counter-rotating" term, as it models a circularly polarized field rotating oppositely to the transformation. The counter-rotating term oscillates at twice the driving frequency. This term is inherent to a linearly polarized drive and would not appear if the drive is perfectly circular. The last term is the longitudinal component, which was conserved under the rotation. The longitudinal component oscillates at the driving frequency and is inherent to a tilted drive. Thus, a tilted linearly polarized field introduces fast oscillating terms to the rotating frame Hamiltonian.

Under the rotating wave approximation (RWA), which holds for $\Omega_d \ll \omega_0, \omega_d$, the last two rapidly oscillating terms are neglected, assuming that their small contribution periodically averages out.

A.2 INTERACTION FRAME OF SENSOR QUBIT

We start with the static lab-frame ground-state spin Hamiltonian of the NV center (Eq. 1.2). To simplify, we assume a field along the NV center's axis $\mathbf{B} = B_0\hat{z}$. We assume a drive in the transverse plane (e.g., along $\hat{x}$), at ω_d that is slightly detuned from one of the NV's transitions $D \pm \gamma_{nv} B_0$. We then transform the equation to a rotating frame, similar to that described in the previous section. Finally, the "fast" rotating terms are neglected. If the drive is not circularly polarized, then there is the "counter rotating" term to be neglected. Further, in the hyperfine terms, only the $\hat{z}$ is static and thus not neglected. The interaction (rotating) frame Hamiltonian is thus:

$$\mathcal{H}_I = \left(\Delta + \gamma_{nv}\delta B_z(t)\right) S^z_{nv} + \sum_j a_{z,j} S^z_{nv} I^z_j \tag{A.19}$$

where $\Delta = \omega_d - \left(D - \gamma_{nv} B_0\right)$ is a drive detuning; $\delta B_z(t)$ is some variable magnetic field to be sensed; and $\mathbf{I}_j$ is a nuclear spin in the vicinity.

In the next section, the case of an NV spin interacting with another electron spin via dipole-dipole coupling is treated rigorously.

A.3 EVOLUTION IN DOUBLE ELECTRON-ELECTRON RESONANCE

In what follows, we calculate the result of a DEER measurement. We start with a lab frame Hamiltonian of the NV ($S = 1$)-target spin ($S = 1/2$) system. We focus on only two levels of the NV center ($|0\rangle, |1\rangle$), neglecting the third level under the assumption that it is very detuned. Thus:

$$S^z_{nv} = \begin{pmatrix} 1 & 0 \\ 0 & 0 \end{pmatrix} \tag{A.20}$$

and so forth. The time-dependent Hamiltonian under RF driving is:

$$\mathcal{H} = (D + \omega_0) S^z_{nv} + \omega_0 S^z_e + \omega_{dd} S^z_{nv} S^z_e + \Omega\left(t, S^x_{nv}, S^x_e\right) \tag{A.21}$$

Here, we invoked the secular approximation to approximate the dipolar coupling to $\omega_{dd} S^z_{nv} S^z_e$. The driving term is $\Omega(\dots)$.

We apply a double rotating frame transformation T on the NV and target spin, with their respective frequencies, which eliminates the time-dependent terms:

$$T = \exp\left(-i\left((D + \omega_0 - \Delta_{nv}) t S^z_{nv}\right) \exp\left(-i\left(\omega_0 - \Delta_e\right) S^z_e\right) t\right) \tag{A.22}$$

To validate the calculation, we leave a detuning, which we expect to cancel out in the echos. We neglect the fast-rotating terms (i.e., we invoke the RWA). The resulting rotating frame Hamiltonian, during the free evolution periods (i.e., when the driving signal is off):

$$\mathcal{H}_{rot} = \Delta_{nv} S^z_{nv} + \Delta_e S^z_e + \omega_{dd} S^z_{nv} S^z_e \tag{A.23}$$

From here on, we discuss only the rotating frame, so the denoted axes refer to the rotating frame axes (e.g., S^y is the operator along the rotating frame $\hat{y}$ axis). We start by calculating the evolution for a general eigenstate of S^z_e:

$$|\psi_{m,0}\rangle = |0\rangle_{nv} |m\rangle_e \tag{A.24}$$

Here $|m\rangle$ is an eigenstate of the target electron spin, such that $m = \pm\frac{1}{2}$, and $S^z_e |m\rangle = m |m\rangle$. For brevity, we drop the nv/e subscripts; $|0\rangle, |1\rangle$ denote exclusively the NV state, while $|m\rangle, |\uparrow\rangle, |\downarrow\rangle$ are used for the target spin states.

The state of the system after the DEER sequence will be:

$$|\psi_m(\tau)\rangle = V(\tau) |0\rangle |m\rangle \tag{A.25}$$

where $V(\tau)$ is the evolution operator of the state over the sequence:

$$V(\tau) = Y^{\frac{\pi}{2}}_{nv} U\left(\frac{\tau}{2}\right) Y^{\pi}_e Y^{\pi}_{nv} U\left(\frac{\tau}{2}\right) Y^{\pi}_e Y^{\frac{\pi}{2}}_{nv} \tag{A.26}$$

we defined:

$$Y^{\phi}_j = \exp\left(-i S^y_j \phi\right) \tag{A.27}$$

$$U(\tau) = e^{-i\mathcal{H}_{rot}\tau} = e^{-i\Delta_{nv} S^z_{nv}\tau} e^{-i\Delta_e S^z_e \tau} e^{-i\omega_{dd} S^z_{nv} S^z_e \tau} \tag{A.28}$$

and the time evolution of the state:

$$\begin{aligned} |\psi_m(\tau)\rangle &= V(\tau) |\psi_{0,m}\rangle = Y^{\frac{\pi}{2}}_{nv} U\left(\frac{\tau}{2}\right) Y^{\pi}_e Y^{\pi}_{nv} U\left(\frac{\tau}{2}\right) Y^{\pi}_e Y^{\frac{\pi}{2}}_{nv} |0\rangle |m\rangle = \\ &= -e^{-i\Delta_{nv}\frac{\tau}{2}} |m\rangle \left(\cos\left(m\omega_{dd}\frac{\tau}{2}\right)|0\rangle - i\sin\left(m\omega_{dd}\frac{\tau}{2}\right)|1\rangle\right) \end{aligned} \tag{A.29}$$

Optical detection of the NV center is proportional to the $|0\rangle\langle 0|$ operator, so we calculate the projection of the final state $\psi_m(\tau)$:

$$\begin{aligned} \mathrm{tr}\left(|\psi(\tau)\rangle\langle\psi(\tau)|\,|0\rangle\langle 0|\right) &= \cos^2\left(m\omega_{dd}\frac{\tau}{2}\right) = \\ &\underbrace{=}_{m=\pm\frac{1}{2}} \cos^2\left(\omega_{dd}\frac{\tau}{4}\right) = \frac{1}{2}\left(1 + \cos\left(\frac{\omega_{dd}}{2}\tau\right)\right) \end{aligned} \tag{A.30}$$

We obtain that the measurement does not depend on $|m\rangle$, the initial state of the target electron. Thus, the result of the measurement for an initially mixed state of the target electron would be identical:

$$
\begin{aligned}
\rho_0 &= |0\rangle\langle 0| \otimes \frac{|\uparrow\rangle\langle\uparrow| + |\downarrow\rangle\langle\downarrow|}{2} && \text{(A.31)}\\
\rho(\tau) &= V(\tau)\left(|0\rangle\langle 0| \otimes \frac{|\uparrow\rangle\langle\uparrow| + |\downarrow\rangle\langle\downarrow|}{2}\right)V^{\dagger}(\tau) = && \text{(A.32)}\\
&= \frac{1}{2}\sum_{m=\pm 1} |\psi_m(\tau)\rangle\langle\psi_m(\tau)|
\end{aligned}
$$

and calculating the result of a measurement of this state:

$$
\begin{aligned}
\operatorname{tr}\left(\rho(\tau)|0\rangle\langle 0|\right) &= \frac{1}{2}\sum_{m=\pm 1}\operatorname{tr}\left(|\psi_m(\tau)\rangle\langle\psi_m(\tau)|\,|0\rangle\langle 0|\right) = && \text{(A.33)}\\
&= \frac{1}{2}\left(1+\cos\left(\frac{\omega_{dd}}{2}\tau\right)\right)
\end{aligned}
$$

We note that, in a measurement where we sweep the value of τ, we obtain a signal that oscillates at a frequency (ω_{deer}) that is half the dipolar coupling strength (ω_{dd}):

$$\omega_{dd} = 2\omega_{deer} \qquad \text{(A.34)}$$

B

Nanoscale proton NMR

In Chapter 5, I presented results on strong driving of proton spins in an immersion oil sample on the diamond's surface. To observe proton Rabi oscillations, the proton's NMR signal must first be observed by the NV center. In this appendix, I complement the chapter with further data from the nanoscale proton NMR experiments using single NV centers. This appendix shows some comparisons between pulse sequences, namely XY8 and phase-randomized XY8 sequence, CPMG and XY8, and XY8 with varying pulse numbers. I also show a broadband spectrum of dynamical decoupling measurements beyond the local vicinity of the NMR resonance. Part of the information here is inconclusive but presented for transparency and future reference.

B.1 Data normalization

The data in Fig. 5.5 is shown in terms of the probability of the NV being in one of the qubit states. The calibrated NV photon count rate determined the NV state. The calibration may be done in several ways, such as using a spin echo measurement (Hahn). The two alternating traces of the spin echo were fit to decaying exponents, from which the photon count rate for the $|0\rangle$, $|1\rangle$ state was calculated. Another possible calibration curve is a Rabi measurement.

Fig. B.1 shows the calibration curve and the XY8 measurement before and after the calibration. The average photon count rate (in photons/sec) for each data point $\mathcal{S}_i$ was calculated for a chosen counting window (80–280 ns since the start of the readout laser pulse). Then, the data points p_i were calibrated against the photo count rate of a Hahn measurement, according to $p_i = (\mathcal{S}_i - \mathcal{I}_1) / (\mathcal{I}_0 - \mathcal{I}_1)$, where the maximal (minimal) value of the decay curve was set to be $\mathcal{I}_0$, the count rate for the $|0\rangle$ state ($\mathcal{I}_1$, for the $|1\rangle$ state).

In this appendix, the experiments used the phase alternation technique, alternating the readout

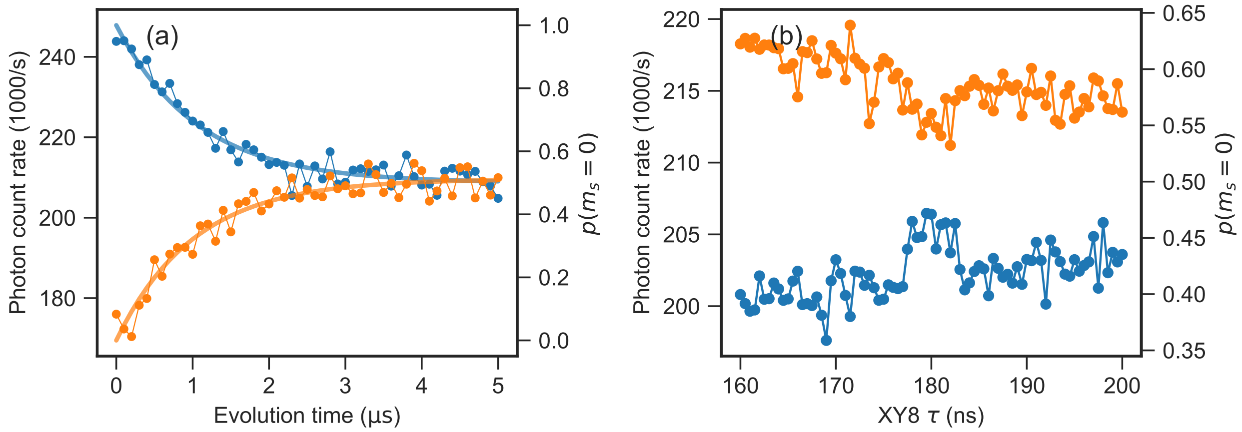

Figure B.1: Data normalization process for the proton sensing experiment. (a) A Hahn experiment, from which the calibration photon count rates for $|0\rangle$ and $|1\rangle$ are extracted. (b) The XY8 measurement in terms of photon count rates and the probability as calculated using the calibration in (a).

axis between $\pm x$, such that there are two signal traces - $\mathcal{S}_{\pm x}$. The contrast in the plots is given by $\mathcal{C} = (\mathcal{S}_{+x} - \mathcal{S}_{-x}) \,/\, (\mathcal{S}_{+x} + \mathcal{S}_{-x})$. A contrast of zero thus implies that the sequence ended with the NV in an equally distributed state (e.g., $\rho = \frac{1}{2}\begin{pmatrix} 1 & \alpha \\ \alpha* & 1 \end{pmatrix}$, $|\alpha| \leq 1$). A maximal (minimal) contrast otherwise implies a maximally polarized state into $|0\rangle$ ($|\pm 1\rangle$), e.g., $\rho = \begin{pmatrix} 1 & \alpha \\ \alpha* & 0 \end{pmatrix}$.

B.2 XY8 measurements of single NV centers in a diamond with a proton sample

Fig. B.2 depicts broadband XY8 measurements of two different NVs. The resonances of ^{1}H and ^{13}C are marked according to the magnetic field, and they are apparent in some cases. However, there are much more prominent resonances, e.g., at ∼500 ns in Fig. B.2(b). These are probably due to interactions with strongly coupled nuclear spins, such as the NV's own ^{15}N spin. With small tilts in the magnetic field, the spin's 3.65 MHz transverse hyperfine component induces an AC signal on the NV center. Due to the strong hyperfine interaction ($A_{\parallel} = 3.03$ MHz, this results in dominant resonances in the DD spectra, dwarfing the resonance of the weakly interacting proton ensemble. Fig. B.2(a) also depicts that the proton resonance may often be concealed, as is the case for the 662 G measurement, while at 427 G the resonance was prominent.

In Fig. B.2(b) the ^{13}C resonance is also marked. The ^{13}C tends to be strong, as it is mediated by relatively strongly coupled ^{13}C spins, which are found closer to the NV center than the distant proton bath on the surface. The ^{13}C resonance appears wide due to stretching in the time domain; in the frequency domain ($f = 1/2\tau$), it is comparable in width to the proton resonance.

Fig. B.3(a) depicts results of XY8 measurement with varying number of pulses on the proton resonance ($\tau = 277$ ns) and in its vicinity ($\tau = 300$ ns). From this, we can see that at least 48 pulses (XY8-6 and above) are required to observe the resonance beyond the baseline. By subtracting the

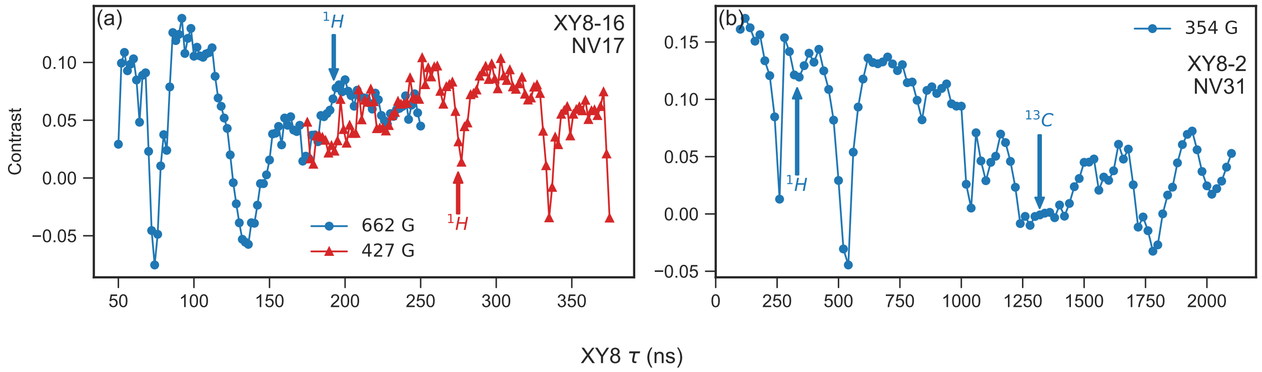

Figure B.2: Broadband XY8 measurements of a protons. (a) XY8-16 (128 pulses) measurements over a broad range of pulse spacing (τ) values. The measurements were taken at two different fields, and the expected proton resonance at each field ($\tau = 1/\left(2f_H\right)$ is marked by an arrow. Several other prominent resonances are probably due to various interactions with nuclear spins. (b) A broadband measurement for a different NV at a single magnetic field. The expected proton resonance and ^{13}C are marked.

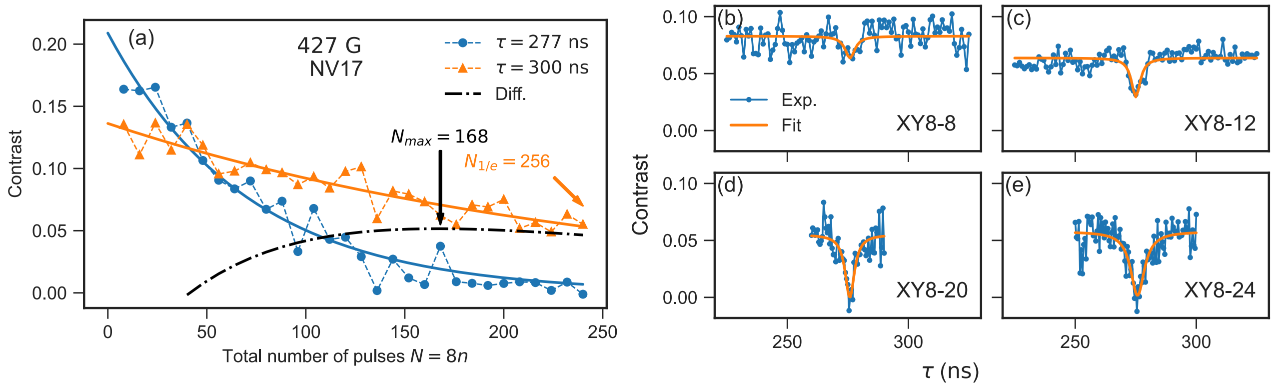

Figure B.3: The proton resonance as a function of number of XY8 pulses. (a) XY8-n contrast as a function of total number of pulses $N = 8n$, on the proton resonance ($\tau = 277\,\text{ns}$) and off the resonance ($\tau = 300\,\text{ns}$). The resonance becomes apparent for $n > 6\ (N > 48)$. The optimal SNR is found at the maximal difference between the curves obtained for XY8-21 (~ 168) pulses. For this NV, $T_2^{XY8} \approx 77\,\mu\text{s}$. (b) Example XY8-n spectra around the proton resonance, demonstrating the overall coherence and the resonance's contrast as a function of the number of pulses.

curves (black dash-dot curve), we can also find the number of pulses for optimal SNR to be 168 (XY8-21), for which the resonance is most prominent above the background. From the decay of the off-resonance curve (orange, $\tau = 300\,\text{ns}$), we also estimate the decoherence under this DD scheme to be $T_2^{XY8} \approx 77\,\mu\text{s}$. Fig. B.3(b-e) depict XY8 sequences around the proton resonance (for the same NV at the same field), demonstrating the contrast as a function of number of pulses.

Fig. B.4 compares standard XY8-20 and -24 sequences with phase-randomized XY8-20 and -24 (RXY8). A random phase[174] is added to each XY8 block to suppress spurious resonances[220], which may lead to the erroneous assignment of the ^{13}C fourth harmonic as a proton resonance. The positions of these resonances are marked in Fig. B.4(a). There are minor variations between the XY8 and RXY8 spectra, which probably arise due to the effect of the phase randomization on the sequence's filter function. The prominent resonance at RXY8-20 and RXY8-24 supports that this is a proton resonance, not a spurious harmonic. There is no apparent feature to attribute to the ^{13}C fourth harmonic and it may be hidden under the prominent ^{1}H resonance. The contrasts are similar between XY8 and RXY8. These traces are from the same NV as in Fig. 5.5 and Fig. B.3.

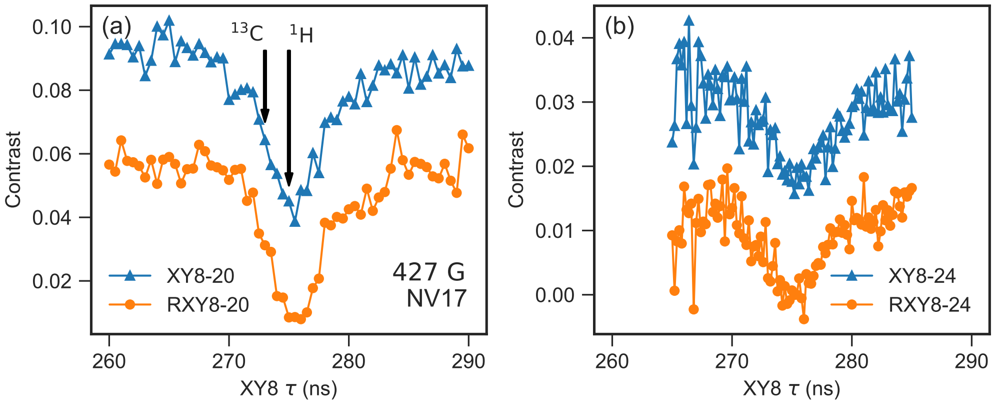

Figure B.4: Comparing a standard XY8 with a phase-randomized XY8. (a) A standard XY8-20 (160 pulses) sweep around the expected proton resonance (marked by ^{1}H), and compared with a phase-randomized XY8 (RXY8), which eliminates spurious harmonics. The XY8-20 trace was shifted up for clarity. The fourth harmonic of the ^{13}C resonance is also marked. The two spectra are similar. (b) Similar to (a), but with XY8-24 (192 pulses), the higher order DD measurement's contrast is lower. The XY8-24 and RXY8-24 spectra are almost identical, ruling out spurious harmonics as the origin of the peak.

B.3 COMPARING CPMG AND XY8 SEQUENCES

Fig. B.5 compares CPMG and XY8 DD sequences. In this context, we define CPMG as having a uniform phase for all the π-pulses and a phase difference of 90° to the initializing $\pi/2$-pulse. Fig. B.5(a) compares the decay curves of the sequences as a function of number of pulses (CPMG-N and XY8-n, such that $N = 8n$). The curves were fit with decaying exponents to find the decay constant $N_{1/e}$. Interestingly, the CPMG decay was almost 30% slower, with $N_{1/e} = 49 \pm 5$, compared to $N_{1/e} = 38 \pm 3$. In other words, $T_2^{CPMG} = (8.8 \pm 0.9)$ µs, vs. $T_2^{XY8} = (6.8 \pm 0.5)$ µs. Fig. B.5(b) compares XY8-4 and CPMG32 (same number of pulses) on the same NV and under the same conditions, around the expected resonance of ^{13}C (at ~780 ns). Here, the baseline contrast of CPMG was significantly higher (the data is not shifted and shows actual values); however, neither sequence exhibits the expected resonance.

XY8 sequences are cited as more robust to pulse errors compared with CPMG[221], although, the data in Fig. B.5 demonstrate a slight advantage to CPMG. For this reason, XY8 are most common in the literature for proton detection[37,102,87,121]. To my knowledge, observation of proton resonance with NV centers in diamond using a CPMG sequence was not reported, but for no apparent reason. CPMG sequences were reported to be used for ^{13}C NMR[37]. Interestingly, CPMG sequences were reported to avoid the spurious harmonics characteristic of XY8[220]. I did not compare the sequence rigorously to confirm the possibility of sensing proton resonance with CPMG, but there is no apparent reason it should not be possible. It remains an outstanding issue to elucidate the benefits of CPMG for surface proton detection, or lack thereof.

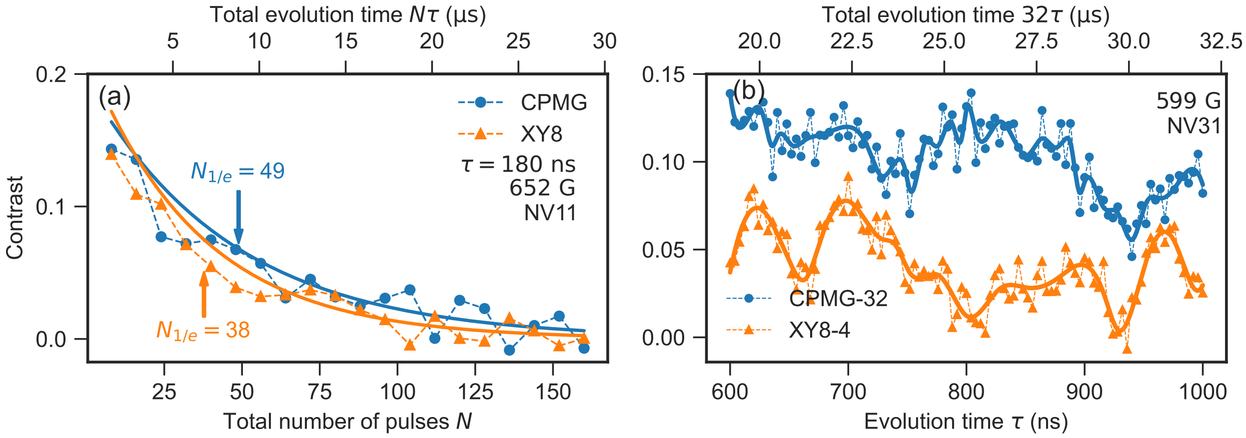

Figure B.5: Comparing dynamical decoupling sequences - CPMG and XY8. (a) Comparison of CPMG pulse sequence vs XY8, as a function of the total number of pulses, at a constant evolution time of $\tau = 180\,\mathrm{ns}$. The sequences follow a similar trend, but the CPMG has a slower decay. (b) Comparison of CPMG-32 and XY8-4 sequences over a narrowband around the expected $^{13}\mathrm{C}$ resonance ($\sim 780\,\mathrm{ns}$). The CPMG has a higher overall contrast but did not exhibit a clear resonance at the expected τ.

C

Additional data from magnetic tomography experiments

In this appendix, I present additional data from the magnetic tomography experiments. I include the characterization of the specific NV on which Chapter 3 experiments were conducted. The NV center was found in a confocal spot with another NV center, but this should not impact the results. I further show results data from additional pulse sequences, including Hahn echo, Ramsey, and a high-resolution DEER spectrum. The additional data, in part, supports the hypothesis on the nature of the target spin introduced in Section 3.6, while some of it raises further questions that may be further discussed in a future study.

C.1 NV CENTER CHARACTERIZATION

Potential NV centers were identified in the sample as bright photoluminescent spots in confocal scans of the sample. The data presented in this work came from a confocal spot consisting of two NV centers, as could be observed in a $g^{(2)}(\tau)$ autocorrelation measurement of the PL signal (Fig. C.1(a)). The antibunching dip at a delay time of $\tau \sim 0$ indicates two single photon emitters within the confocal spot[222]. These are labeled NV A and NV B.

An optically detected magnetic resonance (ODMR) spectrum of the confocal spot (Fig. C.1(b)) exhibits two sets of dips; this indicates that the two NV centers are orientated in different directions. Here, I worked with the transitions belonging to the NV denoted as NV A. The magnetic field was aligned with NV A, so splitting its $|0\rangle \leftrightarrow |\pm 1\rangle$ transitions is larger than the splitting for NV B. The magnetic field lifts the degeneracy of the two centers' spin states. Applying a pulse at the frequency of $|0\rangle_A \leftrightarrow |-1\rangle_A$ does not affect NV B because its transitions are sufficiently

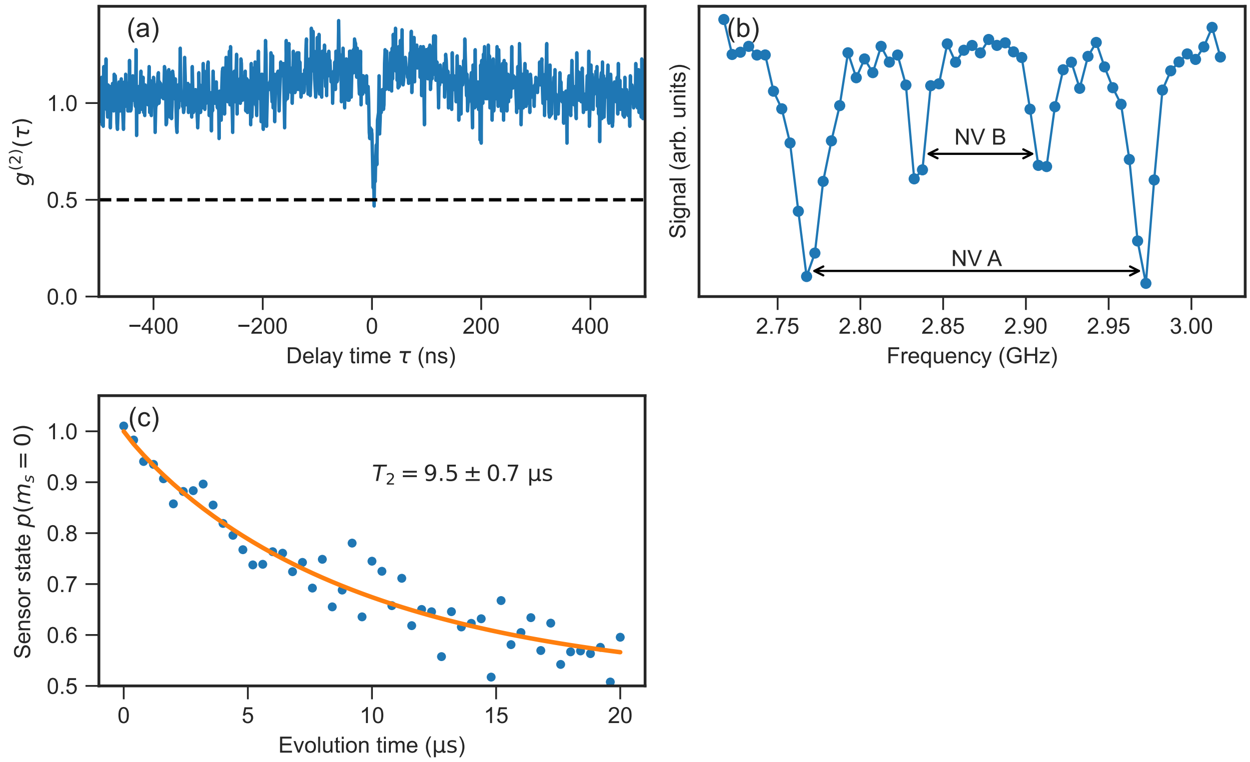

Figure C.1: Characterization of the NV center for the magnetic tomography experiment. (a) $g^{(2)}(\tau)$ autocorrelation measurement of the PL signal from the confocal spot used in this work. (b) ODMR spectrum of the confocal spot used in this work, exhibiting two pairs of transitions belonging to each NV center in the spot. (c) The decoherence of the NV center used in this work, measured with a spin-echo sequence ($\frac{\pi}{2} - \frac{\tau}{2} - \pi - \frac{\tau}{2} - \frac{\pi}{2}$). The experimental data (blue markers) was fitted to an exponential decay - $S(\tau) = Ae^{-(\tau/T_2)^b}$. The fit gave a $T_2 = (9.5 \pm 0.7)$ μs, and $b = 0.94 \pm 0.1$.

detuned (i.e., the Rabi driving frequency is much smaller than the difference in the transition frequencies of A and B). Hence, the presence of NV B in the PL signal only contributes to a constant background.

I assessed the decoherence of the sensor with a spin-echo (Hahn) sequence and extracted a decoherence time of $T_2 = (9.5 \pm 0.7)$ μs, as shown in Fig. C.1(c). The T_2 of the sensor sets the frequency resolution limit for our dipolar coupling measurements. However, during dipolar coupling measurements (DEER), a faster decay is observed, on the order of $\sim$2.3 μs, probably due to the introduction of noise from the farther electron spin-bath. Also, the RF pulses that manipulate the electron spins add noise to the sequence.

C.2 HIGH-RESOLUTION DEER SPECTRA

Fig. C.2 presents a high-resolution DEER spectrum of the NV studied in Chapter 3. The high-resolution spectrum was generated with low amplitude of the RF pulses at the target electron frequency ($\sim$1160 MHz). The spectrum's resolution is proportional to the Rabi driving frequency of the target spins: in the "standard" DEER spectra (e.g., Fig. 3.3(a)), this was $\sim$10 MHz. For the high-resolution DEER spectra, the Rabi frequency was lowered to 3.7 MHz by lowering the RF amplitude by a similar factor. The spectrum acquired with these parameters revealed a splitting of

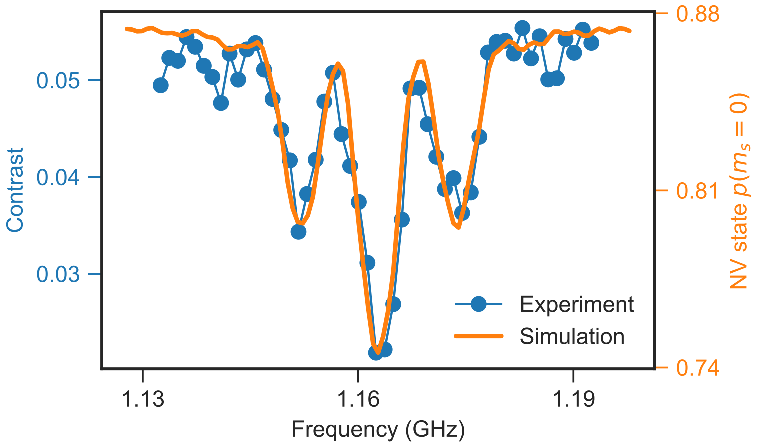

Figure C.2: High-resolution DEER spectrum of NV center. A high-resolution DEER spectrum of the NV center studied in Chapter 3, acquired by applying weaker, selective RF pulses at the DEER frequency. The spectrum features three peaks, possibly related to the hyperfine splitting of one of the target electron spin states. The experiment (blue circles and curve) is compared to a simulation of a relevant system.

the resonant dip into three different dips, spaced by 11 MHz.

The split dip indicates additional features to the spin system beyond the NV sensor spin and the two target spins discussed in Chapter 3. Two possible explanations (not to exclude other possible explanations) are: (i) one of the target spins is coupled to a spin-1 nuclear spin, with a coupling of approximately 11 MHz; (ii) the interaction between the two target spins. Option (ii) of interaction between the two spins is ruled out by considering the DEER time traces (Fig. 3.10): an 11 MHz coupling between the two spins would dominate the dynamics, manifesting as a single frequency oscillation.

The case of an additional nuclear spin coupled to the closer of the two electron spins is simulated and plotted vs. the experimental data in Fig. C.2. I simulated a spin system of an NV center with two electron spins at positions as found in Section 3.6. The closer of the two spins is coupled to a ^{14}N (spin-1 with the gyromagnetic ratio of ^{14}N). I used $A_{\parallel} = 11$ MHz for the parallel hyperfine component, extracted by fitting the experimental spectrum to a three Lorentzian model. The perpendicular hyperfine component was taken arbitrarily to be $A_{\perp} = 15$ MHz. The field was set according to the center of the spectrum, and the DEER evolution time was used as in the experiment. As is clear, the simulation fits the data very well without an excess of fitted parameters.

RAMSEY EXPERIMENTS

Fig. C.3(a) depicts a standard Ramsey sequence, and (b) shows a Ramsey trace of the NV center studied in Chapter 3. The standard Ramsey sequence yielded an unusual triple-frequency signal, as is evident in the FFT in Fig. C.3(c). The FFT spectrum of the Ramsey trace may be interpreted as the transition frequencies of the NV's $|0\rangle \leftrightarrow |-1\rangle$ manifold, shifted by the frequency of the $\pi/2$ pulse (here it is 1449.5 MHz). The center frequency results from an intentionally set detuning of 1.9 MHz. The other frequencies are thus splitting of the $|0\rangle \leftrightarrow |-1\rangle$ transition due to interactions with neighboring spins.

The experiment was done at a field of 507 G, at which strongly interacting nuclear spins are almost entirely polarized (as discussed in depth in Chapter 5). So, we do not expect to observe a splitting due to the hyperfine interaction with the NV's ^{15}N nuclear spin (and if so, this would be at a value of 3.03 MHz). Further, the diamond was made by growing a $\sim$50 μm layer from purified 99.999% ^{12}C (an $S = 0$ isotope), grown on a natural abundance (1.1% ^{13}C) diamond substrate. Thus, the presence of ^{13}C is highly unlikely. So, splitting due to hyperfine interactions may generally be neglected.

Having excluded nuclear hyperfine interactions, the splitting may stem from significant dipolar interactions with electron spins, whose presence has been previously demonstrated in the DEER experiments. This has been further supported by the sequence described in Fig. C.3(d): it consists of a Ramsey sequence, but with a π-pulse, tuned to the frequency of free electron spins, halfway through the evolution period. The π-pulse flips the target electron spins' state halfway through the evolution, such that the phase collected by the NV sensor due to its evolution is refocused. The result, shown in the trace and FFT in Fig. C.3(e-f), demonstrates that the two satellite frequency components to appear in the standard Ramsey (Fig. C.3(c)) have been eliminated. This supports that these frequencies result from interaction with electron spins, which the π-pulse has refocused.

The spectrum of the Ramsey FFT, seen in Fig. C.3(c), a triplet with sidebands distanced by $\sim$400 kHz, indicates the presence of two electron spins with similar coupling to the NV center on the order of $\sim$400 kHz. This picture, however, contradicts the analysis in Chapter 3. Crucially, the DEER time traces measured (e.g. Fig 3.10), do not fit such a system. Attempts to simulate various configurations of multiple electron spin systems did not yield a result that resolves both the DEER data and the Ramsey data of Fig. C.3. Unfortunately, the relevant NV center was extinguished, so further data cannot be collected. Thus, this is an outstanding question, to be resolved in a more rigorous theoretical study, perhaps by thoroughly simulating potential multi-spin systems.

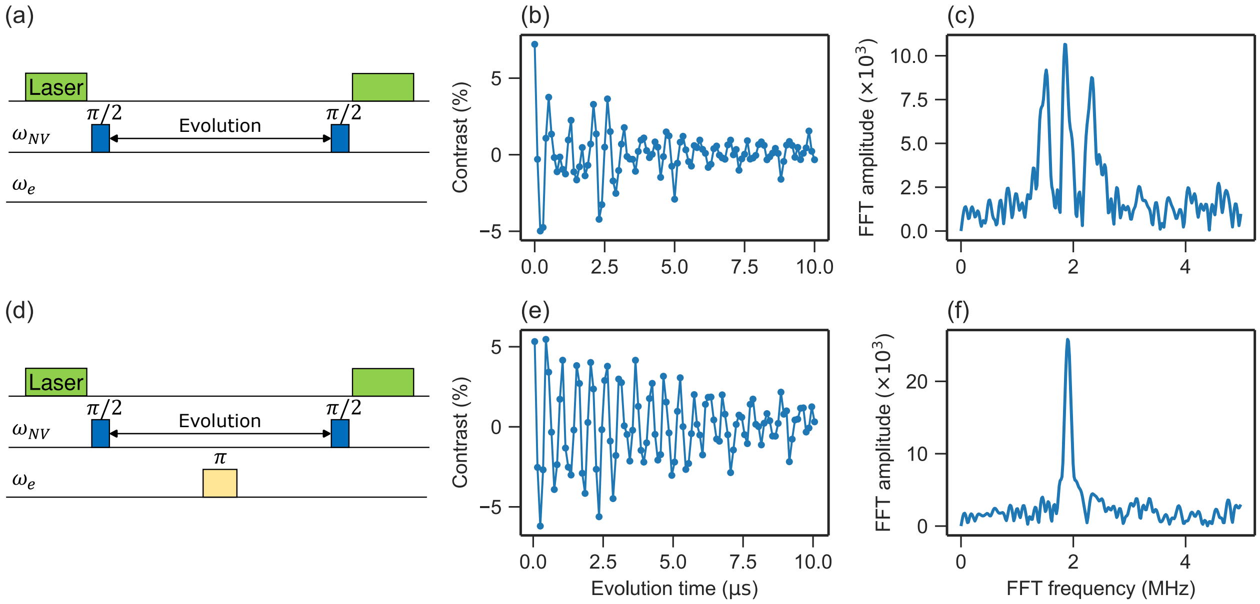

Figure C.3: Ramsey trace of NV with electrons in the vicinity. (a) Schematic of the standard Ramsey sequence. (b) A standard Ramsey experiment on the NV center studied in Chapter 3, exhibiting multiple frequencies. (c) FFT of the Ramsey trace in (b). (d) Schematic of the "decoupled" Ramsey sequence, with a π-pulse at the free electron spin frequency, embedded during the evolution time to decouple the electron spin from the evolution. (e) A "decoupled" Ramsey experiment trace. (f) FFT of the trace in (e).

D

Preliminary experiments toward single-molecule distance measurements

In Chapter 4, I theoretically discussed an experiment to measure the distance between two radicals in a single molecule using the NV center as a sensor. These experiments will be conducted at 5 K using our low-temperature setup. Due to various technical difficulties regarding the system that have since been resolved, these experiments did not materialize. In what follows, I include some information and preliminary data regarding materials procured for this experiment.

D.1 MATERIALS AND METHODS

EPR RULERS

The target molecules for single-molecule distance measurements are rigid organic molecules with radicals attached to two ends. These molecules are known as EPR rulers or yardsticks[115]. We have obtained three different rulers based on different types of radicals (Fig. D.1):

- Trityl biradical - trityls (triphenylmethyl) are an emerging type of spin label molecule. They are distinguished by negligible hyperfine constants, making them ideal for our low-field experiments, and are characterized by long relaxation times ($T_1 \approx 16\ \mu\text{s}$, $T_2 \approx 4\ \mu\text{s}$) at RT. The trityl biradicals were synthesized by the group of Prof. Olav Schiemann (Universität Bonn) and have a radical-radical distance of ~ 4 nm.
- Nitroxide biradical - nitroxides are the most common type of spin labels, and the radicals are commercially available. Nitroxides are characterized by significant hyperfine constants

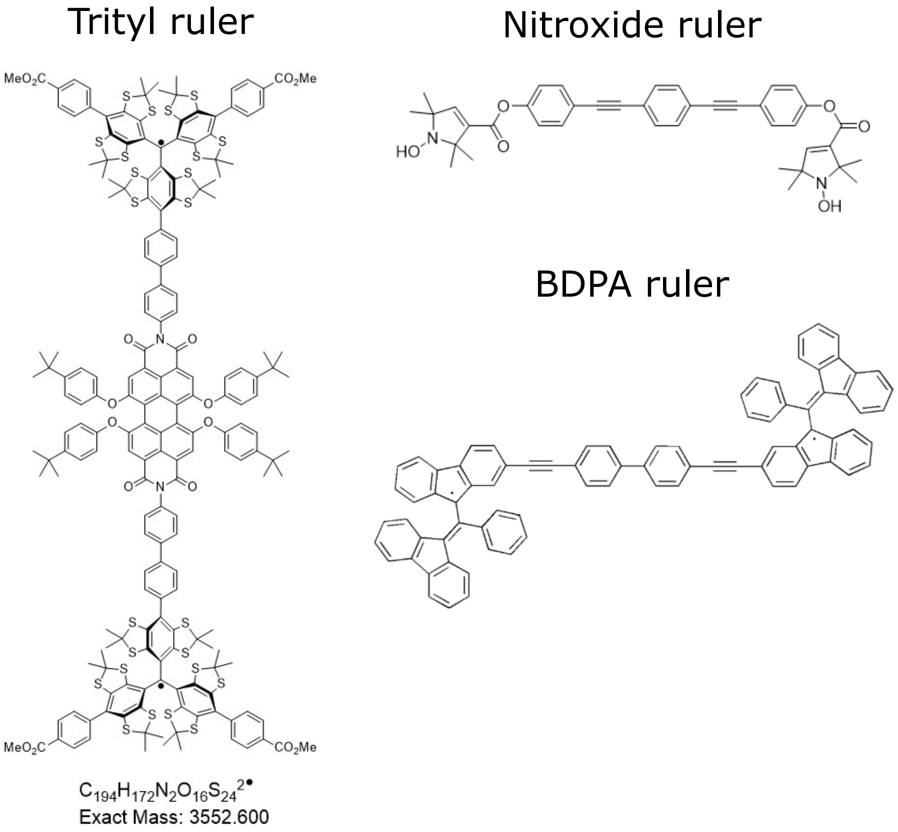

Figure D.1: EPR ”rulers” we have procured for single-molecule distance measurements. The trityl radicals are most suitable for RT experiments. The nitroxide ruler enables selective addressing of each of the radicals owing to the hyperfine splitting.

(∼100 MHz). This may present a challenge in the moderate fields we can apply at our low-temperature setup (<65 G, see Section 3.7 for a discussion on the matter). The nitroxide biradicals have a radical-radical distance of 2.83 nm. They were synthesized by Dr. Khriesto Shurrush of The Nancy and Stephen Grand Israel National Center for Personalized Medicine (G-INCPM), Weizmann Institute of Science.

- BDPA biradical[223] - BDPA (1,3-bisdiphenylene-2-phenylallyl) radicals are also known for long relaxation times at RT and small hyperfine constants. This has been synthesized by Dr. Khriesto Shurrush of The Nancy and Stephen Grand Israel National Center for Personalized Medicine (G-INCPM), Weizmann Institute of Science. These molecules have yet to be characterized.

The experiment paradigm assumes that the molecules are immobilized, i.e., there is no translational or rotational motion. Also, the molecules are to be dispersed and diluted on the surface of the diamond to minimize intermolecular dipolar interactions and optimize the probability of finding a single NV center coupled to a single molecule. The molecules are dissolved in a polystyrene matrix[36], immobilizing them while providing a relatively non-magnetic background. The target density of the molecules is 10^{-4}–10^{-3} nm^{-3}, and the concentration must be calculated according to the polystyrene beads chosen. This density, with a mean molecule-molecule distance of 10–20 nm, will optimize the probability of finding an NV with a single biradical in its sensing region. The polystyrene solution is then spin-coated on a diamond with NV centers, forming a thin, rigid

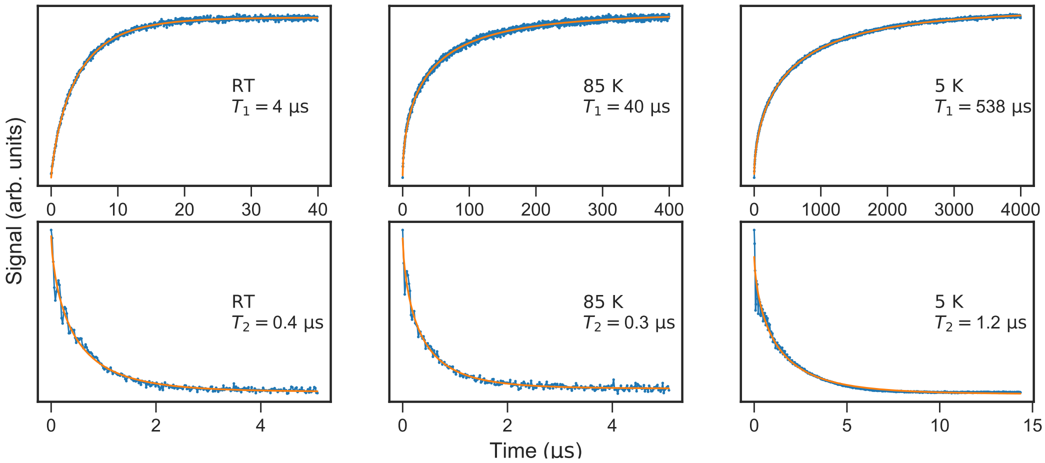

Figure D.2: EPR T_1 and T_2 measurements of nitroxide biradicals, taken at room temperature (RT), at liquid nitrogen temperature (85 K), and at liquid helium temperature (5 K). The data (blue dots) were fit to a stretched exponent (orange curves) to extract the lifetimes appearing in each plot. The values are consistent with literature values and indicate the possibility of working at room temperature.

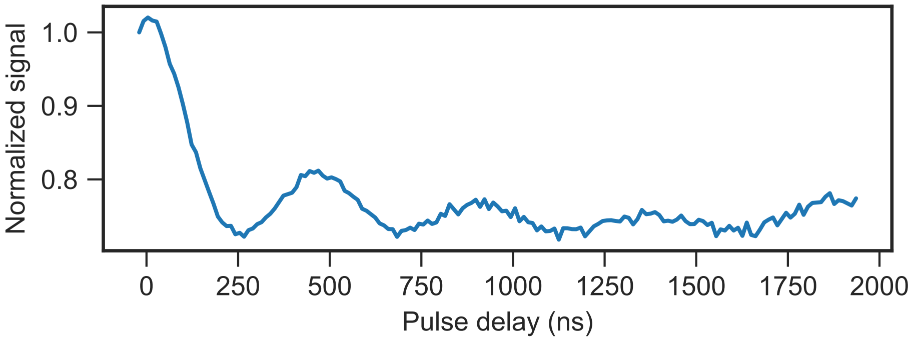

Figure D.3: DEER measurement of nitroxide biradicals in an X-band EPR spectrometer. The oscillations at 2.31 MHz indicate a radical-radical distance of 2.82 nm, as expected from the synthesis protocol.

polystyrene film.

D.2 Preliminary results on nitroxide biradicals

A sample of polystyrene with nitroxide biradicals was synthesized. A bulk sample was characterized using an EPR spectrometer (by Dr. Raanan Carmieli, Chemical Research Support, Weizmann Institute of Science). At RT, the T_2 was shorter than 0.5 μs, and T_1 =3.9 μs, consistent with the literature. At ∼5 K, we observed an appreciable memory time (1.2 μs), and T_1 =538 μs. We successfully measured the biradical distance (Fig. D.2) at 2.82 nm. These experiments verified the successful synthesis of the molecules. The result also confirms the preparation of the film, as dissolution and dispersion in the matrix, as aggregation would have led to damped spin relaxation. The appreciable T_1 at RT also indicates it may be possible to conduct the tomography experiments at RT with these radicals, as the measurement is only limited by the target spin's T_1 (and not T_2, as in conventional EPR).

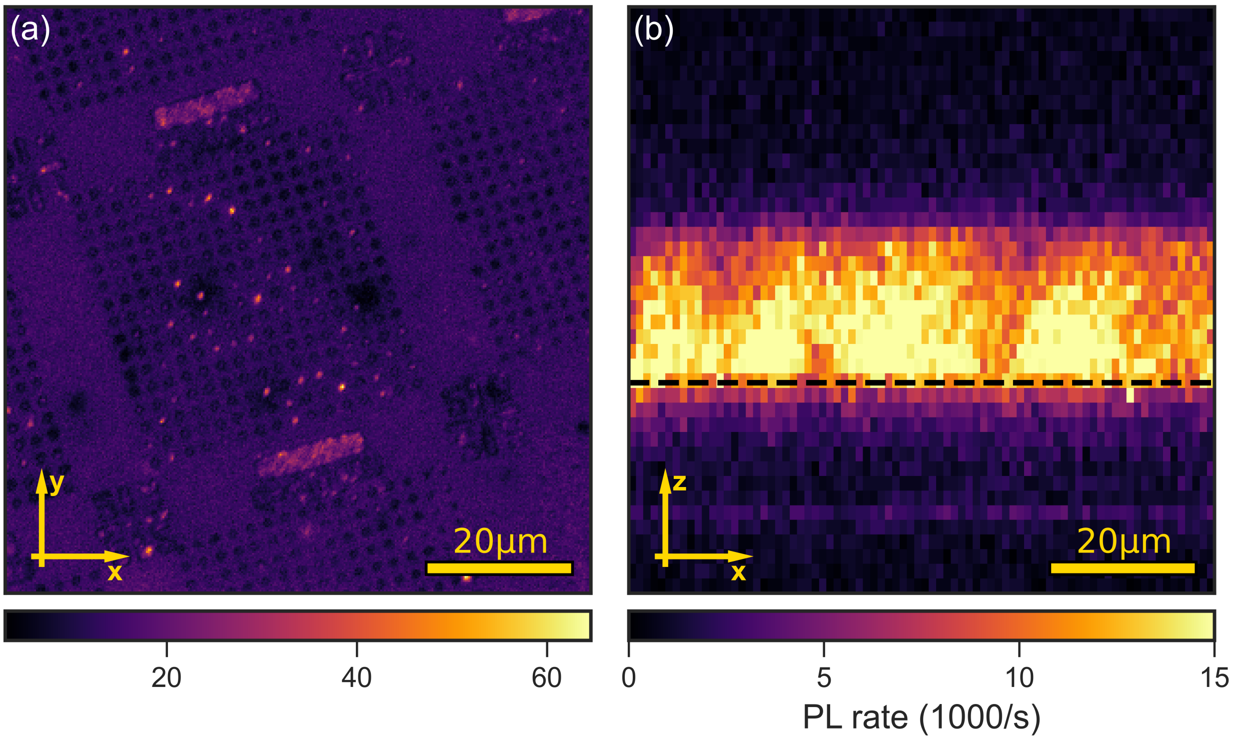

Figure D.4: Confocal image of a diamond membrane coated with polystyrene. (a) A lateral scan of the diamond membrane coated with polystyrene. The bright spots are NV centers, while the pillars appear darker than the background. (b) A depth scan of the membrane; the dashed line marks the focus plane. The polystyrene film appears to be ∼15 µm thick.

I spin-coated the biradical-polyester film to a diamond membrane and inspected it at RT. The spin-coated appeared differently in the confocal image; the nanopillars appeared darker than the flat background between the pillar arrays. This is probably due to laser scattering from the polystyrene matrix, which increases the photon count where the diamond is flat. Nonetheless, NV centers were visible with good contrast in this sample and could be measured by all the standard experiments. The polystyrene film was estimated to be ∼15 µm thick.

DEER signals were present in several of the NV centers. Still, there was no unambiguous fingerprint of the nitroxide biradicals, such as a DEER spectrum with a hyperfine splitting characteristic of nitroxide radicals[118,119]). Possible reasons for this are the nitroxide radical's fast RT relaxation time or a low molecule concentration in the film. These results confirm the validity of the sample-making process, and this route should be further studied, perhaps at 5 K.

The trityl biradical is most suited for RT experiments, and future experiments may focus on this material as a start, while nitroxide radicals at LT offer the possibility of selective excitation to avoid exciting diamond surface spins.

Bibliography

[1] R. M. Fratila and A. H. Velders, "Small-volume nuclear magnetic resonance spectroscopy," Annu. Rev. Anal. Chem. **4**, 227 (2011).

[2] Arthur Schweiger and Gunnar Jeschke, *Principles of Pulse Electron Paramagnetic Resonance*, 1st ed. (Oxford University Press, 2001).

[3] A. Webb, "Increasing the sensitivity of magnetic resonance spectroscopy and imaging," Anal. Chem. **84**, 9 (2012).

[4] N. Abhyankar, A. Agrawal, J. Campbell, T. Maly, P. Shrestha, and V. Szalai, "Recent advances in microresonators and supporting instrumentation for electron paramagnetic resonance spectroscopy," Rev. Sci. Instrum. **93**, 101101 (2022).

[5] Y. Artzi, Y. Twig, and A. Blank, "Induction-detection electron spin resonance with spin sensitivity of a few tens of spins," Applied Physics Letters **106**, 084104 (2015).

[6] A. Blank, Y. Twig, and Y. Ishay, "Recent trends in high spin sensitivity magnetic resonance," Journal of Magnetic Resonance **280**, 20 (2017).

[7] A. Bienfait, J. J. Pla, Y. Kubo, M. Stern, X. Zhou, C. C. Lo, C. D. Weis, T. Schenkel, M. L. W. Thewalt, D. Vion, D. Esteve, B. Julsgaard, K. Mølmer, J. J. L. Morton, and P. Bertet, "Reaching the quantum limit of sensitivity in electron spin resonance," Nature Nanotechnology **11**, 253 (2016).

[8] W. E. Moerner, Y. Shechtman, and Q. Wang, "Single-molecule spectroscopy and imaging over the decades," Faraday Discuss. **184**, 9 (2015).

[9] C. L. Degen, F. Reinhard, and P. Cappellaro, "Quantum sensing," Rev. Mod. Phys. **89**, 035002 (2017).

[10] R. Schirhagl, K. Chang, M. Loretz, and C. L. Degen, "Nitrogen-vacancy centers in diamond: nanoscale sensors for physics and biology," Ann. Phys. Chem. **65**, 83 (2014).

[11] A. T. Collins, "The characterisation of point defects in diamond by luminescence spectroscopy," Diam. Relat. Mater. **1**, 457 (1992).

[12] J. H. N. Loubser and J. A. van Wyk, "Electron spin resonance in the study of diamond," Rep. Prog. Phys. **41**, 1201 (1978).

[13] S. Felton, A. M. Edmonds, M. E. Newton, P. M. Martineau, D. Fisher, D. J. Twitchen, and J. M. Baker, "Hyperfine interaction in the ground state of the negatively charged nitrogen vacancy center in diamond," Phys. Rev. B **79**, 075203 (2009).

[14] M. W. Doherty, N. B. Manson, P. Delaney, F. Jelezko, J. Wrachtrup, and L. C. Hollenberg, "The nitrogen-vacancy colour centre in diamond," Phys. Rep. **528**, 1 (2013).

[15] L. Rondin, J.-P. Tetienne, T. Hingant, J.-F. Roch, P. Maletinsky, and V. Jacques, "Magnetometry with nitrogen-vacancy defects in diamond," Rep. Prog. Phys. **77**, 056503 (2014).

[16] D. Suter and F. Jelezko, "Single-spin magnetic resonance in the nitrogen-vacancy center of diamond," Prog. Nucl. Mag. Res. Sp. **98-99**, 50 (2017).

[17] A. Gruber, A. Dräbenstedt, C. Tietz, L. Fleury, J. Wrachtrup, and C. von Borczyskowski, "Scanning confocal optical microscopy and magnetic resonance on single defect centers," Science **276**, 2012 (1997).

[18] D. A. Hopper, H. J. Shulevitz, and L. C. Bassett, "Spin readout techniques of the nitrogen-vacancy center in diamond," Micromachines **9**, 437 (2018).

[19] L. Robledo, H. Bernien, T. van der Sar, and R. Hanson, "Spin dynamics in the optical cycle of single nitrogen-vacancy centres in diamond," New J. Phys. **13**, 025013 (2011).

[20] Y. Song, Y. Tian, Z. Hu, F. Zhou, T. Xing, D. Lu, B. Chen, Y. Wang, N. Xu, and J. Du, "Pulse-width-induced polarization enhancement of optically pumped N-V electron spin in diamond," Photon. Res. **8**, 1289 (2020).

[21] C. Kurtsiefer, S. Mayer, P. Zarda, and H. Weinfurter, "Stable solid-state source of single photons," Phys. Rev. Lett. **85**, 290 (2000).

[22] H. Paul, "Photon antibunching," Rev. Mod. Phys. **54**, 1061 (1982).

[23] J.-P. Tetienne, L. Rondin, P. Spinicelli, M. Chipaux, T. Debuisschert, J.-F. Roch, and V. Jacques, "Magnetic-field-dependent photodynamics of single NV defects in diamond: an application to qualitative all-optical magnetic imaging," New J. Phys. **14**, 103033 (2012).

[24] A. Wickenbrock, H. Zheng, L. Bougas, N. Leefer, S. Afach, A. Jarmola, V. M. Acosta, and D. Budker, "Microwave-free magnetometry with nitrogen-vacancy centers in diamond," Appl. Phys. Lett. **109**, 053505 (2016).

[25] H. Zheng, Z. Sun, G. Chatzidrosos, C. Zhang, K. Nakamura, H. Sumiya, T. Ohshima, J. Isoya, J. Wrachtrup, A. Wickenbrock, and D. Budker, "Microwave-free vector magnetometry with nitrogen-vacancy centers along a single axis in diamond," Phys. Rev. Appl. **13**, 044023 (2020).

[26] J. R. Maze, P. L. Stanwix, J. S. Hodges, S. Hong, J. M. Taylor, P. Cappellaro, L. Jiang, M. V. G. Dutt, E. Togan, A. S. Zibrov, A. Yacoby, R. L. Walsworth, and M. D. Lukin, "Nanoscale magnetic sensing with an individual electronic spin in diamond," Nature **455**, 644 (2008).

[27] J. M. Taylor, P. Cappellaro, L. Childress, L. Jiang, D. Budker, P. R. Hemmer, A. Yacoby, R. Walsworth, and M. D. Lukin, "High-sensitivity diamond magnetometer with nanoscale resolution," Nat. Phys. **4**, 810 (2008).

[28] G. Balasubramanian, I. Y. Chan, R. Kolesov, M. Al-Hmoud, J. Tisler, C. Shin, C. Kim, A. Wojcik, P. R. Hemmer, A. Krueger, T. Hanke, A. Leitenstorfer, R. Bratschitsch, F. Jelezko, and J. Wrachtrup, "Nanoscale imaging magnetometry with diamond spins under ambient conditions," Nature **455**, 648 (2008).

[29] V. M. Acosta, E. Bauch, M. P. Ledbetter, A. Waxman, L.-S. Bouchard, and D. Budker, "Temperature dependence of the nitrogen-vacancy magnetic resonance in diamond," Phys. Rev. Lett. **104**, 070801 (2010).

[30] D. M. Toyli, C. F. de las Casas, D. J. Christle, V. V. Dobrovitski, and D. D. Awschalom, "Fluorescence thermometry enhanced by the quantum coherence of single spins in diamond," Proc. Natl. Acad. Sci. **110**, 8417 (2013).

[31] M. W. Doherty, V. V. Struzhkin, D. A. Simpson, L. P. McGuinness, Y. Meng, A. Stacey, T. J. Karle, R. J. Hemley, N. B. Manson, L. C. L. Hollenberg, and S. Prawer, "Electronic properties and metrology applications of the diamond NV^- center under pressure," Phys. Rev. Lett. **112**, 047601 (2014).

[32] F. Dolde, H. Fedder, M. W. Doherty, T. Nöbauer, F. Rempp, G. Balasubramanian, T. Wolf, F. Reinhard, L. C. L. Hollenberg, F. Jelezko, and J. Wrachtrup, "Electric-field sensing using single diamond spins," Nat. Phys. **7**, 459 (2011).

[33] R. Amsüss, C. Koller, T. Nöbauer, S. Putz, S. Rotter, K. Sandner, S. Schneider, M. Schramböck, G. Steinhauser, H. Ritsch, J. Schmiedmayer, and J. Majer, "Cavity QED with magnetically coupled collective spin states," Phys. Rev. Lett. **107**, 060502 (2011).

[34] G.-Q. Liu, X. Feng, N. Wang, Q. Li, and R.-B. Liu, "Coherent quantum control of nitrogen-vacancy center spins near 1000 kelvin," Nat. Commun. **10**, 1344 (2019).

[35] T. Wolf, P. Neumann, K. Nakamura, H. Sumiya, T. Ohshima, J. Isoya, and J. Wrachtrup, "Subpicotesla diamond magnetometry," Phys. Rev. X **5**, 041001 (2015).

[36] H. J. Mamin, M. H. Sherwood, and D. Rugar, "Detecting external electron spins using nitrogen-vacancy centers," Phys. Rev. B **86**, 195422 (2012).

[37] T. Staudacher, F. Shi, S. Pezzagna, J. Meijer, J. Du, C. A. Meriles, F. Reinhard, and J. Wrachtrup, "Nuclear magnetic resonance spectroscopy on a (5-nanometer)^3 sample volume," Science **339**, 561 (2013).

[38] A. N. Obraztsov, P. G. Kopylov, B. A. Loginov, M. A. Dolganov, R. R. Ismagilov, and N. V. Savenko, "Single crystal diamond tips for scanning probe microscopy," Rev. Sci. Instrum. **81**, 013703 (2010).

[39] P. Maletinsky, S. Hong, M. S. Grinolds, B. Hausmann, M. D. Lukin, R. L. Walsworth, M. Loncar, and A. Yacoby, "A robust scanning diamond sensor for nanoscale imaging with single nitrogen-vacancy centres," Nat. Nanotechnol. **7**, 320 (2012).

[40] M. S. Grinolds, S. Hong, P. Maletinsky, L. Luan, M. D. Lukin, R. L. Walsworth, and A. Yacoby, "Nanoscale magnetic imaging of a single electron spin under ambient conditions," Nat. Phys. **9**, 215 (2013).

[41] A. M. Edmonds, U. F. S. D'Haenens-Johansson, R. J. Cruddace, M. E. Newton, K.-M. C. Fu, C. Santori, R. G. Beausoleil, D. J. Twitchen, and M. L. Markham, "Production of oriented nitrogen-vacancy color centers in synthetic diamond," Phys. Rev. B **86**, 035201 (2012).

[42] P. Siyushev, M. Nesladek, E. Bourgeois, M. Gulka, J. Hruby, T. Yamamoto, M. Trupke, T. Teraji, J. Isoya, and F. Jelezko, "Photoelectrical imaging and coherent spin-state readout of single nitrogen-vacancy centers in diamond," Science **363**, 728 (2019).

[43] B. J. Shields, Q. P. Unterreithmeier, N. P. de Leon, H. Park, and M. D. Lukin, "Efficient readout of a single spin state in diamond via spin-to-charge conversion," Phys. Rev. Lett. **114**, 136402 (2015).

[44] D. M. Irber, F. Poggiali, F. Kong, M. Kieschnick, T. Lühmann, D. Kwiatkowski, J. Meijer, J. Du, F. Shi, and F. Reinhard, "Robust all-optical single-shot readout of nitrogen-vacancy centers in diamond," Nat. Commun. **12**, 532 (2021).

[45] L. M. K. Vandersypen and I. L. Chuang, "Nmr techniques for quantum control and computation," Rev. Mod. Phys. **76**, 1037 (2005).

[46] E. L. Hahn, "Spin echoes," Phys. Rev. **80**, 580 (1950).

[47] H. Y. Carr and E. M. Purcell, "Effects of diffusion on free precession in nuclear magnetic resonance experiments," Phys. Rev. **94**, 630 (1954).

[48] L. Childress, M. V. G. Dutt, J. M. Taylor, A. S. Zibrov, F. Jelezko, J. Wrachtrup, P. R. Hemmer, and M. D. Lukin, "Coherent dynamics of coupled electron and nuclear spin qubits in diamond," Science **314**, 281 (2006).

[49] G. de Lange, Z. H. Wang, D. Ristè, V. V. Dobrovitski, and R. Hanson, "Universal dynamical decoupling of a single solid-state spin from a spin bath," Science **330**, 60 (2010).

[50] C. A. Ryan, J. S. Hodges, and D. G. Cory, "Robust decoupling techniques to extend quantum coherence in diamond," Phys. Rev. Lett. **105**, 200402 (2010).

[51] B. Naydenov, F. Dolde, L. T. Hall, C. Shin, H. Fedder, L. C. L. Hollenberg, F. Jelezko, and J. Wrachtrup, "Dynamical decoupling of a single-electron spin at room temperature," Phys. Rev. B **83**, 081201 (2011).

[52] N. Bar-Gill, L. Pham, A. Jarmola, D. Budker, and R. Walsworth, "Solid-state electronic spin coherence time approaching one second," Nat. Commun. **4**, 1743 (2013).

[53] M. H. Abobeih, J. Cramer, M. A. Bakker, N. Kalb, M. Markham, D. J. Twitchen, and T. H. Taminiau, "One-second coherence for a single electron spin coupled to a multi-qubit nuclear-spin environment," Nat. Commun. **9**, 2552 (2018).

[54] G. de Lange, D. Ristè, V. V. Dobrovitski, and R. Hanson, "Single-spin magnetometry with multipulse sensing sequences," Phys. Rev. Lett. **106**, 080802 (2011).

[55] Z.-H. Wang, G. de Lange, D. Ristè, R. Hanson, and V. V. Dobrovitski, "Comparison of dynamical decoupling protocols for a nitrogen-vacancy center in diamond," Phys. Rev. B **85**, 155204 (2012).

[56] J. M. Boss, K. Chang, J. Armijo, K. Cujia, T. Rosskopf, J. R. Maze, and C. L. Degen, "One- and two-dimensional nuclear magnetic resonance spectroscopy with a diamond quantum sensor," Phys. Rev. Lett. **116**, 197601 (2016).

[57] B. Grotz, J. Beck, P. Neumann, B. Naydenov, R. Reuter, F. Reinhard, F. Jelezko, J. Wrachtrup, D. Schweinfurth, B. Sarkar, and P. Hemmer, "Sensing external spins with nitrogen-vacancy diamond," New J. Phys. **13**, 055004 (2011).

[58] H. J. Mamin, M. Kim, M. H. Sherwood, C. T. Rettner, K. Ohno, D. D. Awschalom, and D. Rugar, "Nanoscale nuclear magnetic resonance with a nitrogen-vacancy spin sensor," Science **339**, 557 (2013).

[59] P. London, J. Scheuer, J.-M. Cai, I. Schwarz, A. Retzker, M. B. Plenio, M. Katagiri, T. Teraji, S. Koizumi, J. Isoya, R. Fischer, L. P. McGuinness, B. Naydenov, and F. Jelezko, "Detecting and polarizing nuclear spins with double resonance on a single electron spin," Phys. Rev. Lett. **111**, 067601 (2013).

[60] C. Belthangady, N. Bar-Gill, L. M. Pham, K. Arai, D. Le Sage, P. Cappellaro, and R. L. Walsworth, "Dressed-state resonant coupling between bright and dark spins in diamond," Phys. Rev. Lett. **110**, 157601 (2013).

[61] F. Shi, Q. Zhang, B. Naydenov, F. Jelezko, J. Du, F. Reinhard, and J. Wrachtrup, "Quantum logic readout and cooling of a single dark electron spin," Phys. Rev. B **87**, 195414 (2013).

[62] J. Köhler, J. A. J. M. Disselhorst, M. C. J. M. Donckers, E. J. J. Groenen, J. Schmidt, and W. E. Moerner, "Magnetic resonance of a single molecular spin," Nature **363**, 242 (1993).

[63] J. Wrachtrup, C. von Borczyskowski, J. Bernard, M. Orrit, and R. Brown, "Optical detection of magnetic resonance in a single molecule," Nature **363**, 244 (1993).

[64] M. Xiao, I. Martin, E. Yablonovitch, and H. W. Jiang, "Electrical detection of the spin resonance of a single electron in a silicon field-effect transistor," Nature **430**, 435 (2004).

[65] F. H. L. Koppens, C. Buizert, K. J. Tielrooij, I. T. Vink, K. C. Nowack, T. Meunier, L. P. Kouwenhoven, and L. M. K. Vandersypen, "Driven coherent oscillations of a single electron spin in a quantum dot," Nature **442**, 766 (2006).

[66] D. Rugar, R. Budakian, H. J. Mamin, and B. W. Chui, "Single spin detection by magnetic resonance force microscopy," Nature **430**, 329 (2004).

[67] C. L. Degen, M. Poggio, H. J. Mamin, C. T. Rettner, and D. Rugar, "Nanoscale magnetic resonance imaging," Proc. Natl. Acad. Sci. **106**, 1313 (2009).

[68] P. Willke, W. Paul, F. D. Natterer, K. Yang, Y. Bae, T. Choi, J. Fernández-Rossier, A. J. Heinrich, and C. P. Lutz, "Probing quantum coherence in single-atom electron spin resonance," Sci. Adv. **4**, eaaq1543 (2018).

[69] P. Willke, K. Yang, Y. Bae, A. J. Heinrich, and C. P. Lutz, "Magnetic resonance imaging of single atoms on a surface," Nat. Phys. **15**, 1005 (2019).

[70] P. Willke, T. Bilgeri, X. Zhang, Y. Wang, C. Wolf, H. Aubin, A. Heinrich, and T. Choi, "Coherent spin control of single molecules on a surface," ACS Nano **15**, 17959 (2021).

[71] B. Smeltzer, L. Childress, and A. Gali, "^{13}c hyperfine interactions in the nitrogen-vacancy centre in diamond," New J. Phys. **13**, 025021 (2011).

[72] V. Jacques, P. Neumann, J. Beck, M. Markham, D. Twitchen, J. Meijer, F. Kaiser, G. Balasubramanian, F. Jelezko, and J. Wrachtrup, "Dynamic polarization of single nuclear spins by optical pumping of nitrogen-vacancy color centers in diamond at room temperature," Phys. Rev. Lett. **102**, 057403 (2009).

[73] B. Smeltzer, J. McIntyre, and L. Childress, "Robust control of individual nuclear spins in diamond," Phys. Rev. A **80**, 050302 (2009).

[74] S. Kolkowitz, Q. P. Unterreithmeier, S. D. Bennett, and M. D. Lukin, "Sensing distant nuclear spins with a single electron spin," Phys. Rev. Lett. **109**, 137601 (2012).

[75] T. H. Taminiau, J. J. T. Wagenaar, T. van der Sar, F. Jelezko, V. V. Dobrovitski, and R. Hanson, "Detection and control of individual nuclear spins using a weakly coupled electron spin," Phys. Rev. Lett. **109**, 137602 (2012).

[76] N. Zhao, J. Honert, B. Schmid, M. Klas, J. Isoya, M. Markham, D. Twitchen, F. Jelezko, R.-B. Liu, H. Fedder, and J. Wrachtrup, "Sensing single remote nuclear spins," Nat. Nanotechnol. **7**, 657 (2012).

[77] J. R. Maze, J. M. Taylor, and M. D. Lukin, "Electron spin decoherence of single nitrogen-vacancy defects in diamond," Phys. Rev. B **78**, 094303 (2008).

[78] N. Zhao, S.-W. Ho, and R.-B. Liu, "Decoherence and dynamical decoupling control of nitrogen vacancy center electron spins in nuclear spin baths," Phys. Rev. B **85**, 115303 (2012).

[79] N. Zhao, J.-L. Hu, S.-W. Ho, J. T. K. Wan, and R. B. Liu, "Atomic-scale magnetometry of distant nuclear spin clusters via nitrogen-vacancy spin in diamond," Nat. Nanotechnol. **6**, 242 (2011).

[80] F. Shi, X. Kong, P. Wang, F. Kong, N. Zhao, R.-B. Liu, and J. Du, "Sensing and atomic-scale structure analysis of single nuclear-spin clusters in diamond," Nat. Phys. **10**, 21 (2014).

[81] J. Zopes, K. Herb, K. S. Cujia, and C. L. Degen, "Three-dimensional nuclear spin positioning using coherent radio-frequency control," Phys. Rev. Lett. **121**, 170801 (2018).

[82] M. H. Abobeih, J. Randall, C. E. Bradley, H. P. Bartling, M. A. Bakker, M. J. Degen, M. Markham, D. J. Twitchen, and T. H. Taminiau, "Atomic-scale imaging of a 27-nuclear-spin cluster using a quantum sensor," Nature **576**, 411 (2019).

[83] K. S. Cujia, K. Herb, J. Zopes, J. M. Abendroth, and C. L. Degen, "Parallel detection and spatial mapping of large nuclear spin clusters," Nat. Commun. **13**, 1260 (2022).

[84] J. Zopes, K. S. Cujia, K. Sasaki, J. M. Boss, K. M. Itoh, and C. L. Degen, "Three-dimensional localization spectroscopy of individual nuclear spins with sub-angstrom resolution," Nat. Commun. **9**, 4678 (2018).

[85] J. Randall, C. E. Bradley, F. V. van der Gronden, A. Galicia, M. H. Abobeih, M. Markham, D. J. Twitchen, F. Machado, N. Y. Yao, and T. H. Taminiau, "Many-body–localized discrete time crystal with a programmable spin-based quantum simulator," Science **374**, 1474 (2021).

[86] M. H. Abobeih, Y. Wang, J. Randall, S. J. H. Loenen, C. E. Bradley, M. Markham, D. J. Twitchen, B. M. Terhal, and T. H. Taminiau, "Fault-tolerant operation of a logical qubit in a diamond quantum processor," Nature **606**, 884 (2022).

[87] M. Loretz, S. Pezzagna, J. Meijer, and C. L. Degen, "Nanoscale nuclear magnetic resonance with a 1.9-nm-deep nitrogen-vacancy sensor," Appl. Phys. Lett. **104**, 033102 (2014).

[88] A. O. Sushkov, I. Lovchinsky, N. Chisholm, R. L. Walsworth, H. Park, and M. D. Lukin, "Magnetic resonance detection of individual proton spins using quantum reporters," Phys. Rev. Lett. **113**, 197601 (2014).

[89] K. Sasaki, H. Watanabe, H. Sumiya, K. M. Itoh, and E. Abe, "Detection and control of single proton spins in a thin layer of diamond grown by chemical vapor deposition," Appl. Phys. Lett. **117**, 114002 (2020).

[90] T. Staudacher, N. Raatz, S. Pezzagna, J. Meijer, F. Reinhard, C. A. Meriles, and J. Wrachtrup, "Probing molecular dynamics at the nanoscale via an individual paramagnetic centre," Nat. Commun. **6**, 8527 (2015).

[91] D. Rugar, H. J. Mamin, M. H. Sherwood, M. Kim, C. T. Rettner, K. Ohno, and D. D. Awschalom, "Proton magnetic resonance imaging using a nitrogen–vacancy spin sensor," Nat. Nanotechnol. **10**, 120 (2015).

[92] F. Casola, T. van der Sar, and A. Yacoby, "Probing condensed matter physics with magnetometry based on nitrogen-vacancy centres in diamond," Nat. Rev. Mater. **3**, 17088 (2018).

[93] A. Laraoui, F. Dolde, C. Burk, F. Reinhard, J. Wrachtrup, and C. A. Meriles, "High-resolution correlation spectroscopy of ^{13}c spins near a nitrogen-vacancy centre in diamond," Nat. Commun. **4** (2013), 10.1038/ncomms2685.

[94] A. Ajoy, U. Bissbort, M. D. Lukin, R. L. Walsworth, and P. Cappellaro, "Atomic-scale nuclear spin imaging using quantum-assisted sensors in diamond," Phys. Rev. X **5**, 011001 (2015).

[95] I. Lovchinsky, A. O. Sushkov, E. Urbach, N. P. de Leon, S. Choi, K. D. Greve, R. Evans, R. Gertner, E. Bersin, C. Müller, L. McGuinness, F. Jelezko, R. L. Walsworth, H. Park, and M. D. Lukin, "Nuclear magnetic resonance detection and spectroscopy of single proteins using quantum logic," Science **351**, 836 (2016).

[96] N. Aslam, M. Pfender, P. Neumann, R. Reuter, A. Zappe, F. F. de Oliveira, A. Denisenko, H. Sumiya, S. Onoda, J. Isoya, and J. Wrachtrup, "Nanoscale nuclear magnetic resonance with chemical resolution," Science **357**, 67 (2017).

[97] T. Rosskopf, J. Zopes, J. M. Boss, and C. L. Degen, "A quantum spectrum analyzer enhanced by a nuclear spin memory," npj Quantum Inf. **3**, 33 (2017).

[98] J. M. Boss, K. S. Cujia, J. Zopes, and C. L. Degen, "Quantum sensing with arbitrary frequency resolution," Science **356**, 837 (2017).

[99] S. Schmitt, T. Gefen, F. M. Stürner, T. Unden, G. Wolff, C. Müller, J. Scheuer, B. Naydenov, M. Markham, S. Pezzagna, J. Meijer, I. Schwarz, M. Plenio, A. Retzker, L. P. McGuinness, and F. Jelezko, "Submillihertz magnetic spectroscopy performed with a nanoscale quantum sensor," Science **356**, 832 (2017).

[100] M. Pfender, P. Wang, H. Sumiya, S. Onoda, W. Yang, D. B. R. Dasari, P. Neumann, X.-Y. Pan, J. Isoya, R.-B. Liu, and J. Wrachtrup, "High-resolution spectroscopy of single nuclear spins via sequential weak measurements," Nat. Commun. **10**, 594 (2019).

[101] D. R. Glenn, D. B. Bucher, J. Lee, M. D. Lukin, H. Park, and R. L. Walsworth, "High-resolution magnetic resonance spectroscopy using a solid-state spin sensor," Nature **555**, 351 (2018).

[102] S. J. DeVience, L. M. Pham, I. Lovchinsky, A. O. Sushkov, N. Bar-Gill, C. Belthangady, F. Casola, M. Corbett, H. Zhang, M. Lukin, H. Park, A. Yacoby, and R. L. Walsworth, "Nanoscale NMR spectroscopy and imaging of multiple nuclear species," Nat. Nanotechnol. **10**, 129 (2015).

[103] C. Müller, X. Kong, J.-M. Cai, K. Melentijević, A. Stacey, M. Markham, D. Twitchen, J. Isoya, S. Pezzagna, J. Meijer, J. F. Du, M. B. Plenio, B. Naydenov, L. P. McGuinness, and F. Jelezko, "Nuclear magnetic resonance spectroscopy with single spin sensitivity," Nat. Commun. **5**, 4703 (2014).

[104] A. O. Sushkov, N. Chisholm, I. Lovchinsky, M. Kubo, P. K. Lo, S. D. Bennett, D. Hunger, A. Akimov, R. L. Walsworth, H. Park, and M. D. Lukin, "All-optical sensing of a single-molecule electron spin," Nano Lett. **14**, 6443 (2014).

[105] K. Zhang, S. Ghosh, S. Saxena, and M. V. G. Dutt, "Nanoscale spin detection of copper ions using double electron-electron resonance at room temperature," Phys. Rev. B **104**, 224412 (2021).

[106] M. S. Grinolds, M. Warner, K. De Greve, Y. Dovzhenko, L. Thiel, R. L. Walsworth, S. Hong, P. Maletinsky, and A. Yacoby, "Subnanometre resolution in three-dimensional magnetic resonance imaging of individual dark spins," Nat. Nanotechnol. **9**, 279 (2014).

[107] B. Fortman and S. Takahashi, "Understanding the linewidth of the ESR spectrum detected by a single NV center in diamond," J. Phys. Chem. A **123**, 6350 (2019).

[108] F. Kong, P. Zhao, X. Ye, Z. Wang, Z. Qin, P. Yu, J. Su, F. Shi, and J. Du, "Nanoscale zero-field electron spin resonance spectroscopy," Nat. Commun. **9** (2018), 10.1038/s41467-018-03969-4.

[109] F. Kong, P. Zhao, P. Yu, Z. Qin, Z. Huang, Z. Wang, M. Wang, F. Shi, and J. Du, "Kilohertz electron paramagnetic resonance spectroscopy of single nitrogen centers at zero magnetic field," Sci. Adv. **6**, eaaz8244 (2020).

[110] B. Fortman, J. Pena, K. Holczer, and S. Takahashi, "Demonstration of NV-detected ESR spectroscopy at 115 GHz and 4.2 T," Appl. Phys. Lett. **116**, 174004 (2020).

[111] A. Cooper, W. K. C. Sun, J.-C. Jaskula, and P. Cappellaro, "Identification and control of electron-nuclear spin defects in diamond," Phys. Rev. Lett. **124**, 083602 (2020).

[112] H. P. Bartling, M. H. Abobeih, B. Pingault, M. J. Degen, S. J. H. Loenen, C. E. Bradley, J. Randall, M. Markham, D. J. Twitchen, and T. H. Taminiau, "Entanglement of spin-pair qubits with intrinsic dephasing times exceeding a minute," Phys. Rev. X **12**, 011048 (2022).

[113] L. J. Berliner and H. Fujii, "Magnetic resonance imaging of biological specimens by electron paramagnetic resonance of nitroxide spin labels," Science **227**, 517 (1985).

[114] L. J. Berliner, *Spin Labeling The Next Millennium* (Springer New York, NY, 2002).

[115] G. Jeschke, "Distance measurements in the nanometer range by pulse EPR," ChemPhysChem **3**, 927 (2002).

[116] G. Jeschke, "DEER distance measurements on proteins," Ann. Phys. Chem. **63**, 419 (2012).

[117] A. Martorana, G. Bellapadrona, A. Feintuch, E. Di Gregorio, S. Aime, and D. Goldfarb, "Probing protein conformation in cells by EPR distance measurements using Gd^{3+} spin labeling," J. Am. Chem. Soc. **136**, 13458 (2014).

[118] F. Shi, Q. Zhang, P. Wang, H. Sun, J. Wang, X. Rong, M. Chen, C. Ju, F. Reinhard, H. Chen, J. Wrachtrup, J. Wang, and J. Du, "Single-protein spin resonance spectroscopy under ambient conditions," Science **347**, 1135 (2015).

[119] L. Schlipf, T. Oeckinghaus, K. Xu, D. B. R. Dasari, A. Zappe, F. F. de Oliveira, B. Kern, M. Azarkh, M. Drescher, M. Ternes, K. Kern, J. Wrachtrup, and A. Finkler, "A molecular quantum spin network controlled by a single qubit," Sci. Adv. **3**, e1701116 (2017).

[120] J. F. Ziegler, M. Ziegler, and J. Biersack, "SRIM – the stopping and range of ions in matter (2010)," Nucl. Instrum. Methods Phys. Res. Sect. B Beam Interact. Mater. At. **268**, 1818 (2010).

[121] L. M. Pham, S. J. DeVience, F. Casola, I. Lovchinsky, A. O. Sushkov, E. Bersin, J. Lee, E. Urbach, P. Cappellaro, H. Park, A. Yacoby, M. Lukin, and R. L. Walsworth, "NMR technique for determining the depth of shallow nitrogen-vacancy centers in diamond," Phys. Rev. B **93**, 045425 (2016).

[122] B. A. Myers, A. Das, M. C. Dartiailh, K. Ohno, D. D. Awschalom, and A. C. Bleszynski Jayich, "Probing surface noise with depth-calibrated spins in diamond," Phys. Rev. Lett. **113**, 027602 (2014).

[123] Y. Romach, C. Müller, T. Unden, L. J. Rogers, T. Isoda, K. M. Itoh, M. Markham, A. Stacey, J. Meijer, S. Pezzagna, B. Naydenov, L. P. McGuinness, N. Bar-Gill, and F. Jelezko, "Spectroscopy of surface-induced noise using shallow spins in diamond," Phys. Rev. Lett. **114**, 017601 (2015).

[124] B. A. Myers, A. Ariyaratne, and A. C. B. Jayich, "Double-quantum spin-relaxation limits to coherence of near-surface nitrogen-vacancy centers," Phys. Rev. Lett. **118**, 197201 (2017).

[125] A. Stacey, N. Dontschuk, J.-P. Chou, D. A. Broadway, A. K. Schenk, M. J. Sear, J.-P. Tetienne, A. Hoffman, S. Prawer, C. I. Pakes, A. Tadich, N. P. de Leon, A. Gali, and L. C. L. Hollenberg, "Evidence for primal sp^2 defects at the diamond surface: candidates for electron trapping and noise sources," Adv. Mater. Interfaces **6**, 1801449 (2019).

[126] B. L. Dwyer, L. V. Rodgers, E. K. Urbach, D. Bluvstein, S. Sangtawesin, H. Zhou, Y. Nassab, M. Fitzpatrick, Z. Yuan, K. De Greve, E. L. Peterson, H. Knowles, T. Sumarac, J.-P. Chou, A. Gali, V. Dobrovitski, M. D. Lukin, and N. P. de Leon, "Probing spin dynamics on diamond surfaces using a single quantum sensor," PRX Quantum **3**, 040328 (2022).

[127] T. Rosskopf, A. Dussaux, K. Ohashi, M. Loretz, R. Schirhagl, H. Watanabe, S. Shikata, K. M. Itoh, and C. L. Degen, "Investigation of surface magnetic noise by shallow spins in diamond," Phys. Rev. Lett. **112**, 147602 (2014).

[128] D. Bluvstein, Z. Zhang, and A. C. B. Jayich, "Identifying and mitigating charge instabilities in shallow diamond nitrogen-vacancy centers," Phys. Rev. Lett. **122**, 076101 (2019).

[129] Z. Yuan, M. Fitzpatrick, L. V. H. Rodgers, S. Sangtawesin, S. Srinivasan, and N. P. de Leon, "Charge state dynamics and optically detected electron spin resonance contrast of shallow nitrogen-vacancy centers in diamond," Phys. Rev. Res. **2**, 033263 (2020).

[130] D. Bluvstein, Z. Zhang, C. A. McLellan, N. R. Williams, and A. C. B. Jayich, "Extending the quantum coherence of a near-surface qubit by coherently driving the paramagnetic surface environment," Phys. Rev. Lett. **123**, 146804 (2019).

[131] W. Zheng, K. Bian, X. Chen, Y. Shen, S. Zhang, R. Stöhr, A. Denisenko, J. Wrachtrup, S. Yang, and Y. Jiang, "Coherence enhancement of solid-state qubits by local manipulation of the electron spin bath," Nat. Phys. **18**, 1317 (2022).

[132] S. Kawai, H. Yamano, T. Sonoda, K. Kato, J. J. Buendia, T. Kageura, R. Fukuda, T. Okada, T. Tanii, T. Higuchi, M. Haruyama, K. Yamada, S. Onoda, T. Ohshima, W. Kada,

O. Hanaizumi, A. Stacey, T. Teraji, S. Kono, J. Isoya, and H. Kawarada, "Nitrogen-terminated diamond surface for nanoscale NMR by shallow nitrogen-vacancy centers," J. Phys. Chem. C **123**, 3594 (2019).

[133] H. Yamano, S. Kawai, K. Kato, T. Kageura, M. Inaba, T. Okada, I. Higashimata, M. Haruyama, T. Tanii, K. Yamada, S. Onoda, W. Kada, O. Hanaizumi, T. Teraji, J. Isoya, and H. Kawarada, "Charge state stabilization of shallow nitrogen vacancy centers in diamond by oxygen surface modification," Jpn. J. Appl. Phys. **56**, 04CK08 (2017).

[134] S. Sangtawesin, B. L. Dwyer, S. Srinivasan, J. J. Allred, L. V. H. Rodgers, K. De Greve, A. Stacey, N. Dontschuk, K. M. O'Donnell, D. Hu, D. A. Evans, C. Jaye, D. A. Fischer, M. L. Markham, D. J. Twitchen, H. Park, M. D. Lukin, and N. P. de Leon, "Origins of diamond surface noise probed by correlating single-spin measurements with surface spectroscopy," Phys. Rev. X **9**, 031052 (2019).

[135] Y. Hao, Z. Yang, Z. Li, X. Kong, W. Tang, T. Xie, S. Xu, X. Ye, P. Yu, P. Wang, Y. Wang, Z. Qiao, L. Gao, J.-H. Jiang, F. Shi, and J. Du, "Sensing orbital hybridization of graphene-diamond interface with a single spin," (2023), arXiv:2305.09540 [quant-ph].

[136] E. Janitz, K. Herb, L. A. Völker, W. S. Huxter, C. L. Degen, and J. M. Abendroth, "Diamond surface engineering for molecular sensing with nitrogen—vacancy centers," J. Mater. Chem. C **10**, 13533 (2022).

[137] T. Häberle, T. Oeckinghaus, D. Schmid-Lorch, M. Pfender, F. F. de Oliveira, S. A. Momenzadeh, A. Finkler, and J. Wrachtrup, "Nuclear quantum-assisted magnetometer," Rev. Sci. Instrum. **88**, 013702 (2017).

[138] T. van der Sar, F. Casola, R. Walsworth, and A. Yacoby, "Nanometre-scale probing of spin waves using single electron spins," Nat. Commun. **6**, 7886 (2015).

[139] B. A. Myers, *Quantum decoherence of near-surface nitrogen-vacancy centers in diamond and implications for nanoscale imaging*, Ph.D. thesis, University of California, Santa Barbara (2016).

[140] X.-D. Chen, F.-W. Sun, C.-L. Zou, J.-M. Cui, L.-M. Zhou, and G.-C. Guo, "Vector magnetic field sensing by a single nitrogen vacancy center in diamond," Europhys. Lett. **101**, 67003 (2013).

[141] L. Schlipf, *Nanoscale Electron Spin Resonance*, Ph.D. thesis, Universität Stuttgart, Stuttgart (2017).

[142] J. M. Binder, A. Stark, N. Tomek, J. Scheuer, F. Frank, K. D. Jahnke, C. Müller, S. Schmitt, M. H. Metsch, T. Unden, T. Gehring, A. Huck, U. L. Andersen, L. J. Rogers, and F. Jelezko, "Qudi: A modular python suite for experiment control and data processing," SoftwareX **6**, 85 (2017).

[143] S. A. Momenzadeh, R. J. Stöhr, F. F. de Oliveira, A. Brunner, A. Denisenko, S. Yang, F. Reinhard, and J. Wrachtrup, "Nanoengineered diamond waveguide as a robust bright platform for nanomagnetometry using shallow nitrogen vacancy centers," Nano Lett. **15**, 165 (2015).

[144] K. J. Brown, E. Chartier, E. M. Sweet, D. A. Hopper, and L. C. Bassett, "Cleaning diamond surfaces using boiling acid treatment in a standard laboratory chemical hood," J. Chem. Health Saf. **26**, 40 (2019).

[145] D. Yudilevich, R. Stöhr, A. Denisenko, and A. Finkler, "Mapping single electron spins with magnetic tomography," Phys. Rev. Appl. **18**, 054016 (2022).

[146] O. Schiemann and T. F. Prisner, "Long-range distance determinations in biomacromolecules by EPR spectroscopy," Q. Rev. Biophys. **40**, 1–53 (2007).

[147] D. Marion, "An introduction to biological NMR spectroscopy," Mol. Cell. Proteomics **12**, 3006 (2013).

[148] W. L. Hubbell, C. J. López, C. Altenbach, and Z. Yang, "Technological advances in site-directed spin labeling of proteins," Curr. Opin. Struc. Biol. **23**, 725 (2013).

[149] L. Rondin, J.-P. Tetienne, P. Spinicelli, C. Dal Savio, K. Karrai, G. Dantelle, A. Thiaville, S. Rohart, J.-F. Roch, and V. Jacques, "Nanoscale magnetic field mapping with a single spin scanning probe magnetometer," Appl. Phys. Lett. **100**, 153118 (2012).

[150] J. Cai, F. Jelezko, M. B. Plenio, and A. Retzker, "Diamond-based single-molecule magnetic resonance spectroscopy," New J. Phys. **15**, 013020 (2013).

[151] M. R. Wasielewski, M. D. E. Forbes, N. L. Frank, K. Kowalski, G. D. Scholes, J. Yuen-Zhou, M. A. Baldo, D. E. Freedman, R. H. Goldsmith, T. Goodson, M. L. Kirk, J. K. McCusker, J. P. Ogilvie, D. A. Shultz, S. Stoll, and K. B. Whaley, "Exploiting chemistry and molecular systems for quantum information science," Nat. Rev. Chem. **4**, 490 (2020).

[152] C. Durkan and M. E. Welland, "Electronic spin detection in molecules using scanning-tunneling- microscopy-assisted electron-spin resonance," Appl. Phys. Lett. **80**, 458 (2002).

[153] Y. Artzi, O. Zgadzai, B. Solomon, and A. Blank, "Three-dimensional fourier imaging of thousands of individual solid-state quantum bits – a tool for spin-based quantum technology," Physica Scripta **98**, 035815 (2023).

[154] A. Kak, "Computerized tomography with X-ray, emission, and ultrasound sources," Proc. IEEE **67**, 1245 (1979).

[155] R. Nagy, M. Niethammer, M. Widmann, Y.-C. Chen, P. Udvarhelyi, C. Bonato, J. U. Hassan, R. Karhu, I. G. Ivanov, N. T. Son, J. R. Maze, T. Ohshima, �. O. Soykal, �. Gali, S.-Y. Lee, F. Kaiser, and J. Wrachtrup, "High-fidelity spin and optical control of single silicon-vacancy centres in silicon carbide," Nat. Commun. **10**, 1954 (2019).

[156] B. J. Maertz, A. P. Wijnheijmer, G. D. Fuchs, M. E. Nowakowski, and D. D. Awschalom, "Vector magnetic field microscopy using nitrogen vacancy centers in diamond," Appl. Phys. Lett. **96**, 092504 (2010).

[157] P. Neumann, R. Kolesov, B. Naydenov, J. Beck, F. Rempp, M. Steiner, V. Jacques, G. Balasubramanian, M. L. Markham, D. J. Twitchen, S. Pezzagna, J. Meijer, J. Twamley, F. Jelezko, and J. Wrachtrup, "Quantum register based on coupled electron spins in a room-temperature solid," Nat. Phys. **6**, 249 (2010).

[158] J. Michl, T. Teraji, S. Zaiser, I. Jakobi, G. Waldherr, F. Dolde, P. Neumann, M. W. Doherty, N. B. Manson, J. Isoya, and J. Wrachtrup, "Perfect alignment and preferential orientation of nitrogen-vacancy centers during chemical vapor deposition diamond growth on (111) surfaces," Appl. Phys. Lett. **104**, 102407 (2014).

[159] D. Marsh, *Spin-label electron paramagnetic resonance spectroscopy* (CRC Press, 2019).

[160] S. Lee, T. C. Sandreczki, and I. M. Brown, "Analyses of the electron-spin-resonance (ESR) hyperfine powder spectra of nitroxide radicals enriched with 15N (I=1/2)," J. Chem. Phys. **80**, 3983 (1984).

[161] C. Munuera-Javaloy, R. Puebla, B. D'Anjou, M. B. Plenio, and J. Casanova, "Detection of molecular transitions with nitrogen-vacancy centers and electron-spin labels," npj Quantum Inf. **8**, 140 (2022).

[162] J. J. Jassoy, A. Berndhäuser, F. Duthie, S. P. Kühn, G. Hagelueken, and O. Schiemann, "Versatile trityl spin labels for nanometer distance measurements on biomolecules in vitro and within cells," Angew. Chem. - Int. Ed. **56**, 177 (2017).

[163] A. A. Kuzhelev, O. A. Krumkacheva, G. Y. Shevelev, M. Yulikov, M. V. Fedin, and E. G. Bagryanskaya, "Room-temperature distance measurements using RIDME and the orthogonal spin labels trityl/nitroxide," Phys. Chem. Chem. Phys. **20**, 10224 (2018).

[164] S. Trukhan, V. Yudanov, V. Tormyshev, O. Rogozhnikova, D. Trukhin, M. Bowman, M. Krzyaniak, H. Chen, and O. Martyanov, "Hyperfine interactions of narrow-line trityl radical with solvent molecules," J. Magn. Reson. **233**, 29 (2013).

[165] A. A. Kuzhelev, D. V. Trukhin, O. A. Krumkacheva, R. K. Strizhakov, O. Y. Rogozhnikova, T. I. Troitskaya, M. V. Fedin, V. M. Tormyshev, and E. G. Bagryanskaya, "Room-temperature electron spin relaxation of triarylmethyl radicals at the X- and Q-bands," J. Phys. Chem. B **119**, 13630 (2015).

[166] D. Yudilevich, A. Salhov, I. Schaefer, K. Herb, A. Retzker, and A. Finkler, "Coherent manipulation of nuclear spins in the strong driving regime," New J. Phys. **25**, 113042 (2023).

[167] J. Smits, J. T. Damron, P. Kehayias, A. F. McDowell, N. Mosavian, I. Fescenko, N. Ristoff, A. Laraoui, A. Jarmola, and V. M. Acosta, "Two-dimensional nuclear magnetic resonance spectroscopy with a microfluidic diamond quantum sensor," Sci. Adv. **5**, eaaw7895 (2019).

[168] Y.-X. Liu, A. Ajoy, and P. Cappellaro, "Nanoscale vector dc magnetometry via ancilla-assisted frequency up-conversion," Phys. Rev. Lett. **122**, 100501 (2019).

[169] G. Wang, Y.-X. Liu, Y. Zhu, and P. Cappellaro, "Nanoscale vector AC magnetometry with a single nitrogen-vacancy center in diamond," Nano Lett. **21**, 5143 (2021).

[170] C. Munuera-Javaloy, A. Tobalina, and J. Casanova, "High-resolution NMR spectroscopy at large fields with nitrogen vacancy centers," Phys. Rev. Lett. **130**, 133603 (2023).

[171] G. D. Fuchs, V. V. Dobrovitski, D. M. Toyli, F. J. Heremans, and D. D. Awschalom, "Gigahertz dynamics of a strongly driven single quantum spin," Science **326**, 1520 (2009).

[172] K. Herb, J. Zopes, K. S. Cujia, and C. L. Degen, "Broadband radio-frequency transmitter for fast nuclear spin control," Rev. Sci. Instrum. **91**, 113106 (2020).

[173] M. W. Doherty, F. Dolde, H. Fedder, F. Jelezko, J. Wrachtrup, N. B. Manson, and L. C. L. Hollenberg, "Theory of the ground-state spin of the nv$^-$ center in diamond," Phys. Rev. B **85**, 205203 (2012).

[174] Z.-Y. Wang, J. E. Lang, S. Schmitt, J. Lang, J. Casanova, L. McGuinness, T. S. Monteiro, F. Jelezko, and M. B. Plenio, "Randomization of pulse phases for unambiguous and robust quantum sensing," Phys. Rev. Lett. **122**, 200403 (2019).

[175] M. Pfender, N. Aslam, H. Sumiya, S. Onoda, P. Neumann, J. Isoya, C. A. Meriles, and J. Wrachtrup, "Nonvolatile nuclear spin memory enables sensor-unlimited nanoscale spectroscopy of small spin clusters," Nat. Commun. **8**, 834 (2017).

[176] S. Zaiser, T. Rendler, I. Jakobi, T. Wolf, S.-Y. Lee, S. Wagner, V. Bergholm, T. Schulte-Herbrüggen, P. Neumann, and J. Wrachtrup, "Enhancing quantum sensing sensitivity by a quantum memory," Nat. Commun. **7**, 12279 (2016).

[177] C. E. Bradley, J. Randall, M. H. Abobeih, R. C. Berrevoets, M. J. Degen, M. A. Bakker, M. Markham, D. J. Twitchen, and T. H. Taminiau, "A ten-qubit solid-state spin register with quantum memory up to one minute," Phys. Rev. X **9**, 031045 (2019).

[178] S. L. N. Hermans, M. Pompili, H. K. C. Beukers, S. Baier, J. Borregaard, and R. Hanson, "Qubit teleportation between non-neighbouring nodes in a quantum network," Nature **605**, 663 (2022).

[179] T. K. Unden, D. Louzon, M. Zwolak, W. H. Zurek, and F. Jelezko, "Revealing the emergence of classicality using nitrogen-vacancy centers," Phys. Rev. Lett. **123**, 140402 (2019).

[180] I. Schwartz, J. Scheuer, B. Tratzmiller, S. Müller, Q. Chen, I. Dhand, Z.-Y. Wang, C. Müller, B. Naydenov, F. Jelezko, and M. B. Plenio, "Robust optical polarization of nuclear spin baths using hamiltonian engineering of nitrogen-vacancy center quantum dynamics," Sci. Adv. **4**, eaat8978 (2018).

[181] D. Pagliero, A. Laraoui, J. D. Henshaw, and C. A. Meriles, "Recursive polarization of nuclear spins in diamond at arbitrary magnetic fields," Appl. Phys. Lett. **105**, 242402 (2014).

[182] T. Chakraborty, J. Zhang, and D. Suter, "Polarizing the electronic and nuclear spin of the nv-center in diamond in arbitrary magnetic fields: analysis of the optical pumping process," New J. Phys. **19**, 073030 (2017).

[183] P. Neumann, J. Beck, M. Steiner, F. Rempp, H. Fedder, P. R. Hemmer, J. Wrachtrup, and F. Jelezko, "Single-shot readout of a single nuclear spin," Science **329**, 542 (2010).

[184] S. Sangtawesin, C. A. McLellan, B. A. Myers, A. C. B. Jayich, D. D. Awschalom, and J. R. Petta, "Hyperfine-enhanced gyromagnetic ratio of a nuclear spin in diamond," New J. Phys. **18**, 083016 (2016).

[185] M. Chen, M. Hirose, and P. Cappellaro, "Measurement of transverse hyperfine interaction by forbidden transitions," Phys. Rev. B **92**, 020101 (2015).

[186] A. G. Fowler, M. Mariantoni, J. M. Martinis, and A. N. Cleland, "Surface codes: Towards practical large-scale quantum computation," Phys. Rev. A **86**, 032324 (2012).

[187] R. Barends, J. Kelly, A. Megrant, A. Veitia, D. Sank, E. Jeffrey, T. C. White, J. Mutus, A. G. Fowler, B. Campbell, Y. Chen, Z. Chen, B. Chiaro, A. Dunsworth, C. Neill, P. O'Malley, P. Roushan, A. Vainsencher, J. Wenner, A. N. Korotkov, A. N. Cleland, and J. M. Martinis, "Superconducting quantum circuits at the surface code threshold for fault tolerance," Nature **508**, 500 (2014).

[188] Y. Song, J. P. Kestner, X. Wang, and S. Das Sarma, "Fast control of semiconductor qubits beyond the rotating-wave approximation," Phys. Rev. A **94**, 012321 (2016).

[189] Y.-C. Yang, S. N. Coppersmith, and M. Friesen, "Achieving high-fidelity single-qubit gates in a strongly driven silicon-quantum-dot hybrid qubit," Phys. Rev. A **95**, 062321 (2017).

[190] N. Khaneja, R. Brockett, and S. J. Glaser, "Time optimal control in spin systems," Phys. Rev. A **63**, 032308 (2001).

[191] U. Boscain and P. Mason, "Time minimal trajectories for a spin 1/2 particle in a magnetic field," J. Math. Phys. **47**, 062101 (2006).

[192] Z.-H. Wang and V. V. Dobrovitski, "Time-optimal rotation of a spin $\frac{1}{2}$: Application to the NV center spin in diamond," Phys. Rev. B **84**, 045303 (2011).

[193] C. Avinadav, R. Fischer, P. London, and D. Gershoni, "Time-optimal universal control of two-level systems under strong driving," Phys. Rev. B **89**, 245311 (2014).

[194] J. Scheuer, X. Kong, R. S. Said, J. Chen, A. Kurz, L. Marseglia, J. Du, P. R. Hemmer, S. Montangero, T. Calarco, B. Naydenov, and F. Jelezko, "Precise qubit control beyond the rotating wave approximation," New J. Phys. **16**, 093022 (2014).

[195] C. T. Nguyen, D. D. Sukachev, M. K. Bhaskar, B. Machielse, D. S. Levonian, E. N. Knall, P. Stroganov, C. Chia, M. J. Burek, R. Riedinger, H. Park, M. Lončar, and M. D. Lukin, "An integrated nanophotonic quantum register based on silicon-vacancy spins in diamond," Phys. Rev. B **100**, 165428 (2019).

[196] K. C. Miao, J. P. Blanton, C. P. Anderson, A. Bourassa, A. L. Crook, G. Wolfowicz, H. Abe, T. Ohshima, and D. D. Awschalom, "Universal coherence protection in a solid-state spin qubit," Science **369**, 1493 (2020).

[197] H. L. Stern, Q. Gu, J. Jarman, S. Eizagirre Barker, N. Mendelson, D. Chugh, S. Schott, H. H. Tan, H. Sirringhaus, I. Aharonovich, and M. Atatüre, "Room-temperature optically detected magnetic resonance of single defects in hexagonal boron nitride," Nat. Commun. **13**, 618 (2022).

[198] F. Yan, S. Gustavsson, J. Bylander, X. Jin, F. Yoshihara, D. G. Cory, Y. Nakamura, T. P. Orlando, and W. D. Oliver, "Rotating-frame relaxation as a noise spectrum analyser of a superconducting qubit undergoing driven evolution," Nat. Commun. **4**, 2337 (2013).

[199] I. I. Rabi, N. F. Ramsey, and J. Schwinger, "Use of rotating coordinates in magnetic resonance problems," Rev. Mod. Phys. **26**, 167 (1954).

[200] F. Bloch and A. Siegert, "Magnetic resonance for nonrotating fields," Phys. Rev. **57**, 522 (1940).

[201] D. E. MacLaughlin, "Suppression of nutation angle variation in pulsed nuclear magnetic resonance," Rev. Sci. Instrum. **41**, 1202 (1970).

[202] P. London, P. Balasubramanian, B. Naydenov, L. P. McGuinness, and F. Jelezko, "Strong driving of a single spin using arbitrarily polarized fields," Phys. Rev. A **90**, 012302 (2014).

[203] K. R. K. Rao and D. Suter, "Nonlinear dynamics of a two-level system of a single spin driven beyond the rotating-wave approximation," Phys. Rev. A **95**, 053804 (2017).

[204] C. P. Bidinosti, G. Tastevin, and P.-J. Nacher, "Generating accurate tip angles for NMR outside the rotating-wave approximation," J. Magn. Reson. **345**, 107306 (2022).

[205] J. Johansson, P. Nation, and F. Nori, "QuTiP 2: A Python framework for the dynamics of open quantum systems," Comput. Phys. Commun. **184**, 1234 (2013).

[206] D. Zeuch, F. Hassler, J. J. Slim, and D. P. DiVincenzo, "Exact rotating wave approximation," Ann. Phys. **423**, 168327 (2020).

[207] A. P. Peirce, M. A. Dahleh, and H. Rabitz, "Optimal control of quantum-mechanical systems: Existence, numerical approximation, and applications," Phys. Rev. A **37**, 4950 (1988).

[208] J. P. Palao and R. Kosloff, "Optimal control theory for unitary transformations," Phys. Rev. A **68**, 062308 (2003).

[209] R. Kosloff, S. Rice, P. Gaspard, S. Tersigni, and D. Tannor, "Wavepacket dancing: Achieving chemical selectivity by shaping light pulses," Chem. Phys. **139**, 201 (1989).

[210] J. Werschnik and E. K. U. Gross, "Quantum optimal control theory," (2007), arXiv:0707.1883.

[211] I. Schaefer, "Quantum optimal control theory of harmonic generation," (2012), arXiv:1202.6520.

[212] G. Balasubramanian, P. Neumann, D. Twitchen, M. Markham, R. Kolesov, N. Mizuochi, J. Isoya, J. Achard, J. Beck, J. Tissler, V. Jacques, P. R. Hemmer, F. Jelezko, and J. Wrachtrup, "Ultralong spin coherence time in isotopically engineered diamond," Nat. Mater. **8**, 383 (2009).

[213] Z. Zhao, X. Ye, S. Xu, P. Yu, Z. Yang, X. Kong, Y. Wang, T. Xie, F. Shi, and J. Du, "Sub-nanotesla sensitivity at the nanoscale with a single spin," Natl. Sci. Rev. **10**, nwad100 (2023).

[214] K. Yamauchi, J. Janssen, and A. Kentgens, "Implementing solenoid microcoils for wide-line solid-state NMR," J. Magn. Reson. **167**, 87 (2004).

[215] E. W. Hagaman, J. Jiao, and T. Moore, "The generation of intense radiofrequency fields in μcoils," J. Magn. Reson. **193**, 150 (2008).

[216] A. Webb, "Radiofrequency microcoils for magnetic resonance imaging and spectroscopy," J. Magn. Reson. **229**, 55 (2013).

[217] L. Jiang, J. S. Hodges, J. R. Maze, P. Maurer, J. M. Taylor, D. G. Cory, P. R. Hemmer, R. L. Walsworth, A. Yacoby, A. S. Zibrov, and M. D. Lukin, "Repetitive readout of a single electronic spin via quantum logic with nuclear spin ancillae," Science **326**, 267 (2009).

[218] S. Valera and B. E. Bode, "Strategies for the synthesis of yardsticks and abaci for nanometre distance measurements by pulsed epr," Molecules **19**, 20227 (2014).

[219] C. P. Slichter, *Principles of Magnetic Resonance*, Springer Series in Solid-State Sciences, Vol. 1 (Springer Berlin Heidelberg, Berlin, Heidelberg, 1990).

[220] M. Loretz, J. M. Boss, T. Rosskopf, H. J. Mamin, D. Rugar, and C. L. Degen, "Spurious harmonic response of multipulse quantum sensing sequences," Phys. Rev. X **5**, 021009 (2015).

[221] T. Staudacher, *Nuclear magnetic resonance spectroscopy on a nanoscopic sample volume*, Ph.D. thesis, Stuttgart University, Stuttgart (2015).

[222] I. Aharonovich, S. Castelletto, D. A. Simpson, C.-H. Su, A. D. Greentree, and S. Prawer, "Diamond-based single-photon emitters," Rep. Prog. Phys. **74**, 076501 (2011).

[223] H. H. Haeri, P. Spindler, J. Plackmeyer, and T. Prisner, "Double quantum coherence ESR spectroscopy and quantum chemical calculations on a BDPA biradical," Phys. Chem. Chem. Phys. **18**, 29164 (2016)

List of publications

[1] **D. Yudilevich**, R. Stöhr, A. Denisenko, and A. Finkler, "Mapping single electron spins with magnetic tomography," Phys. Rev. Appl. 18, 054016 (2022).

[2] **D. Yudilevich**, A. Salhov, I. Schaefer, K. Herb, A. Retzker, and A. Finkler, "Coherent manipulation of nuclear spins in the strong driving regime," New J. Phys. 25, 113042 (2023).

[3] J. Kumar, **D. Yudilevich**, A. Smooha, I. Zohar, A. K. Pariari, R. Stöhr, A. Denisenko, M. Hücker, and A. Finkler, "Room temperature relaxometry of single nitrogen-vacancy centers in proximity to $\alpha-\mathrm{RuCl}_3$ nanoflakes," (2023), arXiv:2312.15541 [cond-mat.mes-hall] *(submitted, under review)*.

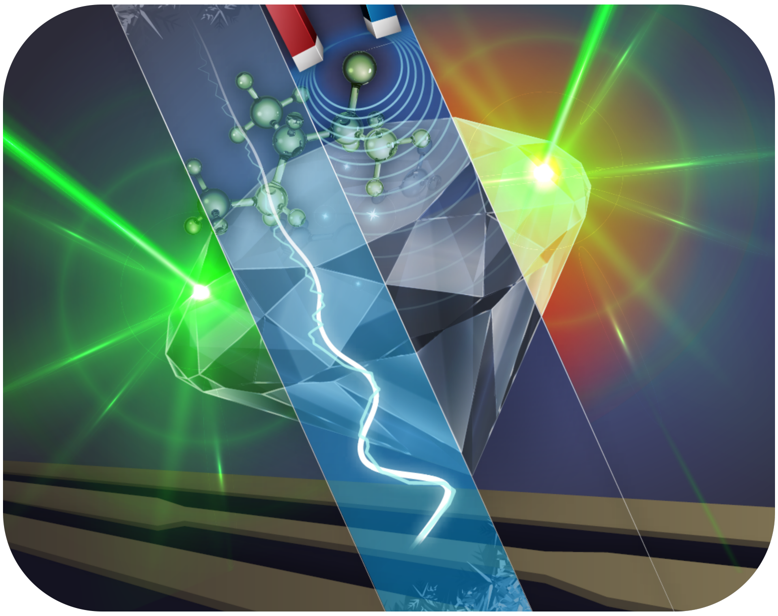

This thesis was typeset using LaTeX, originally developed by Leslie Lamport and based on Donald Knuth's TeX. The body text is set in 11 point Egenolff-Berner Garamond, a revival of Claude Garamont's humanist typeface. A template that can be used to format a PhD thesis with this look and feel has been released under the permissive MIT (X11) license and can be found online at github.com/suchow/Dissertate or from its author, Jordan Suchow, at suchow@post.harvard.edu.